Dissertation zur Erlangung des Doktorgrades

der Fakultät für Chemie und Pharmazie

der Ludwig-Maximilians-Universität München

Post-Synthetic Modification of MOF Nanoparticles

Olaf Alberto Dario von Mankowski

aus

München, Deutschland

2018

ERKLÄRUNG

Diese Dissertation wurde im Sinne von § 7 der Promotionsordnung vom 28. November 2011 von Frau Prof. Dr. Bettina V. Lotsch betreut.

EIDESSTATTLICHE VERSICHERUNG

Diese Dissertation wurde eigenständig und ohne unerlaubte Hilfe erarbeitet.

München, 12.11.2018

_____

Olaf Alberto Dario von Mankowski

Dissertation eingereicht am	21.09.2018
1. Gutachterin:	Prof. Dr. Bettina V. Lotsch
2. Gutachter:	Prof. Dr. Thomas Bein
Mündliche Prüfung am	30.10.2018

A mi madre

ACKNOWLEDGMENTS

Acknowledgments

Ebenso möchte ich meinem ehemaligen Kollegen und fortwährenden Freund Dr. Christian Ziegler danken, für die Motivation, Aufmunterung, Ablenkung und natürlich grandiose Wandertour. Es ist mir immer eine große Freude mit dir etwas zu unternehmen.

Dr. Felix Hartrampf, dir als ewigen Begleiter in meinem Leben, will ich dir meinen unendlichen Dank für dein Vertrauen und die unzertrennliche Freundschaft ausdrücken. Martin und Peter Schaefer, ihr steht dem in Nichts nach. Ich denke immer mit großer Freude an Euch und danke für die Zeit in der Landwehrstraße und auch außerhalb. Katharina und Laura, ihr natürlich auch!

Ana, mil gracias. Y otros mil más, que tampoco serán suficientes para expresar mi gratitud y agradecimiento.

Ich danke ebenso meiner ganzen Familie, meinem Vater Henry und meinen Brüdern Alejandro und Daniel. Auch wenn es manchmal schwierig war, ich freue mich euch zu haben. Auch dich Przemek. Ewa, dir einen ganz herzlichen Dank, es ist schön in dir eine zweite Mutter zu finden.

Stebbo, dir gebührt mein letzter Dank. Ich hätte mir nie erträumt einen so wundervollen Menschen zu finden und dann noch als Freund bezeichnen zu dürfen. Du warst mir eine unglaubliche Stütze in all diesen Jahren. Kein Wort könnte meine Dankbarkeit, die ich dir gegenüber empfinde, ausdrücken!

Findet die Wahrheit,

denn die Wahrheit macht euch frei!

(Albertus Magnus)

TABLE OF CONTENTS

1   INTRODUCTION

Many phenomena in both animate and inanimate nature would be unthinkable without the structural feature we know as porosity. For example, the renewal of potable ground water due to the permeation of rainwater through geological strata[1] or the human respiratory system, precisely the pores of Kohn,[2] are vital to human life and depend on porous structures. Evidently, the innumerable manifoldness in function, structure, morphology, degree of hierarchical organization, etc. of porous materials largely depends on their composition. For the examples given, this is contrasted by poorly ordered inorganic rock formations which evolved throughout millions of years vs. highly ordered, complex biological tissue that is formed within a few years, genetically coded through millions of years of evolution as well.

In order to design porous materials for specific applications and needs, the ability to control, engineer and manipulate the components and structures as a whole, is indispensable. Within the last two decades, metal-organic frameworks (MOFs) have emerged as a promising material class that covers these requisites within the world of porous materials.[3] MOFs are composed of coordinatively linked molecular building units, which can be manipulated and targeted individually, both pre- and post-synthetically, for the introduction of a specific functionality or adjusted to a specific need.

This thesis aims at exploring the possibilities of post-modification routes to manipulate established MOF structures for specific applications.

In Chapter 1.1, an introduction to the material class of metal-organic frameworks is given, with the Subchapters 1.1.1 and 1.1.2 treating the MOF structures investigated in this work. The concept of post-synthetic modification is explained in Chapter 1.2. Further, the applications for which the modified MOFs are used, are described in the Chapters 1.3 to 1.5. These include the technique of pulsed laser deposition (PLD) (Chapter 1.3), photonic crystal based optical sensors (Chapter 1.4), and gas storage and separation (Chapter 1.5). The objectives of this thesis are formulated in more detail in Chapter 1.6.

1.1   METAL-ORGANIC FRAMEWORKS

Generally, materials exhibiting pores, e.g. cavities, channels, slits or interstices, are considered to be porous. They can be of natural origin, such as rocks, soil or biological tissue, or can be synthetically produced, e.g. cements or polymeric foams. Apart from the pore shape, properties like the pore size and chemical affinity to potential guest-species are important pore characteristics that can differ extremely between porous materials. In all cases, the pore properties are defined by the composition of the scaffold material itself. Not surprisingly, tailoring and engineering the pore characteristics is of fundamental interest in order to exploit these structures for specific applications. In turn, this requires a high degree of control of the constituent materials. With the emergence of metal-organic frameworks (MOFs) two decades ago, a new material class is at disposal to fabricate custom-designed, ordered, porous structures.

Since then, the field of MOFs has evolved rapidly, initially being driven by the exploration of new structures and now experiencing a focus shift towards exploiting the promising properties for diverse applications of known structures.[4] The fascination of this research area is easily understood when considering the underlying basic structure of MOFs. IUPAC recommends the definition as coordination compounds that extend through repeating coordination entities in 2 or 3 dimension with organic ligands potentially containing voids.[5] In principle, this is reflected in a hybrid structure of an inorganic building block, referred to as secondary building unit (SBU), that is coordinatively linked by organic multidental ligand molecules to yield a potentially porous, often but not necessarily crystalline framework (Figure 1.1.1 (a)).
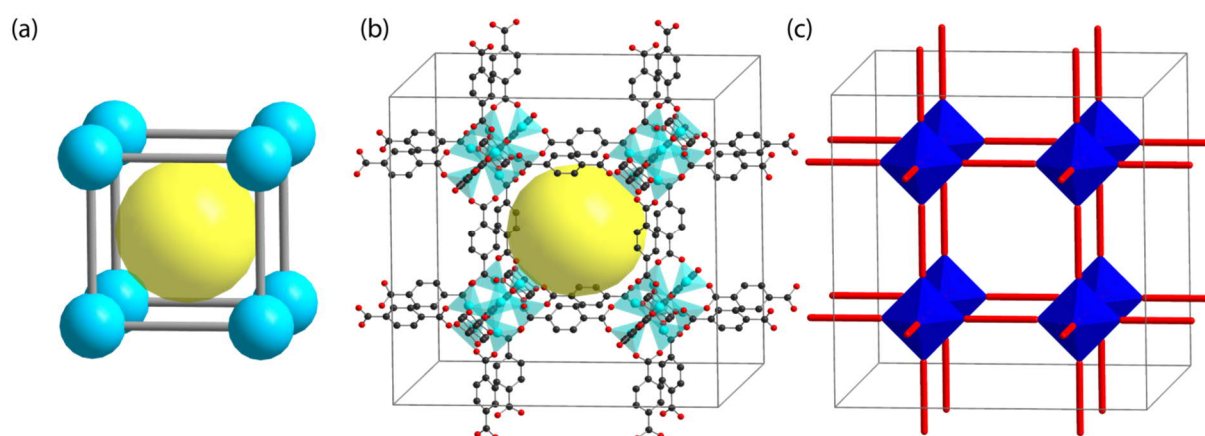
Figure 1.1.1: (a) Schematic illustration of a MOF structure with the SBU in light blue and the linker unit in grey yielding a porous framework (yellow sphere), (b) structure of prototypical MOF-5 with zinc atoms given in light blue, carbon in black, oxygen in red, the yellow sphere represents the pore, the grey lines the cell edges; for clarity, hydrogen atoms are omitted, and (c) abstraction into the augmented form of the pcu net, with the $Zn_4O(CO_2)_6$ SBU as an octahedron in blue and the ditopic terephthalate as a rod in red.

The SBU is generally composed of (transition) metal ions forming well-defined clusters that can be abstracted into simple geometrical shapes, e.g. squares, tetrahedra, or octahedra. The vertices of these geometric figures act as nodes at which functional groups of rigid organic ligands, that can be abstracted into geometric shapes themselves, bind coordinatively and, thus, interconnect the SBUs into an extensive framework of a specific network topology (e.g. pcu net topology, Figure 1.1.1 (c)).[5-7] Judiciously designed molecular building blocks (MBBs) can therefore be assembled into predetermined ordered structures/networks, a process known as reticular synthesis.[8] This modular approach allows the design, engineering and control of the framework (topologies).[9] Obviously, the innumerable number of MBBs and combination possibilities give rise to a plethora of structures that can, basically, be pre-designed and adjusted for specific purposes. In most cases, the structures exhibit voids of up to several nanometers, the structural feature decisive for the great interest and success of MOFs. The intrinsic porosity with large accessible surface areas render MOFs the ideal material for adsorption of guest species.

MOFs have therefore been studied extensively for the storage and separation of gases, including greenhouse gases (CO_2) and energy-related gases (H_2, CH_4, C_xH_y), as well as for the removal of toxic gases (CO, H_2S, NH_3, SO_x, NO_x).[10-14] In Chapter 1.5, the aspect of CO_2 storage and separation from N_2 and CH_4 is explained in more detail. Furthermore, water adsorption covers an increasingly important aspect as MOFs can be used for dehumidification, heat-pumps and chillers, thermal batteries and storage of potable water in remote areas.[15,16] Catalysis is another fundamental application, as the high intrinsic surface areas and the ability to potentially impregnate the framework with co-catalysts or to act as the catalyst itself, make them an ideal platform for Lewis-acidic, photo- or electrocatalytic conversions.[17-20] MOFs have also been proposed for biomedical applications, e.g. for drug delivery or as MRI contrast agents,[21-23] as proton conductors for fuel cells,[24] or as sensors.[25-27] The latter aspect is discussed in Chapter 1.4 for photonic crystal based sensors, where MOFs can act as the stimuli-responsive material. More recently, MOFs have been discussed for photochemical, magnetic and electrochemical applications,[27-33] with probably more application fields to come.

For many of the applications given above, the control of structuring MOFs at different length scales is of utmost importance. The successful integration of MOFs into functional devices does not only depend on the crystal structure itself, but to a large extent on the ability to control it at the nano-, meso- and macroscale as well. For example, this includes manipulation of the crystallite size and morphology (nanoscale), organizing the crystallite ensemble into the desired orientation and/or pattern (mesoscale), and, all in all, shaping the assembly into an overall structure at the macroscale for the specific applicative need. As a matter of fact, structuring at a certain length scale will in turn have consequences on the other length scales, and, hence, the techniques employed for structuring

can affect various length scales. Figure 1.1.2 gives an exemplary overview of different synthetic methods, approaches and (deposition) techniques for this purpose.
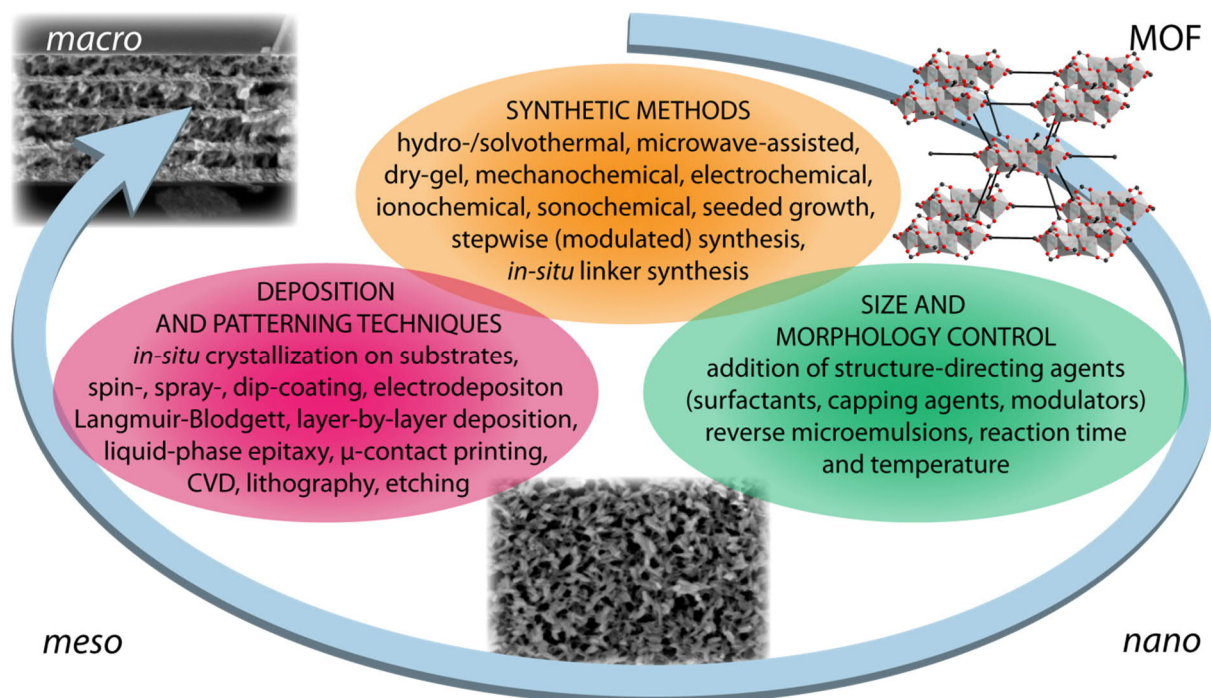
Figure 1.1.2: Schematic overview of exemplary synthetic methods and routes, fabrication and deposition techniques for the structuring of MOFs at different length scales. Representative images of the simplified CAU-1 (MOF) structure, scanning electron microscope image of a thin film of rice-corn shaped CAU-1 particles (nano/mesoscale) and hierarchical architecture of a one-dimensional photonic crystal (macroscale), in clockwise order.

Naturally, the obtained MOF structure depends on the precursors employed, namely the linker and the metal salt, the concentration, solvent, reaction time and temperature, etc. However, the applied synthetic methods can have a strong impact on the resulting morphology or crystallite size. Apart from the conventional solvothermal reactions, carried out at room-temperature or elevated temperatures by conventional oil-bath heating, many other approaches have been implemented for MOF synthesis, which include microwave-assisted and ultrasonic heating, ionothermal, electro- and mechanochemical syntheses, dry-gel conversions, (reverse) microemulsions and microfluidic methods.[34,35] Morphological and size control can further be achieved by the addition of surfactants, polymers, modulators and other structure-directing and capping agents during synthesis, or by etching the MOF particles post-synthetically.[34,36-39] Even hollow structures are accessible by making use of the Kirkendall effect.[40] When it comes to patterning, localization and the fabrication of larger structures, a variety of both bottom-up and top-down procedures are employed. Especially for thin films, numerous techniques have been proven to be effective, either by direct growth or deposition, for example by in-situ crystallization on a substrate, seeded growth, evaporation induced crystallization, sequential immersion of a functionalized substrates, e.g. self-assembled monolayers, into solutions of the precursors (SURFMOFs), liquid-phase epitaxy, Langmuir-Blodgett and layer-by-layer techniques or

electrochemical deposition.[41-44] In addition, preformed MOF nanocrystals can be deposited by dip-, spray- and spin-coating, μ-contact printing or inkjet-printing.[44-47] Lithographic processing allows further patterning and structuring of the MOF films.[45,47]

More recently, Stassen et al. described the chemical vapor deposition of the MOF ZIF-8 by atomic-layer deposition of a metal-oxide film, which consecutively undergoes a vapor-solid reaction with the vaporized organic linker.[48] Nonetheless, deposition methods involving the physical evaporation of already assembled MOFs are still challenging, as the compounds are generally non-volatile and are prone to decomposition rather than evaporation. Within this thesis, the physical vapor deposition of the prototypic ZIF-8 by means of pulsed laser deposition was investigated. A description of this method is given in Chapter 1.3. Furthermore, the spin-coating technique was employed for the fabrication of MOF thin film and photonic crystal structures (Chapter 1.4) and is described in more detail in Chapter 1.4.1.

In the following, the MOFs ZIF-8 and CAU-1 (Chapters 1.1.1 and 1.1.2), which were synthesized and employed within the projects of this thesis, are presented.

1.1.1   ZIF-8

Zeolitic imidazolate frameworks (ZIFs) belong to one of the best studied subclasses of MOFs, in which the metals (M) are bridged by imidazolates linkers (Im). As their name implies, the comprised structures are related to that of zeolites, where the M-Im-M bridging angle of ≈145° is similar to that of Si-O-Si in (alumino-)silicates resulting in similar network topologies (Figure 1.1.3).[49] Furthermore, ZIFs combine outstanding thermal and chemical stabilities with permanent porosity.[50,51]
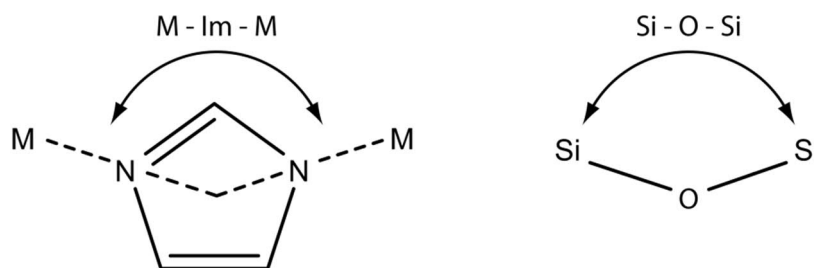
Figure 1.1.3: Schematic illustration of the M-Im-M bridging angle in a ZIF (left) and Si-O-Si in (alumino-)silicates.

Among the most prominent representatives of the ZIF family is ZIF-8, $Zn(H_3C-Im)_2$, with over 2600 related publications by the end of 2017.[a] In 2006, Park et al. described a series of ZIFs that included a cubic structure (a = 16.9932 Å) with the sodalite (sod) topology.[50] The compound consists of zinc atoms that form the nodes of a sodalite cage and are coordinated tetrahedrally by four 2-methylimidazolates (Figure 1.1.4). At the center of the polyhedron, a pore with a diameter of 11.6 Å is formed, which is accessible through 3.4 Å wide apertures. Interestingly, ZIF-8 can undergo a structural deformation

---

[a] Reference results for the keyword "ZIF-8" by SciFinder® (Chemical Abstract Service).

upon adsorption of guest molecules, which induce the rotation of the imidazolate linkers (Figure 1.1.4 (c)).[52-54] Hence, the effective pore window is enlarged, and molecular sieving studies suggest that the aperture windows widen up significantly to 4.0 – 5.8 Å,[55-60] consequently, giving access to much larger molecules than permitted by the smaller initial window. In this thesis, ZIF-8 was employed as prototypic MOF for thin film fabrication by pulsed laser deposition (Chapter 1.3).
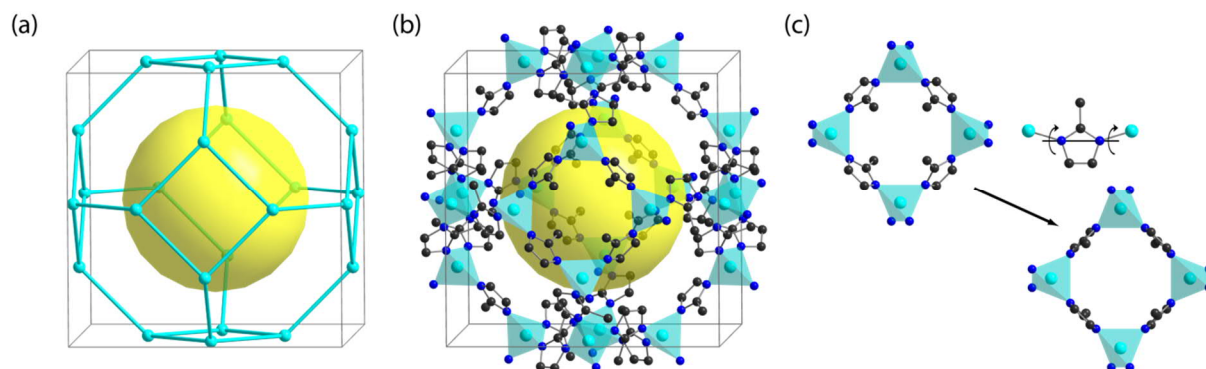
Figure 1.1.4: (a) Schematic representation of the sodalite net topology including the pore of ZIF-8, (b) crystal structure of ZIF-8 with pore and (c) structural deformation caused by the rotation of the imidazolate linkers. Zinc is given in turquois, carbon in black, nitrogen in blue, the yellow sphere represents the pore, the grey lines the cell edges. For clarity, hydrogen atoms are omitted.

1.1.2   CAU-1

CAU-1 is named after the Christian-Albrechts-University in Kiel, Germany, where it was first synthesized. It is a 12-connected porous aluminum based MOF of tetragonal crystal lattice (a = 18.3517 Å, c = 17.7720 Å) in which the inorganic clusters are interconnected by 2-aminoterephthalates.[61] Figure 1.1.5 shows how the SBUs, consisting of wheel-shaped 8-rings of corner- and edge-sharing AlO_6 octahedra, are bridged by the organic linker to form a distorted octahedral pore of 10 Å diameter and an adjacent smaller distorted tetrahedral pore of 4.5 Å diameter, leaving a 3 – 4 Å wide aperture for cage access. As each wheel is connected to 12 linker units, four of them in-plane, and additional four above and four below the ring, it leaves the inorganic cluster with an uncompensated positive twelvefold charge. These residual coordinative sites are saturated with hydroxy and methoxy groups, which are provided by the precursors and the reaction solvent, to achieve charge neutrality resulting in a SBU of the composition $Al_8(OH)_4(OCH_3)_8^{12+}$ and 12 negatively charged 2-aminoterephthalates. Like similar aluminum based frameworks, CAU-1 exhibits a high thermal stability up to 360 °C. In this thesis, CAU-1 was employed as functional layer material in one-dimensional photonic crystal based sensors (Chapter 1.4) and as a storage and separation material for CO_2 and CH_4 (Chapter 1.5).
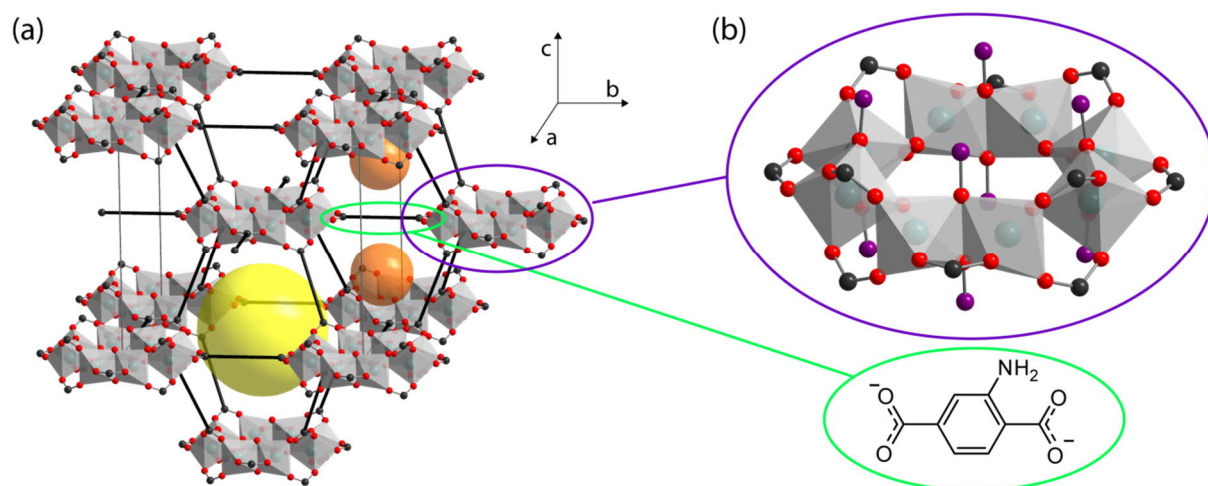
Figure 1.1.5: (a) Simplified representation of the CAU-1 structure showing the two types of pores (yellow and orange spheres) and (b) the detailed structure of the $Al_8(OH)_4(OCH_3)_8^{+12}$ cluster and the 2-aminoterephthalate linker. Aluminum is given in teal, bridging carbon in black, methanolate carbon in violet, oxygen in red, the grey lines represent the cell edges. For clarity, hydrogen atoms are omitted.

1.2   POST-MODIFICATION OF METAL-ORGANIC FRAMEWORKS

Although the MBB approach enables the design of MOFs on a theoretical level, synthetic limitations often encumber the practical realization of certain structures. Isoreticular MOFs often cannot be synthesized by application of synthetic conditions that were valid for other representatives of the same isoreticular series as altered solubilities can lead to unforeseen kinetic and thermodynamic (by-)products or the interpenetration of the frameworks. All in all, there are manifold reasons that require the readjustment of the synthetic conditions, such as the reaction temperature, time, solvent, pressure, precursor concentration, to mention a few. Unfortunately, this process is often tedious, time consuming and expensive, rendering it unviable. In the worst case, the desired MOF might be even unattainable under the new conditions.

Nonetheless, an alternative strategy has been proven efficient for tuning and engineering the framework properties and has become a well-established tool: the post-synthetic modification (PSM). This approach allows the introduction and manipulation of chemical functionalities on already synthesized MOFs, avoiding the need of adjustments at a pre-synthetic level. In principle, the modification is directed at the MBBs, namely, the SBU and/or the organic linker. To a certain extent, the pores can also be considered a possible post-synthetic target for processes that typically include guest removal, exchange or insertion, as well as ion exchange for charged MOFs.[62] Furthermore, several types of modifications can be distinguished: initially, the post-synthetic covalent and coordinative, also termed dative, modification, as well as the deprotection.[62-65] More recently, post-synthetic exchange, insertion, polymerization and post-metalation have been added to the library of available modifications.[66-69] Abundant examples can be found in the reviews cited. An overview of the different concepts is illustrated in Figure 1.2.1.
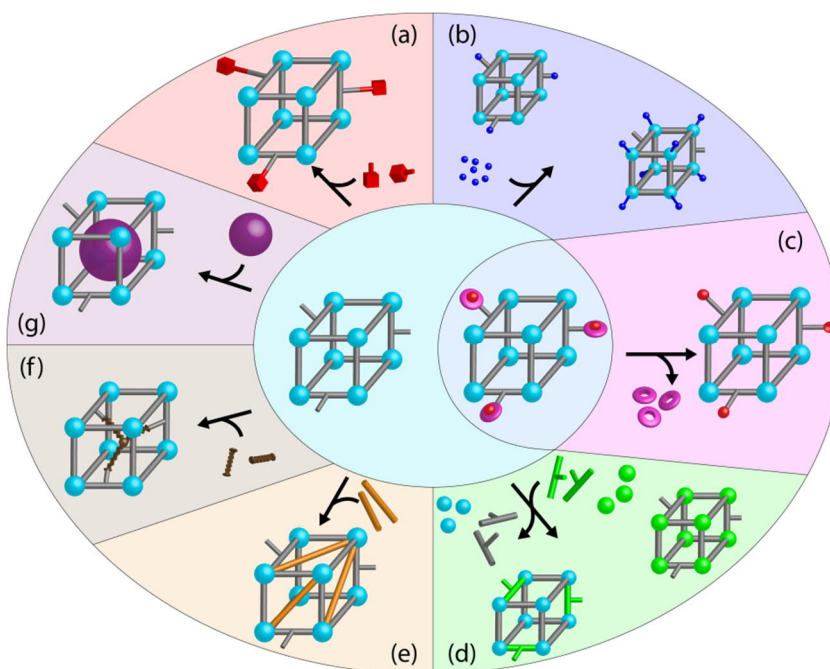
Figure 1.2.1: Schematic illustration of post-synthetic (a) covalent modification, (b) coordinative/dative modification, (c) deprotection, (d) exchange, (e) insertion, (f) polymerization and (g) encapsulation. The SBUs are represented as spheres, linkers as rods. The relevant changes for each modification are highlighted by different colors.

One of the earliest and most common forms of PSM is the one of covalent nature. Many classical approaches known from the organic chemistry have been implemented, e.g. the direct nitration of the terephthalate linker and subsequent reduction to form amines,[70] the conversion of functional groups (amines, alcohols, thiols, etc.)[63,71] and even "click-chemistry".[72]

Another possibility is the coordinative modification, e.g. the coordination of a bipyridin linker with a transition metal.[73] Additionally, the coordinative modification can target the SBU of the MOF.[74] The term post-metalation is also used for the coordination of the linker porphyrinic unit,[75] although this can also refer to the encapsulation of a metal into the pore (see below). These modifications are often used to impart catalytic functionality.

Instead of a post-synthetic bond formation, a cleavage is also sensible for particular cases. For example, the pre-synthetic protection of functional groups, which might interfere with the MOF formation, can be cleaved after the MOF assembly, although the protecting step can be performed on the already assembled MOF as well.[76,77] Here, the typical protecting groups from amino-acid chemistry can be used.[78] The cleavage can be done via pyrolysis, photolysis or chemically.

Among the more recent forms of modifications are the complete exchange and insertion of building blocks.[79-81] Solvent-assisted ligand exchange is performed by placing the MOF into an excess solution of the desired linker. Upon exchange of the linkers, the framework topology is retained while imparting new chemical functionality. Solvent-assisted ligand insertion is performed similarly and relies on the

substitution of terminal ligands at the SBU as long as there is sufficient space to accommodate the new ligand.

The concept of post-synthetic polymerization targets at the creation of a composite material, in which MOF particles or structures are interconnected through polymeric units. This is often beneficial if the MOF is desired to be implemented into a membrane or gel, as the polymer can be more easily shaped into the desired structure.[82-84]

In general, reversible uptake or release of guest species, e.g. for gas ad- and desorption, are not considered classical post-synthetic modification processes. In contrast, the encapsulation of metals or metal oxides, into the pores, a form of post-metalation, has drawn a considerable amount of attention of the community, as the composite material might exhibit enhanced catalytic, magnetic and optical properties.[85] For example, the insertion of metal (oxides) as co-catalysts offers further possibilities to enhance the catalytic performance of the MOF.[86,87]

Although the PSM approach largely expands the possibilities and scope at which the MOF properties can be fine-tuned and engineered, some important challenges remain. In particular, the degree of modification might not be quantitative, if the reactants are too large. In that case, only the external surface of a MOF particle might be modified. This leads to another crucial aspect of PSM: the question of the modification distribution and localization, which can have important consequences for intended applications. For example, obstruction and blocking of the inner pores can corrupt the diffusion of guest-species downgrading significantly the MOF performance for storage, separation or catalytic applications. Here, mixed-component MOFs (multivariative, MTV-MOFs) or core-shell MOFs can be a remedy,[88,89] in which only a limited number of functional sites are available or, as in the latter case, only on the core or shell region of the composite MOF.[90]

At the heart of this thesis is the PSM of MOF nanoparticles for the use and implementation in specific applications. These applications are further described in Chapter 1.3 for pulsed laser deposition, in Chapter 1.4 for one dimensional photonic crystal based sensors and in Chapter 1.5 for gas storage and separation.

1.3 PULSED LASER DEPOSITION

Physical vapor deposition (PVD) techniques comprise methods that transfer a target material into the gas phase from which it is redeposited onto a substrate for the fabrication of thin films. One of the most crucial steps is the initial ablation of the material that can be achieved by various methods, such as evaporation, sputtering or ion plating.[91-93] In pulsed laser deposition (PLD) this is done by focusing a high-energy pulsed laser on a target leading to the ejection of the material and the formation of a plasma plume from which it condenses onto a substrate to form a thin film.[94] A schematic illustration of a typical PLD setup is shown in Figure 1.3.1. In general, a high vacuum is applied to facilitate the

transition of the material into the gas phase. Naturally, the film will depend on the species ablated and formed within the plume as well as their velocities. These species or its deposits can be further influenced by applying a background gas, e.g. H_2, O_2, CH_2 or N_2, to the chamber allowing to influence the film growth and modify its chemistry.[95] Furthermore, to minimize damage and other effects from continuous radiation of the same irradiation spot, the target material can be rotated.
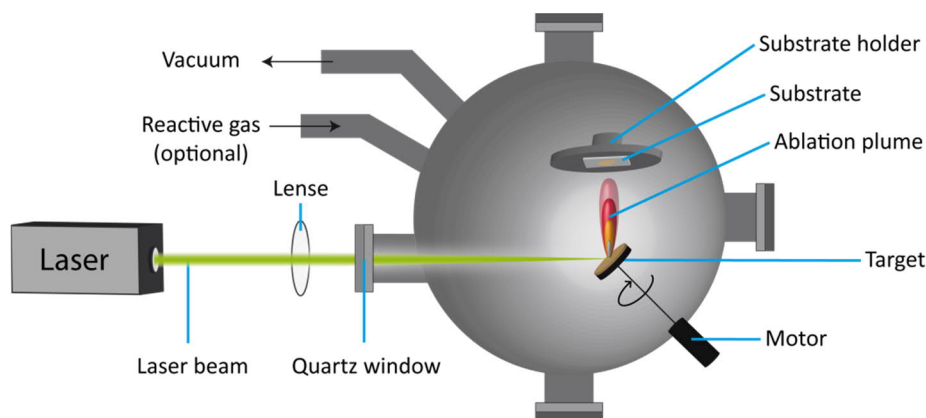
Figure 1.3.1: Schematic illustration of a typical PLD setup. A laser beam (green) is focused on a rotating target from which material is ejected forming a plume (red). The ejected material condenses on a substrate.

At the heart of this technique is the ablation of the material. For this purpose, the experimental conditions have to be chosen adequately and will depend on the irradiation source and the target material reciprocally. For the former, several parameters can be varied. For instance, the laser wavelengths employed can range from the NIR to the UV, pulse durations can be in the femtosecond regime up to several nanoseconds and the laser fluence, defined as the laser energy per pulse and unite area, can be varied to control the amount of material ablated. Although one can think of the ablation process as a rapid boiling of the target material within the laser interaction volume, the interaction of the laser with the target material is much more complex and will further depend on the absorptive behavior of the target. Therefore, the focus of many studies has been the light-matter interaction and the ablation plume formation. A more in-depth discussion on the reigning mechanisms can be found in the literature.[94,95]

While the PLD technique is regularly used to fabricate films of inorganic materials, its use to deposit soft material is limited. Although pulsed laser irradiation is widely used for the ablation of soft material, e.g. in ophthalmology[96] and matrix-assisted laser desorption/ionization mass spectrometry,[97] it is often accompanied with the decomposition of the material. This is associated with the thermal stress due to material heating. Nonetheless, it has been demonstrated for polymers that crystalline films can indeed be obtained.[98-100] Furthermore, with the development of matrix-assisted pulsed laser evaporation (MAPLE) in which the material is embedded in a matrix solution ,[101] biomaterials can be deposited as well.

Another major milestone within the PLD technique was the implementation of pulses of femtosecond (fs) duration. These very short pulses have substantial consequences. As the coupling of the electronic energy to the lattice happens on a time scale of picoseconds, heat diffusion becomes insignificant for shorter pulse lengths minimizing thermal collateral damage to the target material.[95]

All in all, the successful deposition of a film depends on a considerable number of parameters, such as those concerning the laser, the target material, the geometry of the setup and potential presence of background gases. In this thesis, a crystalline MOF, ZIF-8, was chosen as the target material for femtosecond PLD (Chapter 3). It is demonstrated that this target material can be made attainable for PLD by modifying it with a non-toxic polymer (PEG-400) to prevent its structural degradation and decomposition due to laser irradiation.

1.4 PHOTONIC CRYSTALS

Color is an ubiquitous phenomenon in both the vivid and non-vivid nature that has fascinated humanity for centuries. This is for example reflected by the importance of dyes and pigments in all cultures, which were partly traded as luxury goods. One of the intriguing aspects of colors is how they are formed. In case of the dyes and pigments, part of the reflected or transmitted light lacks a range of wavelengths due to absorption by the material and is hence perceived as colored. Closely related to that, emission processes like luminescence, e.g. fluorescence and phosphorescence, involve a change in the energy levels of the material. In addition to these pathways, there are structural colors, that find their origin in light interference in different structures.[102,103]

Among these, interference in periodic systems are structurally realized in so-called photonic crystals (PCs). In nature, they are the cause of the iridescence of natural opals and butterfly wings as shown in Figure 1.4.1. For example, in opals the silica particles are arranged regularly into a fcc lattice. The periodic pattern is also realized in the microstructure of many butterfly wings, giving them their characteristic color. The scales of the European peacock are layered periodically and the close-up view shows further structuring that, additionally, provides the basis for diffraction grating.
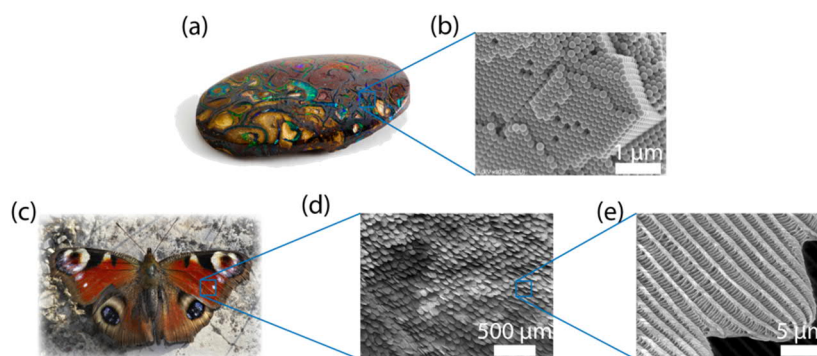
Figure 1.4.1: (a) Irridescence of a natural opal[104] and (b) a SEM image showing the underlying nanostructure of densely packed silica particles as in a fcc lattice.[105] (c) Coloration of the butterfly wings of an European peacock (Aglais io),[106] SEM images of (d) a patch of wing made of scales[107] and (e) close-up view of the microstructure of a scale.[108] Reproduced and adapted under the ☺ Creative Commons Licence, details in the bibliography.

All together, the term crystal can be interpreted in analogy to classical crystalline materials, where the atoms are packed into repetitive periodic units, e.g. by a lattice constant, giving rise to an electronic band structure. Similarly, PCs consist of regularly arranged building blocks, e.g. particles, films or rods, that, depending on their refractive index (RI), result in a photonic band gap like in semiconductors. The photonic band gap corresponds to a range of forbidden wavelengths, which are thus reflected and perceived as the color. The decisive parameters for the position and size of the photonic band gap is on one hand the materials RIs, on the other, the length scale of the periodic units. It is usually in the order of magnitude of the visible part of the electromagnetic spectrum. A more detailed description on the photonic band structure and how to calculate it can be found in the literature.[109-111] The periodicity of the PC can be in one, two or three dimensions of which the first one is also referred to as Bragg stacks (BSs) and can be seen as the hierarchically simplest assembly of a PC.

Basically, a BS can be fabricated by layering thin films of varying RIs, in which a high RI contrast ensures a wide photonic band gap. In Figure 1.4.2 (a) the pathway of the light through a BS is depicted. At each interface part of the light is reflected and transmitted, finally undergoing interference. The reflected wavelengths correspond to the frequencies of the forbidden energies, i.e. the photonic band gap. Note that different incident angles result in distinct reflectance and transmission spectra. Figure 1.4.2 (b) shows the theoretically calculated spectra that correspond to a BS of a total of ten layers. The alternating layers are 100 nm thick with refractive indices (RIs) of n_{low} = 1.4 and n_{high} = 1.9.
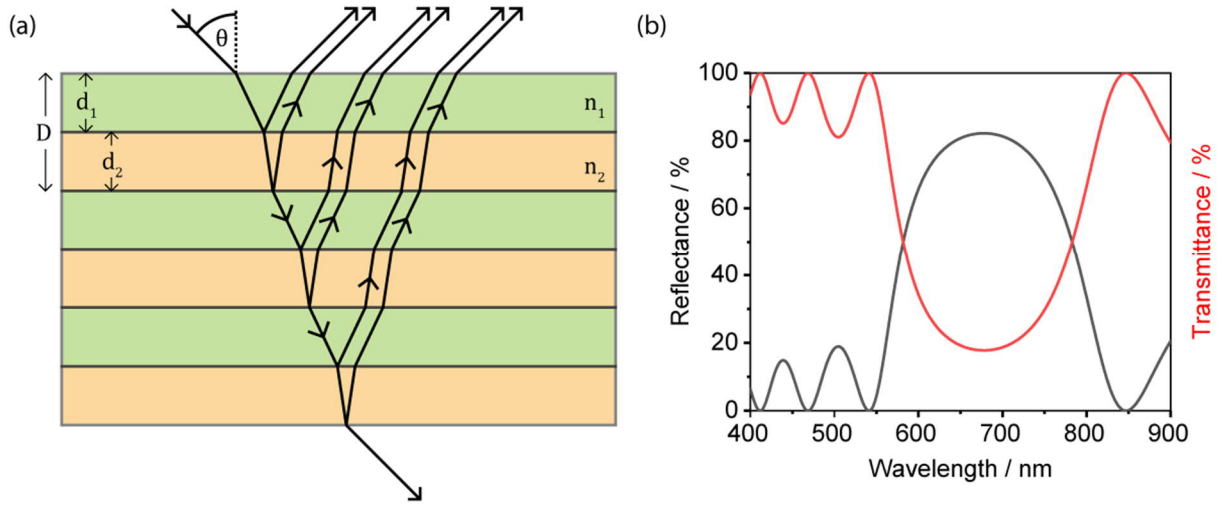
Figure 1.4.2: (a) Representative pathway of light impinging on a BS of three unit cells of different RIs (n_{low} and n_{high}) and thicknesses (d_{low} and d_{high}). The light is reflected and transmitted at each layer interface, and finally undergoes interference. (b) Exemplary theoretical reflectance and transmittance spectra of a BS with 10 layers of 100 nm thickness each and alternating RI (n_1 = 1.40 and n_2 = 1.90).

The term Bragg stack is readily understood when applying the same criteria as for the Bragg condition upon X-ray diffraction. The same principle applied in photonic crystals by combining the Bragg law with the Snell-law to account for two different optical media, yields Equation 1.4.1, where m is the order of reflection, λ the reflected wavelength, d the periodicity, n_{eff} the effective RI and θ the angle of incident light.[112]

$$m\lambda = 2D\left(n_{eff}^2 - \sin\theta^2\right)^{\frac{1}{2}} \qquad (1.4.1)$$

The effective RI is calculated according to Equation 1.4.2 with n_1, n_2, V_1 and V_2 the RIs and the respective volume fractions of the corresponding layers.

$$n_{eff} = n_1^2 V_1 + n_2^2 V_2 \qquad (1.4.2)$$

At normal incidence the equation simplifies to Equation 1.4.3.

$$m\lambda = 2(d_1 n_1 + d_2 n_2) \qquad (1.4.3)$$

Due to the fact that PCs are ideal platforms for the manipulation of the light propagation, they have attracted much attention for use in fiber and laser optics,[113,114] but also in sensor applications.[112,113,115] As evident from Equation 1.4.3, every change in the refractive index or thickness of any of the layers, directly translates into an altered photonic band gap, and, hence, into another reflected color. This can be exploited for optical sensing. Therefore, the integration of a stimuli-responsive material into the PC that either undergoes swelling/shrinkage, or exhibits a change of the effective RI upon analyte exposure is required. Former materials include phosphatoantimonic acid nanosheets ($H_3Sb_3P_2O_{14}$)[116,117] and lithium tin sulfide nanosheets ($Li_2Sn_2S_5$)[118], which both show extraordinary

swelling properties under humidity, or the polymer polyacrylamide, which was polymerized on a photonic crystal template into a hydrogel.[119] Also, materials amenable to intercalation processes are of interest.[120] However, the swelling properties are often closely linked to the material properties itself. In contrast, a change of the effective RI within a layer can be achieved more easily. In general, this can be done by guaranteeing a degree of (textural) porosity within the alternating layers of different RIs. The effective RI of the layer can then be simplified into a combination of the RI of the layer comprising material and the RI of the void. Usually, filling of the voids in all cases is accompanied by a change of the RI. This is given in most cases, as many vapors condense in the confined space of the pores despite having a RI value close to 1 in their gaseous phase. Naturally, the change of the RI will in turn depend on the filling fraction. All in all, a great number of materials has already been successfully implemented, as layers made of particles pack sufficiently loose to leave enough textural porosity for the accommodation of guest species. Among the materials are SiO_2,[121,122] TiO_2,[122,123] ZrO_2,[124] mixed-metal oxides,[125] clays[126] and polymers.[127-129] The great versatility and chemical flexibility of MOFs has also led to their integration into photonic crystal based sensors, where they have mainly been used for sensing of volatile organic compounds.[130-133]

It should be borne in mind that the above derived equations assume non-absorbing dielectric media, ideal interfaces and a sufficiently high number of layers. Despite being idealized conditions, the optical quality of many BSs is not significantly downgraded by impurities and ill-defined interfaces. To the largest extent, the preparation conditions of the BSs define the final optical properties of the PC. For the fabrication of one dimensional PCs, several different techniques can be employed, which include both top-down, e.g. lithography,[134,135] and bottom up methods, e.g. colloidal crystal approach,[130] layer-by-layer deposition,[136] chemical vapor deposition,[137] sputtering[138] or the most widely used spin-coating technique.[139] As the latter technique is used exclusively throughout this thesis, it will be described briefly in the following Subchapter.

1.4.1 SPIN-COATING

Deposition of a material on a substrate by the spin-coating technique is experimentally easy executable, inexpensive and fast, rendering it a popular method for the fabrication of thin films. In principle, a material dissolved or dispersed in a solvent is applied on the surface of a substrate that, rotating under high speeds, e.g. 3000-8000 rpm, leaves the material evenly casted on the substrate surface.[140,141] However, the process is much more complex.

Generally, four main steps can be distinguished,[140-142] which are depicted in Figure 1.4.3: (a) The initial step is the wetting of the substrate with the solution/suspension. Often, colloidal suspensions of the already synthesized compounds are used. At this stage, the wetting properties and substrate affinity to the suspension are crucial to guarantee a complete coverage of the surface. (b) At the spin-up phase,

the substrate is accelerated and leads to the expulsion of large fluid quantities by the rotational motion and centripetal forces. Low acceleration speeds tend to lead to curved patterns as the inertia of the fluid causes a twisted motion. (c) When a constant speed is reached, the observed interference colors reflect the gradual fluid thinning, which is predominated by drainage due to the viscous flow of the fluid. (d) In the final step, which may overlap with the antecedent stage, solvent evaporation and film drying takes place.
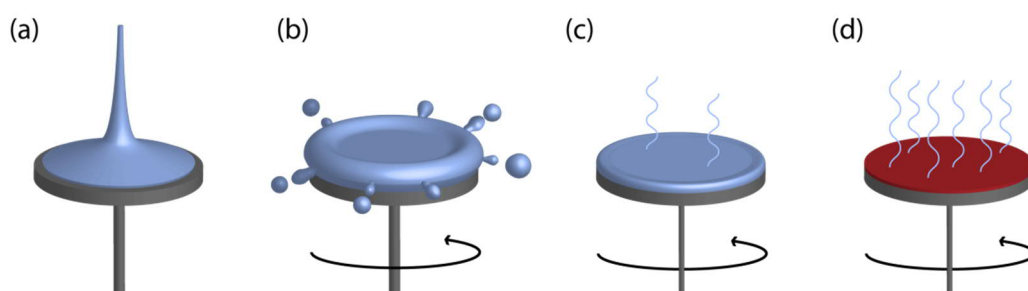
Figure 1.4.3: The four stages during the spin-coating process: (a) wetting of the substrate with the coating fluid, (b) rotational acceleration of the substrate accompanied by fluid expulsion (c) spinning at constant rate characterized by gradual fluid thinning and (d) solvent evaporation and film drying.

Theoretically, the correct choice of materials (particle size, substrate affinity, concentration), solvents (viscosity, vapor pressure, wetting properties), substrates, spin-coating speeds and accelerations, allow the fabrication of thin films of the precise desired thicknesses and uniformity. In reality, the adequate choice of parameters is challenging as they influence each other and a poor choice can corrupt the final film quality. Additionally, environmental conditions are responsible for further defects and non-uniformity.[140] Defect sources are typically dust particles on the substrate or within the suspension, which cause comet like patterns. Inherent to the technique are also striations, radial ridges oriented along the fluid flow caused by the Marangoni effect and edge effects.[143] Evidently, a broad particle size distribution will also add to film roughness, demanding colloidal suspensions of defined narrow particle size distributions.

1.5 CO_2 GAS STORAGE AND SEPARATION

The climate change is increasingly being recognized as one of the greatest threats to humankind on the long term. The Intergovernmental Panel on Climate Change (IPCC) points at anthropogenic greenhouse gas emissions as one of the relevant contributions to global warming.[144] Figure 1.5.1 outlines the development of the globally averaged gas concentrations of CO_2, CH_4 and N_2O.
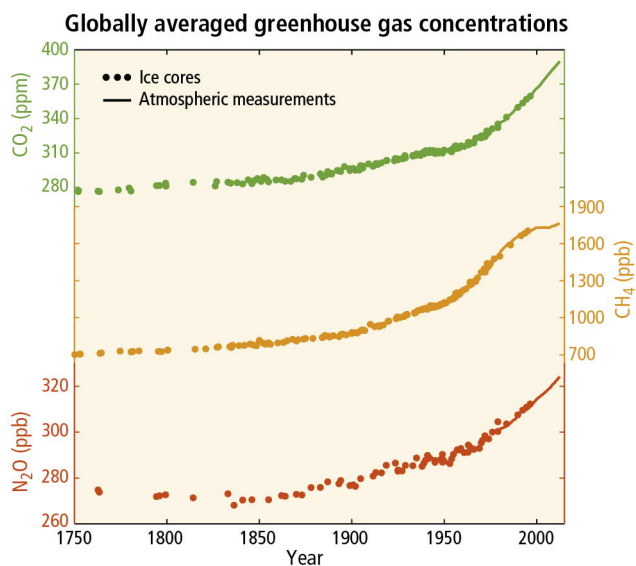
Figure 1.5.1: Observed changes in atmospheric greenhouse gas concentrations. Atmospheric concentrations of carbon dioxide (CO_2, green), methane (CH_4, orange), and nitrous oxide (N_2O, red). Data from ice cores (symbols) and direct atmospheric measurements (lines) are overlaid.[145] © 2014 IPCC.

In order to alleviate and mitigate the effects of the climate change and to counter global warming, the removal of greenhouse gases from the atmosphere has been proposed.[144] Large potential is attributed to the capture and storage of carbon dioxide.[146] However, CO_2 is not only a main combustion product but often found as a component in natural gas, biogas and landfill gas. Therefore, the separation of carbon dioxide from methane is also of fundamental interest to obtain a fuel with superior energy content and to minimize pipeline corrosion due to CO_2 contamination.[147]

The permanent and intrinsic nano- and mesoporosity of MOFs make them ideal materials for both purposes. Tunable pore sizes, ultrahigh surface areas and the ability to decorate the voids with chemical functionalities allows to specifically create pore environments for the selective adsorption of gaseous species. Naturally, the utility of MOFs extends to other gaseous media than carbon dioxide and methane. MOFs are also highly valuable for the capture and degradation of toxic gases,[148] the separation of higher hydrocarbons,[149,150] or moisture farming.[151,152]

In the case of CO_2, MOFs have been proven to exceed the storage capacity of benchmark materials like zeolites and activated carbons.[153,154] The capacity can further be enhanced by decorating the MOF with amino-moieties.[155-157] A chemisorptive mechanism is proposed in amine-containing frameworks, where carbamic acid or – in presence of water – ammonium carbamate is formed.[157] An extensive overview of carbon dioxide capture in MOFs can be found in the review of Sumida et al.[158] and other literature.[159]

The interest in methane is especially due to its use as a fuel. However, its low volumetric energy density is a constraint for a large scale use. To counter this problem, methane in form of natural gas can either be stored as liquefied natural gas (LNG), compressed natural gas (CNG), natural gas hydrate (NGH) or

adsorbed natural gas (ANG). As for CO_2, MOFs exhibit the ideal properties for the storage of this hydrocarbon. In principle, a study revealed that the gravimetric methane uptake of the investigated MOFs scale essentially linearly with surface area.[160] Furthermore, open metal sites and van der Waals potential pocket sites seem to be beneficial for an increased uptake.[161] Also, doping of a carbon nanotube–MOF composite with Li+ showed increased methane storage capacity.[162] More details and examples of methane storage can be found in the literature.[154,159,163] Generally, gas storage is performed at high pressures (up to 80 bar) to fully exploit the MOF loading capacity. A MOF-filled canister of a given volume can be used to hold more gas as without or to transport an equivalent amount of gas at lower pressures.[164]

For the separation and purification of gases, several methods such as cryogenic distillation, membrane-based, and adsorption-based technologies are available.[165] In general, two main mechanisms in porous media can be distinguished.[158] On one hand, the separation can occur kinetically. The molecules are separated due to different pore sizes which aggravate the diffusion of molecules of distinct kinetic diameters. On the other hand, thermodynamic separation is based on the different affinity of the gaseous media to the framework. Here, beneficial pore decoration can significantly increase the selectivity to particular gases or vapors. For the kinetic mechanism, breakthrough experiments are used to evaluate the separation performance.[166] In this kind of experiment, a gas mixture is passed through a compressed pellet or membrane of the material and the outgoing gas stream monitored, e.g. by gas chromatography or mass spectrometry to assess its composition. In case of the thermodynamic mechanism, it is difficult to measure the selectivity directly in practice. Usually, single adsorption isotherms are recorded and used to predict the selectivity via modeling. Besides the Henry theory, the ideal adsorbed solution theory (IAST) is generally employed to gas mixtures. Both methods are described in Chapter 2.9.4. Further information on MOF based gas separation can be found in the literature.[10,13,165,167]

In all cases, an important aspect is the complete "activation" of the MOF. Typically, residual solvent molecules and other volatile compounds remain in the pores of the as-synthesized MOFs. Classically, the material is "activated" by applying a high vacuum at elevated temperatures to remove chemicals obstructing the pores. However, this can induce stress on the framework. The process is comparable to the boiling of the solvent, which can cause a partial or full collapse of the framework. To avoid this, prior solvent exchange, supercritical CO_2 exchange, freeze drying and chemical treatment can be employed.[168,169] In this thesis, the MOFs were activated by heating under high vacuum.

In this work, a series of post-synthetically modified CAU-1 nanoparticles were investigated towards their storage and separation capacity of CO_2/N_2 and CO_2/CH_4 at different temperatures. Furthermore, the heats of adsorption were calculated to assess their framework affinity to reveal the impact of the modification.

1.6 OBJECTIVES

After a decade with a research focus on the exploration and expansion of the structural variety of MOFs, the interest has shifted gradually towards the integration of the frameworks into functional devices to exploit their promising properties. For many applications, not only the MOFs crystal structure but also its structuring on the nano- to mesoscale ultimately defines the final performance demanding versatile fabrication and deposition methods. Furthermore, to tap the full potential, post-synthetic strategies allow the fine-tuning and engineering of the framework else unattainable. This thesis aims at exploring the possibilities of PSM strategies of MOF nanoparticles to adjust the properties to the applicative needs. This work is divided into three topic, which are described briefly in the following.

Chapter 3 engages the challenge of MOF film formation by PVD rather than on a specific application. As the fabrication of thin films is of crucial importance for many applications, generally employable techniques are desired for the deposition of MOFs. Here, PVD methods could become popular as they have become for other – especially for inorganic – materials as well. However, MOFs are prone to decomposition when transferred into the gas phase by conventional "evaporation" techniques. This chapter explores the possibility to deposit MOFs by pulsed laser ablation. Therefore, ZIF-8 particles were used as a model system, which were non-covalently and reversibly modified with a bio-degradable polymer (PEG-400) to reinforce the porous structure and protect the MOF against decomposition. Additionally, the as-obtained films could easily be freed from the polymer by a simple washing step.

In Chapter 4, MOF based one-dimensional PC sensors are taken to the next level. MOFs are ideal materials for integration into PC sensors due to their permanent porosity. The uptake of analytes translates into an optical shift of the reflectance spectra useful for the differentiation of volatile organic compounds. Although they have already been implemented successfully in BS sensors, the comparability of the optical responses and their selectivity are still weak points. Especially differences in the film thicknesses yield sample specific spectra, which are barely comparable. The objective within this work is the development of a modification approach that is performed on the as-assembled, already functional BS sensor. This is done on a generic BS platform of CAU-1 and TiO_2, where the functional MOF layer is targeted. Both the SBU and organic linker are modified within the BS by a mild approach to guarantee the structural stability of both the MOF and the hierarchical PC structure. The post-assembly modification not only retains the initial BS optical properties making the pristine and modified PC structures comparable, the altered chemical environment translates into distinct shifts of the reflectance spectra enhancing analyte discrimination capacity.

Chapter 5 examines the gas storage and separation performance of post-synthetically modified MOF nanoparticles towards nitrogen, carbon dioxide and methane. The intrinsic, permanent and defined nano- to mesoporosity of MOFs render them ideal materials for the adsorption of gases and small molecules. In the light of greenhouse gas emission driven climate change, the capture and storage of carbon dioxide from combustion processes is traded as an option to tackle global warming. Furthermore, its presence in natural gas and biogas, claims for its selective and economic separation from the energy sources to improve their energetic footprint. For this purpose, CAU-1 nanoparticles were modified either by demethoxylation of the SBU or with various anhydrides. Adsorption isotherms using argon at 87 K and CO_2, CH_4 and N_2 at 273 and 288 K were measured to characterize their sorption behavior and the selectivities towards CO_2/N_2 and CO_2/CH_4 up to 1 bar. Furthermore, heats of adsorption were calculated to assess the affinity of the adsorptives to the different CAU-1 modifications.

1.7 REFERENCES

1   D. K. Todd, Groundwater hydrology, Wiley, 1980.

2   C. Desplechain, B. Foliguet, E. Barrat, G. Grignon and F. Touati, Bull. Eur. Physiopathol. Respir. 1983, 19, 59-68.

3   J. Caro, Chem. Ing. Tech. 2018, 90, 1-11.

4   P. Silva, S. M. F. Vilela, J. P. C. Tome and F. A. Almeida Paz, Chem. Soc. Rev. 2015, 44, 6774-6803.

5   S. R. Batten, N. R. Champness, X.-M. Chen, J. Garcia-Martinez, S. Kitagawa, L. Ohrstrom, M. O'Keeffe, M. P. Suh and J. Reedijk, Pure Appl. Chem. 2013, 85, 1715-1724.

6   D. Kim, X. Liu and M. S. Lah, Inorg. Chem. Front. 2015, 2, 336-360.

7   F. Hoffmann and M. Fröba, in The Chemistry of Metal–Organic Frameworks, Ed. S. Kaskel, Wiley, 2016.

8   O. M. Yaghi, M. O'Keeffe, N. W. Ockwig, H. K. Chae, M. Eddaoudi and J. Kim, Nature 2003, 423, 705.

9   V. Guillerm, D. Kim, J. F. Eubank, R. Luebke, X. Liu, K. Adil, M. S. Lah and M. Eddaoudi, Chem. Soc. Rev. 2014, 43, 6141-6172.

10   B. Li, H. Wang and B. Chen, Chem. – Asian J. 2014, 9, 1474-1498.

11   M. S. Shah, M. Tsapatsis and J. I. Siepmann, Chem. Rev. (Washington, DC, U. S.) 2017, 117, 9755-9803.

12   Z. Kang, L. Fan and D. Sun, J. Mater. Chem. A 2017, 5, 10073-10091.

13   H. Li, K. Wang, Y. Sun, C. T. Lollar, J. Li and H.-C. Zhou, Mater. Today 2018, 21, 108-121.

14   X. Yang and Q. Xu, Cryst. Growth Des. 2017, 17, 1450-1455.

15   H. Furukawa, F. Gándara, Y.-B. Zhang, J. Jiang, W. L. Queen, M. R. Hudson and O. M. Yaghi, J. Am. Chem. Soc. 2014, 136, 4369-4381.

16   J. Canivet, A. Fateeva, Y. Guo, B. Coasne and D. Farrusseng, Chem. Soc. Rev. 2014, 43, 5594-5617.

17   J. Lee, O. K. Farha, J. Roberts, K. A. Scheidt, S. T. Nguyen and J. T. Hupp, Chem. Soc. Rev. 2009, 38, 1450-1459.

18   M. B. Majewski, A. J. Howarth, P. Li, M. R. Wasielewski, J. T. Hupp and O. K. Farha, CrystEngComm 2017, 19, 4082-4091.

19   M. B. Solomon, T. L. Church and D. M. D'Alessandro, CrystEngComm 2017, 19, 4049-4065.

20   X. Yu, L. Wang and S. M. Cohen, CrystEngComm 2017, 19, 4126-4136.

21   S. Keskin and S. Kızılel, Ind. Eng. Chem. Res. 2011, 50, 1799-1812.

22   M. A. Chowdhury, J. Biomed. Mater. Res., Part A 2017, 105, 1184-1194.

23   Z. Luo, S. Fan, C. Gu, W. Liu, B. Li and J. Liu, Curr. Med. Chem. 2018.

24   P. Ramaswamy, N. E. Wong and G. K. H. Shimizu, Chem. Soc. Rev. 2014, 43, 5913-5932.

25   L. E. Kreno, K. Leong, O. K. Farha, M. Allendorf, R. P. Van Duyne and J. T. Hupp, Chem. Rev. (Washington, DC, U. S.) 2012, 112, 1105-1125.

26   M. G. Campbell and M. Dincă, Sensors (Basel, Switzerland) 2017, 17, 1108.

27   E. A. Dolgopolova, A. M. Rice, C. R. Martin and N. B. Shustova, Chem. Soc. Rev. 2018.

28   D. Maspoch, D. Ruiz-Molina and J. Veciana, J. Mater. Chem. 2004, 14, 2713-2723.

29   A. Doménech, H. García, M. T. Doménech-Carbó and F. Llabrés-i-Xamena, J. Phys. Chem. C 2007, 111, 13701-13711.

30   M. Kurmoo, Chem. Soc. Rev. 2009, 38, 1353-1379.

31   H. B. Wu and X. W. Lou, Sci. Adv. 2017, 3.

32   G. Xu, P. Nie, H. Dou, B. Ding, L. Li and X. Zhang, Mater. Today 2017, 20, 191-209.

33   G. Minguez Espallargas and E. Coronado, Chem. Soc. Rev. 2018, 47, 533-557.

34   E. A. Flugel, A. Ranft, F. Haase and B. V. Lotsch, J. Mater. Chem. 2012, 22, 10119-10133.

35   N. Stock and S. Biswas, Chem. Rev. (Washington, DC, U. S.) 2012, 112, 933-969.

36   L. Hu, P. Zhang, Q. Chen, H. Zhong, X. Hu, X. Zheng, Y. Wang and N. Yan, Cryst. Growth Des. 2012, 12, 2257-2264.

37   C. Avci, J. Ariñez-Soriano, A. Carné-Sánchez, V. Guillerm, C. Carbonell, I. Imaz and D. Maspoch, Angew. Chem., Int. Ed. 2015, 54, 14417-14421.

38   W. S. Chi, D. K. Roh, C. S. Lee and J. H. Kim, J. Mater. Chem. A 2015, 3, 21599-21608.

39   C. Guo, Y. Zhang, Y. Guo, L. Zhang, Y. Zhang and J. Wang, Chem. Commun. (Cambridge, U. K.) 2018, 54, 252-255.

40   X. Xu, Z. Zhang and X. Wang, Adv. Mater. (Weinheim, Ger.) 2015, 27, 5365-5371.

41   D. Zacher, R. Schmid, C. Wöll and R. A. Fischer, Angew. Chem., Int. Ed. 2011, 50, 176-199.

42   O. Shekhah, J. Liu, R. A. Fischer and C. Woll, Chem. Soc. Rev. 2011, 40, 1081-1106.

43   A. Carne, C. Carbonell, I. Imaz and D. Maspoch, Chem. Soc. Rev. 2011, 40, 291-305.

44   A. Bétard and R. A. Fischer, Chem. Rev. (Washington, DC, U. S.) 2012, 112, 1055-1083.

45   M. D. Allendorf, A. Schwartzberg, V. Stavila and A. A. Talin, Chem. – Eur. J. 2011, 17, 11372-11388.

46   J. L. Zhuang, D. Ar, X. J. Yu, J. X. Liu and A. Terfort, Adv. Mater. (Weinheim, Ger.) 2013, 25, 4631-4635.

47   I. Stassen, N. Burtch, A. Talin, P. Falcaro, M. Allendorf and R. Ameloot, Chem. Soc. Rev. 2017, 46, 3185-3241.

48   I. Stassen, M. Styles, G. Grenci, Hans V. Gorp, W. Vanderlinden, Steven D. Feyter, P. Falcaro, D. D. Vos, P. Vereecken and R. Ameloot, Nat. Mater. 2015, 15, 304.

49   M. Eddaoudi, D. F. Sava, J. F. Eubank, K. Adil and V. Guillerm, Chem. Soc. Rev. 2015, 44, 228-249.

50   K. S. Park, Z. Ni, A. P. Côté, J. Y. Choi, R. Huang, F. J. Uribe-Romo, H. K. Chae, M. O'Keeffe and O. M. Yaghi, Proceedings of the National Academy of Sciences 2006, 103, 10186-10191.

51   J. T. Hughes, T. D. Bennett, A. K. Cheetham and A. Navrotsky, J. Am. Chem. Soc. 2013, 135, 598-601.

52   S. A. Moggach, T. D. Bennett and A. K. Cheetham, Angew. Chem., Int. Ed. 2009, 48, 7087-7089.

53   D. Fairen-Jimenez, S. A. Moggach, M. T. Wharmby, P. A. Wright, S. Parsons and T. Düren, J. Am. Chem. Soc. 2011, 133, 8900-8902.

54   C. O. Ania, E. García-Pérez, M. Haro, J. J. Gutiérrez-Sevillano, T. Valdés-Solís, J. B. Parra and S. Calero, J. Phys. Chem. Lett. 2012, 3, 1159-1164.

55   C. Zhang, R. P. Lively, K. Zhang, J. R. Johnson, O. Karvan and W. J. Koros, J. Phys. Chem. Lett. 2012, 3, 2130-2134.

56   L. Diestel, H. Bux, D. Wachsmuth and J. Caro, Microporous Mesoporous Mater. 2012, 164, 288-293.

57   D. Peralta, G. Chaplais, A. Simon-Masseron, K. Barthelet, C. Chizallet, A.-A. Quoineaud and G. D. Pirngruber, J. Am. Chem. Soc. 2012, 134, 8115-8126.

58   D. Peralta, G. Chaplais, A. Simon-Masseron, K. Barthelet and G. D. Pirngruber, Ind. Eng. Chem. Res. 2012, 51, 4692-4702.

59   D. Peralta, G. Chaplais, J.-L. Paillaud, A. Simon-Masseron, K. Barthelet and G. D. Pirngruber, Microporous Mesoporous Mater. 2013, 173, 1-5.

60   K. Zhang, R. P. Lively, C. Zhang, R. R. Chance, W. J. Koros, D. S. Sholl and S. Nair, J. Phys. Chem. Lett. 2013, 4, 3618-3622.

61   T. Ahnfeldt, N. Guillou, D. Gunzelmann, I. Margiolaki, T. Loiseau, G. Férey, J. Senker and N. Stock, Angew. Chem. 2009, 121, 5265-5268.

62   Z. Wang and S. M. Cohen, Chem. Soc. Rev. 2009, 38, 1315-1329.

63   Y. F. Song and L. Cronin, Angew. Chem., Int. Ed. 2008, 47, 4635-4637.

64   K. K. Tanabe and S. M. Cohen, Chem. Soc. Rev. 2011, 40, 498-519.

65   S. M. Cohen, Chem. Rev. (Washington, DC, U. S.) 2012, 112, 970-1000.

66   D. Farrusseng, J. Canivet and A. Quadrelli, in Metal-Organic Frameworks, Ed. D. Farrusseng, Wiley-VCH Verlag GmbH & Co. KGaA, 2011, 23-48.

67   A. D. Burrows, in Metal Organic Frameworks as Heterogeneous Catalysts, Eds. F. X. Llabrés i Xamena and J. Gascon, Royal Society of Chemistry, 2013, 31-75.

68   P. Deria, J. E. Mondloch, O. Karagiaridi, W. Bury, J. T. Hupp and O. K. Farha, Chem. Soc. Rev. 2014, 43, 5896-5912.

69   S. M. Cohen, J. Am. Chem. Soc. 2017, 139, 2855-2863.

70   S. Bernt, V. Guillerm, C. Serre and N. Stock, Chem. Commun. (Cambridge, U. K.) 2011, 47, 2838-2840.

71   J. Marshall Ross and S. Forgan Ross, Eur. J. Inorg. Chem. 2016, 2016, 4310-4331.

72   B. Li, B. Gui, G. Hu, D. Yuan and C. Wang, Inorg. Chem. 2015, 54, 5139-5141.

73   T. Toyao, K. Miyahara, M. Fujiwaki, T.-H. Kim, S. Dohshi, Y. Horiuchi and M. Matsuoka, J. Phys. Chem. C 2015, 119, 8131-8137.

74   Y. K. Hwang, D. Y. Hong, J. S. Chang, S. H. Jhung, Y. K. Seo, J. Kim, A. Vimont, M. Daturi, C. Serre and G. Férey, Angew. Chem., Int. Ed. 2008, 47, 4144-4148.

75   C.-W. Kung, T.-H. Chang, L.-Y. Chou, J. T. Hupp, O. K. Farha and K.-C. Ho, Chem. Commun. (Cambridge, U. K.) 2015, 51, 2414-2417.

76   T. Yamada and H. Kitagawa, J. Am. Chem. Soc. 2009, 131, 6312-6313.

77   A. S. Gupta, R. K. Deshpande, L. Liu, G. I. N. Waterhouse and S. G. Telfer, CrystEngComm 2012, 14, 5701-5704.

78   J. Canivet, S. Aguado, G. Bergeret and D. Farrusseng, Chem. Commun. (Cambridge, U. K.) 2011, 47, 11650-11652.

79   O. Karagiaridi, W. Bury, J. E. Mondloch, J. T. Hupp and O. K. Farha, Angew. Chem., Int. Ed. 2014, 53, 4530-4540.

80   M. B. Lalonde, J. E. Mondloch, P. Deria, A. A. Sarjeant, S. S. Al-Juaid, O. I. Osman, O. K. Farha and J. T. Hupp, Inorg. Chem. 2015, 54, 7142-7144.

81   P. Deria, W. Bury, I. Hod, C.-W. Kung, O. Karagiaridi, J. T. Hupp and O. K. Farha, Inorg. Chem. 2015, 54, 2185-2192.

82   Y. Furukawa, T. Ishiwata, K. Sugikawa, K. Kokado and K. Sada, Angew. Chem., Int. Ed. 2012, 51, 10566-10569.

83   T. Ishiwata, Y. Furukawa, K. Sugikawa, K. Kokado and K. Sada, J. Am. Chem. Soc. 2013, 135, 5427-5432.

84   B. J. Yao, W. L. Jiang, Y. Dong, Z. X. Liu and Y. B. Dong, Chem. – Eur. J. 2016, 22, 10565-10571.

85   L. Chen, R. Luque and Y. Li, Dalton Trans. 2018, 47, 3663-3668.

86   H.-L. Jiang, B. Liu, T. Akita, M. Haruta, H. Sakurai and Q. Xu, J. Am. Chem. Soc. 2009, 131, 11302-11303.

87   G. Lu, S. Li, Z. Guo, O. K. Farha, B. G. Hauser, X. Qi, Y. Wang, X. Wang, S. Han, X. Liu, J. S. DuChene, H. Zhang, Q. Zhang, X. Chen, J. Ma, S. C. J. Loo, W. D. Wei, Y. Yang, J. T. Hupp and F. Huo, Nature Chem. 2012, 4, 310.

88   H. Deng, C. J. Doonan, H. Furukawa, R. B. Ferreira, J. Towne, C. B. Knobler, B. Wang and O. M. Yaghi, Science 2010, 327, 846-850.

89   Q. Xia, Z. Li, C. Tan, Y. Liu, W. Gong and Y. Cui, J. Am. Chem. Soc. 2017, 139, 8259-8266.

90   K. Koh, A. G. Wong-Foy and A. J. Matzger, Chem. Commun. (Cambridge, U. K.) 2009, 6162-6164.

91   J. E. Mahan, Physical Vapor Deposition of Thin Films, Wiley, 2000.

92   K. Seshan, Handbook of Thin Film Deposition Techniques, Second Edition; Principles, Methods, Equipment and Applications, William Andrew Publishing, 2000.

93   D. M. Mattox and Editor, Handbook of Physical Vapor Depositions (PVD) Processing, 2nd Edition, Elsevier, 2010.

94   M. N. R. Ashfold, F. Claeyssens, G. M. Fuge and S. J. Henley, Chem. Soc. Rev. 2004, 33, 23-31.

95   P. R. Willmott and J. R. Huber, Rev. Mod. Phys. 2000, 72, 315-328.

96   F. Fankhauser and S. Kwasniewska, Lasers in Ophthalmology: Basic, Diagnostic, and Surgical Aspects : a Review, Kugler Publications, 2003.

97   F. Hillenkamp and J. Peter-Katalinic, MALDI MS: A Practical Guide to Instrumentation, Methods and Applications, Wiley, 2013.

98   S. T. Li, E. Arenholz, J. Heitz and D. Bäuerle, Appl. Surf. Sci. 1998, 125, 17-22.

99   D. B. Chrisey, A. Piqué, R. A. McGill, J. S. Horwitz, B. R. Ringeisen, D. M. Bubb and P. K. Wu, Chem. Rev. (Washington, DC, U. S.) 2003, 103, 553-576.

100   H. Jeong, Study of Polymer Crystallization by Physical Vapor Deposition, Ph.D. thesis, Princeton University, 2017.

101   A. Piqué, Applied Physics A 2011, 105, 517-528.

102   S. Kinoshita and S. Yoshioka, ChemPhysChem 2005, 6, 1442-1459.

103   A. R. Parker and N. Martini, Optics & Laser Technology 2006, 38, 315-322.

104 "Opal from Yowah, Queensland, Australia. Length: about 20mm." (2009) by J. Harrison, licensed by CC-BY-SA-2.5, retrieved from Wikimedia Commons website: https://upload.wikimedia.org/wikipedia/commons/9/93/Opal_from_Yowah%2C_Queensland %2C_Australia_2.jpg

105 "*日本語*: Resolt 10-26" (2013) by T. Ueki, licensed by CC-BY-SA-3.0, retrieved from Wikimedia Commons website: https://upload.wikimedia.org/wikipedia/commons/8/87/Results%26Methods_Fig._1._1.2.png

106 "European Peacock" (2007) by M. I, licensed by CC BY-SA 2.5, retrieved from Wikimedia Commons website: https://upload.wikimedia.org/wikipedia/commons/b/b7/Inachis_io_top_MichaD.jpg

107 "SEM image of a Peacock butterfly wing, slant view 1" (2007) by SecretDisc, licensed by CC BY-SA 3.0, retrieved from Wikimedia Commons website: https://upload.wikimedia.org/wikipedia/commons/e/e2/SEM_image_of_a_Peacock_wing%2C _slant_view_1.JPG

108 "SEM image of a Peacock butterfly wing, slant view 4" (2007) by SecretDisk, licensed by CC BY-SA 3.0, retrieved from Wikimedia Commons website: https://upload.wikimedia.org/wikipedia/commons/6/63/SEM_image_of_a_Peacock_wing%2C _slant_view_4.JPG

109 R. D. Meade, A. M. Rappe, K. D. Brommer, J. D. Joannopoulos and O. L. Alerhand, Phys. Rev. B 1993, 48, 8434-8437.

110 J. B. Pendry, J. Phys.: Condens. Matter 1996, 8, 1085.

111 J. D. Joannopoulos, S. G. Johnson, J. N. Winn and R. D. Meade, Photonic Crystals: Molding the Flow of Light - Second Edition, Princeton University Press, 2011.

112 C. Fenzl, T. Hirsch and S. Wolfbeis Otto, Angew. Chem., Int. Ed. 2014, 53, 3318-3335.

113 R. V. Nair and R. Vijaya, Prog. Quantum Electron. 2010, 34, 89-134.

114 A. Cerqueira S. Jr., Rep. Prog. Phys. 2010, 73, 024401.

115 A. M. R. Pinto and M. Lopez-Amo, J. Sens. 2012, 2012, 21.

116 K. Szendrei, P. Ganter, O. Sànchez-Sobrado, R. Eger, A. Kuhn and V. Lotsch Bettina, Adv. Mater. (Weinheim, Ger.) 2015, 27, 6341-6348.

117 P. Ganter, K. Szendrei and B. V. Lotsch, Adv. Mater. (Weinheim, Ger.) 2016, 28, 7436-7442.

118 K. Szendrei-Temesi, O. Sanchez-Sobrado, S. B. Betzler, K. M. Durner, T. Holzmann and B. V. Lotsch, Adv. Funct. Mater. 2018, 28, 1705740.

119 E. Tian, J. Wang, Y. Zheng, Y. Song, L. Jiang and D. Zhu, J. Mater. Chem. 2008, 18, 1116-1122.

120 P. Ganter, L. M. Schoop, M. Däntl and B. V. Lotsch, Chem. Mater. 2018, 30, 2557-2565.

121   V. N. Bogomolov, S. V. Gaponenko, I. N. Germanenko, A. M. Kapitonov, E. P. Petrov, N. V. Gaponenko, A. V. Prokofiev, A. N. Ponyavina, N. I. Silvanovich and S. M. Samoilovich, Phys. Rev. E 1997, 55, 7619-7625.

122   D. Bonifacio Leonardo, P. Puzzo Daniel, S. Breslav, M. Willey Barbara, A. McGeer and A. Ozin Geoffrey, Adv. Mater. (Weinheim, Ger.) 2009, 22, 1351-1354.

123   J. E. G. J. Wijnhoven and W. L. Vos, Science 1998, 281, 802-804.

124   C. F. Blanford, R. C. Schroden, M. Al-Daous and A. Stein, Adv. Mater. (Weinheim, Ger.) 2001, 13, 26-29.

125   Y. Dou, J. Han, T. Wang, M. Wei, D. G. Evans and X. Duan, J. Mater. Chem. 2012, 22, 14001-14007.

126   B. V. Lotsch and G. A. Ozin, Adv. Mater. (Weinheim, Ger.) 2008, 20, 4079-4084.

127   A. C. Edrington, A. M. Urbas, P. DeRege, C. X. Chen, T. M. Swager, N. Hadjichristidis, M. Xenidou, L. J. Fetters, J. D. Joannopoulos, Y. Fink and E. L. Thomas, Adv. Mater. (Weinheim, Ger.) 2001, 13, 421-425.

128   Y. Kang, J. J. Walish, T. Gorishnyy and E. L. Thomas, Nat. Mater. 2007, 6, 957.

129   C. Paquet and E. Kumacheva, Mater. Today 2008, 11, 48-56.

130   Y.-n. Wu, F. Li, Y. Xu, W. Zhu, C.-a. Tao, J. Cui and G. Li, Chem. Commun. (Cambridge, U. K.) 2011, 47, 10094-10096.

131   F. M. Hinterholzinger, A. Ranft, J. M. Feckl, B. Ruhle, T. Bein and B. V. Lotsch, J. Mater. Chem. 2012, 22, 10356-10362.

132   Z. Hu, C.-a. Tao, F. Wang, X. Zou and J. Wang, J. Mater. Chem. C 2015, 3, 211-216.

133   A. Ranft, F. Niekiel, I. Pavlichenko, N. Stock and B. V. Lotsch, Chem. Mater. 2015, 27, 1961-1970.

134   S. Cabrini, L. Businaro, M. Prasciolu, A. Carpentiro, D. Gerace, M. Galli, L. C. Andreani, F. Riboli, L. Pavesi and E. D. Fabrizio, J. Opt. A: Pure Appl. Opt. 2006, 8, S550.

135   P. S. Nunes, N. A. Mortensen, J. P. Kutter and K. B. Mogensen, Sensors 2010, 10, 2348.

136   T. C. Wang, R. E. Cohen and M. F. Rubner, Adv. Mater. (Weinheim, Ger.) 2002, 14, 1534-1537.

137   H. Jiang, W. E. Johnson, J. T. Grant, K. Eyink, E. M. Johnson, D. W. Tomlin and T. J. Bunning, Chem. Mater. 2003, 15, 340-347.

138   U. Schürmann, H. Takele, V. Zaporojtchenko and F. Faupel, Thin Solid Films 2006, 515, 801-804.

139   H. Shen, Z. Wang, Y. Wu and B. Yang, RSC Advances 2016, 6, 4505-4520.

140   D. P. Birnie, in Sol-Gel Technologies for Glass Producers and Users, Eds. M. A. Aegerter and M. Mennig, Springer US, Boston, MA, 2004, 49-55.

141   D. Grosso, C. Boissière and M. Faustini, in The Sol-Gel Handbook, Eds. D. Levy and M. Zayat, Wiley, 2015.

142   N. Sahu, B. Parija and S. Panigrahi, Indian J. Phys. 2009, 83, 493-502.

143   J. Rehg Timothy and G. Higgins, AIChE J. 1992, 38, 489-501.

144   IPCC, 2014, Climate Change 2014: Synthesis Report. Contribution of Working Groups I, II and III to the Fifth Assessment Report of the Intergovernmental Panel on Climate Change, Eds. R. K. Pachauri and L. A. Meyer, Geneva, Switzerland.

145   P. Ciais, C. Sabine, G. Bala, L. Bopp, V. Brovkin, J. Canadell, A. Chhabra, R. DeFries, J. Galloway, M. Heimann, C. Jones, C. Le Quéré, R. B. Myneni, S. Piao and P. Thornton, in Climate Change 2013: The Physical Science Basis. Contribution of Working Group I to the Fifth Assessment Report of the Intergovernmental Panel on Climate Change, Eds. T. F. Stocker, D. Qin, G.-K. Plattner, M. Tignor, S. K. Allen, J. Boschung, A. Nauels, Y. Xia, V. Bex and P. M. Midgley, Cambridge University Press, Cambridge, United Kingdom and New York, NY, USA, 2013, 465–570.

146   IPCC, 2005, IPCC special report on carbon dioxide capture and storage, Eds. B. Metz, O. Davidson, H. de Coninck, M. Loos and L. Meyer, Cambridge, UK.

147   Y. Zhang, J. Sunarso, S. Liu and R. Wang, Int. J. Greenhouse Gas Control 2013, 12, 84-107.

148   E. Barea, C. Montoro and J. A. R. Navarro, Chem. Soc. Rev. 2014, 43, 5419-5430.

149   Y. He, W. Zhou, R. Krishna and B. Chen, Chem. Commun. (Cambridge, U. K.) 2012, 48, 11813-11831.

150   Z. R. Herm, E. D. Bloch and J. R. Long, Chem. Mater. 2014, 26, 323-338.

151   H. Kim, S. Yang, S. R. Rao, S. Narayanan, E. A. Kapustin, H. Furukawa, A. S. Umans, O. M. Yaghi and E. N. Wang, Science 2017, 356, 430.

152   H. Kim, S. R. Rao, E. A. Kapustin, L. Zhao, S. Yang, O. M. Yaghi and E. N. Wang, Nat. Commun. 2018, 9, 1191.

153   A. R. Millward and O. M. Yaghi, J. Am. Chem. Soc. 2005, 127, 17998-17999.

154   Y. Lin, C. Kong, Q. Zhang and L. Chen, Adv. Energy Mater. 2016, 7, 1601296.

155   A. Demessence, D. M. D'Alessandro, M. L. Foo and J. R. Long, J. Am. Chem. Soc. 2009, 131, 8784-8786.

156   J. An, S. J. Geib and N. L. Rosi, J. Am. Chem. Soc. 2010, 132, 38-39.

157   R. W. Flaig, T. M. Osborn Popp, A. M. Fracaroli, E. A. Kapustin, M. J. Kalmutzki, R. M. Altamimi, F. Fathieh, J. A. Reimer and O. M. Yaghi, J. Am. Chem. Soc. 2017, 139, 12125-12128.

158   K. Sumida, D. L. Rogow, J. A. Mason, T. M. McDonald, E. D. Bloch, Z. R. Herm, T.-H. Bae and J. R. Long, Chem. Rev. (Washington, DC, U. S.) 2012, 112, 724-781.

159   S. Ma and H.-C. Zhou, Chem. Commun. (Cambridge, U. K.) 2010, 46, 44-53.

160   Y. Peng, V. Krungleviciute, I. Eryazici, J. T. Hupp, O. K. Farha and T. Yildirim, J. Am. Chem. Soc. 2013, 135, 11887-11894.

161   H. Wu, M. Simmons Jason , Y. Liu, M. Brown Craig , X. S. Wang, S. Ma, K. Peterson Vanessa , D. Southon Peter , J. Kepert Cameron , H. C. Zhou, T. Yildirim and W. Zhou, Chem. – Eur. J. 2010, 16, 5205-5214.

162   Z. Xiang, Z. Hu, D. Cao, W. Yang, J. Lu, B. Han and W. Wang, Angew. Chem., Int. Ed. 2010, 50, 491-494.

163   Y. He, W. Zhou, G. Qian and B. Chen, Chem. Soc. Rev. 2014, 43, 5657-5678.

164   U. Mueller, M. Schubert, F. Teich, H. Puetter, K. Schierle-Arndt and J. Pastre, J. Mater. Chem. 2006, 16, 626-636.

165   J.-R. Li, R. J. Kuppler and H.-C. Zhou, Chem. Soc. Rev. 2009, 38, 1477-1504.

166   R.-B. Lin, S. Xiang, H. Xing, W. Zhou and B. Chen, Coord. Chem. Rev. 2017.

167   B. Li, H.-M. Wen, W. Zhou and B. Chen, J. Phys. Chem. Lett. 2014, 5, 3468-3479.

168   A. P. Nelson, O. K. Farha, K. L. Mulfort and J. T. Hupp, J. Am. Chem. Soc. 2009, 131, 458-460.

169   J. E. Mondloch, O. Karagiaridi, O. K. Farha and J. T. Hupp, CrystEngComm 2013, 15, 9258-9264.

2 METHODS

In order to elucidate the properties of the materials, films and multilayers synthesized and fabricated within this thesis, an in-depth characterization is crucial. For this purpose, multiple characterization techniques were employed, which are introduced in the following. These analytical methods comprehend techniques for the structural and morphological characterization of the nanoparticles (Chapters 2.1 – 2.5), the elucidation of their composition (Chapters 2.5.3, 2.6 – 2.7), particle size distributions (Chapter 2.8) and investigation of their ad- and desorptive behavior (Chapter 2.9). Films and multilayer structures were further characterized towards their refractive indices and thicknesses (Chapter 2.10), optical properties (Chapter 2.11) and hydrophilicity (Chapter 2.12). In addition, theoretical calculations were employed to determine refractive indices and thicknesses in multilayer structures (Chapter 2.11.1) and selectivities towards gas mixtures (Chapter 2.9.4). Furthermore, the statistical method of principal component analysis for the assessment of color based discrimination capacities is briefly explained (Chapter 2.11.2).

2.1   X-Ray Diffraction

X-ray diffraction (XRD) is the method of choice for the characterization of crystalline phases and structures and further reveals information on their purity, orientation and particle size.[1] This non-destructive method relies on the diffraction of monochromatic X-rays, consisting of wavelengths comparable to atomic spacings, in periodic structures. In a typical experiment, X-rays are generated from an anode and monochromated, e.g. Cu-K$_\alpha$ radiation, which is then collimated on either a single crystal or a powdered sample. X-rays that are scattered from the atoms undergo constructive interference if the Bragg condition is met as outlined in Figure 1.3.1. At specific scattering angles θ and interplanar spacings d, the path difference of the X-ray waves equal the incident X-ray wavelength or its multiple integer and, hence, undergo constructive interference visible as a reflection in the diffraction pattern at the angle 2θ.
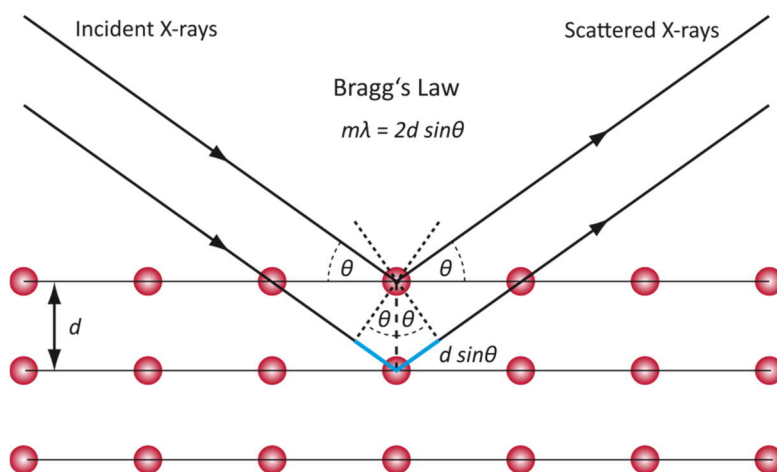
Figure 2.1.1: Schematic representation of the Bragg condition in a crystal lattice with atomic positions in red. X-rays are scattered in phase for angles θ so that the path difference equals multiple integers of λ.

As the diffraction angles 2θ are directly connected to the spacings d associated with a set of planes with the Miller Indices (hkl), not only the lattice parameters but also the positions of the atoms can be calculated for each crystal system. The intensities of the corresponding planes can further be used for complete crystal structure solution and subsequent refinement. Additional information can be obtained by analysis of the reflections that reveal possible defects and strain within the crystal, preferred orientation of the crystallites or crystallite sizes. The latter one can be estimated from the broadening of the diffraction peaks by using the Scherrer equation (Equation 2.1.1),[2]

$$\tau = \frac{K \cdot \lambda}{\beta \cdot \cos \theta}, \qquad\qquad (2.1.1)$$

where τ is the mean crystallite size, K a dimensionless shape factor (typically $\approx$0.9), λ the X-ray wavelength, β the line broadening (full width at half the maximum) and θ the Bragg angle.

XRD measurements were performed on three different instruments: a Huber G670 Guinier Imaging Plate diffractometer with Cu-K$_\alpha$-radiation, λ = 154.051 pm, Ge(111)-monochromator, external

standard SiO_2 (HUBER X-Ray Diffraction Equipment, Germany), a STOE Stadi P powder diffractometer in Debye–Scherrer-geometry (STOE & Cie GmbH, Germany) with Cu-K$_{\alpha1}$ radiation, Ge(111)-monochromator, equipped with a Mythen detector, and a Bruker D8 Advance diffractometer (Bruker, USA) with Cu-K$_{\alpha1}$ radiation, in Bragg Brentano geometry.

2.1.1 GRAZING-INCIDENCE SMALL- AND WIDE-ANGLE SCATTERING

Grazing incidence small- and wide-angle scattering (GISAXS/GIWAXS) are X-ray scattering techniques useful for the structural characterization of micro- and nanoscaled surface structures and thin films.[3,4] In contrast to conventional X-ray diffraction, the samples are measured at a grazing-incident geometry. Due to the very small angles in GISAXS, not only ordering at large length scales can be investigated, but the scattering events are also prone to reflection-refraction effects at the surface at grazing incidence. For that case, the scattered waves interfere coherently, giving rise to an effective form factor that will also depend on the morphology of the scatterers. By considering larger angles as in the wide-angle analogue technique GIWAXS, probing at the atomic scale is possible revealing the crystalline structure. Furthermore, off-plane scattering events bear further information on the orientation and patterning of the scatterers. A more in-depth description can be found in the literature.[4]

GIWAXS experiments for Chapter 4 were performed by Torben Sick on an Anton Paar SAXSpace at the working group of Prof. Dr. Thomas Bein (LMU Munich). The experiments were performed with a Xenocs GeniX3D microfocus X-ray source with a Cu target for the generation of the monochromatic beam of 0.154 nm wavelength. The 2D scattering patterns were collected on a DectrisEIGER R 1M detector at an incident angle near 0.23°. The sample-to-detector distance was 200 mm.

2.2 INFRARED SPECTROSCOPY

Infrared (IR) spectroscopy is a fundamental method in chemical analysis generally employed for the investigation of vibrational-rotational modes revealing structural features in both organic and inorganic materials.[5] The samples under study are exposed to the IR region of the electromagnetic spectrum, most commonly the mid-IR (4000 – 400 cm^{-1}). IR absorption occurs if the energy of the IR light matches the energy level difference of a vibrational and/or rotational mode which further needs to undergo a change of the permanent electric dipole with respect to the bond distance. Hence, the amount of absorbed IR radiation as a function of energy reflects the presence of characteristic functional groups, such as alcohols, alkenes, amines and carbonyls, among many others. Typically, below 1500 cm^{-1} complex absorption patterns are observed, which are often referred to as the fingerprint region due to the variety of bending and stretching vibrations that create a unique pattern for the different materials and molecules.

IR spectroscopic measurements were performed either on a Perkin Elmer Spektrum BX II FT-IR (Perkin Elmer, USA) or a Spectrum Two IR Spectrometer (Perkin Elmer, USA), both equipped with an attenuated total reflectance unit.

2.3 RAMAN SPECTROSCOPY

Raman spectroscopy is also used to investigate the vibrational and rotational modes of materials based on the inelastic scattering of photons typically originating from a monochromatic UV, Vis or near-IR laser light source. To observe Raman scattering, a change of the electric dipole-electric dipole polarizability with respect to the vibrational coordinate of the vibrational-rotational mode is required and therefore allows the investigation of modes inaccessible to IR spectroscopy, especially for centro-symmetric compounds.[6] After excitation of the system into a virtual energy state, relaxation can occur in different ways: by elastic Rayleigh scattering, in which the energy of the photons remains unchanged, by Stokes Raman scattering, in which energy of the photon is transferred to the material or by Anti-Stokes Raman scattering, where the photon absorbs energy from the material as sketched in Figure 2.3.1. Hereby, the energy difference of the photon is equal to the energy difference of the vibrational-rotational state. Due to the different scattering probabilities and occupied states, the signal intensities decrease from Rayleigh, Stokes to Anti-Stokes scattering.
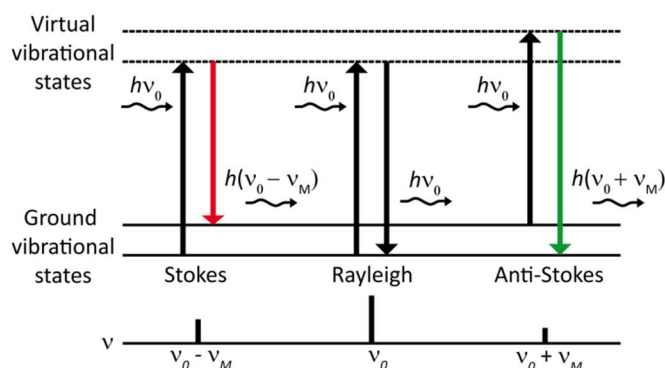
Figure 2.3.1: Energy transfer model of Stokes Raman, Rayleigh and anti-Stokes Raman scattering.

In this thesis, in situ Raman spectra of thin films were recorded on a laser-microscope Raman spectrometer iHR 550 spectrometer on a BXFM microscope (HORIBA, Germany) with confocal geometry. The incident laser beam (532 nm at 10 mW) passes through a window in a vacuum chamber and is focused by an objective (100x) on the samples whereas Raman spectra of the powder materials were taken with a Jobin Yvon Typ V 010 Labram single grating spectrometer, equipped with a double super razor edge filter and a Peltier-cooled CCD camera using the linearly polarized 632.8 nm line of a He/Ne gas laser with power less than 1 mW (HORIBA, Germany). The measurements were performed by Dieter Fischer, MPI-FKF.

2.4 NUCLEAR MAGNETIC RESONANCE SPECTROSCOPY

All isotopes with a non-zero nuclear spin S can absorb and re-emit electromagnetic radiation in a magnetic field, a physical phenomenon that is exploited in nuclear magnetic resonance (NMR) spectroscopy.[7] Nuclei with a spin number S have an associated magnetic moment μ, which is given by $\mu = \gamma S$, where γ is the gyromagnetic ratio. In a magnetic field B, the previously degenerate magnetic energy levels of the isotopes split according to the number of spin states. The overall magnetization precess in this magnetic field at the so-called Larmor frequency, which is the product of the gyromagnetic ratio with the magnetic field strength. The resulting magnetic energy levels can be calculated by

$$E = -\mu B_0 \tag{2.4.1}$$

For a magnetic field along the z-axis, a positive gyromagnetic ratio and a spin number ½ results in an energy difference of

$$\Delta E = \gamma \hbar B_0 \tag{2.4.2}$$

As evident from Equation 2.4.2, the energy splitting will depend on the gyromagnetic value as well as the strength of the magnetic field. This energy difference can be absorbed from radiofrequency (RF) radiation, precisely, if it equals the Larmor precession frequency. However, the surrounding electron shells create a magnetic field opposite to that of the nucleus, "shielding" it. As a consequence, the energy gap is altered and, therefore, the resonance frequency. These perturbation of the magnetic resonant absorption are the basis of the NMR technique. The degree of the shift is called chemical shift σ. Depending on whether the shielding is stronger or lower to a reference, the chemical shifts is upfield ($\sigma < \sigma_{reference}$) or lowfield ($\sigma > \sigma_{reference}$).

In general, the electronic environment of nuclei is non-spherical. Consequently, chemical shifts are anisotropic and change with the orientation of a molecule with respect to the magnetic field. In liquid NMR, fast molecular rotation averages the chemical shift into a isotropic signal. In solid state NMR, magic-angle-spinning (MAS) can minimize anisotropy related peak broadening significantly by fast rotation of the sample at the magic angle, 54.7°, at 8 – 70 kHz. At this angle, any magnetic vector along the z-axis (parallel to the magnetic field B) will rotate through the x and y axes removing the anisotropy. For many elements, the natural abundance of suitable NMR isotopes is low resulting in poor signal-to-noise ratios which in turn imply long measurement times or the need of isotope enrichment. In a cross-polarization (CP) experiment, an abundant isotope can circumvent this problem by spin-transfer of the nuclei of an abundant isotope to the observed nucleus when the Hartmann-Hahn condition is met. For ^{1}H as the abundant nucleus, it also allows faster repetition rates increasing signal-to-noise ratio significantly. Depending on the contact times in which cross-polarization takes place, the transfer of

polarization can vary. The different contact times can be summarized in CP build up profiles which contain information on the environment of the observed nuclei. 2D-NMR, like heteronuclear correlation (HETCOR) or heteronuclear single quantum coherence (HSQC) experiments, reveal further insights into the local environment and vicinity of observed nuclei by uncovering their direct and spatial coupling.

Solid-state NMR experiments were carried out on a Bruker Avance 500 NMR operating at frequencies of 500.1, 125.7, 50.7 and 470 MHz for ^{1}H, ^{13}C, ^{15}N and ^{19}F respectively. The samples were contained in a 4 mm ZrO_2 rotor (Bruker Biospin, Germany) which was mounted in a standard double resonance MAS (magic angle spinning) probe. The ^{1}H, ^{13}C and ^{15}N chemical shifts were referenced relative to TMS and nitromethane, respectively. The ^{1}H-^{15}N and ^{1}H-^{13}C cross-polarization (CP) MAS spectra were recorded at a spinning speed of 10 kHz using a ramped-amplitude (RAMP) CP pulse on ^{1}H, centered on the n = +1 Hartmann-Hahn condition.

For 2D ^{1}H-^{13}C HETCOR in Chapter 3, measurements were done at a field strength of 16.45 T (700 MHz ^{1}H Larmor frequency) using and Avance NEO spectrometer (Bruker Biospin, Germany). The corresponding CP-MAS NMR spectra were acquired with a 1.9 mm triple channel probe and a spinning speed of 40 kHz. The measurements were performed by Suresh Vasa, LMU Munich.

Liquid NMR experiments were performed on a Bruker AV 400 TR by the service group of the Department of Chemistry, LMU Munich.

2.5   ELECTRON MICROSCOPY

Classical optical microscopy is limited by the diffraction limit of light impeding the study of structures on the nanometer scale.[8] However, when electrons are used, their much shorter wavelengths allow to push this limit beyond the nanometer scale. In electron microscopy, specimen are illuminated by a beam of accelerated electrons that interact with the sample by inelastic and elastic scattering.[9] As outlined in Figure 2.5.1, the impingement of electrons onto a specimen can lead to various interactions. Depending on the energy of the electrons, their penetration depth can vary significantly and as they traverse the sample, the loss of energy can be attributed to different kinds of interaction predominant in different penetration depths. It is therefore possible to study both the surface of a specimen and its interior. All in all, the diffracted electrons not only allow the structural, topological and morphological study, but also contain additional spectroscopic information of the specimen composition.
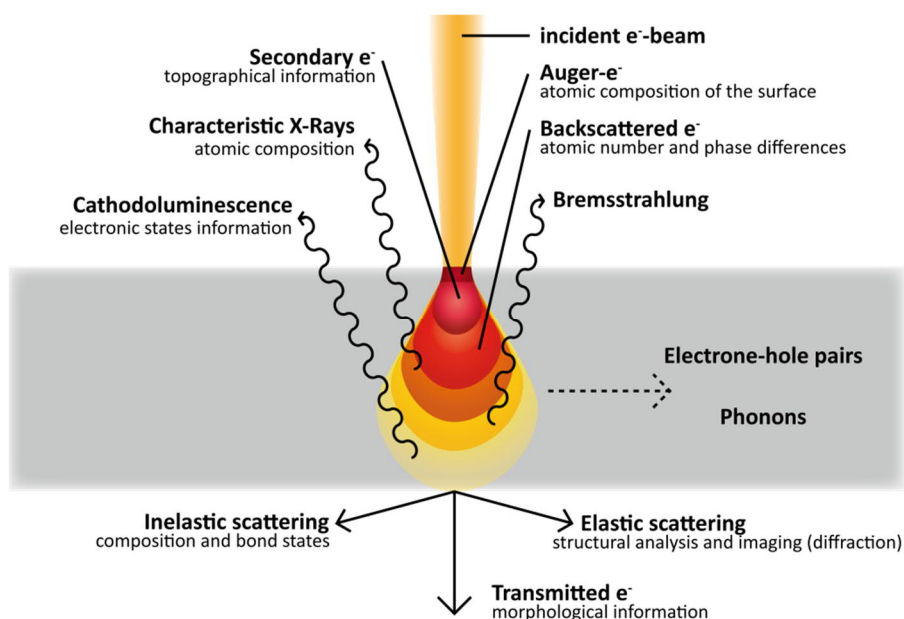
Figure 2.5.1: Schematic illustration of possible electron beam-matter interactions and their information content.

These electrons are either detected directly or focused and magnified by an array of electromagnetic lenses analogous to those in a conventional optical microscope. A more detailed schematic of different types of electron microscopes are displayed in Figure 2.5.2 and Figure 2.5.3.

2.5.1   SCANNING ELECTRON MICROSCOPY

Scanning electron microscopy (SEM) is primarily used for the study of the topography and element contrast of a sample by detection of secondary and backscattered electrons.[10] Figure 2.5.2 illustrates the components and operating principle of a SEM. First, an electron gun, e.g. a Schottky or cold field emitter, generates an electron beam which is accelerated to energies between 1-30 kV. A complex array of electromagnetic lenses is used to deflect and focus the electron beam in a raster scan pattern on the specimen. Upon impingement on each sample point, secondary electrons are inelastically scattered from the sample surfaces and collected to generate a topological image of the sample. While small scattering angles assure a large depth of field, the small penetration depth of the incident electrons allow the mapping of the sample surface topology. For the quasi-elastically backscattered electrons, the energies are close to that of the incident electrons. Regions consisting of elements with high atomic numbers reflect electrons stronger than those of low atomic number, allowing the distinction of areas with different chemical composition due to the image contrast. Generated X-rays provide information on the chemical composition as discussed in Chapter 2.5.3.
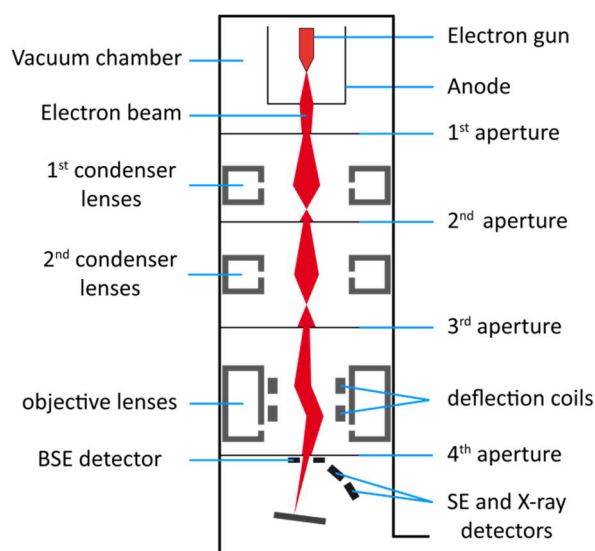
Figure 2.5.2: Schematic illustration of a SEM including the pathway of the electron beam (red).

SEM measurements were performed on a Zeiss Merlin FE-SEM (Carl Zeiss Microscopy GmbH, Germany) by Viola Duppel, MPI-FKF.

2.5.2 TRANSMISSION ELECTRON MICROSCOPY

In a transmission electron microscope (TEM), a parallel electron beam is transmitted through a very thin sample film, generally less than 100 nm thickness, and the transmitted beam is magnified by a series of electromagnetic lenses as depicted in Figure 2.5.3.[11] The signal is recorded by a phosphor screen or a charge-coupled device (CCD) camera. TEM extracts information on both the morphology and inner structure of the sample, by imaging and electron diffraction, respectively. The TEM can be operated in different modes, in imaging, these are the bright and dark field mode. In the former, only the non-diffracted electrons are projected yielding images defined by a mass-thickness contrast due to differences in composition or thickness in the specimen. In dark field, the opposite is the case, only the diffracted beams are detected. Here, the strong scattering centers show the highest intensities. When the diffracted electron beam image focused at the back focal plane of the objective lens is projected by change of the strength of the intermediate lens, the diffraction pattern can be observed giving valuable information on the atomic structure of the sample. Phase-contrast imaging in High Resolution TEM (HRTEM) even opens up the possibility to enhance the point resolution to 0.5 Å. Combined with electron energy loss spectroscopy[12] (EELS) or energy dispersive X-ray[13] (EDX) analysis this characterization technique opens up further possibilities to investigate the chemical composition, bond states, phonons or band gap.
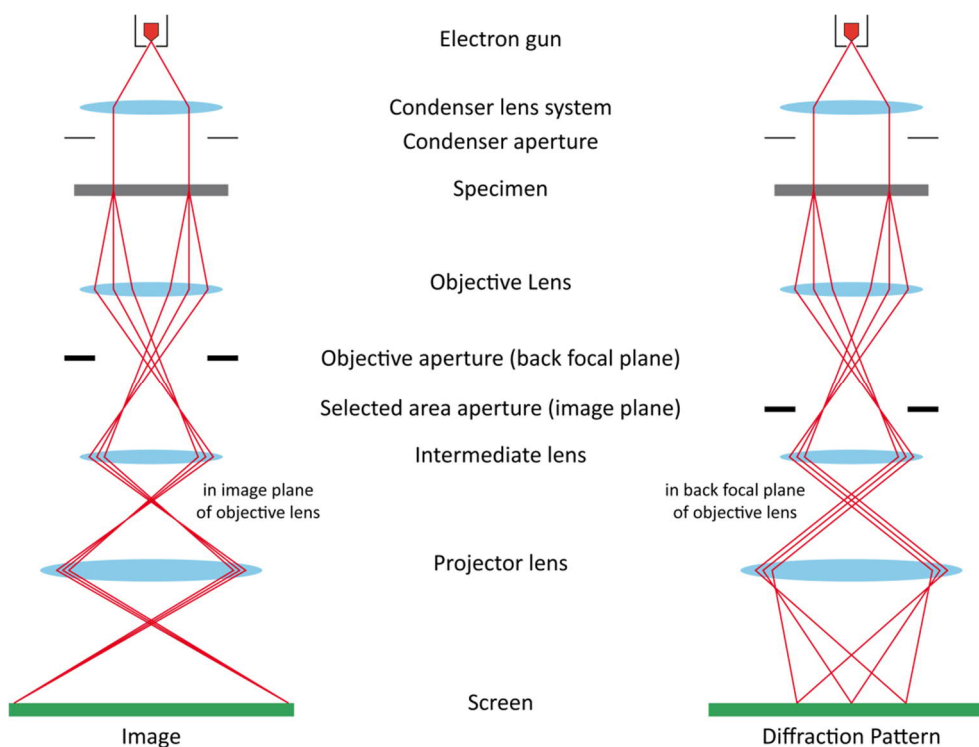
Figure 2.5.3: Schematic illustration of a TEM including the pathway of the electron beam (red) through electromagnetic lenses (blue). Changing of the projection of the image plane to the back focal plane (diffraction pattern) is controlled by changing the strength of the intermediate lens.

TEM and EDX measurements were performed by Viola Duppel on a Philips CM30 ST at 300 kV (FEI, Netherlands) equipped with an energy-dispersive X-ray (EDX) system (NSS, Thermo Scientific, Germany). Images were recorded with a CMOS Camera (TVIPS, Germany).

2.5.3   ENERGY DISPERSIVE X-RAY SPECTROSCOPY

Energy dispersive X-ray (EDX) spectroscopy is a powerful tool to analyze local differences in composition in both SEM and TEM measurement.[13] Characteristic X-rays are emitted when an incident electron ionizes an atom by exciting an inner shell electron to an unoccupied energy level or ejecting it into the vacuum, followed by the filling of the arising vacancy by an electron from a higher state. The energy difference between these two states is then emitted as characteristic X-Ray to compensate for the surplus energy. Alternatively, excess energy can be transferred to an electron, which is subsequently ejected into vacuum, a process taken advantage of in Auger electron spectroscopy.[14] The characteristic transitions are denoted after the shells involved. However, this method is most utile for elements with atomic numbers higher than $Z > 13$, as X-rays of lower energy are easily absorbed by the sample or the detector window.

2.6 X-RAY PHOTOELECTRON SPECTROSCOPY

X-ray photoelectron spectroscopy (XPS) allows the investigation of the surface chemistry, including the detection of the elemental composition and their electronic state except for hydrogen and helium.[15] This technique relies on the photoelectric effect. The sample surface is irradiated with photons of a characteristic energy that interact with the inner shell electrons. Ionization of the atom can lead to the emission of photoelectrons with kinetic energies that can be roughly estimated by the difference of the initial photon energy and the binding energy of the atom giving rise to a characteristic set of peaks that can be assigned to specific electron energy levels and oxidation states. In addition, signal intensities are proportional to the amount of the atoms permitting an approximate relative quantification of the elements, if factors, such as Scofield's photoelectron cross-section and the inelastic mean free paths, are taken into account. Due to scattering events of the photoelectrons, the predominant part of detected electrons originates from the sample surface, thus, yielding information at depths of a few nanometers.

Measurements were performed on an Axis Ultra (Kratos Analytical Ltd., UK) X-ray photoelectron spectrometer with an Al anode (Al K_α radiation, hv = 1486.6 eV, energy resolution ~0.1 eV). The binding energy scale was calibrated using the C 1s peak at 284.80 eV. The measurements were done by Mitsuharu Konuma (Chapter 3).

2.7 ELEMENTAL ANALYSIS

In elemental analysis the elemental composition of a substance is determined. For organic compounds, C, H, N, S analysis is most commonly used in order to determine the content of the elements.[16] The method is based on the complete combustion of a defined amount of material at high temperatures (> 1100 °C) in a highly oxygenated helium atmosphere. The gaseous products, e.g. CO_2, H_2O, NO_2 and SO_2, are separated and subsequently quantified through a thermal conductivity detector, giving the weight percentages of C, H, N, S and indirectly of O.

Alternatively, inductively coupled plasma optical emission spectrometer (ICP-OES) can be used.[17] In this method, the atoms and molecules are heated in a high temperature plasma up to 7000 K. Molecules dissociate into atoms and ions. Excitation of these species in the plasma leads to the formation and recombination of electron-hole pairs accompanied by emission of characteristic wavelengths which are detected by an optical spectrometer with a CCD-detector.

Elemental analysis experiments for Chapter 3 were performed by the chemical service group at the Max-Planck Institute for solid state research using an inductively coupled plasma optical emission spectrometer (ICP-OES; Vista Pro, Fa. Varian, Germany) for Zn and combustion analysis using a Vario EL apparatus (Fa. Elementar Analysensysteme, Germany) for C, N, and H determination. The samples

were completely dissolved in HNO_3 (conc.) using Berghof pressure systems for the ICP-OES measurements. All other measurements were performed by the chemical service group at the department of Chemistry, LMU Munich, on a Vario micro apparatus (Fa. Elementar Analysensysteme, Germany).

2.8 DYNAMIC LIGHT SCATTERING

Dynamic light scattering (DLS), also known as photon correlation spectroscopy, is an optical method for the determination of particle size distributions in suspensions.[18] In a typical experiment, a strongly diluted suspension is irradiated with monochromatic laser light that can undergo Rayleigh or Mie scattering by particles. The scattered light will undergo interference and as the particles move due to Brownian motion, the detected light intensity will fluctuate over time. A correlator analyses the rate of this intensity fluctuation by an autocorrelation function that can be fitted with an exponential decay function. The determined decay rate is directly linked to the diffusion coefficient of the particles allowing the calculation of the hydrodynamic radii of the particles using the Stokes-Einstein-equation. When using a Taylor series of exponential decay functions for fitting, a particle size distribution can be calculated. In addition, this method allows the determination of molecular weights and zeta-potentials. DLS measurements were performed on a Zetasizer Nano ZS (Malvern Instruments, UK) using a 633 nm laser in 173° backscatter detection geometry.

2.9 PHYSISORPTION

The porosity of materials can be assessed by numerous methods, including gas adsorption, small angle X-ray and neutron scattering, mercury porosimetry, electron microscopy and NMR methods.[19] Out of this group, gas sorption is one of the most versatile methods as it covers a wide range of pore sizes (0.35 – 100 nm), excellent accuracy and pore size resolution.[20] More importantly, it measures the uptake of guest-molecules and, hence, directly reflects the sorption behavior of materials upon guest-molecule accommodation.

The process of adsorption is defined as the enrichment of one or more components in an interfacial layer, where the adsorbable gas is denominated adsorptive, the solid adsorbent and the gas in the adsorbed state the adsorbate.[21] In general, pores are classified according to their pore size resulting in micro- (< 2nm), meso- (2 – 50 nm) and macropores (> 50 nm).[21] Furthermore, a distinction between physisorption and chemisorption is made based on the energies and forces prevailing. While the former is marked by weak, physical van-der-Waals forces and reversible adsorption, the latter comprises the formation of a chemical bond often associated with an activation energy and limited to a single adsorption site and layer. Physisorption is best observed for small, inert gas molecules that behave similar to an ideal gas, such as argon and nitrogen. For that reason, both gases are commonly used for

pore characterization by measuring the gas uptake at different partial pressures at their respective condensation temperatures. By additionally measuring the desorption, different shapes of physisorption isotherms are obtained depending on the interaction of the adsorbate with itself and the adsorbent. IUPAC defined six types of isotherms and four types of hysteresis (Figure 2.9.1).
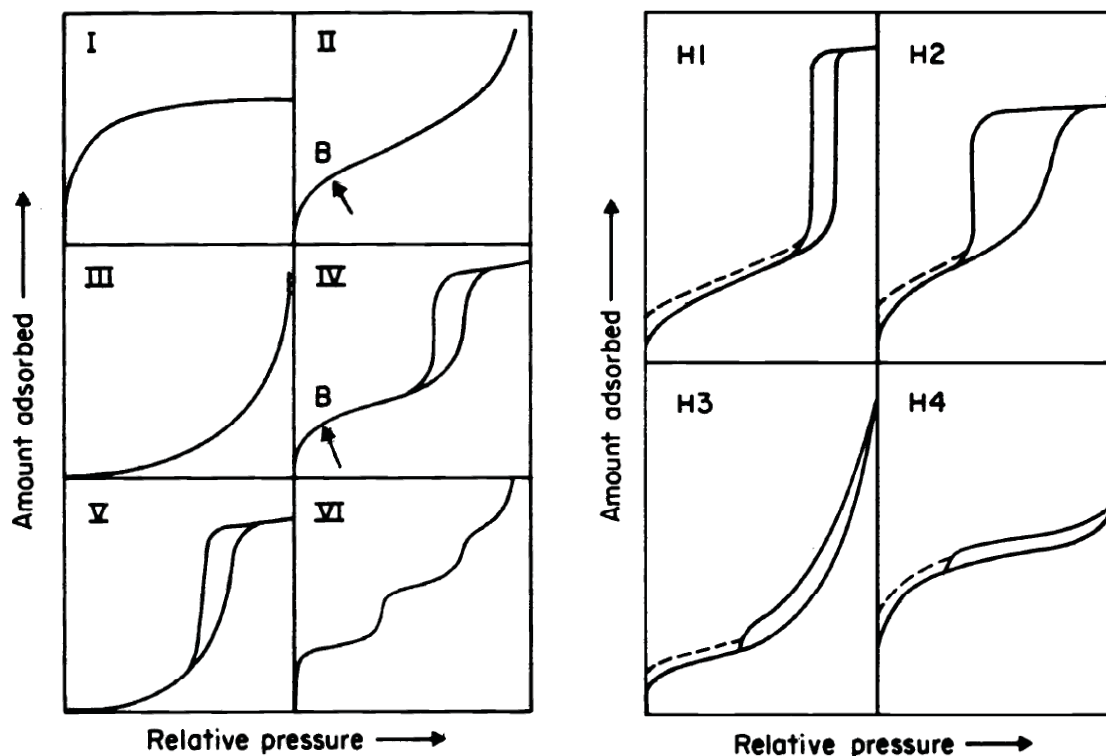
Figure 2.9.1: IUPAC classification of (left) physisorption isotherms and (right) hysteresis loops.[21] © 1985 IUPAC.

Type I isotherms are found for microporous materials with high adsorption potentials, such as Zeolithes, MOFs and activated carbons, in which the uptake takes place at very low partial pressures and with increasing pressures saturates. This is often associated with the formation of a monolayer. In type II isotherms, monolayer formation is reached at point B and followed by multilayer adsorption typical for macroporous materials. Adsorption isotherms characterized by weak adsorptive-adsorbent interactions and strong adsorptive-adsorptive interactions are represented in type III isotherms. The type II resembling type IV isotherm is marked by a hysteresis reaching a limiting value at high partial pressures, mostly found in mesoporous materials. The hysteresis is caused by capillary condensation, visible as a pronounced uptake before reaching a limit. The adsorbate undergoes a first-order phase transition from a gas-like state to a condensed-liquid state in the confined space. Here, intermolecular forces are dominant. For example, in a cylindrical pore, open at both ends, the menisci upon adsorption (cylindrical) and desorption (hemispherical) are different and, thus, according to the Kelvin equation, will exhibit shifted transition pressures.[22] Type V isotherms can be described as a combination of type III (low p/p_0) and type IV (high p/p_0) isotherms and are observed for materials with low adsorbate-

adsorbent affinity but strong adsorbate-adsorbate interactions, as for water on porous carbons. Type VI isotherms are found for uniform non-porous materials with stepwise multilayer formation.

The hysteresis loops shown in Figure 2.9.1 (right) give further insights into the pore structure, with type H1 and H4 as the extreme cases and, H2 and H3 intermediate states. Type H1 hysteresis loops are due to narrow pore size distributions of uniforms pores or agglomerates of regularly ordered, uniform spheres. In case of non-uniform pore sizes or ill-defined pore shapes, type H2 is observed. H3 types are characterized by no limiting saturation at high p/p_0 often found in aggregates of plate-like particles resulting in slit-shaped pores. H4 hysteresis is observed for narrow slit-pores that can also cover the micropores region.

In this thesis argon (87 K), carbon dioxide (273 K, 288 K), nitrogen (273 K, 288 K), and water (273 K, 288 K), adsorption/desorption measurements were performed on an Autosorb-iQ MP2 gas sorption analyzer (Quantachrome Instruments, USA). Samples were outgassed in vacuum (10^{-7} mbar) at 120 °C for 6-12 h to remove all guests molecules.

2.9.1 BRUNNAUER-EMMETT-TELLER THEORY FOR SURFACE AREA CALCULATION

The surface area is one of the most common quantities for the systematic study of porous materials. Today, the standard method for the calculation of a mass-weighted surface area is based on the Brunnauer-Emmett-Teller (BET) theory.[23] The fundament of this theory is the Langmuir model of adsorption,[24] which assumes monolayer formation for a perfectly flat, homogeneous, defect free surface. Further, all adsorption sites are believed to be equivalent, each physically adsorbing only one molecule into an immobile state without any further interactions with other adsorbates or the adsorbent. In the BET model, the gas molecules are assumed to adsorb on a solid in layers and interaction occurs only with adjacent layers that follow the Langmuir model. At the heart of the BET theory is Equation 2.9.1,

$$\frac{1}{W\left[\frac{p_0}{p} - 1\right]} = \frac{1}{W_m C} + \frac{C-1}{W_m C}\left(\frac{p}{p_0}\right), \qquad (2.9.1)$$

where p and p_0 are the equilibrium and saturation pressure, W and W_m the adsorbed gas weight and monolayer weights of the adsorbate, e.g. in volume units, and C the BET constant yielding a linear relation with the partial pressure p/p_0 as the variable from which the constants W_m and C can be extracted. Equation 2.9.2 gives the mass-weighted surface area,

$$S_{BET} = \frac{W_m N_A A_x}{mM}, \qquad (2.9.2)$$

where N_A is the Avogadro's constant, m the adsorbent mass, A_x the cross-sectional area and M the molecular weight of the adsorbate. Generally, either argon and nitrogen isotherms are used for the

calculation of surface areas as adsorbate-adsorbate and adsorbate-adsorbent interactions are minimal compared to other adsorptives.

Classically, the BET method is performed in the range of 0.05 – 0.30 p/p_0 due to the assumption that monolayer formation occurs in that pressure range. However, in (ultra-)microporous materials formation of monolayers takes place at lower pressures. Hence, it is indispensable to adapt the used pressure range to the linear range of the BET equation in order to obtain reliable accessible surface areas, e.g. for MOFs.[25,26] Therefore, multipoint BET calculations pressure ranges of the Ar isotherms were chosen with the help of the BET Assistant in the ASiQwin software, which chooses BET tags equal or below the maximum in V · (1 - P/P₀) in accordance with the ISO recommendations and consistency criteria.[27]

2.9.2 PORE-SIZE DISTRIBUTIONS BY DENSITY FUNCTIONAL THEORY

In addition to the accessible surface area of a material, pore sizes are of fundamental interest in the characterization of porous materials. Classical structure models obtained by XRD analysis can disclose voids in crystalline materials but fail to account for a realistic behavior of the entire material that may include textural porosity or breathing effects. Density functional theory (DFT) based approaches allow a theoretical description of adsorption and phase behavior of adsorbates in a porous, which can be fitted to the experimental data giving a pore size distribution (PSD) according to the DFT model.[28] The DFT models consist of a set of theoretical isotherms, the kernel functions N(p/p₀, W), over the micro- and mesopore range. These set of kernels differ in the pore shape assumed, e.g. slit, spherical or cylindrical, and material behavior and can take into account isotherm hysteresis. To obtain a PSD, the adsorption integral equation (Equation 2.9.3) is solved,

$$N\left(\frac{p}{p_0}\right) = \int_{W_{min}}^{W_{max}} N\left(\frac{p}{p_0}, W\right) f(W) dW,$$

(2.9.3)

where N(p/p₀) is the experimental adsorption isotherm data, W the pore width, N(p/p₀,W) the kernel of theoretical isotherms and f(W) the PSD function. To this date, various kernels are commercially available and for example non-local DFT (NLDFT) methods are already a common standard for PSD calculation since 2007.[29] As nitrogen and argon are generally used as adsorptives, both fluid-fluid and solid-fluid are calculated with Lennard-Jones potentials for given pore geometries as these describe dispersion interactions sufficiently well.[28] However NLDFT methods assume homogeneous pore walls, whereas the more advanced quenched solid DFT (QSDFT) model introduces surface roughness and heterogeneity.[30] Based on these models, DFT based surface areas can be calculated.

PSDs were determined using the calculation model for Ar at 87 K on zeolites/silica (spherical/cylindrical pores, NLDFT equilibrium model and for CO_2 at 273 K on carbon (NLDFT model)) of the ASiQwin software (v5.2) from Quantachrome.

2.9.3   HEAT OF ADSORPTION

In general, adsorption lowers the energy of a system and is consequently thermodynamically seen an exothermic process. The amount of heat released during this process provides insights into the attractive forces between the adsorbate and adsorbent. This chemical affinity can be calculated as the differential heat of adsorption Q_{st} which gives the released heat upon the addition of a differential amount of adsorbate to the surface.[31] The value of Q_{st} depends on the degree of surface already covered by the adsorbate, it is often given as a variation of the surface coverage θ. The isosteric heat of adsorption can be calculated according to the Clausius-Clapeyron equation given in Equation 2.9.4,

$$Q_{st} = R \cdot \left(\frac{\partial \ln(p)}{\partial \frac{1}{T}} \right)_\theta , \qquad (2.9.4)$$

with R being the gas constant, p the pressure, and T the temperature. Two isotherms at different temperatures are sufficient to calculate Q_{st}.

The isosteric heats of adsorption were calculated from the CO_2 and CH_4 adsorption isotherms at 273 and 288 K using the AsiQwin software.

2.9.4   GAS SELECTIVITY

Gas selectivity is of major importance for storage and separation applications, however the measurement of mixed-gas adsorption equilibrium remains very challenging. As the direct measurement of gas mixtures is often linked to challenging experimental set-ups and sophisticated instrumentation, theoretical approaches using independent single isotherms have been developed to determine the gas selectivity of two adsorptives.

Henry calculation

The most simple method assumes that the amount of adsorbate follows Henry's law (Equation 2.9.5),[32] which states that the surface coverage θ is directly proportional to the Henry constant K_H in function of the partial pressure p/p$_0$.

$$\theta = K_H \frac{p}{p_0} \tag{2.9.5}$$

The selectivity is calculated as the ratio the initial slopes of the experimental isotherms, being K_H the slope. Generally, fitting of the isotherms is done assuming the Langmuir model.

Ideal adsorbed solution theory

To this day, the ideal adsorbed solution theory (IAST) remains the benchmark method for selectivity determination out of independent, pure-component isotherms.[33,34] Despite its limitations for adsorbates, which differ strongly in polarity, size or affinity and adsorbents with very heterogeneous surfaces, the IAST method is commonly used. It assumes that the adsorbate forms an ideal solution on the adsorbent surface and does not exhibit interactions within the adsorbate mixture, with the components having equal spreading pressures. For a pure component, the spreading pressure π can be calculated using Equation 2.9.6,

$$\pi = \frac{A}{RT} \int_0^{p_0^i} n_i(p) d \ln p, \tag{2.9.6}$$

where A is the area, R is the gas constant, T the temperature, n_i the adsorbed amount of component i and p its pressure. The partial pressure for component i at equilibrium follows Raoult's law and is linked to the partial pressure $p_i^0(\pi)$ of pure component i calculated at the spreading pressure and temperature of the mixture by Equation 2.9.7,

$$P_i = y_i P_t = x_i p_i^0(\pi), \tag{2.9.7}$$

with y_i being the mole fraction of the gas phase and x_i the mole fraction in the adsorbed phase of component i and P_t the total pressure. Furthermore, the total loading n_T is given by

$$\frac{1}{n_T} = \sum_{i=1}^N \frac{x_i}{n_i^0} \tag{2.9.8}$$

Algebraic manipulation of Equation 2.9.6 yields the following condition for a two-component system,

$$\int_0^{\frac{y_1 P_t}{x_1}} n_1(p) d \ln p = \int_0^{\frac{y_2 P_t}{x_2}} n_2(p) d \ln p \tag{2.9.9}$$

The loadings $n(p)$ can be calculated by fitting m-site Langmuir isotherms to the experimental isotherms,

$$n(p) = \sum_{j=1}^{m} q_j = \sum_{j=1}^{m} \frac{q_{sat,j} a_j p}{1 + a_j p} \qquad (2.9.10)$$

where q_{sat} is the saturation loading and a the Langmuir constant. In general, single- or dual-site Langmuir isotherms describe the experimental isotherm sufficiently well. Solving Equation 2.9.9 needs to be done iteratively and yields x_1 and x_2, which can then be used to calculate the selectivity, by Equation 2.9.11,

$$S = \frac{x_1/y_1}{x_2/y_2} \qquad (2.9.11)$$

Selectivities were calculated with a standardized procedure written in Matlab by Alberto Jiménez-Solano, MPI-FKF.

2.10   Spectroscopic Ellipsometry

Light reflection (or transmission) of thin films can be exploited for their optical characterization as it is done in ellipsometry. It measures the change of the amplitude φ and phase difference Δ between s- and p-polarized light waves upon reflection from a film.[35] The reflected light is often elliptically polarized, giving the name to this optical method. For measurements including a broad range of wavelengths, e.g. the near-IR or UV-Vis range, it is referred to as spectroscopic ellipsometry (SE). This non-destructive technique allows the fast measurement of the layer thickness d with nm resolution, the refractive index (RI) n (or dielectric function ε) and absorption coefficient k of a thin film,[35] although it can be used for multi-layers as well. Best results are obtained for smooth and homogeneous surfaces, as scattering due to surface roughness and defects may corrupt the data. Figure 2.12.1 describes a typical SE experiment.
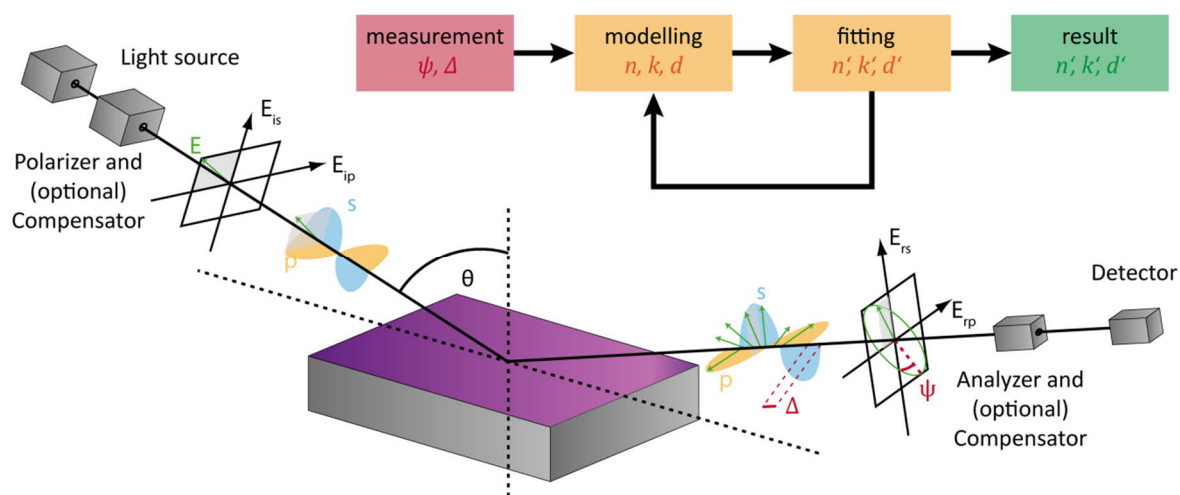
Figure 2.10.1: Schematic approach for the evaluation of ellipsometric data and experimental setup. Linearly polarized light (s- and p-polarized) interacts with the film and gets reflected. The amplitude ratio φ and the phase difference Δ of the ellipsometric light are detected. Based on a structural model, φ and Δ are calculated and the model iteratively adapted until consistency with the experimental data is reached.

Linearly polarized light is focused on the film and reflected. Interaction of the light with the sample leads a modified amplitude ratio φ and phase difference Δ between the s- and p-polarized light, which is detected as the complex reflectance ratio ρ, linked to φ and Δ by Equation 2.10.1.

$$\rho = \frac{r_p}{r_s} = tan(\varphi)\,e^{i\Delta} \tag{2.10.1}$$

A model is constituted describing the structure with appropriate dispersion laws and the calculated φ and Δ compared to the experimental data. The experimental data is then fitted by the model until the values converge yielding d, n and k. To ensure reliable results, correct model constitution is as crucial as proper fitting. Dielectric materials, as employed in this thesis, are well described by the Cauchy model or the Cauchy with Urbach-Tail model.[36]

Ellipsometric measurements were performed on a Semilab PS-1000 (Semilab, Hungary) in 60° or 75° geometry with a Xe-lamp. Data analysis was done with the SEA program (v1.4.12, Semilab, Hungary). Fitting range was limited to 300 – 1000 nm and models constituted with exclusively or a combination of Cauchy, Cauchy with Urbach-Tail and Lorentz dispersion law.[36] Fitting was performed with the Levenberg–Marquardt algorithm and the Nelder-Mead simplex algorithm.[37,38]

2.10.1 ELLIPSOMETRIC POROSIMETRY

Ad- and desorption of guest molecules can lead either to thickness change of the film due to material swelling or shrinkage, or, to a change in the effective refractive index. Monitoring of these change by ellipsometry permit the indirect measurement of ad- and desorption isotherms in which the effective refractive index and/or film thickness is a function of the partial pressure of the vapor. The porosity or volume fraction $P(p/p_0)$ of the film can then be calculated by Equation 2.10.2.[39]

$$P\left(\frac{p}{p_0}\right) = \frac{\frac{n_{\text{eff}}^2\left(\frac{p}{p_0}\right)-1}{n_{\text{eff}}^2\left(\frac{p}{p_0}\right)+2} - \frac{n_{\text{eff}}^2\left(\frac{p}{p_0}=0\right)-1}{n_{\text{eff}}^2\left(\frac{p}{p_0}=0\right)+2}}{\frac{n_a^2-1}{n_a^2+2} - \frac{n_v^2-1}{n_v^2+2}}, \tag{2.10.2}$$

where the subscripts eff denominate the effective RI in function of the partial pressure, a that of the adsorptive and v that of the void, which, in most cases, can be assumed to be 1. Nevertheless, different chemical affinity of adsorptives to the adsorbent may lead to incomplete pore filling and, hence, differing porosities depending on the adsorptive employed.

Samples were directly activated in the measurement chamber at high vacuum for at least 1 h. The measurements were performed with Semilab PS-1000 (Semilab, Hungary) in 60° geometry with a Xe-lamp as the light source. Water, methanol, ethanol and iso-propanol vapors were measured. Data analysis was performed as described in Chapter 2.10 fitting either or both n and k.

2.11   MICROSCOPE SPECTROPHOTOMETRY

Ultraviolet (UV-) and visible (Vis-)spectroscopy are fundamental in the optical characterization of materials or, as in this thesis, specimen showing structural color. This technique comprises wavelength-dependent measurement of light intensity, either as spectral reflectance, transmission or absorptance. To this end, samples are focused in a microscope and illuminated through an array of lenses. The light beam can be split to be resolved in a spectrometer and, simultaneously, be directed to a camera for the acquisition of photographic images. In addition, real-time imaging and spectroscopy allow the study of the optical response for dynamic processes, e.g. exposition to vapors. The experimental setup to monitor the reflectance of the specimen in function of volatile organic vapor exposure is depicted in Figure 2.11.1. The samples were fixed in a custom-build steel chamber with two quartz windows allowing the measurement of reflectance and transmission spectra of enclosed samples. The chamber could be flushed with a pure nitrogen stream or saturated with vapors of volatile organic solvents or water by directing the nitrogen stream through gas washing bottles filled with the corresponding solvents.
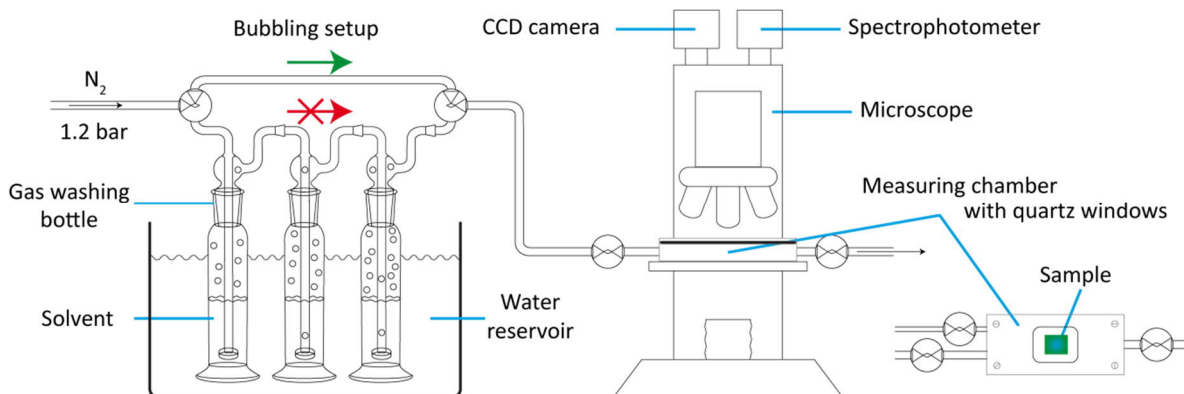
Figure 2.11.1: Schematic illustration of the experimental setup for microscopic and spectroscopic measurement with or without dynamic vapor exposure. The specimen is fixed on the microscope in a steel chamber with transparent quartz windows on both sides for reflectance and/or transmission measurements. The chamber, controlled by various valves, can either be flushed with pure nitrogen or a stream of volatile organic compounds with nitrogen as a carrier gas, kept at a constant temperature by a water reservoir.

For microscopic measurements, a Leica DM 2500M microscope (Leica Microsystems GmbH, Germany) with an attached digital camera DFC295 was used. Optical measurements were acquired simultaneously with an attached USB4000-XR1-ES spectrophotometer (Ocean Optics Inc., USA). Measurements with vapor exposure were performed by fixing the sample in a closed custom-built steel chamber with two transparent quartz windows on opposite sides. The chamber was attached to a bubbling system that could be run in two modes. Either with pure nitrogen or by enriching the nitrogen stream with solvent vapor by bubbling through solvent filled gas washing bottles. To assure quantitative saturation, three bottles were stringed together. Reflectance measurements were referenced to a calibrated WS-1-SL mirror (Ocean Optics Inc., USA)

2.11.1 THEORETICAL CALCULATION OF REFLECTANCE SPECTRA

A theoretical description for the propagation of electromagnetic waves in layered media can be done via the transfer-matrix method, allowing the simulation of transmission and reflectance spectra for given reflective indices (RIs) and layer thicknesses.

In the following, the method is explained for light passing through a stack of layers at normal incidence, neglecting material absorbance, media with magnetic properties and the polarization state of the light, nevertheless, it can be generalized to consider these properties.

Equation 2.11.1 describes the electromagnetic wave along normal incidence (z-axis) as a superposition of a right (r) and left-traveling (l) wave with the wave number k.

$$\begin{pmatrix} E(z) \\ F(z) \end{pmatrix} = \begin{pmatrix} E(z) \\ dE(z)/dz \end{pmatrix} = \begin{pmatrix} E_r e^{ikz} + E_l e^{-ikz} \\ ik E_r e^{ikz} - ik E_l e^{-ikz} \end{pmatrix} \tag{2.11.1}$$

Passing through a medium over a distance d can be expressed by a matrix multiplication with the matrix (Equations 2.11.2 and 2.11.3). For various layers, the system transfer matrix is calculated by multiplication of the transfer matrices.

$$M = \begin{pmatrix} \cos kd & \frac{1}{k}\sin kd \\ -k\sin kd & \cos kd \end{pmatrix} \tag{2.11.2}$$

$$\begin{pmatrix} E(z+d) \\ F(z+d) \end{pmatrix} = M \begin{pmatrix} E(z) \\ F(z) \end{pmatrix} \tag{2.11.3}$$

Given that the stack starts at 0, negative z describe reflection at the layer (Equation 2.11.4), while positive z describe transmission (Equation 2.11.5).

$$E_l = E_0 e^{ik_l z} + r E_0 e^{ik_l z} \tag{2.11.4}$$

$$E_r = t E_0 e^{-ik_r z} \tag{2.11.5}$$

Hereby, r and t describe the amplitude reflectance coefficient and amplitude transmission coefficient, respectively. The wavenumbers k_l and k_r are those of the left and right medium. By solving Equation 2.11.3 for r and t, the reflectance and transmission can be calculated (Equations 2.11.6)

$$T = \frac{k_r}{k_l}|t^2| \ and \ R = |r^2| \tag{2.11.6}$$

2.11.2 COLOR IMAGE ANALYSIS BY PRINCIPAL COMPONENT ANALYSIS

In photographic images, colors are represented by a combination of elementary colors of different intensities, e.g. red (R), blue (G) and green (B) values, and, hence, lack a good portion of spectral information. Nevertheless, RGB values contain sufficient information to measure changes indirectly in the optical behavior of a system. If a system reacts to an external stimulus, it can be measured as a change in the RGB values. For various stimuli, for example organic vapor exposure and various samples, this yields a large set of characteristic $\Delta(R, G, B)$ values that can be expressed mathematically as a matrix.

Principal component analysis (PCA) is a statistical method in which a set of observables depending on correlated variables is transformed so that it can be expressed with a set of orthogonal components.

Hereby, the first component represents the largest possible variance of the observables. In principle, the transformation can be understood as a transformation into principal axes, a detailed mathematical description on principal can be found in the literature.[40] In color image analysis, this method can help to unravel seemingly random observables into a set of values of independent principal components, allowing to express stimuli in function of significantly less variables. In reverse, observables can be assigned to specific stimuli more easily.

PCA was performed with the statistical PCA tool of the program OriginLab 2017 (b9.4.0.220) (OriginLab Corporation, USA).

2.12   CONTACT ANGLE

The measurement of contact angles quantifies the wettability of a solid surface. Hence, it is an indirect but yet simple method to evaluate the solvophilicity, in case of water hydrophilicity, of thin films and the materials comprising it. In general, a static contact angle θ is determined as shown in Figure 2.12.1. Further information on wetting, dewetting and adhesion characteristics can be extracted by dynamic measurements in which the advancing and receding contact angles of the drops are determined. In case of water, surfaces exhibiting contact angles with θ < 90° are commonly considered to be hydrophilic, those with θ < 90° hydrophobic.[41]
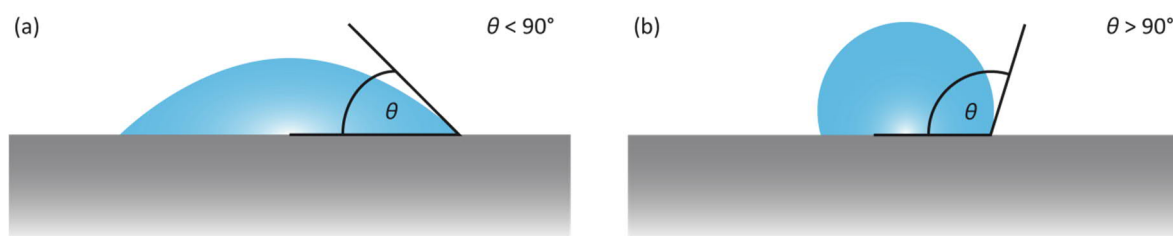
Figure 2.12.1: Schematic illustration of a liquid drop of water and the contact angle between the solid-liquid and the liquid-vapor interface of a (a) hydrophilic and (b) hydrophobic film.

Contact angles were determined statically by Sessile drop measurements on a by Katalin Szendrei-Temesi (LMU Munich).

2.13   REFERENCES

1   L. Spiess, G. Teichert, R. Schwarzer, H. Behnken and C. Genzel, Moderne Röntgenbeugung: Röntgendiffraktometrie für Materialwissenschaftler, Physiker und Chemiker, Vieweg+Teubner Verlag, 2009.

2   P. Scherrer, Nachrichten von der Gesellschaft der Wissenschaften zu Göttingen, Mathematisch-Physikalische Klasse, 1918, 1918, 98-100.

3   P. Müller-Buschbaum, in Applications of Synchrotron Light to Scattering and Diffraction in Materials and Life Sciences, Eds. M. Gomez, A. Nogales, M. C. Garcia-Gutierrez and T. A. Ezquerra, Springer Berlin Heidelberg, Berlin, Heidelberg, Edn., 2009, pp. 61-89.

4   G. Renaud, R. Lazzari and F. Leroy, Surf. Sci. Rep., 2009, 64, 255-380.

5   B. H. Stuart, Infrared Spectroscopy: Fundamentals and Applications, John Wiley & Sons, Ltd, 2004.

6   E. Smith and G. Dent, Modern Raman Spectroscopy: A Practical Approach, John Wiley & Sons, Ltd, 2013.

7   J. Keeler, Understanding NMR Spectroscopy, Wiley, 2011.

8   S. Wischnitzer, Introduction to electron microscopy, 3d edn., Pergamon Press, New York, 1981.

9   S. Amelinckx, D. van Dyck, J. van Landuyt and G. van Tendeloo, Electron Microscopy: Principles and Fundamentals, Wiley, 2008.

10   J. Goldstein, Scanning electron microscopy and x-ray microanalysis, 3rd edn., Kluwer Academic/Plenum Publishers, New York, 2003.

11   D. B. Williams and C. B. Carter, Transmission electron microscopy : a textbook for materials science, 2nd edn., Springer, New York, 2008.

12   R. F. Egerton, Electron Energy-Loss Spectroscopy in the Electron Microscope, Springer US, 2012.

13   D. Shindo and T. Oikawa, in Analytical Electron Microscopy for Materials Science, Springer Japan, Tokyo, Edn., 2002, pp. 81-102.

14   C. L. Briant, Auger Electron Spectroscopy, Elsevier Science, 2012.

15   S. Hofmann, Auger- and X-Ray Photoelectron Spectroscopy in Materials Science: A User-Oriented Guide, Springer Berlin Heidelberg, 2012.

16   W. Kirmse, Organic Elemental Analysis: Ultramicro, Micro, and Trace Methods, Elsevier Science, 2012.

17   J. Nölte, ICP Emissionsspektrometrie für Praktiker: Grundlagen, Methodenentwicklung, Anwendungsbeispiele, Wiley, 2012.

18   B. Chu, in Soft Matter Characterization, Eds. R. Borsali and R. Pecora, Springer Netherlands, Dordrecht, Edn., 2008, pp. 335-372.

19   J. Rouquerol, D. Avnir, C. W. Fairbridge, D. H. Everett, J. H. Haynes, N. Pernicone, J. D. F. Ramsay, K. S. W. Sing and K. K. Unger, Pure Appl. Chem., 1994, 66, 1739-1758.

20   J. U. Keller and R. Staudt, Gas Adsorption Equilibria: Experimental Methods and Adsorptive Isotherms, Springer, 2005.

21   K. S. W. Sing, D. H. Everett, R. A. W. Haul, L. Moscou, R. A. Pierotti, J. Rouquerol and T. Siemieniewska, Pure Appl. Chem., 1985, 57, 603-619.

22   L. H. Cohan, J. Am. Chem. Soc., 1938, 60, 433-435.

23   S. Brunauer, P. H. Emmett and E. Teller, J. Am. Chem. Soc., 1938, 60, 309-319.

24   I. Langmuir, J. Am. Chem. Soc., 1918, 40, 1361-1403.

25   Y.-S. Bae, A. Ö. Yazaydın and R. Q. Snurr, Langmuir, 2010, 26, 5475-5483.

26   K. S. Walton and R. Q. Snurr, J. Am. Chem. Soc., 2007, 129, 8552-8556.

27   I. O. f. Standardization, Determination of the specific surface area of solids by gas adsorption - BET method, 2010, ISO 9277:2010, Geneve, Switzerland.

28   J. Landers, G. Y. Gor and A. V. Neimark, Colloids Surf., A, 2013, 437, 3-32.

29   ISO, Pore size distribution and porosity of solid materials by mercury porosimetry and gas adsorption -- Part 3: Analysis of micropores by gas adsorption, 2007, ISO 15901-3:2007, Geneve, Switzerland.

30   A. M. Puziy, O. I. Poddubnaya, B. Gawdzik and M. Sobiesiak, Adsorption, 2016, 22, 459-464.

31   S. Lowell, J. E. Shields, M. A. Thomas and M. Thommes, Characterization of Porous Solids and Powders: Surface Area, Pore Size and Density, Springer, Dordrecht, Netherlands, 2004.

32   W. Henry, Philosophical Transactions of the Royal Society of London, 1803, 93, 29-274.

33   K. S. Walton and D. S. Sholl, AIChE J., 2015, 61, 2757-2762.

34   A. L. Myers and J. M. Prausnitz, AIChE J., 1965, 11, 121-127.

35   H. Fujiwara, Spectroscopic Ellipsometry: Principles and Applications, Wiley, 2007.

36   M. Born and E. Wolf, Principles of Optics: Electromagnetic Theory of Propagation, Interference and Diffraction of Light, Elsevier Science, 2013.

37   J. A. Nelder and R. Mead, The Computer Journal, 1965, 7, 308-313.

38   D. W. Marquardt, Journal of the Society for Industrial and Applied Mathematics, 1963, 11, 431-441.

39   A. Bourgeois, Y. Turcant, C. Walsh and C. Defranoux, Adsorption, 2008, 14, 457-465.

40   I. T. Jolliffe, Principal component analysis, 2nd edn., Springer, New York, 2002.

41   K.-Y. Law, J. Phys. Chem. Lett., 2014, 5, 686-688.

3 PHYSICAL VAPOR DEPOSITION OF MOFS

As outlined in Chapter 1.1, structuring of materials at different length scales is of upmost importance, especially when they act as the functional component in a device with a hierarchical architecture. Hence, fabrication methods that yield deposits of defined thicknesses are required. Here, methods compromising the material deposition from the gas phase have proven to be advantageous as they offer the possibility of transferring a target material onto a substrate while controlling the final film thicknesses avoiding a solution-based approach. However, the preceding ablation of the material into the gas phase can be very challenging, as the phase transition is often accompanied by severe thermal stress, which, in case of soft matter, often leads to the material decomposition.

This chapter describes the femtosecond-PLD, a form of PLD, of the prototypic MOF, ZIF-8, which was non-covalently modified with the polymer PEG-400 prior to ablation preventing its degradation under laser irradiation. Furthermore, the interaction of the polymer with the MOF and the particle was studied and the reversible nature of the modification proven. Hence, this work proves the successful PLD of a porous MOF retaining its crystallinity and porosity, adding another method to the deposition possibilities of MOFs.

3.1 ZIF-8 FILMS PREPARED BY FEMTOSECOND PULSED-LASER DEPOSITION

Dieter Fischer, Alberto von Mankowski, Annekathrin Ranft, Suresh K. Vasa, Rasmus Linser, Jochen Mannhart, and Bettina V. Lotsch

Abstract

As metal–organic frameworks (MOFs) are coming of age, processing strategies and morphology engineering have gained considerable importance, given the need of thin film geometries for many applications. Using the femtosecond pulsed-laser deposition (femto-PLD) technique, we have fabricated films of the zeolitic imidazolate framework (ZIF) zinc 2-methylimidazolate (ZIF-8) for the first time, thus extending the available film fabrication techniques for MOFs to physical vapor deposition. While deposition of pristine ZIF-8 turned out to be unsuccessful, we demonstrate that hybrid ZIF-8 impregnated with polyethylene glycol 400 as a "vehicle" ablate under ultrahigh vacuum conditions to form films with approximate composition $Zn(C_3N_2H_2–CH_3)_2 \cdot \frac{1}{8}PEG\text{-}400$. By washing the films with ethanol, the polyethylene glycol (PEG) additive can be removed, leading to pure ZIF-8 films on sapphire substrates. The target films and powders were comprehensively characterized by diffraction, spectroscopic and microscopic techniques as well as thermogravimetry and Ar physisorption measurements.
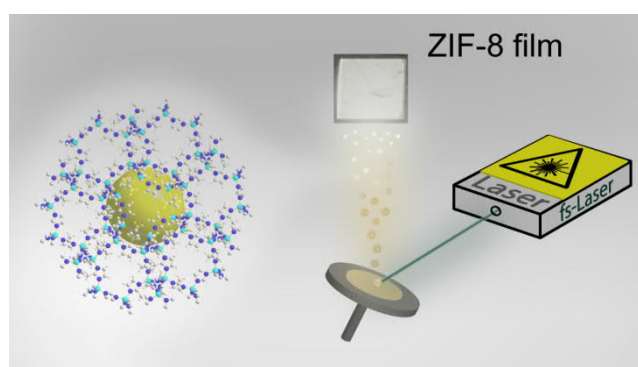

Table of content: ZIF-8 films have been fabricated via femtosecond pulsed laser deposition. Impregnation of ZIF-8 with the biodegradable polymer PEG-400 yielded a target material ablatable by femtosecond pulsed laser irradiation to form thin ZIF-8 films, where the polymer could be easily removed to recover the MOF porosity.

3.1.1 INTRODUCTION

Metal–organic frameworks (MOFs) are porous coordination polymers built of metal-containing nodes connected by organic linkers, which renders them chemically versatile platforms for applications in gas storage and separation, catalysis, sensing, and drug delivery, among many others.[1-3] More recently, their use as tunable photocatalytic platforms and in optoelectronic devices has been discussed.[4-6] For these applications in particular, the fabrication of thin films is of major importance. Numerous deposition techniques for the fabrication of thin films have been reported, ranging from direct deposition from the mother liquor, seeded growth, or liquid phase epitaxy to dip- and spin-coating or electrochemical growth methods.[7-10] More recently, the first chemical vapor deposition of the zeolitic imidazolate framework ZIF-8 has been reported by Stassen et al.[11] Following this procedure, a metal oxide film is deposited from vaporized precursors which subsequently undergoes a solid–vapor reaction with the vaporized linker. Another gas phase deposition technique was reported by Ahvenniemi and Karppinen, who successfully produced crystalline thin films of MOF-2, a copper(II)terephthalate, by atomic layer deposition.[12]

Regarding physical vapor deposition (PVD) methods such as conventional thermal evaporation, sputtering, or pulsed-laser deposition (PLD) of MOFs, literature reports on PVD of intact MOFs are still elusive.[13] Usually, thermal stress results in decomposition or amorphization of MOFs.[14] In fact, there are no literature reports in which a MOF or its fragments were transferred into the gas phase and deposited from there onto a substrate. In general, decomposition of the organic components occurs upon thermal stress, ion bombardment, or laser irradiation. For sputtering organic/polymeric materials, only polytetrafluoroethylene (PTFE) targets were used so far, forming hydrophobic fluorocarbon films with divergent C_xF_y compositions.[15] Using conventional nanosecond PLD, excimer lasers can only be applied for a few polymers (e.g., polyethylene, PTFE, polyimide), and even at low laser fluence, some polymers are very sensitive to photochemical activation and decomposition.[16,17] During the ablation process, the polymers are converted to a vapor that consists of monomers and small oligomeric fragments. Thus, neither conventional thermal evaporation techniques nor the standard PLD can be suitably employed for porous MOFs as their organic building blocks usually suffer from low vapor pressure and limited thermal stability.

To overcome these challenges, alternative approaches have been developed for the deposition of polymers and other organic matter which are known as matrix-assisted pulsed-laser evaporation (MAPLE), photosensitized ablation, or resonant infrared PLD.[18,19] These methods are successfully used, e.g., for the deposition of polyethylene glycol (PEG) films with different molecular weights, which show properties analogous to those of the starting materials.[20,21] However, these processes need either special absorption conditions or frozen polymer solutions at very low polymer concentrations.

As a potential remedy to those limitations, ultrashort laser pulses in the femtosecond (fs) range can be applied, which excite nonthermal transitions during the ablation process.[22] Up to now, however, the femtosecond laser ablation of polymers was only applied to modify the surface, e.g., by direct laser writing, with minimal thermal damage of the polymers,[23,24] rather than for film deposition.

Recently, the dense metal–organic framework compound europium(II) imidazolate (EuIm$_2$) was successfully deposited as thin film by a scanning PLD technique using a femtosecond laser. This is the first example utilizing an ultrashort pulsed laser for coatings with framework compounds.[25] To the best of our knowledge, no deposition of a porous MOF by the PLD technique has been reported to date.

In this study, the zeolitic imidiazolate framework ZIF-8 (ZnC$_8$H$_{10}$N$_4$) was chosen as a model system for femtosecond pulsed-laser deposition (femto-PLD). In ZIF-8, zinc is coordinated tetrahedrally by 2-methylimidazolate to form a cubic porous structure of sodalite (SOD) topology with 11.6 Å wide pores connected by 3.4 Å wide apertures.[26] ZIF-8 possesses a remarkable thermal stability up to 550 °C as well as high chemical stability. Thus, ZIF-8 has been extensively studied for applications in molecular sieving and is also one of the four metal–organic frameworks being manufactured commercially. Here, we demonstrate for the first time that intact thin films of ZIF-8 can be deposited by femto-PLD using polyethylene glycol 400 (PEG-400) as a vehicle. Furthermore, we characterized the powdered samples and deposited films to investigate the role of PEG-400 in the hybrid compound.

3.1.2 EXPERIMENTAL

Synthesis of ZIF-8 Hybrids

Pure ZIF-8 was prepared according to the literature.[27] A solution of Zn(NO$_3$)$_2$·6H$_2$O (0.744 g, 2.5 mmol, Sigma-Aldrich) in deionized water (10 mL) was added to a solution of 2-methylimidazole, Hmim, (8.211 g, 100 mmol, Merck) in deionized water (90 mL) and stirred for 24 h. The product was obtained by filtration and washed with 3 × 20 mL water and 2 × 20 mL ethanol (VWR). For comparison, we also used purchased ZIF-8 (Santa Cruz Biotechnology, Inc., USA) for our investigations.

The white ZIF-8 powder was soaked with PEG-400 (M = 380 – 420 g·mol^{-1}, ~C$_{18}$H$_{38}$O$_{10}$; Sigma-Aldrich) or stabilization. Excess PEG-400 was removed by filtration over a Büchner funnel under vacuum yielding a pasty mass, which was further dried under high vacuum (10^{-6} mbar, 24 h) forming ZIF-8·$^1/_2$PEG-400. For removal of PEG, the powder was washed with 3 × 20 mL of ethanol.

The chemical compositions were determined using an inductively coupled plasma optical emission spectrometer (ICP-OES; Vista Pro, Fa. Varian, Germany) for Zn and combustion analysis using a Vario EL apparatus (Fa. Elementar Analysensysteme, Germany) for C, N, and H determination. The samples were completely dissolved in HNO$_3$ (conc.) using Berghof pressure systems for the ICP-OES measurements.

Film Preparation

For film deposition, targets were prepared by pressing 0.5 g of the material at 3 tons into a pellet (ø = 13 mm, 2 – 3 mm thick). Opaque films of PEG@ZIF-8 were deposited at room temperature onto polished sapphire substrates (orientation (001), CrysTec GmbH, Germany) by the ablation of a ZIF-8·$^1/_2$PEG-400 target in an ultrahigh vacuum chamber with a process pressure of 5×10^{-7} mbar for a period of 6 h. The pellet was mounted on a rotating target holder inside the chamber (1.5 rpm, operating distances of 150 mm) and ablated by a horizontal line scan of 50 mm·s^{-1} (HurryScan25, Scanlab AG, Puchheim, Samlight, Scaps GmbH, Deisenhofen, Germany). The femtosecond laser (femtoRegen IC-375, High-Q-Laser GmbH, Hohenems, Austria) with a wavelength of 516 nm at 442 fs was operated with a laser power of 30 mW (energy per pulse of 0.03 mJ at 1 kHz), and the laser beam was focused on the target surface with a spot size of 0.05 mm. The residual gas was analyzed and monitored by quadrupole mass spectrometers (Prisma Plus QMG 220, Pfeiffer Vacuum GmbH, Germany).

Characterization

X-ray powder diffraction patterns of the films were measured in situ using a θ/θ-diffractometer (D8-Advance, Bruker AXS, Germany) with a Goebel mirror (Cu-K$_\alpha$) inside a vacuum chamber ($\sim 10^{-7}$ mbar) in reflection mode. The chamber is supplied with a slit to absorb scattered radiation which considerably reduces the background under vacuum condition from 20° on in 2θ. Each X-ray pattern was monitored at an angle of incidence of 10° using an area sensitive detector (GADDS, Bruker AXS); for further details, see Bach et al.[28] X-ray diffraction (XRD) of powder materials was measured using a Stoe Stadi P diffractometer with Ge filtered Cu Kα-radiation on a DECTRIS Mython 1K Detector (Stoe, Germany). The lattice constants were refined by the Rietveld method using crystal structure data from the literature via the TOPAS software (TOPAS Vers. 4.2, Bruker AXS).[29] In situ Raman spectra of the deposited films were recorded on a laser-microscope Raman spectrometer (iHR 550 spectrometer; BXFM microscope, manufactured by HORIBA, Bensheim) with confocal geometry. The incident laser beam (532 nm at 10 mW) passes through a window in a vacuum chamber and is focused by an objective (100×) on the samples. The Raman spectra of the powder materials were taken with a Jobin Yvon Typ V 010 Labram single grating spectrometer, equipped with a double super razor edge filter and a Peltier-cooled CCD camera. The resolution of the spectrometer (grating 1800 L/mm) is 1 cm^{-1}. Spectra are taken in quasi-backscattering geometry, using the linearly polarized 632.8 nm line of a He/Ne gas laser with power less than 1 mW, focused to a 10 μm spot through a 50× microscope objective on the top surface of the sample. IR spectra were recorded on a PerkinElmer Spektrum BX II FT-IR (PerkinElmer, USA) equipped with an ATR unit (Smith Detection Dura-Sample IIR diamond). The spectra were background-corrected and acquired with a resolution of 1 cm^{-1}. The IR spectra of the films are cropped at 850 cm^{-1} due to the intense sapphire substrate related vibrational modes. X-ray

photoelectron spectra were recorded by using monochromatic Al-K$_\alpha$ radiation (1486.58 eV), and during measurements, the vacuum was kept below 10^{-9} mbar. All spectra were calibrated to the Zn(2p) line at a binding energy of 1023.1 eV. The peaks were fitted to Gaussian functions. Scanning electron microscopy (SEM) images were acquired with a Merlin instrument (Zeiss, Germany). Transmission electron microscopy (TEM) was performed with a Philips CM30 ST at 300 kV (FEI, Netherlands) equipped with an energy-dispersive X-ray (EDX) system (NSS, Thermo Scientific, Germany). Images were recorded with a CMOS Camera (TVIPS, Germany). Ad- and desorption measurements were performed on an Autosorb iQ-MP2 (Quantachrome Instruments, Florida, USA) with argon of 99.9999% purity at 87 K. Prior to the measurements, the samples were outgassed under high vacuum at 120 °C for at least 12 h. In accordance with the ISO recommendations, multipoint BET tags equal to or below the maximum in $V \cdot (1 - p/p_0)$ were chosen. The ^{13}C and ^{15}N MAS NMR spectra were recorded at ambient temperature on a Bruker Avance 500 solid-state NMR spectrometer, operating at frequencies of 500.1, 125.7, and 50.7 MHz for ^{1}H, ^{13}C, and ^{15}N, respectively. The sample was contained in a 4 mm ZrO$_2$ rotor (Bruker) which was mounted in a standard double resonance MAS (magic angle spinning) probe. The ^{1}H, ^{13}C, and ^{15}N chemical shifts were referenced relative to TMS and nitromethane, respectively. The ^{1}H–^{15}N and ^{1}H–^{13}C cross-polarization (CP) MAS spectra were recorded at a spinning speed of 10 kHz using a ramped-amplitude (RAMP) CP pulse on ^{1}H, centered on the n = +1 Hartmann–Hahn condition. 2D HETCOR and CP-buildup solid-state NMR measurements were performed at 16.45 T (700 MHz ^{1}H Larmor frequency) on a NEO spectrometer (Bruker Biospin, Germany) with a 1.9 mm channel probe at a spinning speed of 40 kHz. Thermogravimetric analysis (TGA) measurements were performed on a Netzsch STA 409 C/CD (Selb, Germany) at a heating rate of 5 K min^{-1} under argon.

3.1.3 RESULTS AND DISCUSSION

ZIF–8 was synthesized from aqueous solution, and the structural integrity was confirmed by XRD (see Figure 3.1.2). In a first attempt, ZIF-8 was used as a compressed target material for the femto-PLD experiments. However, laser ablation of the pure ZIF-8 material did not yield any crystalline deposit on the substrate; instead, material was distributed in the entire vacuum chamber. The same behavior was observed for purchased ZIF-8. We assume that during the direct laser impingement ZIF-8 undergoes random fragmentation caused by the labile, porous structure.

In order to prevent or at least limit uncontrolled fragmentation, we identified polymer stabilization of the porous framework as a promising route. It is evident that the employed polymer needs to fulfill certain conditions: It should not alter the structure and integrity of the framework, and interaction should be reversible. Furthermore, the polymer itself must exhibit high stability during the laser irradiation. We identified polyethylene glycol of relatively low molecular mass as a suitable agent. Although PEG is well-known as stabilizer in biomedical applications due to its biocompatibility,[30-32] the

use of PEG or derivatives in MOF chemistry is poorly described. So far, PEG has only been employed as a structure-directing agent or (co-)solvent for MOF nanoparticle formation[33-37] or as a polymer for MOF embedment.[38,39] In this study, we employed PEG with an average molecular mass of 400 g·mol^{-1}. The oily polymer can easily be dissolved in ethanol or water and is nontoxic. The ZIF-8 powders were treated with PEG-400, and excess PEG was removed by filtration and further dried under high vacuum to obtain a noncovalent polymer stabilized material.

Elemental analysis of the product yields an approximate composition of half a molecule of PEG-400 per formula unit of ZIF-8, i.e., $Zn(C_3N_2H_2–CH_3)_2 \cdot {}^1/_2 PEG$-400 and will further be referred to as ZIF-8$\cdot{}^1/_2$PEG-400 (Anal. calcd. for $ZnC_8H_{10}N_4 \cdot {}^1/_2 C_{18}H_{38}O_{10}$: Zn, 15.0; C, 47.0; H, 6.7; N, 12.9; O, 18.4. Found: Zn, 14.1; C, 45.4; H, 7.0; N, 12.4; O, 21,1). This hybrid compound was then pressed to a target that was ablated under the same conditions as those described above for pure ZIF-8. In this case, opaque, white deposits were formed on the sapphire substrate at room temperature (see Figure 3.1.1(a)).
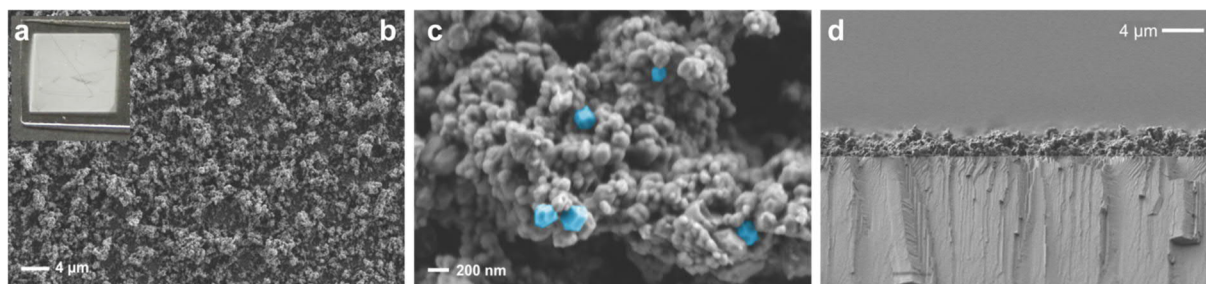
Figure 3.1.1: Optical photograph of a PEG@ZIF-8 film on a sapphire substrate (a), SEM images of PEG@ZIF-8 films on sapphire films, top (b, c) and cross-sectional view (d). Crystals showing the typical ZIF-8 morphology are highlighted in light blue.

SEM images, shown in Figure 3.1.1 (b – d), were acquired to study the surface morphology of the deposited films. The films do not exhibit a flat surface but cover the complete substrate. Although a large degree of the deposits appear blurred with poorly defined surfaces, particles with the typical rhombic dodecahedron crystal shape of ZIF-8 can be found distributed across the film. The cross-sectional view shows a rough, nonuniform deposit of 1.5 – 2.0 μm in height. TEM investigations (see Figure S3.1.1) reveal that the deposited particles are highly radiation sensitive. Furthermore, selected-area electron diffraction of these areas reveals the expected d-values of ZIF-8. For the main part of the sample, EDX analysis detects Zn together with oxygen as well as a disproportionally high carbon content compared to imidazole. These results support the coexistence of ZIF-8 and PEG in the deposited film. Minor parts of the sample consist almost exclusively of carbon and nitrogen, which may correspond to the free ligand or decomposition products thereof. Overall, our microscopy study suggests that no phase separation of PEG and ZIF-8 occurs, while the film morphology is fairly rough and particulate. TEM investigations of the ZIF-8$\cdot{}^1/_2$PEG-400 powder reveal the same crystal morphology as observed for ZIF-8, cf. Figure S3.1.2.

X-ray diffraction of the film further confirms the presence of intact ZIF-8 (Figure 3.1.2, details in Figure S3.1.3 and Figure S3.1.4), proving that the framework material could be deposited successfully by femto-PLD yielding a polycrystalline film. The mode of PEG incorporation into the ZIF-8 film was further analyzed by closer inspection of the XRD pattern and comparison to that of the powdered samples. The refined cell parameter a = 17.048(6) Å (Rietveld method using the single-crystal X-ray data) agrees with the lattice parameter of the bulk material a = 17.033(2) Å.[41] However, the intensities of the three Bragg reflections in the range between 14° and 19° in 2θ deviate from the simulated pattern, with the reflection at ≈18° 2θ having the highest intensity in the deposited films. As this is also the case in the X-ray diffraction pattern of the PEG-infiltrated ZIF-8 powder sample, we conclude that the obtained films consist of PEG-containing ZIF-8 (referred to as PEG@ZIF-8 film) where PEG resides in the pores of ZIF-8. This can be concluded from the fact that Rietveld refinement of both patterns with an empty-pore structure of ZIF-8 was unsuccessful, whereas a refinement is possible if PEG in the pores is considered.
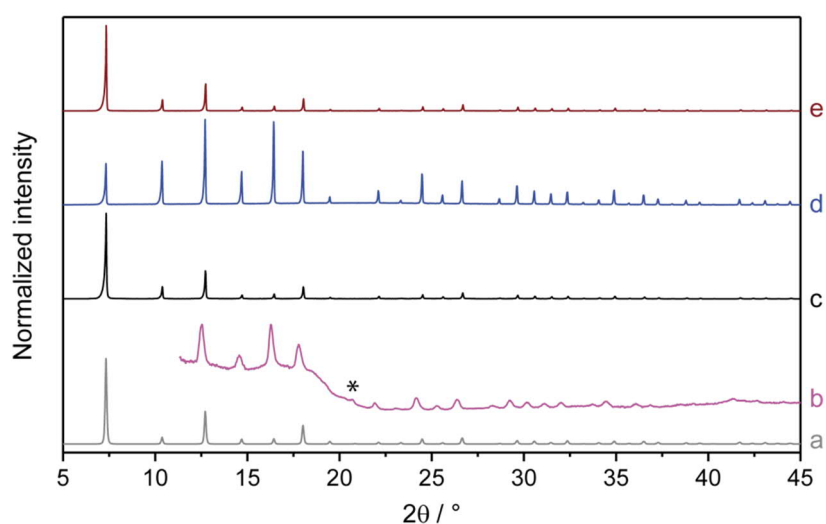
Figure 3.1.2: XRD patterns of (a) simulated ZIF-8, (b) PEG@ZIF-8 film, (c) ZIF-8, (d) ZIF-8·^{1}/$_2$PEG-400, and (e) washed ZIF-8·^{1}/$_2$PEG-400 powders.

Subsequently, the film was submerged into ethanol to remove the polymer. After this treatment, the reflection intensities of the washed film are nearly identical to pristine ZIF-8 while retaining the crystallinity of the film.

The composition $Zn(C_3N_2H_2-CH_3)_2 \cdot ^1/_2 PEG\text{-}400$ determined by elemental analysis implies 3 PEG-400 molecules per pore. Thus, because of the size of PEG-400 (helical structure with length ~25 Å and diameter ~4 Å),[40] we expect both pore filling by PEG and excess PEG enveloping the particles. Due to the framework flexibility, the effective aperture size of ZIF-8 has been shown to be larger than the XRD-derived value of 3.4 Å and is in the range of 4.0 to 4.5 Å as derived from gas kinetic analysis.[41-43] Thus, relatively large molecules such as PEG-400 can enter the pore system of ZIF-8 by the swing movement of the imidazole moieties at room temperature, thus widening the aperture window.

The samples were further characterized by in situ Raman spectroscopy (Figure 3.1.3) and compared to pure ZIF-8 and PEG-400 powders. The complete band assignment can be found in Table S3.1.1. The PEGylated ZIF-8 samples, the ZIF-8·$^1/_2$PEG-400 powder and PEG@ZIF-8 film, agree very well. Both spectra exhibit the typical ZIF-8-related bands, and the PEG region is clearly evidenced by the most intense Raman bands, i.e., the C–H stretching modes around 2800 – 3000 cm^{-1}, which are visible as a broadened band in the powder and film. However, the PEG component is more pronounced in the ZIF-8·$^1/_2$PEG-400 powder compared to the PEG@ZIF-8 film (cf. bands around 820 and 1250 cm^{-1}), which indicates a lower PEG content in the film. Thus, PEG-400 is partially lost during the deposition process in the vacuum chamber.

Figure 3.1.3: Raman spectra of (a) ZIF-8 powder, (b) the washed ZIF-8 film, (c) ZIF-8·$^1/_2$PEG-400 powder, (d) the PEG@ZIF-8 film, and (e) PEG-400 (*, sapphire substrate).

To fully release the PEG-400 stabilizer and retrieve pure ZIF-8 films, the as-deposited films were submerged into ethanol three times for 30 min. In agreement with the findings for the PEG-modified powder and PXRD films washed with ethanol, the subsequently measured Raman spectra show only the bands of pristine ZIF-8. Thus, the spectra of the washed ZIF-8 film (curve b in Figure 3.1.3) match very well with the spectra of pure ZIF-8, which again demonstrates that PEG-free ZIF-8 films were indeed obtained on the substrate.[44,45]

Next, IR spectra of the samples were recorded (cf. Figure 3.1.4) of which a full assignment can be found in Table S3.1.2. The data confirm the results of the Raman spectra, and all samples show the characteristic vibrational bands of ZIF-8. For the PEG-400-related samples, the dominant broad alkyl-related stretching modes appear between 2790 and 2990 cm^{-1}, as well as the chain-related –C–O–C–stretch at ~1100 cm^{-1}. In agreement with the findings from Raman spectroscopy, the films contain less PEG compared to ZIF-8·$^1/_2$PEG-400 as derived from the intensities of the PEG vibrational bands at ~1100 and 2900 cm^{-1}, again suggesting that PEG is partially lost during ablation. Note that the broad water-related band at 3500 cm^{-1}, present in the powder, diminishes in the film as well. After dipping

the films into ethanol, all ZIF-8 bands are maintained, while the PEG-400-related vibrational modes at ~1100, 1250, and 1350 cm^{-1} disappear and the intensity of the bands between 2790 and 2990 cm^{-1} are reduced. Thus, the IR spectra also support the formation of pure ZIF-8 films on the sapphire substrate.
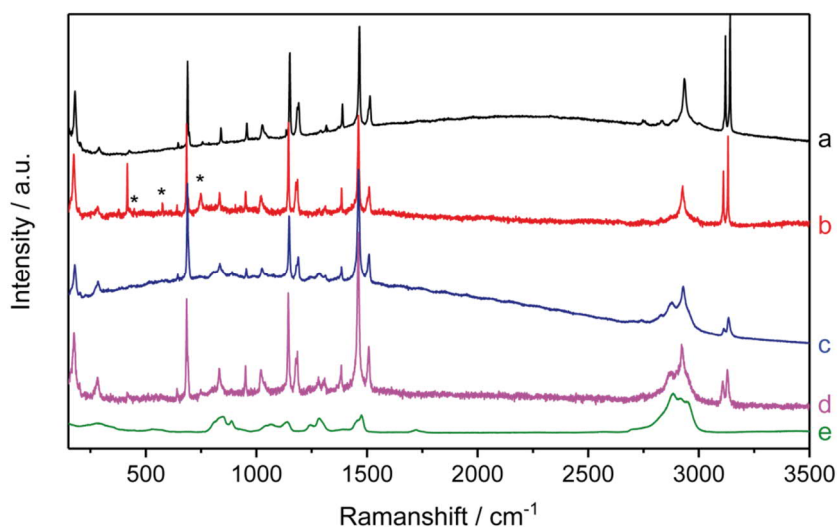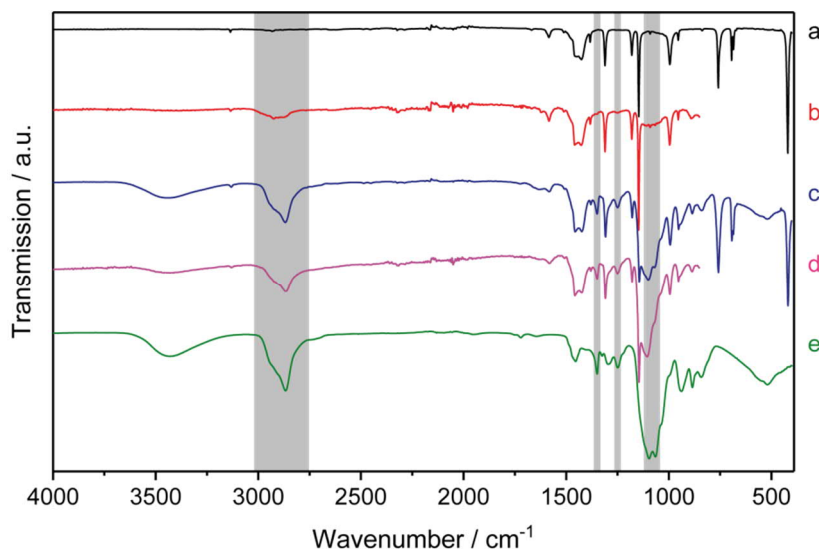

Figure 3.1.4: IR spectra of (a) ZIF-8 powder, (b) washed ZIF-8 film, (c) ZIF-8·^{1}/$_2$PEG-400 powder, (d) PEG@ZIF-8 film, and (e) PEG-400. Characteristic PEG-400 related vibrational bands are highlighted in gray.

To better understand the molecular-level interaction between PEG and the ZIF-host lattice, powdered samples were characterized by ^{13}C and ^{15}N-CP-MAS NMR (see Figure 3.1.5). Pure ZIF-8 and the washed sample show the expected three carbon resonances of unloaded ZIF-8, consistent with the literature values.[46] However, not only does ZIF-8·^{1}/$_2$PEG-400 exhibit additional carbon resonances related to PEG (60.3 and 69.8 ppm), but also its imidazolate-related signals are slightly shifted, suggesting pore confinement of the polymer: Both the methyl group γ and the two equivalent imidazolate carbon atoms β are shifted downfield by +1.6 and +1.2 ppm, respectively. We therefore assume that these atoms point toward the pore and are subject to deshielding by the spatial proximity of the impregnated polymer.[47,48] The fact that incomplete infiltration of ZIF-8 with larger molecular weight polymer (PEG-2000) gives rise to split β and γ signals (Figure S3.1.7) further corroborates that pore confinement is the origin of the observed downfield shift. In addition, ^{1}H and ^{1}H–^{13}C-HETCOR measurements confirm constitutive interaction of PEG with the framework material (see Figure S3.1.8 and Figure S3.1.9). These findings add further evidence that the polymer resides in the porous framework, in addition to enveloping it.
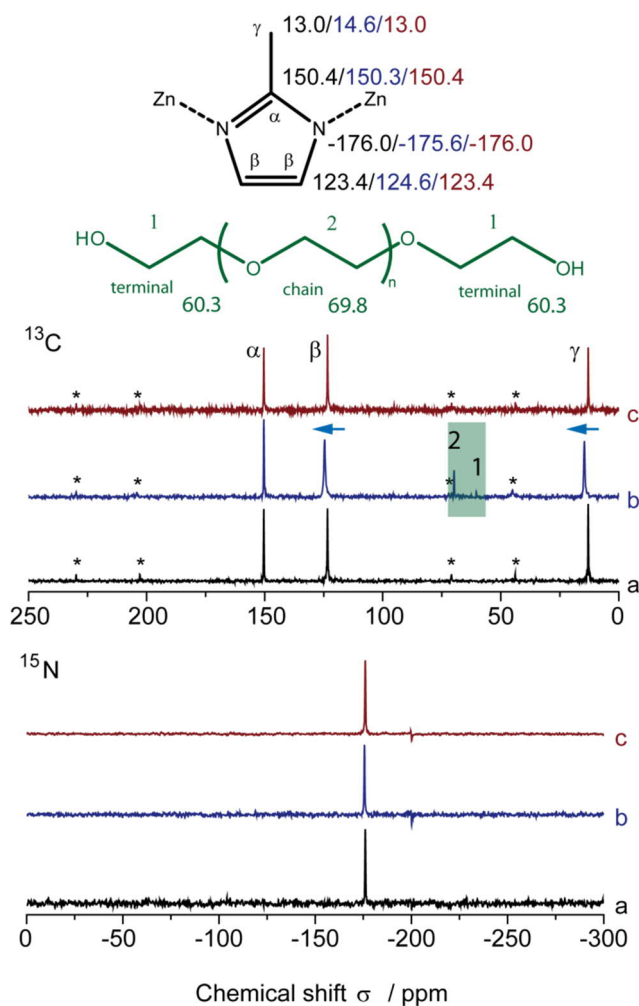
Figure 3.1.5: Chemical shift assignment (top) and ^{13}C- (center) and ^{15}N-CP-MAS NMR spectra (bottom) of (a) ZIF-8, (b) ZIF-8·$^1/_2$PEG, and (c) washed ZIF-8·$^1/_2$PEG powder. Black chemical shifts (in ppm) are assigned to (a), blue to (b), and ruby to (c). The green area highlights the PEG-related chemical shifts with 1 for terminal and 2 for in-chain carbon chemical shifts. Note that the dephased signals at −200 ppm in the ^{15}N spectra are artifacts of the NMR experiment. Asterisks denote spinning side bands.

To further investigate the nature of the host–guest interactions, the core-level binding energies of C(1s) and N(1s) in PEG@ZIF-8 films were investigated by XPS measurements and compared to those of ZIF-8·$^1/_2$PEG-400 and pure ZIF-8 powders (see Figure 3.1.6). The complete binding energies with fitted peak areas can be found in Table S3.1.3 and Figure S3.1.11. The binding energies of the pure ZIF-8 powder were fitted for C(1s) to 286.0 and 287.2 eV, which correspond to the C–C and C–N bonds of imidazole, respectively. The C(1s) signal of the ZIF-8·$^1/_2$PEG-400 powder is fitted to three peaks at 285.7, 287.5, and 289.1 eV. The first two peaks correspond to ZIF-8, whereby the most intense one at 287.5 matches also very well with the C(1s) signal of PEG. For PEG-2000, the C(1s) binding energy is determined to be 287.4 eV. Thus, the high intensity of this peak suggests a high content of PEG in the ZIF-8·$^1/_2$PEG-400 powder, which is also responsible for the comparatively low intensity of the N(1s) signal for the ZIF-8·$^1/_2$PEG-400 powder. The maximum of the N(1s) peak of ZIF-8·$^1/_2$PEG-400 powder is at 400.2 eV and agrees with that of ZIF-8 powder and of the PEG@ZIF-8 films. The C(1s) binding

energies of the PEG@ZIF-8 film are fitted with three peaks to 286.1, 287.4, and 289.1 eV and are in excellent agreement with the values obtained for the ZIF-8·$^{1}/_{2}$PEG-400 powder. However, the signal heights of the first two peaks (286.1, 287.4 eV) are nearly equal, which again indicates a reduced PEG content in the film as compared to the powder.
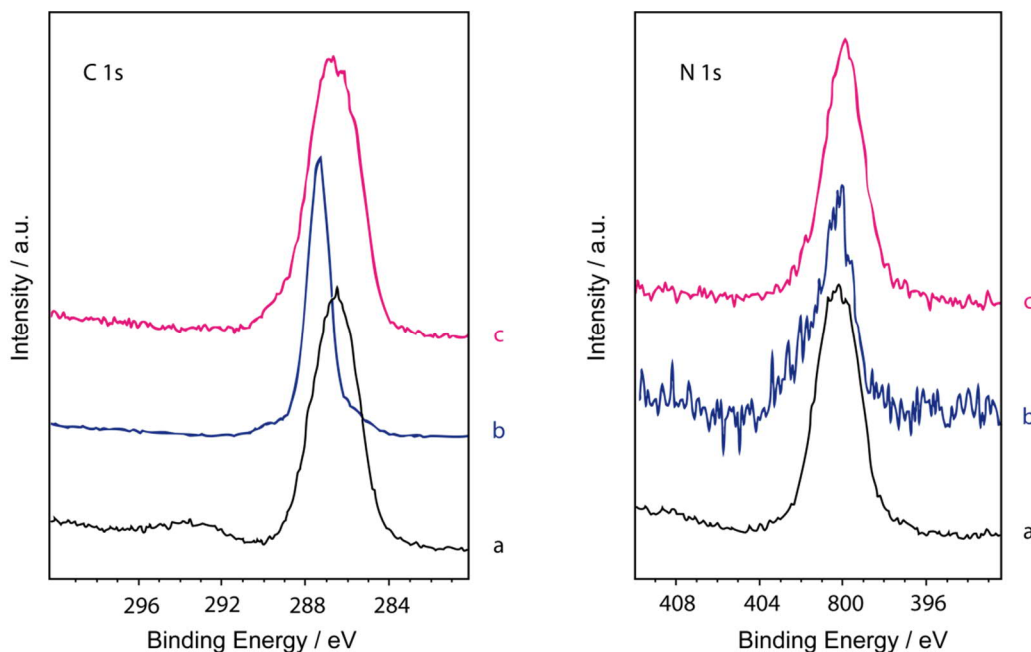
Figure 3.1.6: C(1s) and N(1s) XPS spectra of (a) ZIF-8, (b) ZIF-8·$^{1}/_{2}$PEG powder, and (c) PEG@ZIF-8 film.

Thus, the XPS measurements confirm that the PEG content is reduced in the PEG@ZIF-8 films, and no significant deviation in the binding energies in the film is detected as compared to the bulk material. From the semiquantitative XPS measurements, the composition of the PEG@ZIF-8 film can be estimated to be $^{1}/_{6}$PEG-400 molecules per Zn, equivalent to one PEG-400 molecule per pore. From the length of PEG-400 ($\sim$25 Å) together with the distance from pore to pore ($\sim$17 Å), it is reasonable to assume that the PEG molecule can bridge and therefore interconnect the pores.[49] On the basis of the combined evidence from XRD, solid-state NMR spectroscopy (see Figure 3.1.5), and the literature,[49] we suppose that most of the PEG molecules are located inside the pores of ZIF-8, resulting in a composition of ZIF-8·$\sim^{1}/_{6}$PEG-400. We hypothesize that the polymer inclusion, leading to a PEG-mediated stabilization of ZIF-8, is responsible for the reassembly of the ZIF-8 structure on the substrate and hence makes an important difference compared to the deposition of pure ZIF-8.

In order to determine how PEGylation influences the sorption behavior and, hence, porosity of the ZIF-8 compounds, Ar adsorption–desorption isotherms were acquired at 87 K and compared (Figure 3.1.7). Pure ZIF-8 shows the typical sorption behavior with a hysteresis between 0.2 and 0.4 partial pressures associated with the gate-opening phenomenon.[50] Treatment with PEG-400 leads to a complete loss of porosity attributed to pore blocking by the polymer and, potentially, pore filling. Upon washing with ethanol, the porosity of the material is fully restored. This trend is confirmed by the BET surface areas

with 1369 m^2g^{-1} for pure ZIF-8 and 1376 m^2g^{-1} for the washed sample. The data thus strongly suggest the complete removal of the PEG guest by ethanol washing and, hence, reversible binding of PEG in ZIF-8. The same behavior is expected for the washed ZIF-8 film, as corroborated by the spectroscopic characterizations outlined above.
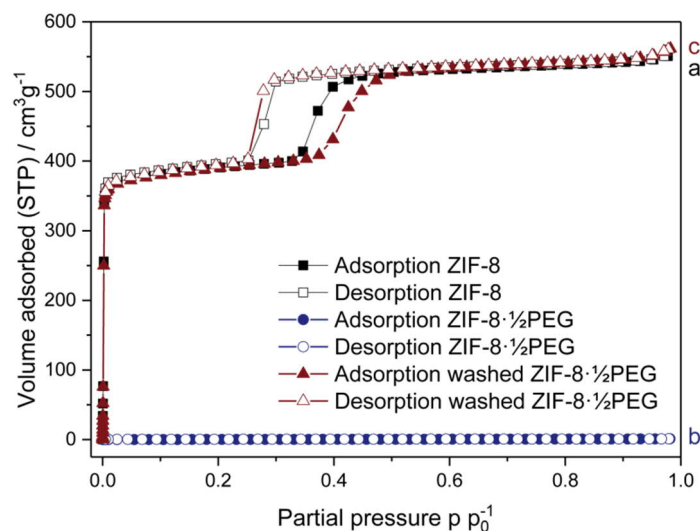
Figure 3.1.7: Argon ad- and desorption isotherms of (a) ZIF-8, (b) ZIF-8·$^1/_2$PEG, and (c) washed ZIF-8·$^1/_2$PEG powders.

3.1.4   CONCLUSIONS

An overview scheme of the steps used for the preparation of ZIF-8 films via the femto-PLD technique is presented in Figure 3.1.8. PLD attempts using a pristine ZIF-8 target failed to produce any crystalline deposits. In contrast, we have shown that PEG-400 can be used as a vehicle to deposit ZIF-8 films via femto-PLD. We argue that PEG-400 acts as a stabilizing agent that may assist in the controlled fragmentation of ZIF-8 during ablation by means of pore filling along with enclosing the particles while retaining their crystallinity. Deposition by femto-PLD using ZIF-8·½PEG-400 as target yields films with approximate composition ZIF-8·⅛PEG-400, which show the same structural features as the bulk but with reduced PEG content. Thus, during the deposition process under vacuum, a loss of approximately ⅔ of the PEG is observed and the porous imidazolate framework is reassembled on the substrate. We therefore suggest two effects operating upon infiltration of ZIF-8 with PEG: First, stabilization of the hybrid compound during ablation through interconnection of the ZIF-8 pores by PEG and, second, support for the reassembly of ZIF-8 on the substrate, likely due to structure-directing interactions between PEG and ZIF-8. Clearly, further experiments will be required to elucidate the underlying mechanism. The results from the sorption measurements on the bulk powders further suggest reversible pore blocking by PEGylation, which can be removed by simple immersion of the film into ethanol. Thus, starting from PEG-modified ZIF-8 powder, pure ZIF-8 films were obtained on sapphire substrates.
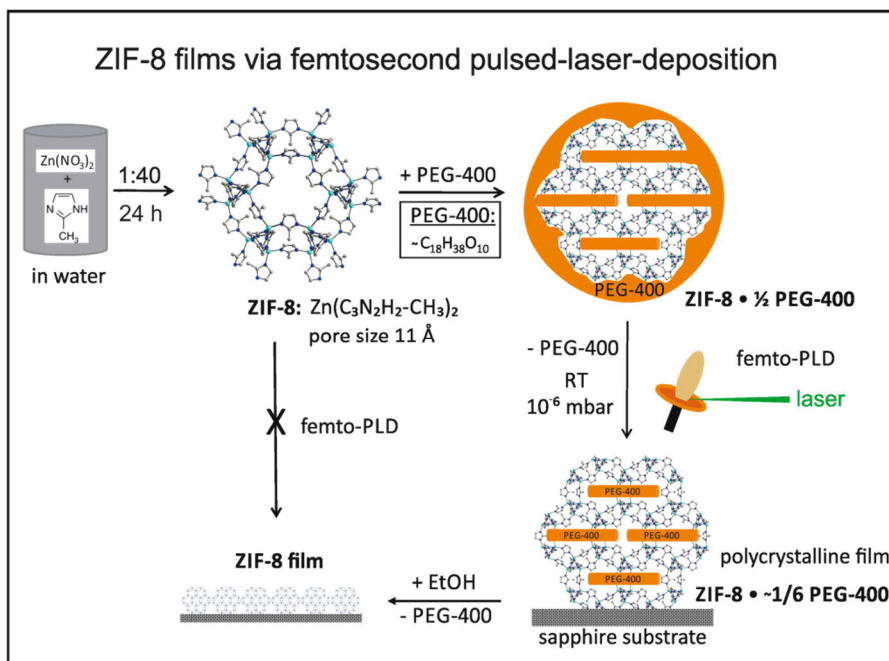
Figure 3.1.8: Scheme of the steps used for the ZIF-8 film preparation via the femtosecond pulsed-laser-deposition technique.

In summary, we have demonstrated for the first time that PEGylation allows the deposition of porous MOF thin films by a physical vapor deposition technique. Our study further suggests the broad applicability of the femto-PLD technique to other highly porous and thermally labile MOFs by using stabilizing additives, thus enlarging the portfolio of existing strategies for the fabrication of MOF films.

3.1.5 ACKNOWLEDGMENTS

3.1.6 REFERENCES

1   R. J. Kuppler, D. J. Timmons, Q.-R. Fang, J.-R. Li, T. A. Makal, M. D. Young, D. Yuan, D. Zhao, W. Zhuang and H.-C. Zhou, Coord. Chem. Rev. 2009, 253, 3042-3066.

2   H. Furukawa, K. E. Cordova, M. O'Keeffe and O. M. Yaghi, Science 2013, 341, 1230444.

3   P. Silva, S. M. F. Vilela, J. P. C. Tome and F. A. Almeida Paz, Chem. Soc. Rev. 2015, 44, 6774-6803.

4   J.-L. Wang, C. Wang and W. Lin, ACS Catal. 2012, 2, 2630-2640.

5   V. Stavila, A. A. Talin and M. D. Allendorf, Chem. Soc. Rev. 2014, 43, 5994-6010.

6   T. Zhang and W. Lin, Chem. Soc. Rev. 2014, 43, 5982-5993.

7   D. Zacher, O. Shekhah, C. Woll and R. A. Fischer, Chem. Soc. Rev. 2009, 38, 1418-1429.

8   O. Shekhah, J. Liu, R. A. Fischer and C. Woll, Chem. Soc. Rev. 2011, 40, 1081-1106.

9   A. Bétard and R. A. Fischer, Chem. Rev. (Washington, DC, U. S.) 2012, 112, 1055-1083.

10   J.-L. Zhuang, A. Terfort and C. Wöll, Coord. Chem. Rev. 2016, 307, Part 2, 391-424.

11   I. Stassen, M. Styles, G. Grenci, H. V. Gorp, W. Vanderlinden, S. D. Feyter, P. Falcaro, D. D. Vos, P. Vereecken and R. Ameloot, Nat. Mater. 2016, 15, 304-310.

12   E. Ahvenniemi and M. Karppinen, Chem. Commun. 2016, 52, 1139-1142.

13   I. Stassen, D. De Vos and R. Ameloot, Chem. Eur. J. 2016, 22, 14452-14460.

14   T. D. Bennett and A. K. Cheetham, Acc. Chem. Res. 2014, 47, 1555-1562.

15   O. Kylián, M. Drábik, O. Polonskyi, J. Čechvala, A. Artemenko, I. Gordeev, A. Choukourov, I. Matolínová, D. Slavínská and H. Biederman, Thin Solid Films 2011, 519, 6426-6431.

16   D. B. Chrisey, A. Piqué, R. A. McGill, J. S. Horwitz, B. R. Ringeisen, D. M. Bubb and P. K. Wu, Chem. Rev. (Washington, DC, U. S.) 2003, 103, 553-576.

17   T. Lippert, in Laser-Surface Interactions for New Materials Production: Tailoring Structure and Properties, Eds. A. Miotello and M. P. Ossi, Springer, Berlin, Heidelberg, 2010, 141-175.

18   D.-D. McAlevy Bubb and R. F. Haglund, in Pulsed Laser Deposition of Thin Films, John Wiley & Sons, Inc., 2006, 33-61.

19   S. L. Johnson, M. R. Papantonakis and R. F. Haglund, in Laser-Surface Interactions for New Materials Production: Tailoring Structure and Properties, Eds. A. Miotello and M. P. Ossi, Springer, Berlin, Heidelberg, 2010, 177-202.

20   D. M. Bubb, J. S. Horwitz, J. H. Callahan, R. A. McGill, E. J. Houser, D. B. Chrisey, M. R. Papantonakis, R. F. Haglund, M. C. Galicia and A. Vertes, J. Vac. Sci. Technol. A 2001, 19, 2698-2702.

21   D. M. Bubb, A. O. Sezer, D. Harris, F. Rezae and S. P. Kelty, Appl. Surf. Sci. 2006, 253, 2386-2392.

22   S. K. Sundaram and E. Mazur, Nat. Mater. 2002, 1, 217-224.

23   M. Hashida, H. Mishima, S. Tokita and S. Sakabe, Opt. Express 2009, 17, 13116-13121.

24   C. Florian, F. Caballero-Lucas, J. M. Fernández-Pradas, J. L. Morenza and P. Serra, Appl. Surf. Sci. 2014, 302, 226-230.

25   D. Fischer, L. V. Meyer, M. Jansen and K. Müller-Buschbaum, Angew. Chem. Int. Ed. 2014, 53, 706-710.

26   K. S. Park, Z. Ni, A. P. Côté, J. Y. Choi, R. Huang, F. J. Uribe-Romo, H. K. Chae, M. O'Keeffe and O. M. Yaghi, Proceedings of the National Academy of Sciences 2006, 103, 10186-10191.

27   K. Kida, M. Okita, K. Fujita, S. Tanaka and Y. Miyake, CrystEngComm 2013, 15, 1794-1801.

28   A. Bach, D. Fischer, X. Mu, W. Sigle, P. A. van Aken and M. Jansen, Inorg. Chem. 2011, 50, 1563-1569.

29   A. Coelho, Bruker AXS GmbH, Karlsruhe, Germany, 2009.

30   Z. Harris and S. Zalipsky, Poly(ethylene glycol), American Chemical Society, Washington DC, 1997.

31   S. Rawat, C. Raman Suri and D. K. Sahoo, Biochem. Biophys. Res. Commun. 2010, 392, 561-566.

32   D. Hutanu, M. D. Frishberg, L. Guo and C. C. Darie, Mod. Chem. Appl. 2014, 2014.

33   C. Cruje and D. B. Chithrani, Rev. Nanosci. Nanotechnol. 2014, 3, 20-30.

34   J. Gao, K. Ye, L. Yang, W.-W. Xiong, L. Ye, Y. Wang and Q. Zhang, Inorg. Chem. 2014, 53, 691-693.

35   Z. Xue, J. Zhang, L. Peng, B. Han, T. Mu, J. Li and G. Yang, ChemPhysChem 2014, 15, 85-89.

36   V. Agostoni, P. Horcajada, M. Noiray, M. Malanga, A. Aykaç, L. Jicsinszky, A. Vargas-Berenguel, N. Semiramoth, S. Daoud-Mahammed, V. Nicolas, C. Martineau, F. Taulelle, J. Vigneron, A. Etcheberry, C. Serre and R. Gref, Sci. Rep. 2015, 5, 7925.

37   R. Mejia-Ariza and J. Huskens, J. Mater. Chem. B 2016, 4, 1108-1115.

38   R. Senthil Kumar, M. Raja, M. Anbu Kulandainathan and A. Manuel Stephan, RSC Adv. 2014, 4, 26171-26175.

39   K. Xie, Q. Fu, Y. He, J. Kim, S. J. Goh, E. Nam, G. G. Qiao and P. A. Webley, Chem. Commun. 2015, 51, 15566-15569.

40   H. Tadokoro, Y. Chatani, T. Yoshihara, S. Tahara and S. Murahashi, Makromol. Chem. 1964, 73, 109-127.

41   O. Karagiaridi, M. B. Lalonde, W. Bury, A. A. Sarjeant, O. K. Farha and J. T. Hupp, J. Am. Chem. Soc. 2012, 134, 18790-18796.

42   C. Zhang, R. P. Lively, K. Zhang, J. R. Johnson, O. Karvan and W. J. Koros, J. Phys. Chem. Lett. 2012, 3, 2130-2134.

43   O. Shekhah, R. Swaidan, Y. Belmabkhout, M. du Plessis, T. Jacobs, L. J. Barbour, I. Pinnau and M. Eddaoudi, Chem. Commun. 2014, 50, 2089-2092.

44   D. A. Carter and J. E. Pemberton, J. Raman Spectrosc. 1997, 28, 939-946.

45   G. Kumari, K. Jayaramulu, T. K. Maji and C. Narayana, J. Phys. Chem. A 2013, 117, 11006-11012.

46   W. Morris, C. J. Stevens, R. E. Taylor, C. Dybowski, O. M. Yaghi and M. A. Garcia-Garibay, *J. Phys. Chem. C* 2012, 116, 13307-13312.

47   C. Chmelik, D. Freude, H. Bux and J. Haase, *Microporous Mesoporous Mater.* 2012, 147, 135-141.

48   N. Liédana, A. Galve, C. Rubio, C. Téllez and J. Coronas, *ACS Appl. Mater. Interfaces* 2012, 4, 5016-5021.

49   T. Uemura, N. Yanai, S. Watanabe, H. Tanaka, R. Numaguchi, M. T. Miyahara, Y. Ohta, M. Nagaoka and S. Kitagawa, *Nat. Comm.* 2010, 1, 83.

50   S. Tanaka, K. Fujita, Y. Miyake, M. Miyamoto, Y. Hasegawa, T. Makino, S. Van der Perre, J. Cousin Saint Remi, T. Van Assche, G. V. Baron and J. F. M. Denayer, *J. Phys. Chem. C* 2015, 119, 28430-28439.

3.1.7   SUPPORTING INFORMATION
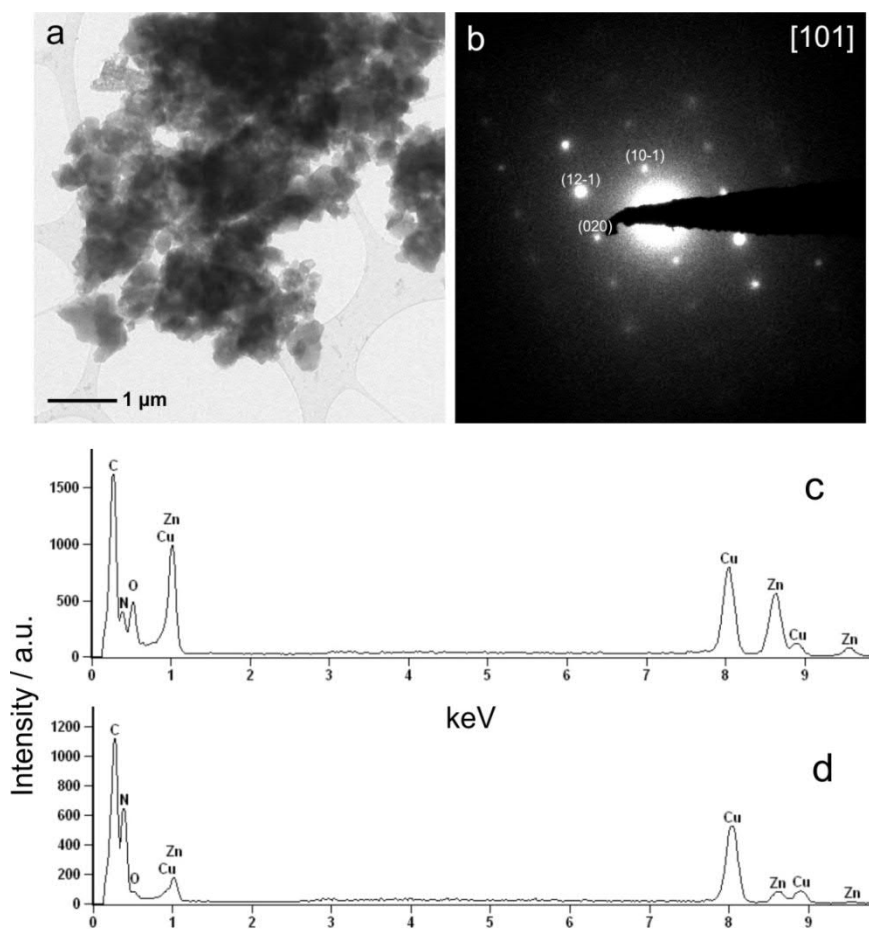
Figure S3.1.1: TEM image of (a) PEG@ZIF-8 film, (b) electron diffraction image of a PEG@ZIF-8 particle, (c) corresponding EDX spectrum and (d) EDX spectrum of a particle with low Zn content. The Cu-signal originates from used TEM grids.
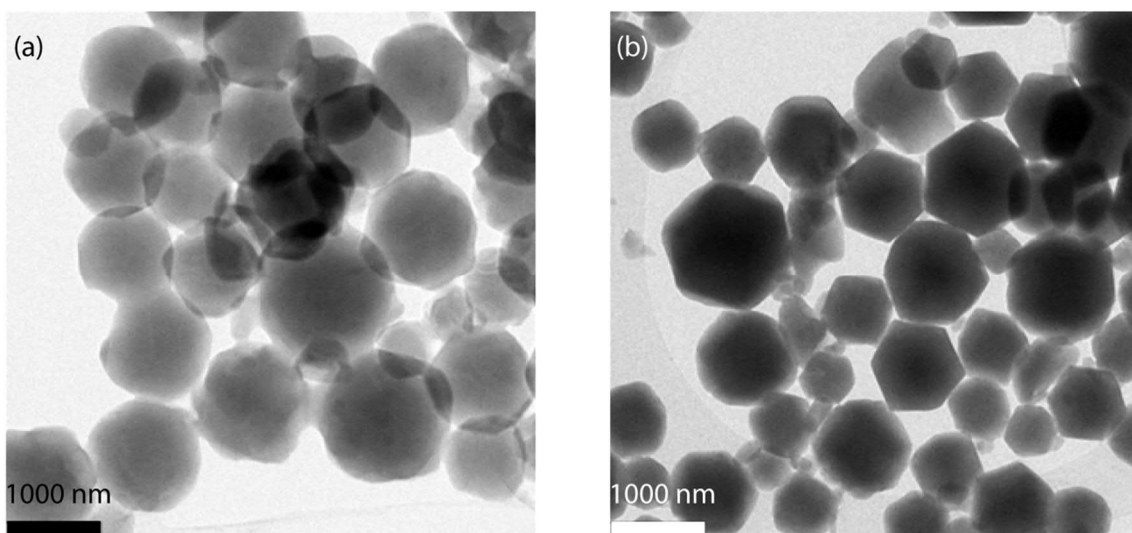
Figure S3.1.2: HRTEM images of (a) ZIF-8 and (b) ZIF-8·½PEG-400 particles.
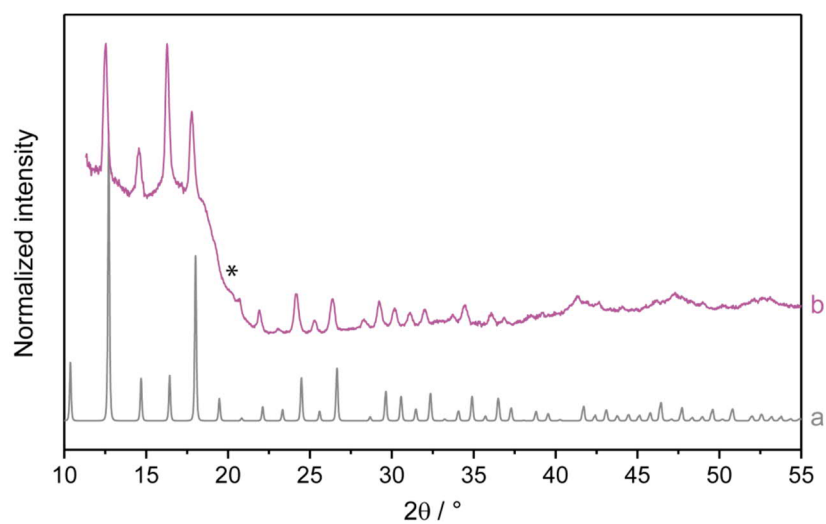
Figure S3.1.3: XRD patterns of (a) simulated ZIF-8 and (b) PEG@ZIF-8 film (* sapphire substrate).
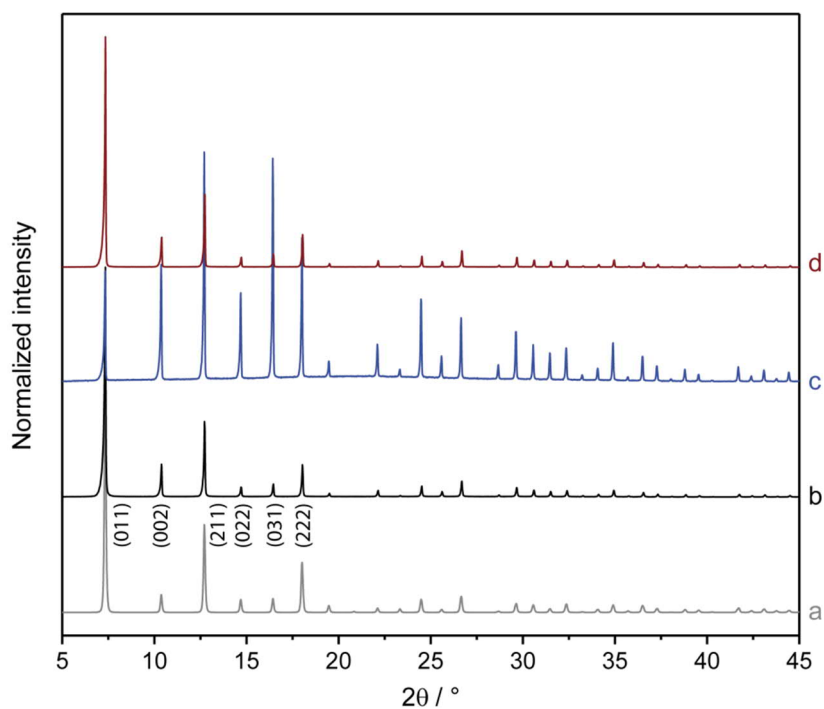
Figure S3.1.4: XRD patterns of (a) simulated ZIF-8, (b) ZIF-8, (c) ZIF-8·½PEG-400 and (d) washed ZIF-8·½PEG-400 powders. Index values are given in brackets.
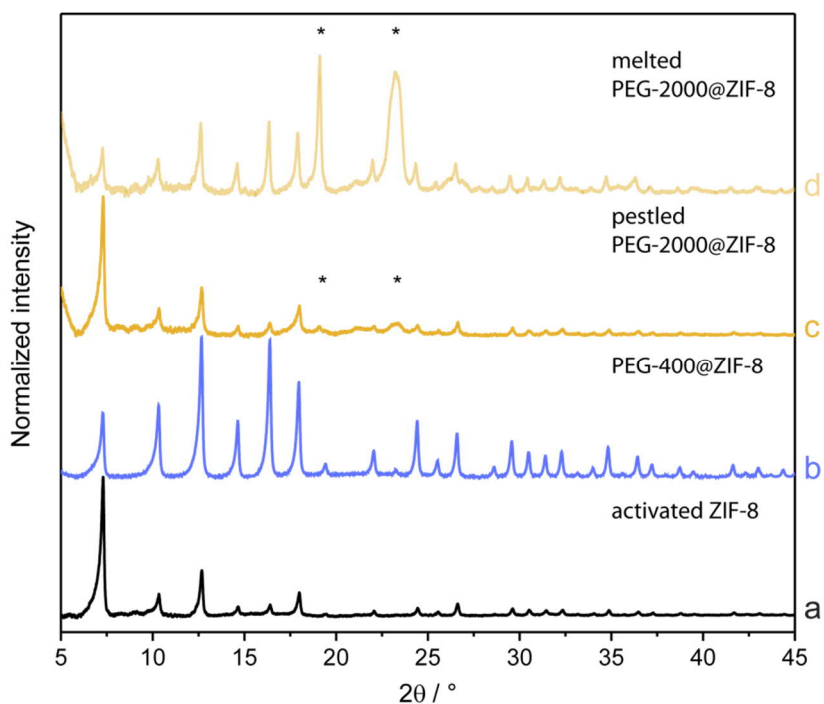
Figure S3.1.5: XRD patterns of activated (a) ZIF-8, (b) PEG-400@ZIF-8, (c) pestled PEG-2000@ZIF-8, (d) melted PEG-2000@ZIF-8. PEG-2000 reflections are marked with asterisks. Note that pestling PEG-2000 with ZIF-8 does not change reflex intensities noticeably, whereas melting the mixture yields considerably altered intensity ratios suggesting pore filling.

Table S3.1.1: Relevant Raman vibrational bands (wavenumbers/cm^{-1}) including vibrational assignments of ZIF-8 and ZIF-8·½PEG-400 powders as well as PEG@ZIF-8 films together with PEG-400.

ZIF-8	ZIF-8·½PEG-400	PEG@ZIF-8 film	Washed ZIF-8 film	PEG-400	Assignment
180	179	176	174		ν Zn–N
288	284	283	283		ν Zn–N
689	688	685	684		ring puckering, δ H oop
839	835	831	833		δ C–H oop (C4–C5)
				848	ν C-C
				887	ρ CH2
956	955	951	952		δ C–H oop (C2)
1026	1025	1019	1022		δ C–H oop
				1069	ν C-O
				1141	ρ CH2
1152	1148	1144	1145		ν C5–N
1192	1189	1185	1186		ν C–N
				1245, 1283	ω C–H2
1389	1384	1384	1386		δ CH3
1466	1462	1461	1461		C–H wag
				1475	δ CH2
1514	1510	1510	1510		ν C4–C5
				2884	ν$_s$ C–H (methyl)
2935	2930	2922	2927	2918, 2947	ν$_a$ C–H (methyl)
3120	3113	3108	3110		ν C–H (ar)
3141	3134	3129	3132		ν C–H (ar)

ν: stretching, δ: bending, ω: wagging, ρ: rocking, oop: out of plane, ar: aromatic, a: aymmetric, s: symmetric

Figure S3.1.6: IR spectra of (a) ZIF-8 powder, (b) washed ZIF-8·½PEG-400 powder, (c) washed ZIF-8 film, (d) ZIF-8·½PEG-400 powder, (e) PEG@ZIF-8 film compared to the IR spectra (f) PEG-400 and (g) 2-methylimidazole. The IR spectra of the films are cropped at 850 cm^{-1} due to the intense sapphire substrate related vibrational modes. PEG related modes are marked in grey.

Table S3.1.2: Relevant infrared vibrational bands (wavenumbers/cm^{-1}) including vibrational assignments of ZIF-8, ZIF-8·½PEG-400 powders as well as PEG@ZIF-8 films compared to PEG-400 and Hmim.

ZIF-8 powder	ZIF-8·½PEG-400 powder	Washed ZIF-8·½PEG-400 powder	PEG@ZIF-8 film	Washed ZIF-8 film	PEG-400	Hmim	Assignment
420	419	420					ring deform.†
	523				519 (br)		ring deform.*
685	684 (sh)	684				680	ring deform.†
694	692	694				680	ring deform.†
						742	δ CH$_{ar}$ oop†
759	758	759				756	δ CH$_{ar}$ oop†
838	839						ρ CH$_3$†
	885		885		886		ρ CH$_2$, C–C, C–O*
954	952	954	952	954	941	938	ring deform.†
995	993	995		996		992	ρ CH$_3$, ring deform†
	1071 (sh)		1070 (sh)		1067 (sh)		C–O, C–C*
1091	occl.	1091	occl.				ν C2/4–N, ν C4–H, Zn–N†
	1106		1100		1094		C–O, C–C*
	occl.		occl.			1114	ν C2/4–N, (Zn–N?) †
1146	1143	1146	1145	1147		1154	ν C2/4–N, (Zn–N?) †
1180	1179	1180		1180			Zn–N†
	1250		1250		1250		CH$_2$ twist.*
	1290 (sh)		1294 (sh)		1296		CH$_2$ twist.*
1311	1309	1311		1310	1296		ν C2/4–N†
	1349		1349		1349		ω CH$_2$*
1386	1380	1383	1379	1385			CH$_3$ deform. †
1426	1424	1425	1427	1425		1440 (br)	ν C2/4–N, (Zn–N?) †
	occluded		occluded		1456 (br)		CH$_2$ scis. *
1448	1456	1456	1457	1456		1440 (br)	CH$_3$ deform. †
1584	1583	1584	1572	1583		1593	ν C4–C5
	2871		2874		2866		ν$_s$ CH$_2$*
	2940 (sh)		2939 (sh)		2941 (sh)		ν$_a$ CH$_2$*
3135	3130	3136	3131			3136	ν CH$_3$†
	3437 (br)		3443		3445 (br)		ν –OH*

ν: stretching, δ: bending, ω: wagging, ρ: rocking, oop: out of plane, ar: aromatic, a: asymmetric, s: symmetric.
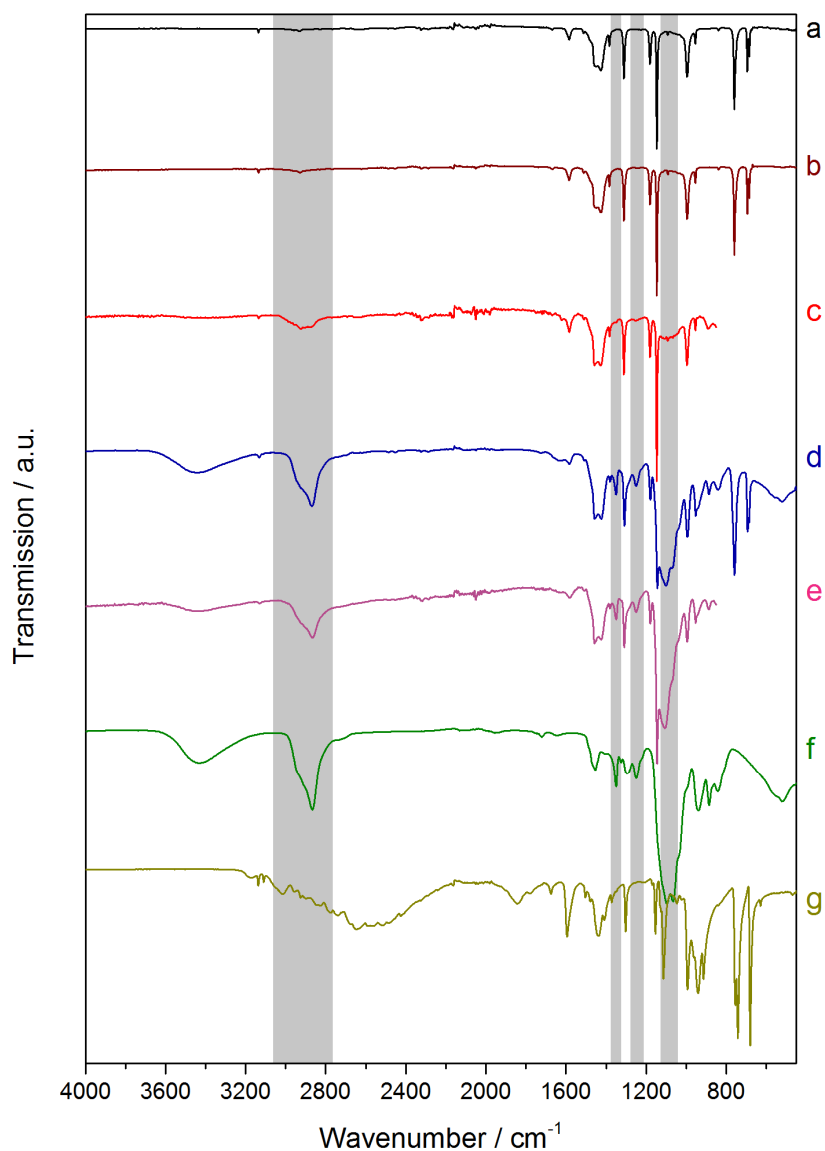* vibrational modes are related to PEG.
† vibrational modes are related to 2-methylimidazole or 2-methylimidazolate.
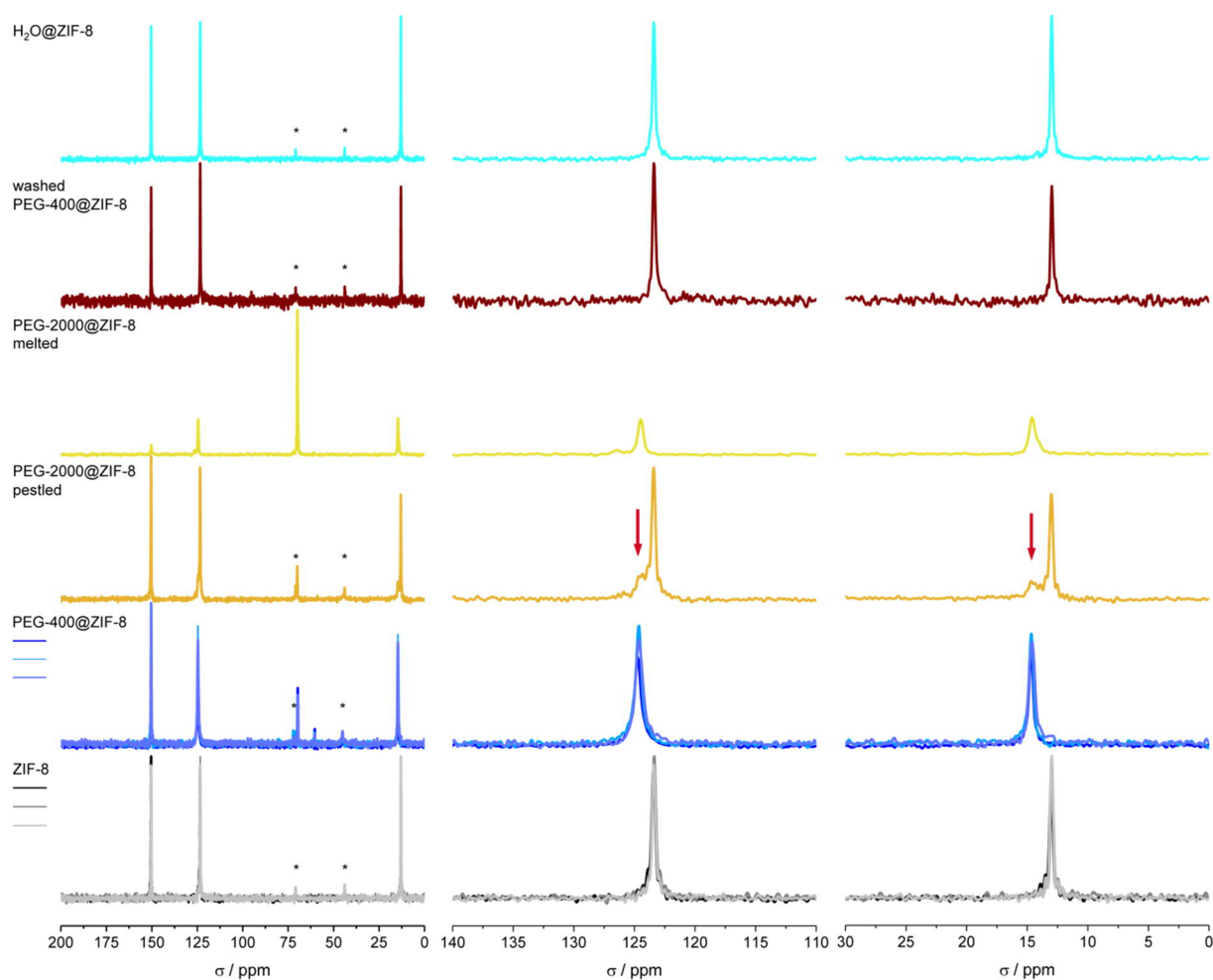
Figure S3.1.7: ^{13}C-CP-MAS-NMR (left) with detailed views (center, right) of activated ZIF-8 (three different samples indicated by black and shades of gray), PEG-400@ZIF-8 (three different samples indicated by shades of blue), pestled PEG-2000@ZIF-8, melted PEG-2000@ZIF-8, washed ZIF-8·½PEG powder and H_2O@ZIF-8. The red arrows indicate the rise of ZIF-8 carbons interacting with the PEG polymer by pestling with PEG-2000. Melting of the mixture yields a more quantitative interaction of the PEG-2000@ZIF-8 compound, accompanied by a downfield shift of the carbon signals. ZIF-8 brought in contact with water shows no significant change of the chemical shifts, indicating that water does not enter the hydrophobic pores of ZIF-8. Asterisks denote spinning side bands.
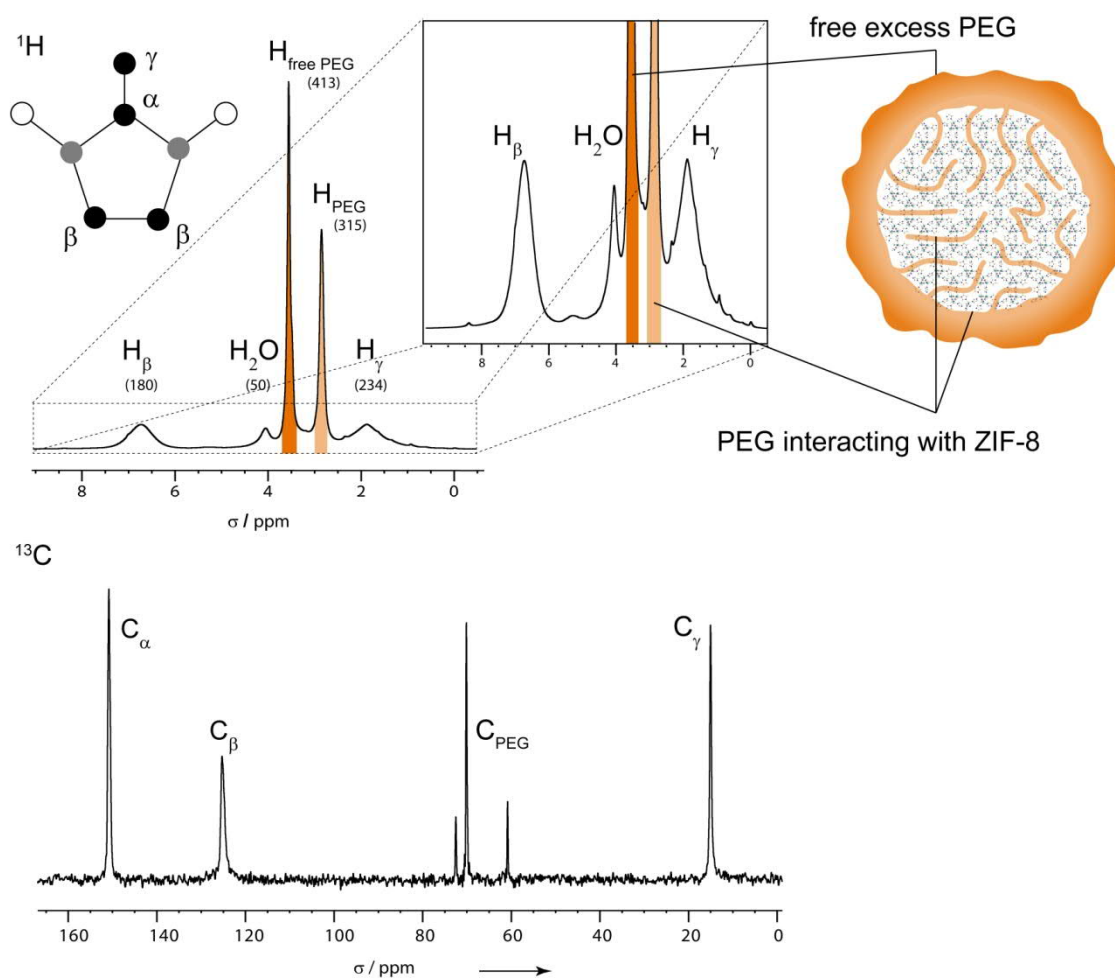
Figure S3.1.8: 1H-MAS-NMR and chemical shift assignment of PEG-400@ZIF-8 (top) and ^{13}C-CP-MAS-NMR (bottom) with a contact time of 20 ms at a spinning speed of 40 kHz. The signal highlighted in bright orange is assigned to non-interacting PEG, while the signal assigned to PEG in close contact with ZIF-8 is marked in pale orange. The additional signals at 72 (-O-CH_2-CH_2-OH) and 60 (-O-CH_2-CH_2-OH) ppm arise from terminal carbons of the polymer chains. The number in brackets represent the integrals of the peaks after deconvolution.
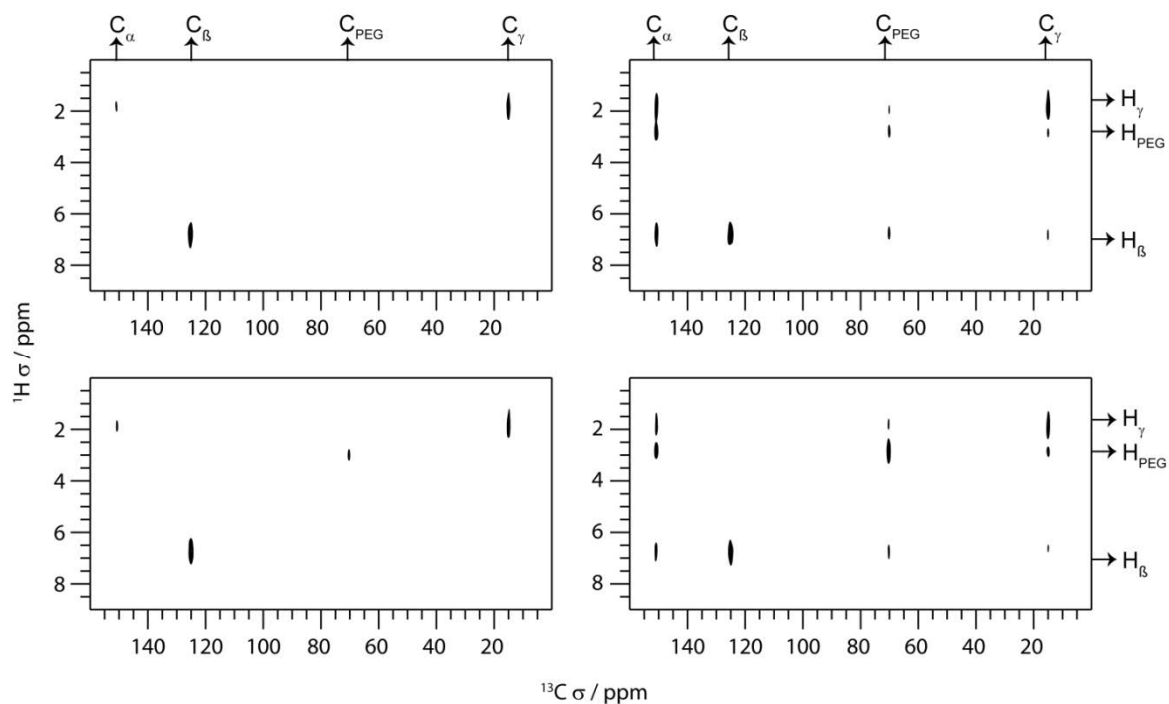
Figure S3.1.9: 2D ^{1}H-^{13}C HETCOR spectra of PEG-400@ZIF-8 (top) and melted PEG-2000@ZIF-8 (bottom) at different contact times (left: 0.5 ms, right: 16 ms). The carbon and proton assignments are indicated at the top and right of the spectra, respectively. Transfer of magnetization between PEG and ZIF-8 via Cross Polarization indicates partial immobilization of PEG on the ZIF-8 surface. Note that only those H-C correlations are observed at longer contact times which correspond to the PEG protons at lower field (2.9 ppm, pale orange in Figure S3.1.7) which are assigned to PEG interacting with ZIF-8.
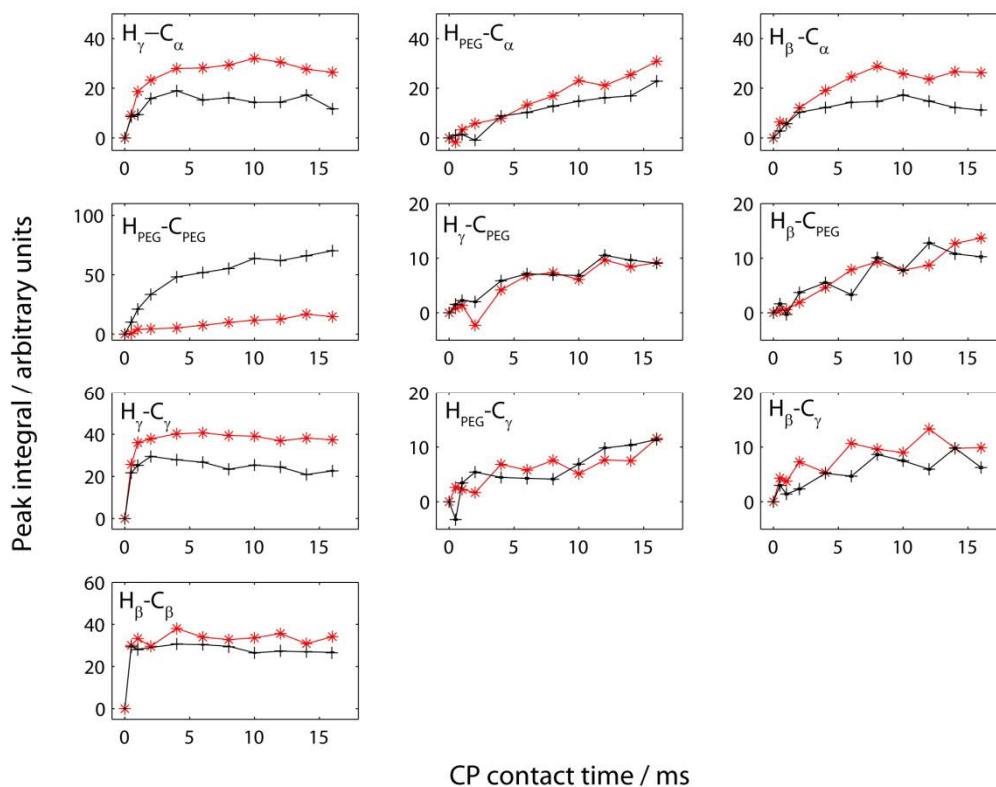
Figure S3.1.10: CP buildup curves of various signals of the 2D ^{1}H-^{13}C HETCOR spectra of PEG-400@ZIF-8 (red) and melted PEG-2000@ZIF-8 (black). Peak assignment is indicated in the subplots. Note the fast buildup for such carbons directly bonded to ZIF-8/PEG protons in contrast to the slower buildup for the more distant through-space interactions.
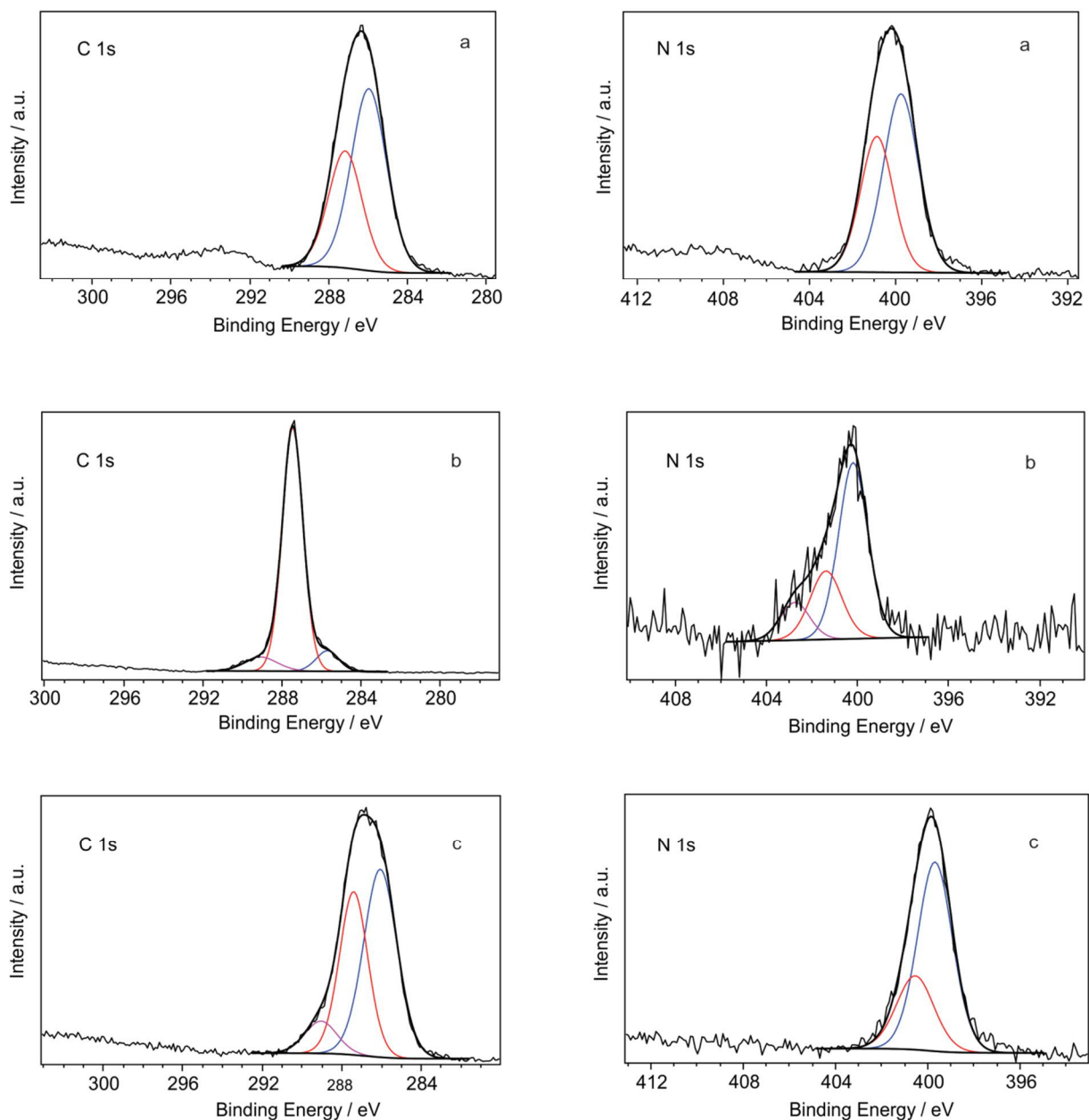
Figure S3.1.11: C(1s) and N(1s) XPS spectra of (a) ZIF-8 powder, (b) ZIF-8·½PEG-400 powder and (c) PEG@ZIF-8 films with their corresponding fitted peak areas; for fitting percentages see Table S3.1.3.

Table S3.1.3: XPS core-level binding energies in eV of ZIF-8, ZIF-8·½PEG-400 powders and PEG@ZIF-8 films compared to values of PEG-2000 and sapphire substrate (Al_2O_3); fitted peak area percentage in parentheses.

	C (1S)	N (1S)	O (1S)
ZIF-8 powder	286.0 (62%) 287.2 (38%)	399.8 (58%) 400.9 (42%)	
ZIF-8·½PEG-400 powder	285.7 (8%) 287.5 (84%) 289.1 (8%)	400.2 (61%) 401.4 (26%) 402.7 (13%)	532.1 (11%) 533.8 (89%)
PEG@ZIF-8 film	286.1 (52%) 287.4 (39%) 289.1 (9%)	399.7 (70%) 400.5 (30%)	532.2 (58% 533.8 (42%))
PEG-2000	287.4		533.8
sapphire			532.4
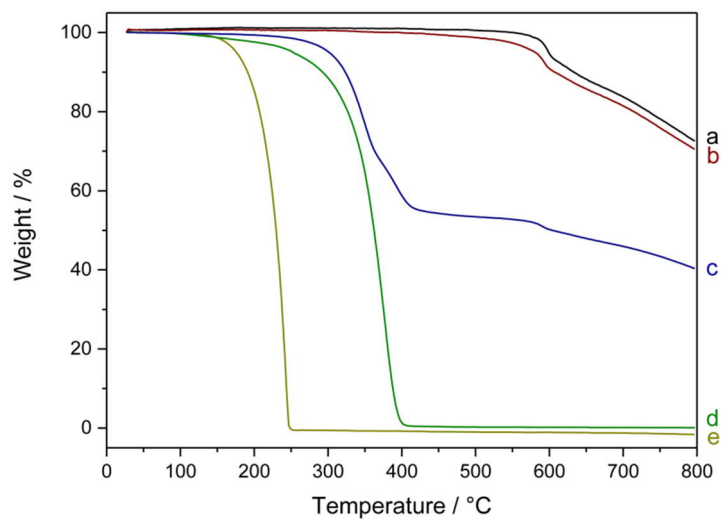
Figure S3.1.12: TGA of (a) ZIF-8, (b) washed ZIF-8·½PEG-400, (c) ZIF-8·½PEG-400, (d) PEG-400 and (e) 2-methylimidazole.

4 POST-MODIFICATION OF MOFS IN BRAGG STACK SENSORS

One-dimensional photonic crystals, so-called Bragg stacks, predominantly owe their structural color to the optical properties and thicknesses of the constituting layers. External stimuli that affect the layer thicknesses or optical properties, e.g. the RIs, translate into an altered color that can be exploited for sensing applications. For example, this can be achieved by stacking MOF nanoparticles with an optically contrasting material. The porous MOF can then act as the functional host-material accommodating the analytes. Based on the resulting optical shift in the reflectance/transmittance spectrum of the BS, these different analytes can be sensed and distinguished. However, structural variations between BS sensors lead to poor comparability of the sensing signals.

As part of this thesis, this problem was tackled by fabricating a generic BS sensor platform, which was accomplished by stacking layers of CAU-1 and TiO_2 nanoparticles. This chapter demonstrates how the post-modification of generic BSs targeting the functional MOF layer provide comparable optical shifts with improved selectivity avoiding batch-to-batch differences.

4.1 IMPROVING ANALYTE SELECTIVITY BY POST-ASSEMBLY MODIFICATION OF METAL–ORGANIC FRAMEWORK BASED PHOTONIC CRYSTAL SENSORS

Alberto von Mankowski, Katalin Szendrei-Temesi, Charlotte Koschnick and Bettina V. Lotsch

Abstract

The porous nature and structural diversity of metal–organic frameworks (MOFs) provide a versatile platform for specific and selective sorption behavior. When integrated as functional layers into photonic crystals (PCs), loading of the porous network with organic solvent vapors translates into an optical response, allowing analyte discrimination according to the specific host–guest interactions and, hence, framework affinity to the analytes. However, the optical response of PCs is critically influenced by the overall PC architecture, leading to batch-to-batch variations, thus rendering unequivocal analyte assignment challenging. To circumvent these problems, we have developed a straightforward and mild "post-assembly" modification strategy to impart differences in chemical selectivity to the MOF layers whilst keeping the overall PC backbone constant. To this end, one-dimensional photonic crystal (1D PC) sensors based on CAU-1 and TiO_2 layers were fabricated to obtain a generic platform for post-assembly modification, targeting either the secondary building unit (SBU) or the linker unit of the as-assembled MOF nanoparticle layers. The optical response to solvent vapor exposure was investigated with the pristine CAU-1 based sensor as well as its modifications, showing enhanced analyte selectivity for the post-modified systems.

Table of content: The porous nature and tailorable host-guest interactions of metal-organic frameworks (MOFs), cast into a 1D photonic crystal architecture, provide a versatile platform for specific and selective sorption, which can be exploited for opto-chemical sensing.

Conceptual insights

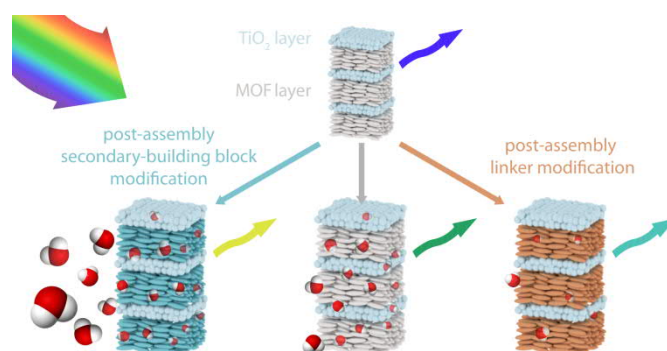The development of integrated nanoscale sensing systems imposes high demands on the materials employed, including chemical versatility, stability and flexibility. The intrinsic porosity, functional diversity and tunability of metal–organic frameworks (MOFs) make them interesting components for integrated sensing systems. In addition, post-synthetic modification of MOFs is a powerful tool enabling judicious property tuning at the molecular level. However, when integrated in sensing devices, MOFs have to be selected and modified prior to the system assembly, thus requiring careful planning at the stage of material synthesis. Here, we develop a novel strategy demonstrating that MOFs can be modified post device fabrication by a mild post-assembly modification route. For this purpose, a generic one-dimensional photonic crystal sensor platform based on amine-bearing CAU-1 as active layer was fabricated. We demonstrate that post-assembly modification of either the metal-oxo clusters of CAU-1 or covalent modification of the organic linkers allows for the fine-tuning of the chemical selectivity and, hence, optical response to volatile organic analytes. The generic post-assembly modification demonstrated herein opens the door to the scalable production of MOF-based photonic crystal sensors with identical backbones, but gradually tunable analyte selectivities.

4.1.1 INTRODUCTION

Since metal–organic frameworks – a versatile class of crystalline organic–inorganic hybrid materials featuring permanent intrinsic porosity – have come of age, the research focus has shifted from structural considerations towards the many fascinating properties enshrined in the manifold framework architectures.[1-3] In particular, the inherent micro- and mesoporosity of MOFs provide a unique platform for exploiting specific host–guest interactions, which are defined by the pore size and accessibility, as well as the surface chemistry, polarity and functionality. Post-synthetic methods such as covalent and coordinative modification, deprotection, solvent-assisted ligand exchange or insertion provide further possibilities to precisely engineer the framework according to the desired applications.[4-6] These applications range from catalysis,[7] gas separation and storage,[8] to drug delivery, electrochemistry[9] and chemical sensing,[10] among many others, where post-synthetic treatment can lead to a significant improvement of the material performance.[11-13] When it comes to sensing applications, the stimuli-responsive material is required to exhibit a property change upon analyte exposure that can be measured as a sensing signal. In general, easy and fast detection of the sensing event is desired. Here, optical sensors have been proven to be both sensitive and selective.[10,14] Signal transduction can be based on simple solvo- and vapochromism, luminescent based mechanisms, thin film Fabry–Pérot interference, as well as photonic crystal (PC) sensor based approaches, the latter comprising nanoscale architectures that can be used to guide and confine light.[14-17] PCs are periodic dielectric structures, the hallmark of which is the photonic band gap (PBG) corresponding to the

frequency range in which the propagation of light is forbidden and photons within this energy range are thus reflected by the PC.[18] For PCs exhibiting periodicity in one dimension – so called Bragg stacks (BSs) – the diffraction maximum λ_{max} at normal incidence is given by

$$m\lambda_{max} = 2(n_l h_l + n_h h_h) \qquad\qquad (4.1.1)$$

where the indices l and h refer to the layers of low and high refractive index (RI) material, respectively, m is the diffraction order, n the refractive index and h the layer thicknesses.[19] Thus, PCs stand out among optical sensors as they impart structural color even to colorless materials, rather than requiring colored or luminescent components. On that account, the sorption properties of MOFs can be exploited when integrated into PCs for sensing applications. As evident from Equation 4.1.1, swelling of a layer or a change in its effective RI, as it is the case for solvent vapor adsorption, is sufficient to alter the PBG. This translates into an observable shift in the reflectance spectrum and, hence, a change in the structural color of the PC. In principle, a change in the RI of a material can be detected by Fabry–Pérot interference devices as reported for thin films of ZIF-8 by Lu et al.[20] or UiO-66 by Cui et al.[21] Hierarchical MOF-based PC structures providing a high quality optical platform for light management have been fabricated by various strategies. 3D photonic MOF architectures were obtained by deposition of MOFs on opal-like structures or using (inverse) opals as templates.[22-26] Also, MOF nanoparticles have been alternately stacked with optical contrast materials such as TiO_2 to form BS sensors.[27,28] Likewise, flexible MOFs can be employed to enhance the shift of the PBG.[29] Nonetheless, a major drawback of these systems is the poor comparability of their optical responses. This is because the absolute optical shifts of the spectra will sensitively depend on the optical quality, porosity and thicknesses as well as numbers and types of active and passive layers.[27-29] In addition, analyte selectivity is largely limited to the type of MOF employed and fine-tuning of the sensing properties requires exchange of the MOF system, which may be limited by synthetic constraints such as availability of nanoparticulate MOFs.

To tackle these issues, we present a facile route for the fabrication of a generic MOF based BS sensing platform that can be chemically modified after the sensor assembly to enhance analyte selectivity, ensure signal reproducibility and guarantee comparability of the optical signals. BS fabrication via spin-coating is generally performed by alternately spin-coating two nanoparticle suspensions until the desired amount of layers is reached. To tune analyte selectivity in MOF based PC sensors, a post-synthetic modification step can be performed at different stages during BS fabrication as outlined in Scheme 4.1.1. Introduction of chemically different groups prior to MOF synthesis (path (a) – precursor modification) usually requires modification of the MOF synthesis conditions, whereas path (b) – post-synthetic modification of the MOF nanoparticles – may require changes in the spin- (dip-, spray) coating conditions, such as solvent or concentration changes of the MOF nanoparticle suspension. For

path (c), modification of every deposited MOF layer separately implies unnecessary repetition steps, rendering the post-assembly path (d) the most convenient and efficient strategy. Furthermore, by fabricating a generic BS platform first, followed by post-assembly modification of the MOF, differences in layer porosity or thicknesses of the different MOF BS sensors are kept to a minimum, thus allowing better comparability of the individual BSs.
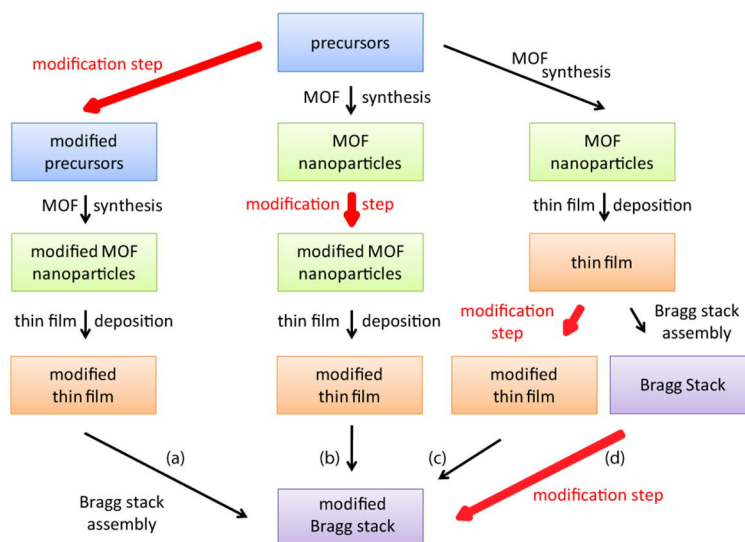
Scheme 4.1.1: Representation of the key steps during BS fabrication in which the modification step (red arrows) takes place (a) prior to MOF synthesis, (b) after MOF nanoparticle synthesis, (c) after each MOF layer deposition, and (d) post-assembly of the entire BS.

Here, we fabricate a generic MOF BS sensor platform based on pristine and modified CAU-1 by following the above described post-assembly strategy. High RI TiO_2 nanoparticle layers are used to provide the optical contrast. We deliberately chose CAU-1, $Al_4(OH)_2(OCH_3)_4(BDC-NH_2)_3$, which is composed of aluminum-hydroxy/methoxy secondary building units (SBUs) linked by 2-aminoterephthalates (Scheme 4.1.2 (b)).[30] Two distinct post-synthetic modifications are possible for this system, one targeting the SBU (coordinative modification) and another the organic linker.[31] Scheme 4.1.2 depicts the procedure, in which the methanolates were replaced by hydroxy groups (CAU-1-SBU) or an amidification of the linker with hexanoic acid took place (CAU-1-Hex). The procedures were first tested on nanoparticles and subsequently applied to the as-assembled BSs. Both modifications turned out to be effective in significantly enhancing the analyte discrimination capability of the MOF based PC sensors. In addition, modification of the as-assembled PCs allows for the direct comparison of the optical responses, thus marking the next step in the development of custom-made optical MOF sensors.
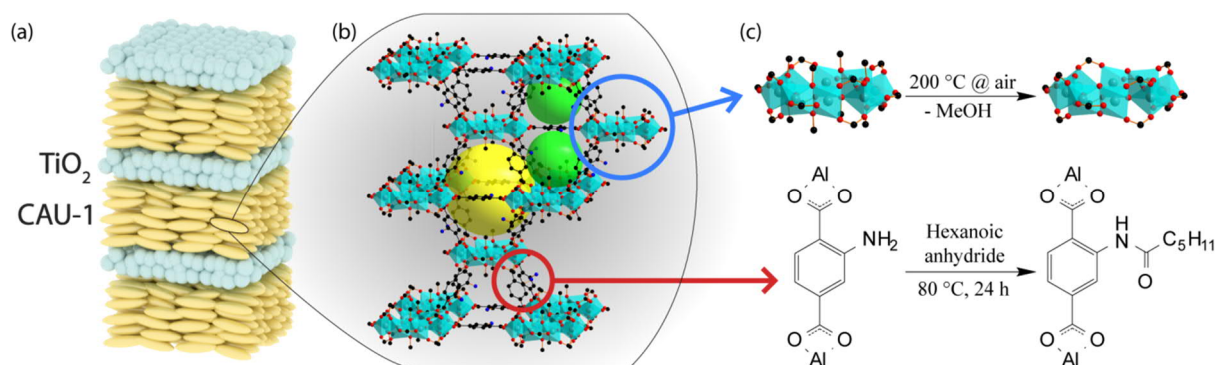
Scheme 4.1.2: (a) Schematic representation of a multilayered photonic crystal comprising CAU-1 and TiO_2 nanoparticle layers; (b) crystal structure of CAU-1 with carbon atoms given in black, oxygen in red, aluminium-oxygen octahedra in turquois and pores indicated by yellow and green spheres; (c) the two post-synthetic modification strategies of the framework applied in this work using (top) de-methoxylation of the SBU (CAU-1-SBU) and (bottom) amidification with hexanoic anhydride of the organic linker (CAU-1-Hex).

4.1.2 EXPERIMENTAL

Experimental details were published as part of the supplementary information.

Synthesis of CAU-1 nanoparticles

In a typical synthesis, 377 mg $AlCl_3 \cdot 6\,H_2O$ (1.55 mmol) and 93.3 mg 2-aminoterephthalic acid (0.515 mmol) were dissolved in 10 mL methanol. The solutions were heated in a microwave (Biotage Initiator, Biotage) at 140 °C for 2 min. The product was obtained by centrifugation at 24 krpm for 10 min and washed twice with 20 mL methanol. The particles were resuspended in methanol by ultra-sonication. To remove agglomerates, the suspension was centrifuged at 9 krpm and filtered with a 0.45 µm PTFE filter (VWR). For spin-coating experiments, the suspension was diluted to 4 wt% with methanol.

Post-synthetic modification of CAU-1 nanoparticles

Three batches of CAU-1 nanoparticles for each modification were prepared according to the synthesis described above and merged.

For de-methoxylation of the SBU, the particles were obtained by centrifugation and heated at 200 °C for 24 h (CAU-1-SBU).

For the covalent modification, the suspended particles were washed twice with 20 mL methanol and twice with 20 mL DMF before resuspending them in 2.5 mL DMF. Then, 2.5 mL of hexanoic anhydride were added to the CAU-1 particles and heated to 80 °C for 16 h (CAU-1-Hex). The modified particles were washed twice with 20 mL MeOH. The particles were the centrifuged and left to dry overnight (CAU-1-Hex).

Synthesis of TiO$_2$ nanoparticles

20 mL of titanium isopropoxide were added dropwise to 36 mL of deionized water under vigorous stirring. The solution was stirred for 1 h. The resulting white solid was filtered and washed with deionized water. The remaining solid was mixed with 3.9 mL of 0.6 M tetramethylammonium hydroxide and transferred to a teflon reactor. The mixture was heated in a furnace at 120 °C for 3 h. Larger particles and agglomerates were removed by centrifugation at 13 krpm. For spin-coating experiments, the TiO$_2$ suspension was diluted to 3 wt% in MeOH.

Spin-coating of CAU-1/TiO$_2$ Bragg stacks

Bragg stacks were produced by spin-coating the CAU-1 suspension at 6 krpm and the TiO$_2$ suspension at 8 krpm with a heating step at 120 °C for 5 min on 1 cm² silicon wafers. Three bilayers were applied (BS).

Post-assembly modification of the Bragg stacks

For post-assembly modification, the Bragg stacks were either immersed in 4 mL hexanoic acid for 16 h at 80 °C (CAU-1-Hex) or heated at 190°C for 24 h (CAU-1-SBU). The Bragg stacks were then washed by immersion in methanol twice for at least 1 h.

Optical measurements

Prior to the measurements, the BSs were heated at 120 °C for at least 1 h in vacuo to remove residual solvents in the pores and for another 30 min in a stream of nitrogen. In order to investigate the optical response of the Bragg stacks, nitrogen gas was bubbled through three gas washing bottles filled with the solvent to be investigated at 1.2 bar. In total, five solvents (water, methanol, ethanol, iso-propanol and heptane) were investigated. The saturated vapor stream was then introduced into a custom-built steel sample chamber with a quartz window in which the samples were fixed. Measurements were repeated at least 3 times to ensure reproducibility. To prevent errors arising from different measurement spots the sample chamber was fixed and not moved during and in between the measurements. Solvent vapor exposure was performed until the change of the reflectance was below 0.5% for a 60 seconds. After solvent vapor exposure, the chamber was flushed with pure nitrogen. To facilitate desorption of the solvent, the chamber was flushed by an alternating flow of nitrogen and saturated water vapor stream to ensure equal conditions between every measurement.

Characterization

Particle size distributions were determined by dynamic light scattering, DLS (Malvern Zetasizer Nano ZS, Malvern).

X-ray diffraction (XRD) patterns of powder materials were measured on a Stoe Stadi P diffractometer with Ge filtered Cu-K$_\alpha$ radiation on a DECTRIS Mythen 1K Detector (Stoe).

IR spectra were recorded on a Spectrum BX FT-IR (Perkin Elmer).

^{13}C- and ^{15}N- cross-polarization solid-state NMR (CP-ssNMR) measurements were performed on a Bruker Avance III HD 500 MHz (500 MHz, 11.74 T, Bruker) under magic angle spinning at 10 kHz using a ramped-amplitude (RAMP) CP pulse on ^{1}H, centered on the n = +1 Hartmann-Hahn condition. Contact times in ^{13}C- ssNMR were 4 ms for all samples, whereas in ^{15}N- ssNMR, contact times were 5 ms for all samples. The ^{13}C and ^{15}N chemical shifts were referenced relative to TMS and nitromethane, respectively. For ^{1}H liquid NMR, samples were digested in $NaOD/D_2O$ and measured on a Bruker AV400TR NMR (400 MHz, 9.39 T, Bruker) spectrometer.

Cross-sectional SEM images were acquired on a Zeiss Merlin (Carl Zeiss AG) at acceleration voltages of 1.5 kV.

Elemental analysis was performed on a Vario micro (Elementar Analysensysteme GmbH).

2D grazing-incidence small angle X-ray scattering (GISAXS) data were recorded with an SAXSpace system (Anton Paar) equipped with a GeniX Cu-K_α microsource and a Dectris Eiger R 1M detector.

Ad- and desorption isotherms were measured on an Autosorb iQ-MP2 (Quantachrome Instruments) with argon of 99.9999% purity at 87 K and water (Milli-Q® Millipore) at 15 °C. Prior to the measurements, the samples were outgassed under high vacuum at 120 °C for at least 12 h. In accordance with the ISO recommendations, multipoint BET tags equal or below the maximum in $V \cdot (1 - p/p0)$ were chosen. Correlation coefficients of all calculated BET surface areas were above 0.9999. For DFT pore size distribution calculations the calculation model "Ar at 87K zeolites/silica (spher./cylindr. pores, NLDFT equ.)" was used. Contact angle measurements were performed with MilliQ water on an Attension Theta Lite (Biolin Scientific).

Ellipsometric porosimetry measurements were carried out on a PS-1000 (Semilab) at an incident angle of 60.25° in the spectral range of 186.23 to 987.24 nm. For data evaluation the model and fitting range was limited from 300 to 1000 nm using a Cauchy-Lorentz model. Measurements were carried out on thin films of CAU-1, CAU-1-SBU and CAU-1-Hex. Thin films of CAU-1-SBU and CAU-1-Hex were obtained by applying the same modification procedure as for the BSs.

For time-dependent reflectance measurements a fiber optic spectrometer USB4000-XR1-ES (Ocean Optics) integrated with an optical light microscope DM2500 M (Leica) was used. The reflectance intensities were monitored at several wavelengths. The spectral shifts were calculated out of the Bragg peaks as $\Delta \lambda = \lambda_{solvent} - \lambda_{N2}$.

Color image analysis by principal component analysis (PCA) was performed according to procedure described previously.[S1] Briefly, images of the BS were acquired during nitrogen exposure and during analyte exposure upon saturation. The images were aligned, an area selected, cropped and splitted into RGB channels. The mean intensities of the R, G and B channels were then used for PCA using the

program Origin 2017 (OriginLab Corporation, USA). The combined array was calculated based on the differences in the RGB values of all three BSs.

4.1.3 RESULTS AND DISCUSSION

Particle characterization

In the first step, the MOF modification procedures to be applied on the BSs were tested on nanoparticle suspensions of CAU-1 to assess the viability of the synthetic procedure and to investigate the properties of the modified MOFs at the bulk level. The focus of this preliminary investigation was to confirm that the synthetic conditions applied maintain the structural integrity of the framework and nanoparticles and guarantee a high reaction yield, in particular for the covalent modification. The latter was done via a mild approach with hexanoic acid anhydride to avoid decomposition of the MOF. Furthermore, a sorption study using water vapor was performed to characterize the sorption behavior towards hydrophilic analytes and the influence of post-synthetic modification on the sorption properties.

Dynamic light scattering (DLS) of the suspensions attested similar average particle sizes of 45–52 nm for the pristine and modified MOF nanoparticles, indicating that the covalent modification procedure preserved the particle size distribution and aggregation state (Figure S4.1.1). For the TiO_2 nanoparticles used for spin-coating, an average size of 27 nm was determined, indicating the suitability of both nanoparticle suspensions to cast them into highly porous thin films. PXRD measurements on the dried particles further establish the structural integrity of the CAU-1 particles after post-synthetic modification (Figure S4.1.2).

To characterize the chemical modifications, IR and ^{13}C-NMR spectra were recorded (Figure 4.1.1). In the IR spectrum of CAU-1-SBU, the alkyl related vibrations at 3000 – 2800 and ≈1078 cm^{-1} disappear completely, suggesting the quantitative de-methoxylation of the SBU. For the amidification (CAU-1-Hex), the free amine related bands at 3390 and 3521 cm^{-1} disappear and those at 1340 and 1261 cm^{-1} shift to 1299 and 1269 cm^{-1}, respectively. Considering the aromatic ring related band, a shift from 1500 to 1517 cm^{-1} can be observed and the alkyl related bands between 2000 – 1800 cm^{-1} become more pronounced, indicating a high degree of modification. The corresponding IR spectra of thin films, in which the modification procedure was applied and confirmed, can be found in Figure S4.1.3. The ^{13}C CP-ssNMR reveals identical linker related signals for CAU-1-SBU and the pristine MOF. Only the methanolate related signal (48 ppm) shows a significant drop in intensity, signaling the almost quantitative de-methoxylation of CAU-1-SBU. For the amidification, the carbon signals 2 – 5 (150 – 110 ppm) are shifted and the alkyl-related signals appear at 40 – 10 ppm, attesting the successful covalent modification of the linker. In both cases, the relevant carbon signal shifts and intensity drops support the IR data and indicate a high degree of modification. In case of ^{15}N-NMR, the only nitrogen related

signal shifts clearly from -320 ppm in the pristine CAU-1 to -252 ppm for the covalent modification, whereas for the de-methoxylation no change is observed (Figure S4.1.4).
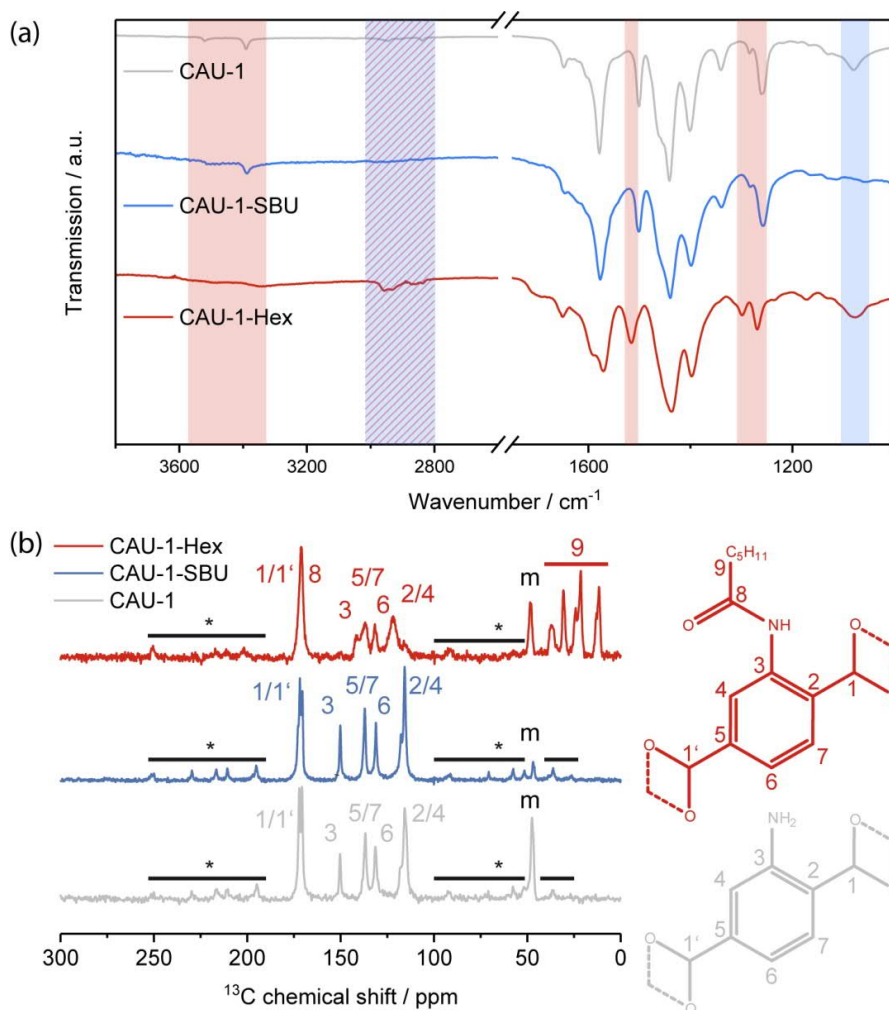
Figure 4.1.1: (a) IR spectra of CAU-1 (grey), CAU-1-SBU (red) and CAU-1-Hex (blue). The characteristic changes in the IR spectra for the SBU modification have been highlighted in blue and those of CAU-1-Hex in red; (b) ^{13}C-CP-ssNMR (left) of CAU-1 (grey), CAU-1-SBU (blue) and CAU-1-Hex (red) with their (right) corresponding chemical shift assignment. Peaks marked with asterisks and a bar denote spinning side bands, peaks marked with m arise from methanolates of the SBU.

Digestion of the MOF and subsequent NMR analysis (Figure S4.1.5) revealed a degree of modification for CAU-1-SBU of 99% and for CAU-1-Hex of 84%. Elemental analysis yielded similar degrees of modification of 96% for CAU-1-SBU and 88.5% for CAU-1-Hex (Table S4.1.1).

The porosity of the nanoparticles was assessed by argon physisorption (Figure 4.1.2(a)). The microporosity of all samples is reflected by a considerable gas uptake at very low partial pressures, for which CAU-1-SBU shows the highest adsorbed volume (310 cm^3g^{-1}@p/p_0 = 0.1), closely followed by CAU-1 (290 cm^3g^{-1}), while CAU-1-Hex shows the lowest uptake (110 cm^3g^{-1}). As expected, BET analysis yields decreasing apparent surface areas of 1099, 1019 and 406 m^2g^{-1}, respectively. In addition, the large hysteresis at higher partial pressures accounts for the textural mesopores due to the nanoparticulate nature of the powder (Figure S4.1.6), which by far exceeds the uptake of the

micropores (800 cm^{3}g^{-1}, 700 cm^{3}g^{-1} and 650 cm^{3}g^{-1}, respectively). Furthermore, water vapor sorption was performed, showing again decreasing uptake from the de-methoxylated to the hexanoylated CAU-1 (Figure 4.1.2 (b)). While the isotherms for CAU-1-SBU and the pristine compound exhibit a sigmoidal shape with a moderate hysteresis loop at 0.2 – 0.3 p/p$_0$ as well as increasing uptake above 0.7 p/p$_0$ attributed to water adsorption into the textural pores, CAU-1-Hex shows a flattened and almost linear isotherm with low water uptake (174 cm^{3}g^{-1}) compared to the other samples (1148 cm^{3}g^{-1} and 1040 cm^{3}g^{-1}). The hydrophobic behavior of CAU-1-Hex is also reflected in the decreased amount of adsorbed water after desorption (30 cm^{3}g^{-1} vs. 86 and 74 cm^{3}g^{-1}). The shapes and values of the sorption isotherms provide striking evidence for the increasing hydrophobicity introduced by the covalent PSM, altering both the intrinsic and textural sorption behavior of the framework. For the SBU modification, the changes are comparably small, but still an increased uptake of both argon and water is observed. Interestingly, the textural porosity contributes considerably to the total uptake of all samples. As a consequence, the water isotherm of CAU-1-Hex demonstrates the significant impact of the modification not only on the intrinsic porosity of the MOF, but on the textural porosity as well. Even if the particles are packed more densely in a BS fabricated by spin-coating, it is reasonable to assume a similar impact of the textural porosity in the MOF layers of the BSs. The increasing hydrophilicity of CAU-1-Hex over CAU-1 to CAU-1-SBU was further confirmed by contact angle measurements on the corresponding thin films (Figure S4.1.7).
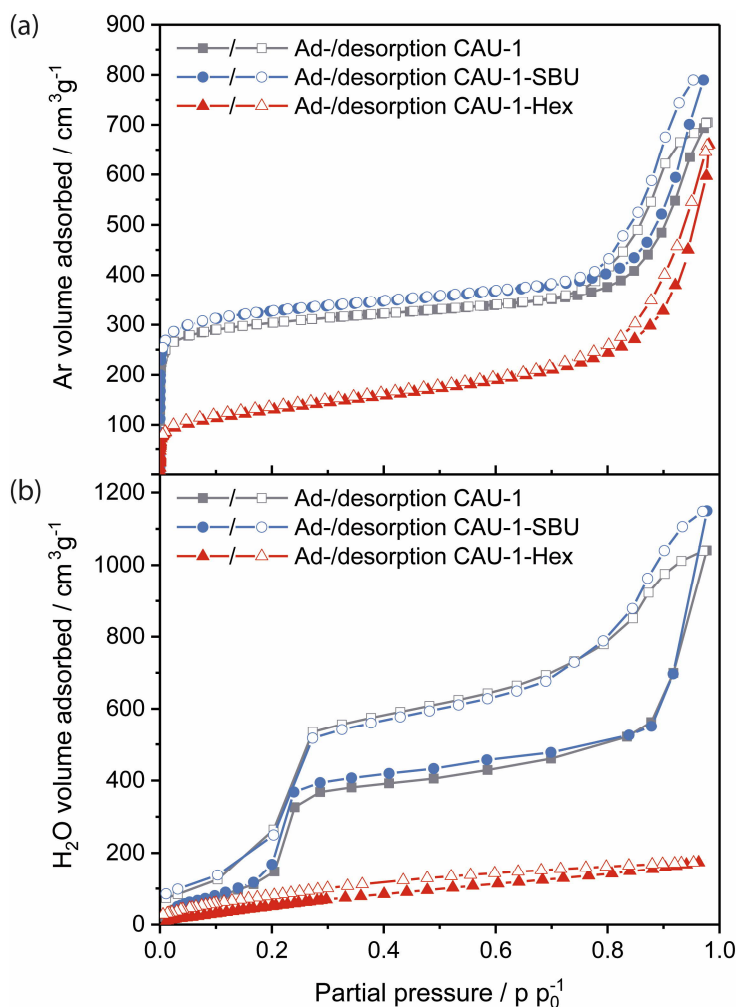
Figure 4.1.2: (a) Argon and (b) water vapor ad- and desorption isotherms of CAU-1-SBU (red), CAU-1 (grey) and CAU-1-Hex (blue).

Bragg stack characterization and optical

BSs were stacked alternatingly with nanoparticles of CAU-1 and the high-RI material TiO_2 to form multilayer structures composed of 3 bilayers and modified according to path d, Scheme 4.1.1 and as described in Scheme 4.1.2. While similar thicknesses of the active MOF layers ensure that the sensitivities of the different sensors can be compared, layers of the optical contrast material TiO_2 were kept thin to minimize the impact of the textural porosity of TiO_2 on the sorption properties. The layer thicknesses and homogeneity of a representative generic BS sample was studied by scanning electron microscopy (SEM) cross-section images (Figure 4.1.3). The images confirm the homogenous periodic structure of the PCs in which the nanocrystalline TiO_2 particles are packed densely into thin layers while the thicker layers of rice-grain shaped CAU-1 are interspersed with an irregular pore network, which is able to accommodate guest molecules. The CAU-1 layer appears darker in the back-scattered SEM image due to the lower average atomic number of the MOF nanoparticles compared to TiO_2. Furthermore, the secondary electron image contrasts the rice-grain shaped morphology of CAU-1 with the dense nanoparticulate appearance of TiO_2 and confirms the successful combination of the two

materials as well as the long-range stacking order with well-defined interfaces as seen in the back-scattered SEM image. The images show thick, homogeneous MOF layers with an average thickness of 120 ± 10 nm that alternate with layers of TiO_2 having thicknesses of 32 ± 5 nm giving rise to a periodic structure with defined interfaces and a total thickness of approximately 420 nm. The structural integrity of the modified BSs was confirmed by additional cross-sectional SEM images (Figure S4.1.8 and Figure S4.1.9). In addition, GISAXS measurements show that the crystallinity of the framework is retained (Figure S4.1.10). Furthermore, digestion and subsequent NMR analysis of the modified MOF layers revealed modification degrees of 100% for CAU-1-SBU and 88% for CAU-1-Hex (Figure S4.1.11), which are similar to the bulk values.
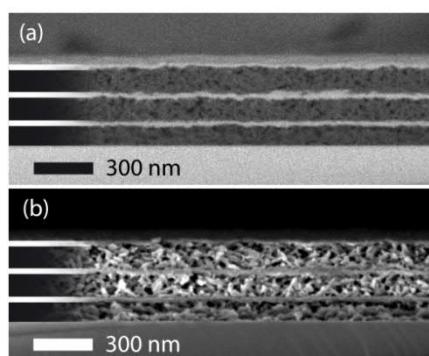
Figure 4.1.3: Cross-sectional SEM images of a representative 6-layer BS on a silicon substrate acquired with a (a) back-scattered electron detector and (b) In-Lense detector. The MOF layers are highlighted in black, the TiO_2 in white.

As discussed above, the PBG shift in a BS caused by an uptake of guest molecules will largely depend on the amount of analyte adsorbed and the adsorbate's RIs. Hence, for complete pore filling for every analyte, the expected shifts should solely depend on its RI. In reality, the amount of analyte adsorbed by the BS will depend on many other factors such as analyte size, pore accessibility and host–guest interactions, i.e. the chemical affinity of the analyte to the constituent layers, which due to its high surface area will largely be defined by the MOF acting as the active BS layer.

To investigate the sensing performance of the CAU-1 based BS and its modifications, the optical responses to the solvent vapors of water, the alcohols methanol, ethanol, and iso-propanol, as well as n-heptane in a nitrogen carrier stream were monitored and repeated three times. The spectral shifts were determined as the absolute optical shifts of the reflectance maxima (Bragg peak) during solvent vapor exposure compared to that of the pure nitrogen stream. In Figure 4.1.4 (a-c), exemplary reflectance spectra are shown for each solvent for the three investigated BSs, while the corresponding shifts are summarized in Figure 4.1.4 (d), sorted by decreasing polarity of the MOF and solvent. Solvent polarities and RIs are provided in Table S4.1.2, the complete set of spectra that confirm the reproducibility of the measurements are given in Figure S4.1.12 to Figure S4.1.14. The results show overall shifts in the range from 17 to 73 nm, in which CAU-1-SBU shows the largest, CAU-1 intermediate

and CAU-1-Hex the lowest shifts. For the unmodified BS with pristine CAU-1, water gives the lowest shift (48 nm) in spite of the lower RI of methanol, which is likely caused by the more efficient interaction of the methoxy-groups of the SBU with the smallest alcohol as compared to water. For the higher alcohols and n-heptane, the measured shifts are slightly increased but still very similar and barely allow a reliable distinction between these analytes. On the contrary, the results clearly show that the modifications nicely address this problem: CAU-1-SBU shows gradually increased shifts along the series methanol, water, ethanol, iso-propanol and heptane which is in accordance with the RI trend of the solvents. We attribute the increased shift seen in CAU-1-SBU for water compared to methanol to the now improved possibility to form hydrogen bonds with the SBU and the overall increased pore accessibility, an effect that seems to dominate in case of the larger analytes. The opposite effect is observed for the CAU-1-Hex modification: here, the water uptake is marginal and probably related to the TiO_2 layers, as expected from the sorption isotherms of the CAU-1-Hex powder. While water and the small polar alcohols show only slight shifts, iso-propanol and n-heptane show intermediate shifts; from these observations, a correlation between analyte size and the accessible pore volume on the one hand, and analyte polarity on the other hand can be derived. Accordingly, n-heptane exhibits a slightly increased shift for CAU-1-Hex compared to pristine CAU-1. We attribute this slightly increased adsorption capability of CAU-1-Hex primarily to the more beneficial hydrophobic interactions between the hydrocarbon chain and CAU-1-Hex. We would like to emphasize at this point that in all three cases, the factors mentioned – RI, size and polarity of the analytes – define the optical response. However, disentangling the relative influence of each of these factors is difficult. Nevertheless, it is clear from these data that the altered pore environments of both post-assembly modifications allow for a more reliable distinction of the investigated analytes, whereas for the pristine BS, signal assignment is ambiguous.
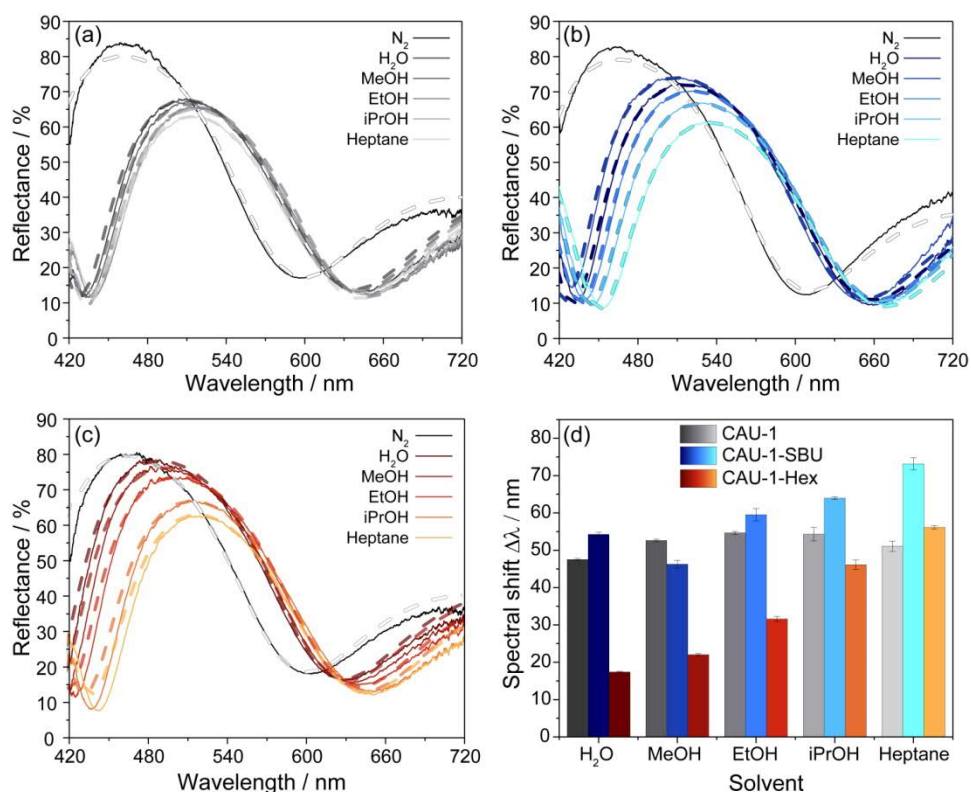
Figure 4.1.4: Reflectance spectra of the BS (a) CAU-1 (shades of grey), (b) CAU-1-SBU (shades of blue) and (c) CAU-1-Hex (shades of red to yellow) upon water, methanol, ethanol, iso-propanol and heptane vapor exposure; (d) summarized spectral shifts of the BSs investigated. The dashed lines represent the modelled reflectance spectra.

To gain further insights into the origin of the observed optical changes for the three BSs upon solvent adsorption, we have carried out calculations of the reflectance spectra using a Matlab code[32] based on the transfer matrix method (details in the experimental section, Chapter 4.1.2). For our model, we estimated the layer thicknesses from the SEM measurements and the RIs of the unloaded MOF layers from spectroscopic ellipsometry measurements (Table S4.1.3). All spectra were modeled with constant layer thicknesses and provide evidence that no pronounced swelling upon analyte adsorption occurs. The RIs of the layers for all calculations are provided in Table S4.1.4. The modeled spectra are depicted in Figure 4.1.4 (a-c) as dashed lines in the color shades corresponding to the experimental spectra and show excellent agreement with the measured spectra. The different analytes have clearly different impacts on the RIs of the CAU-1 layers. The larger changes of the (non-)modified CAU-1 layers compared to the TiO_2 layers upon adsorbing different analytes is also reflected by the larger changes seen for the blue stopband edge, which mainly corresponds to changes in the low RI material, CAU-1. While CAU-1 exhibits similar intermediate changes in the effective RI (Δn_{eff} = 0.185_{Water} − $0.210_{EtOH/iPrOH/Heptane}$), the changes modeled for CAU-1-SBU (Δn_{eff} = 0.140_{MeOH} − $0.255_{Heptane}$) and CAU-1-Hex (Δn_{eff} = 0.080_{Water} − $0.220_{Heptane}$) extend over a broader range. In all samples the differences of the RIs are in line with the observed spectral shifts. The large RI differences in CAU-1-SBU and -Hex confirm the enhanced discrimination capacity of the modified samples. In contrast to the MOF layers, the RI

changes for TiO$_2$ (Δn_{eff} = 0.090$_{Heptane}$ – 0.105$_{Water}$ (CAU-1-SBU); 0.060$_{Heptane}$ – 0.100$_{EtOH}$ (CAU-1); 0.060$_{Heptane}$ – 0.100$_{EtOH}$ (CAU-1-Hex)) are overall smaller and more similar for all three BSs as also indicated by the barely visible red stopband shift in the reflectance spectra. These observations underline that the CAU-1 layers primarily act as the active layer materials and are mainly responsible for the discrimination of the analytes.

Even though for the BS made of pristine CAU-1 the spectra do not provide sufficiently distinct optical shifts for unequivocal analyte assignment, the vapour response kinetics is another key observable that may allow the differentiation of water, the alcohols and heptane. To study the vapour response kinetics, we monitored the reflectance intensity changes at 460 nm of all samples. At this wavelength, the samples undergo the largest intensity drop due to the stopband shifts upon vapor exposure, and, at the same time, this wavelength range is characteristic for the blue band edge of the PBG and represents the changes of the (modified) CAU-1 layers, as mentioned above. From these kinetic plots, the response times, defined as the time needed to reach 90% of the signal change according to IUPAC, were extracted for all analytes. The results of the time-dependent reflectance spectra (Figure S4.1.12 to Figure S4.1.14) are summarized in Figure 4.1.5. For water exposure, the response times seem to correlate with the amount of water adsorbed: while CAU-1-SBU shows the longest response time of over 60 seconds, the hydrophobic CAU-1-Hex responds within 13 seconds. As water is the smallest molecule of the solvents investigated we assume that the prolonged uptake times for CAU-1-SBU and CAU-1 are linked to stronger interactions between the polar solvent water and the framework. Interestingly, the response times for methanol drop to 18 seconds for CAU-1-SBU and CAU-1, while CAU-1-Hex shows only a slightly increased response time of 14 seconds, comparable to that of water. With the exception of ethanol in CAU-1-Hex, the response times for the alcohols increase with the size of the alcohol in all samples, suggesting slower diffusion times within the BSs as the size of the alcohol increases. The most striking behavior is observed for n-heptane that readily saturates within a few seconds independent of the sample investigated, which points to relatively weaker van-der-Waals interactions between the framework and n-heptane suggesting that analyte size plays only a secondary role in the adsorption process. All in all, the longer uptake times observed in the hydrophilic samples CAU-1 and CAU-1-SBU suggest that interactions by hydrogen bonding are the determining factor during adsorption. Although host–guest interactions and, thus, diffusion processes in such multi-modal pore systems having numerous interfaces are complex to describe, the additional information gathered from the wavelength dependent reflectance vs. time measurements opens up additional possibilities to distinguish between different analytes. Comparable MOF-based PCs in the literature were reported to show similar uptake times ranging from a few seconds to approximately a minute.[26,28]
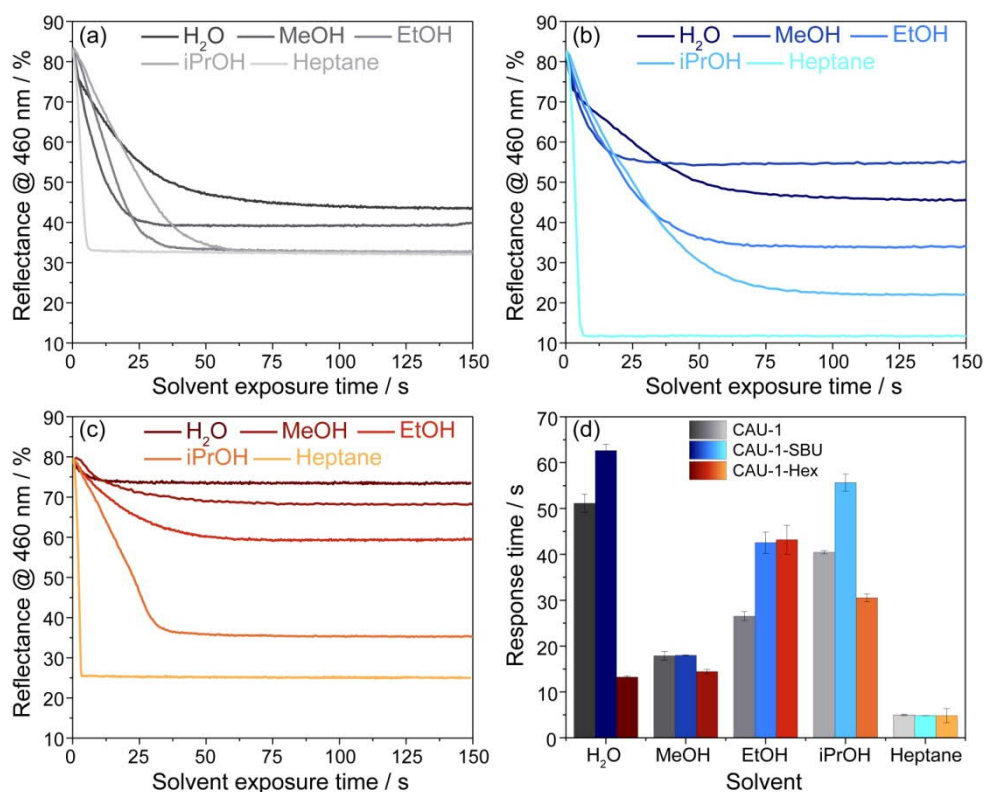
Figure 4.1.5: Reflectance@460 nm vs. time-plots of (a) CAU-1, (b) CAU-1-SBU and (c) CAU-1-Hex upon solvent vapor exposure (blue, grey and red-yellow scales); (d) response times (90% of saturation) of CAU-1, CAU-1-SBU and CAU-1-Hex to water, methanol, ethanol, iso-propanol and heptane.

In addition to spectroscopic evaluation by means of spectral shifts, color image analysis combined with statistical data evaluation, provides another approach to discriminate between analytes, as already pointed out in the literature.[19,28] This method avoids the necessity of spectroscopic instrumentation and, in principle, only requires a camera for image analysis. In our case, the photographic images were recorded simultaneously to spectra acquisition using an alternate stream of nitrogen and solvent vapor. The images were processed by alignment, area selection and red, green and blue (RGB) value extraction. The reversibility in the respective RGB intensities during nitrogen and analyte exposure proves the reproducibility of the measurements (Figure S4.1.15). For data interpretation, principal component analysis (PCA) based on the characteristic differences between the RGB values (Table S4.1.5 to Table S4.1.7) of the stacks during nitrogen exposure and upon vapor saturation was performed. This statistical method allows to express a set of observables (solvents) depending on correlated variables (ΔRGB values) by a reduced set of orthogonal, principal components. For experimental and calculation details, see Chapter 4.1.2.

The score plots for the BSs CAU-1-SBU, CAU-1 and CAU-1-Hex obtained from the PCA are depicted in Figure 4.1.6 (a-c). The 2D projections of the factor scores illustrate the discrimination capability of these BSs based on the principal components F1 and F2. Considering both components F1 + F2, 98.25% (CAU-1-SBU), 99.66% (CAU-1) and 99.21% (CAU-1-Hex) of the variance is taken into account. In case of the pristine and SBU-modified BS, a poor discrimination capability for methanol and ethanol is

observed as indicated by the clustering and overlap of the respective factor scores. For CAU-1-Hex, however, all solvents investigated are readily distinguishable. Although CAU-1-Hex already shows satisfactorily different values for guest molecule recognition, a combination of all three photonic crystal sensors into an array improves the distinction capability even further with all scores being clearly separated from each other (Figure 4.1.6 (d)). Here, the components F1 and F2 account for 89.46% of the variance, which proves to be sufficient for analyte assignment.
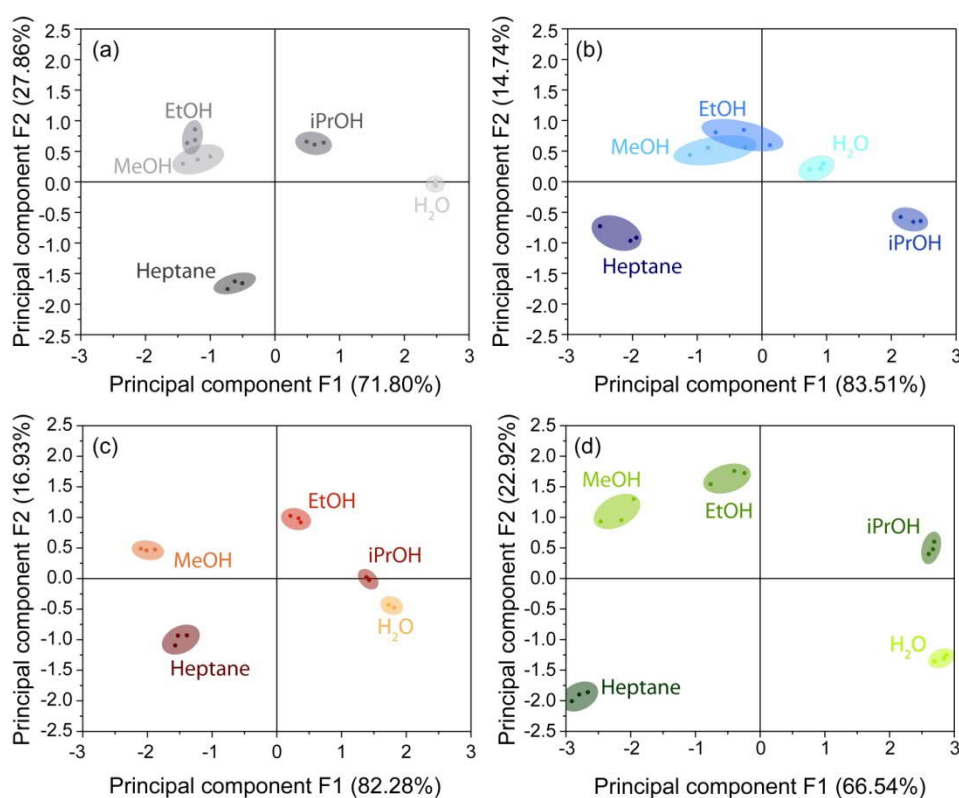
Figure 4.1.6: PCA score plots for (a) CAU-1, (b) CAU-1-SBU and (c) CAU-1-Hex visualizing the discrimination capability of the BSs towards the solvent vapors of water, methanol, ethanol, iso-propanol and heptane; (d) PCA plot for a combined array of the pristine and modified BSs. Different color scales are used for clarity. The percentages of variance of the principal components F1 and F2 are given in brackets.

4.1.4   CONCLUSIONS

We have demonstrated a generic post-assembly modification strategy for MOF-based photonic crystal vapor sensors that can be used to fine-tune the selectivity and sensitivity of the active MOF layers. Importantly, since post-synthetic modification is performed in a one-step process on the as-assembled PC sensor, the need for multi-step modification procedures and time-consuming adjustments of both MOF nanoparticle synthesis and Bragg stack fabrication was avoided. The sorption properties and host–guest interactions between the CAU-1 framework and volatile analytes were varied by either changing the coordination environment of the metal-oxo SBU or by amide-formation at the linker, translating into significant changes in the optical response of the photonic crystal sensor to the analytes.

Repeated exposure to the solvent vapors did not affect reproducibility, thus demonstrating the stability and reusability of the photonic crystal sensor. In addition, we have shown that the time-resolved change in the reflectance intensity can be used as another suitable descriptor for analyte discrimination, even if the optical shifts for two analytes are very similar. Furthermore, color image evaluation by principal component analysis was used as an additional route to classify the altered optical response of the photonic crystal based sensors. All in all, we have shown that combining the distinct sorption behavior of different CAU-1 modifications with the use of complementary signal detection routes – wavelength-shift of the Bragg peak, time-dependent monitoring of the reflectance intensity, and color image analysis – greatly facilitates analyte discrimination. In summary, our study demonstrates that a generic post-assembly modification strategy under mild conditions can be used as a facile, yet powerful tool to fine-tune the selectivity and sensitivity of MOF-based photonic sensing platforms.

4.1.5   ACKNOWLEDGMENTS

4.1.6   REFERENCES

1   J. R. Long and O. M. Yaghi, Chem. Soc. Rev. 2009, 38, 1213-1214.

2   H. Furukawa, K. E. Cordova, M. O'Keeffe and O. M. Yaghi, Science 2013, 341.

3   Y. Cui, B. Li, H. He, W. Zhou, B. Chen and G. Qian, Acc. Chem. Res. 2016, 49, 483-493.

4   K. K. Tanabe and S. M. Cohen, Chem. Soc. Rev. 2011, 40, 498-519.

5   O. Karagiaridi, W. Bury, J. E. Mondloch, J. T. Hupp and O. K. Farha, Angew. Chem. Int. Ed. 2014, 53, 4530-4540.

6   C.-H. Lee, H.-Y. Huang, J.-J. Lee, C.-Y. Huang, Y.-C. Kao, G.-H. Lee, S.-M. Peng, J.-C. Jiang, I. Chao and K.-L. Lu, ChemistrySelect 2016, 1, 2923-2929.

7   J. Lee, O. K. Farha, J. Roberts, K. A. Scheidt, S. T. Nguyen and J. T. Hupp, Chem. Soc. Rev. 2009, 38, 1450-1459.

8   J.-R. Li, R. J. Kuppler and H.-C. Zhou, Chem. Soc. Rev. 2009, 38, 1477-1504.

9   A. Morozan and F. Jaouen, Energy Environ. Sci. 2012, 5, 9269-9290.

10   L. E. Kreno, K. Leong, O. K. Farha, M. Allendorf, R. P. Van Duyne and J. T. Hupp, Chem. Rev. (Washington, DC, U. S.) 2012, 112, 1105-1125.

11   R. M. Abdelhameed, M. M. Q. Simões, A. M. S. Silva and J. Rocha, Chem. Eur. J. 2015, 21, 11072-11081.

12   Y.-Z. Zhang, T. Cheng, Y. Wang, W.-Y. Lai, H. Pang and W. Huang, Adv. Mater. 2016, 28, 5242-5248.

13   S. Jung and S. Park, ACS Catal. 2017, 7, 438-442.

14   W. P. Lustig, S. Mukherjee, N. D. Rudd, A. V. Desai, J. Li and S. K. Ghosh, Chem. Soc. Rev. 2017, 46, 3242-3285.

15   Z.-Z. Lu, R. Zhang, Y.-Z. Li, Z.-J. Guo and H.-G. Zheng, J. Am. Chem. Soc. 2011, 133, 4172-4174.

16   Z. Hu, B. J. Deibert and J. Li, Chem. Soc. Rev. 2014, 43, 5815-5840.

17   J.-M. Yang, Q. Liu and W.-Y. Sun, J. Solid State Chem. 2014, 218, 50-55.

18   J. D. Joannopoulos, S. G. Johnson, J. N. Winn and R. D. Meade, Photonic Crystals: Molding the Flow of Light (Second Edition), Princeton University Press, 2011.

19   L. D. Bonifacio, G. A. Ozin and A. C. Arsenault, Small 2011, 7, 3153-3157.

20   G. Lu and J. T. Hupp, J. Am. Chem. Soc. 2010, 132, 7832-7833.

21   C. Cui, Y. Liu, H. Xu, S. Li, W. Zhang, P. Cui and F. Huo, Small 2014, 10, 3672-3676.

22   G. Lu, O. K. Farha, L. E. Kreno, P. M. Schoenecker, K. S. Walton, R. P. Van Duyne and J. T. Hupp, Adv. Mater. 2011, 23, 4449-4452.

23   Y.-n. Wu, F. Li, Y. Xu, W. Zhu, C.-a. Tao, J. Cui and G. Li, Chem. Commun. (Cambridge, U. K.) 2011, 47, 10094-10096.

24   Y.-n. Wu, F. Li, W. Zhu, J. Cui, C.-a. Tao, C. Lin, P. M. Hannam and G. Li, Angew. Chem. Int. Ed. 2011, 50, 12518-12522.

25   J. Cui, N. Gao, C. Wang, W. Zhu, J. Li, H. Wang, P. Seidel, B. J. Ravoo and G. Li, Nanoscale 2014, 6, 11995-12001.

26   L. Li, X. Jiao, D. Chen, B. V. Lotsch and C. Li, Chem. Mater. 2015, 27, 7601-7609.

27   F. M. Hinterholzinger, A. Ranft, J. M. Feckl, B. Ruhle, T. Bein and B. V. Lotsch, J. Mater. Chem. 2012, 22, 10356-10362.

28   A. Ranft, F. Niekiel, I. Pavlichenko, N. Stock and B. V. Lotsch, Chem. Mater. 2015, 27, 1961-1970.

29   Z. Hu, C.-a. Tao, F. Wang, X. Zou and J. Wang, J. Mater. Chem. C 2015, 3, 211-216.

30   T. Ahnfeldt, N. Guillou, D. Gunzelmann, I. Margiolaki, T. Loiseau, G. Férey, J. Senker and N. Stock, Angew. Chem. 2009, 121, 5265-5268.

31   T. Ahnfeldt, D. Gunzelmann, J. Wack, J. Senker and N. Stock, CrystEngComm 2012, 14, 4126-4136.

32   P. Yeh, Optical waves in layered media, Wiley, New York, 1988.

4.1.7   SUPPORTING INFORMATION

Supplementary Figures and Tables
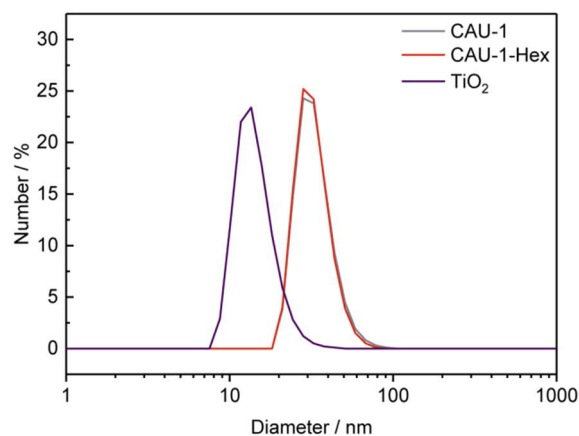
Figure S4.1.1: Size distribution of CAU-1 (0.043, grey), CAU-1-Hex (0.061, red) and TiO_2 (0.176, violet) as measured by dynamic light scattering (DLS). Polydispersity indices are given in the brackets. Note that in CAU-1 the de-methoxylation of the SBUs is only possible on the dried sample.
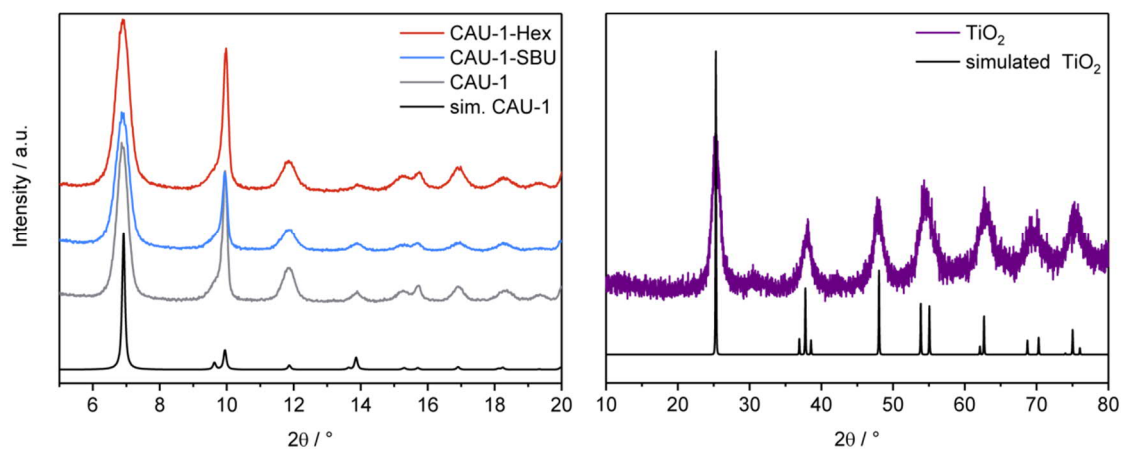
Figure S4.1.2: Powder X-ray diffractograms of (left) simulated CAU-1 (black), as-synthesized CAU-1 (grey), CAU-1-SBU (blue) and CAU-1-Hex (red), and (right) simulated TiO_2 (anatase, black) and as-synthesized TiO_2 (violet).
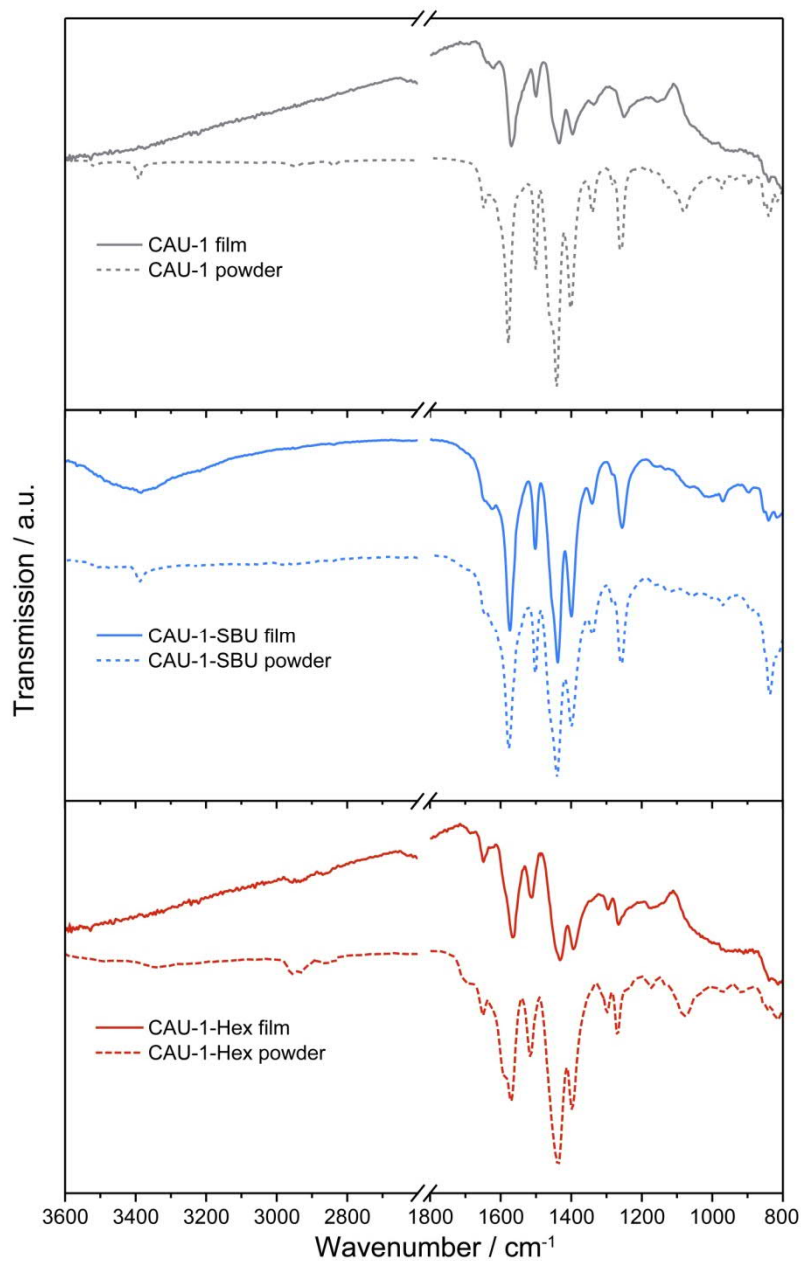
Figure S4.1.3: IR spectra of thin films of CAU-1 (grey), CAU-1-SBU (blue) and CAU-1-Hex (red) layers, dashed lines represent the powdered samples for comparison. Note that for the CAU-1-SBU films, various MOF layers were deposited to improve the signal to noise ratio.
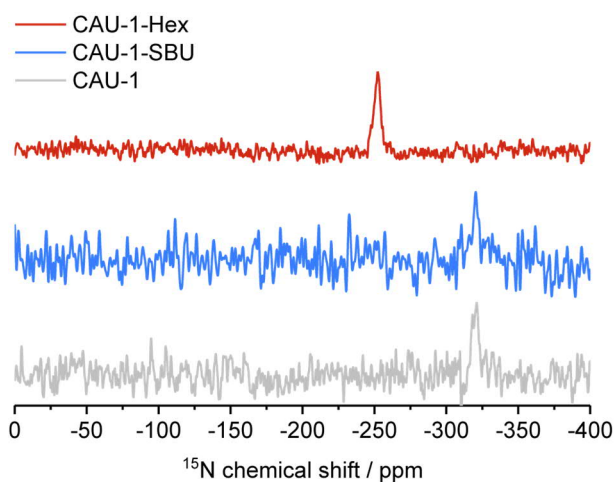
Figure S4.1.4: ^{15}N-CP-ssNMR of CAU-1 (grey), CAU-1-SBU (blue) and CAU-1-Hex (red).
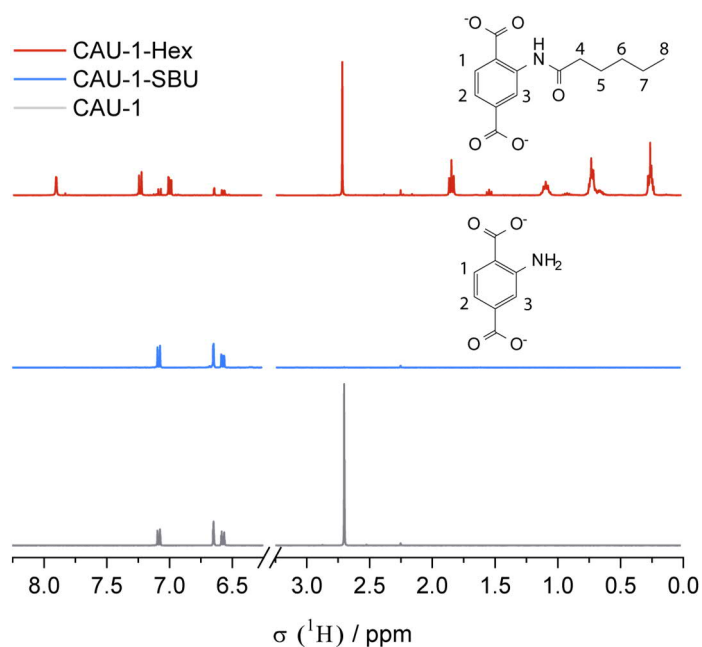
Figure S4.1.5: ^1H-NMR spectra of the directly dissolved CAU-1 (grey), CAU-1-SBU (blue) and CAU-1-Hex (red) powders. Each spectrum is normalized to the sum of aromatic H signals (methylated and unmethylated). All samples were referenced to the ^1H signal of 2H of the unmodified linker.[S2] Labelling of the 1H signals: BDC–NH$_2$: 7.07 (d, 1H, H1, J = 8.1 Hz); 6.64 (s, 1H, H3); 6.56 (d, 1H, H2, J = 8.1 Hz); BDC–NHCOC$_5$H$_{11}$: 7.90 (s, 1H, H3); 7.23 (d, 1H, H1, J = 8.1 Hz); 6.99 (m, 1H, H2); 1.85 (t, 2H, H4, J = 7.4 Hz); 1.09 (m, 2H, H5) 0.73 (m, 4H, H6-7); 0.25 (m, 3H, H8).

To calculate the degree of methoxylation, the integral ratios of the methoxy H-atoms: aromatic H-atoms were determined to be 1.13 for CAU-1, 0.01 for CAU-1-SBU and 1.09 for CAU-1-Hex (1:33 calc.), yielding a methoxylation degree of 85%, 1% and 82%, respectively. For CAU-1 and CAU-1-Hex the obtained degrees are in accordance with those reported in the literature.[S2] The degree of amidification was determined by the ratio of the aromatic H-atoms of the modified linker (1.00) to the total amount of aromatic H-atoms (1.19) yielding a modification degree of 84%. All samples show 1% methylation of the amine similar to those reported in the literature.[S2]

Table S4.1.1: Elemental analysis of the nanoparticle powders CAU-1-SBU, CAU-1 and CAU-1-Hex with the corresponding experimental formula and composition based on the carbon to nitrogen ratio. Crystal water and absorbed carbon dioxide are neglected.

	CAU-1-SBU	CAU-1	CAU-1-Hex
Theoretical formula	$[Al_4(OH)_6-(H_2N-C_6H_3(COO)_2)_3]$	$[Al_4(OH)_2-(OCH_3)_4(H_2N-C_6H_3(COO)_2)_3]$	$[Al_4(OH)_2-(OCH_3)_4(C_5H_{11}CONH-C_6H_3(COO)_2)_3]$
Theoretical composition	$Al_4C_{24}H_{21}N_3O_{18}$	$Al_4C_{28}H_{29}N_3O_{18}$	$Al_4C_{46}H_{59}N_3O_{21}$
Weight % C:N:H	29.98 : 4.33 : 4.37	38.64 : 4.97 : 3.78	47.09 : 3.75 : 5.37
Molar Ratio C:N:H	24.22 : 3.00 : 42.08	27.20 : 3.00 : 31.71	43.93 : 3 : 59.70
Experimental composition	$Al_4C_{24.22}H_{21.44}N_3O_{18}$	$Al_4C_{27.2}H_{27.4}N_3O_{18}$	$Al_4C_{43.93}H_{59}N_3O_{21}$
Degree of modification EA	96.3%	-	88.5%
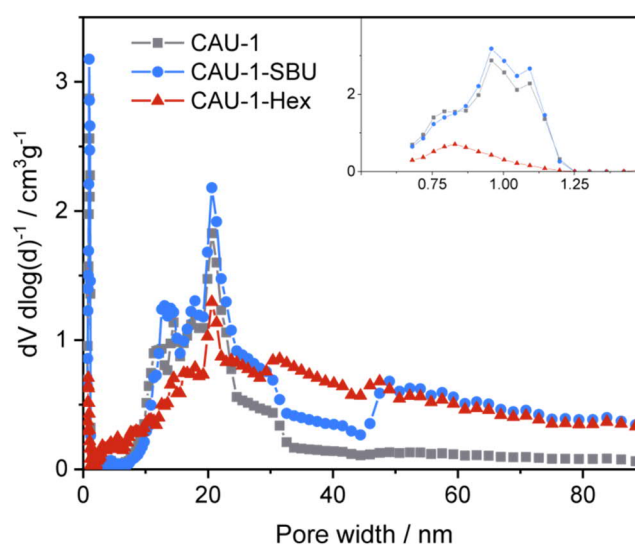
Figure S4.1.6: Pore size distributions of CAU-1 (grey), CAU-1-SBU (blue) and CAU-1-Hex (red). Fitting errors were 0.335%, 0.382% and 0.423%. Calculation details are given in Chapter 4.1.2.

Figure S4.1.7: Contact angle measurements of different (a) CAU-1, (b) CAU-1-SBU and (c) CAU-1-Hex.
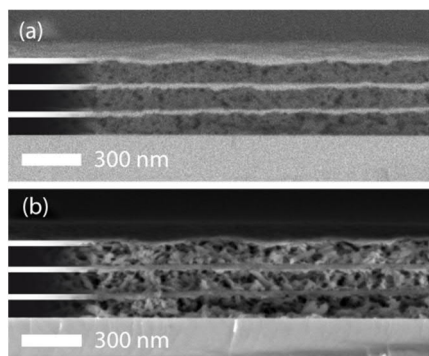
Figure S4.1.8: Cross-sectional SEM images of CAU-1-SBU on a silicon substrate acquired with a (a) back-scattered electron detector and (b) In-Lense detector with MOF layers of 117±9 nm and TiO2 layers of 30±6 nm. The MOF layers are highlighted in black, the TiO_2 in white.
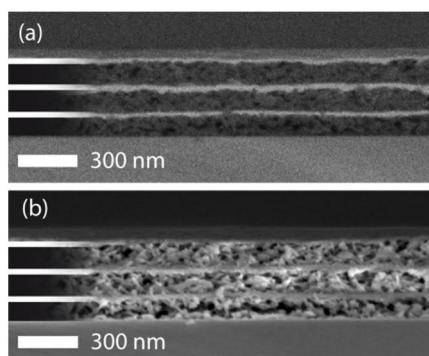
Figure S4.1.9: Cross-sectional SEM images of CAU-1-Hex on a silicon substrate acquired with a (a) back-scattered electron detector and (b) In-Lense detector with MOF layers of 112±8 nm and TiO_2 layers of 30±7 nm. The MOF layers are highlighted in black, the TiO_2 in white.
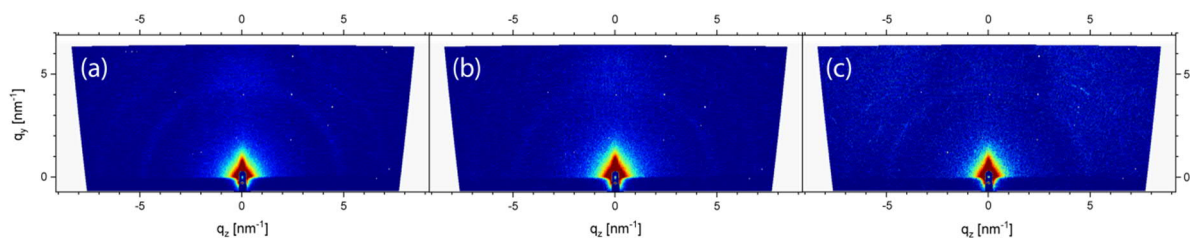
Figure S4.1.10: GISAXS measurements of the BSs (a) CAU-1-SBU, (b) CAU-1 and (c) CAU-1-Hex. Note the semicircle at 4.9 nm^{-1} corresponding to the 2θ reflection at 6.9° of the MOF.
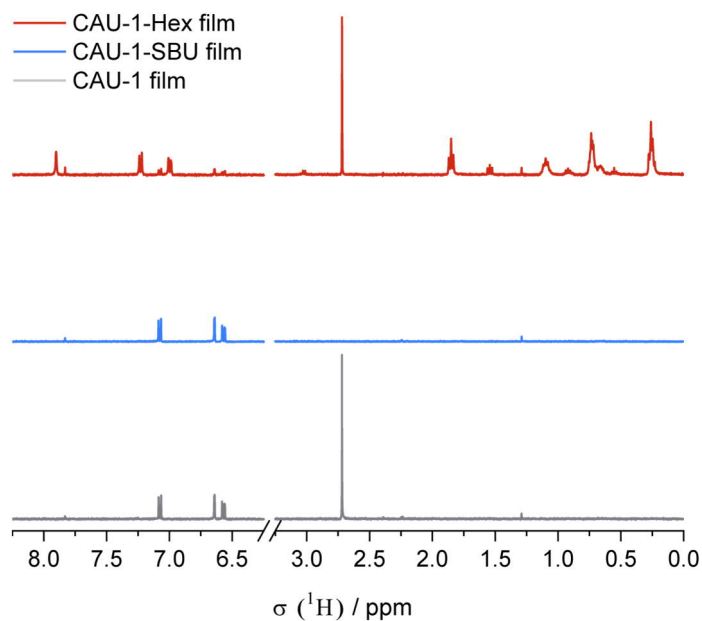
Figure S4.1.11: ^{1}H-NMR spectra of the directly dissolved CAU-1 (grey), CAU-1-SBU (blue) and CAU-1-Hex (red) films. Each spectrum is normalized to the sum of aromatic H signals (methylated and unmethylated). All samples were referenced to the ^{1}H signal of 2H of the unmodified linker.[S2]

The degree of methoxylation was calculated as explained above. The methoxy H-atoms: aromatic H-atoms were determined to be 1.13 for CAU-1, 0.00 for CAU-1-SBU and 1.10 for CAU-1-Hex (1:33 calc.), yielding a methoxylation degree of 85%, 0% and 83%, respectively. The degree of amidification was determined by the ratio of the aromatic H-atoms of the modified linker (1.00) to the total amount of aromatic H-atoms (1.13) yielding a modification degree of 88%. All samples show 1% methylation.

Table S4.1.2: Refractive indices and polarities at 25 °C of the investigated solvents.

	Methanol	Water	Ethanol	iso-Propanol	Heptane
n	1.327	1.333	1.361	1.378	1.389
E_T^N	0.762	1.000	0.654	0.546	0.012
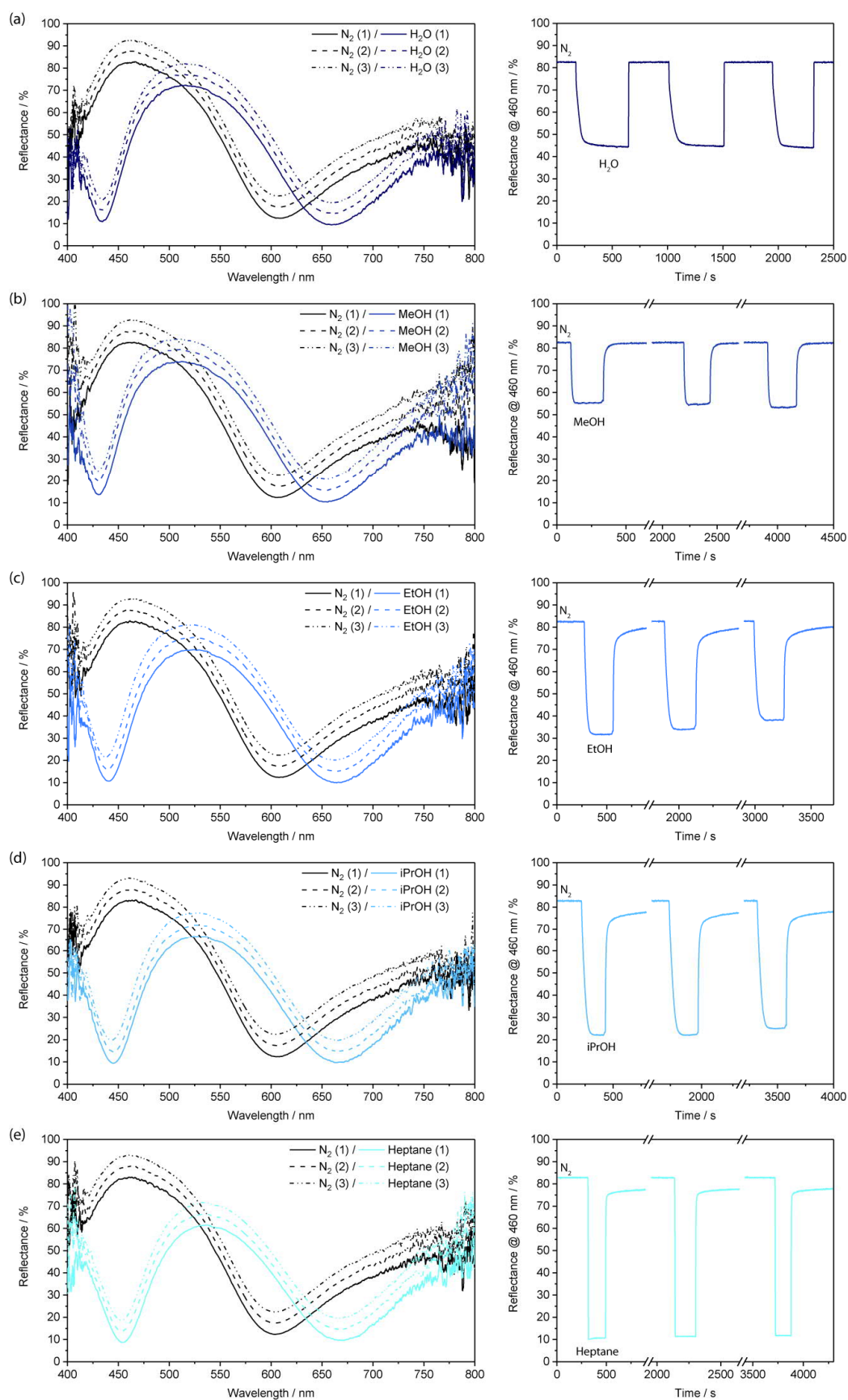
Figure S4.1.12: Reflectance spectra (left) and time-dependent reflectance at 460 nm (right) of the Bragg stack CAU-1-SBU exposed to alternating streams of nitrogen and (a) water, (b) methanol, (c) ethanol, (d) iso-propanol and (e) hexane vapor. The lined, dashed and dotted lines represent the first, second and third acquired spectra.
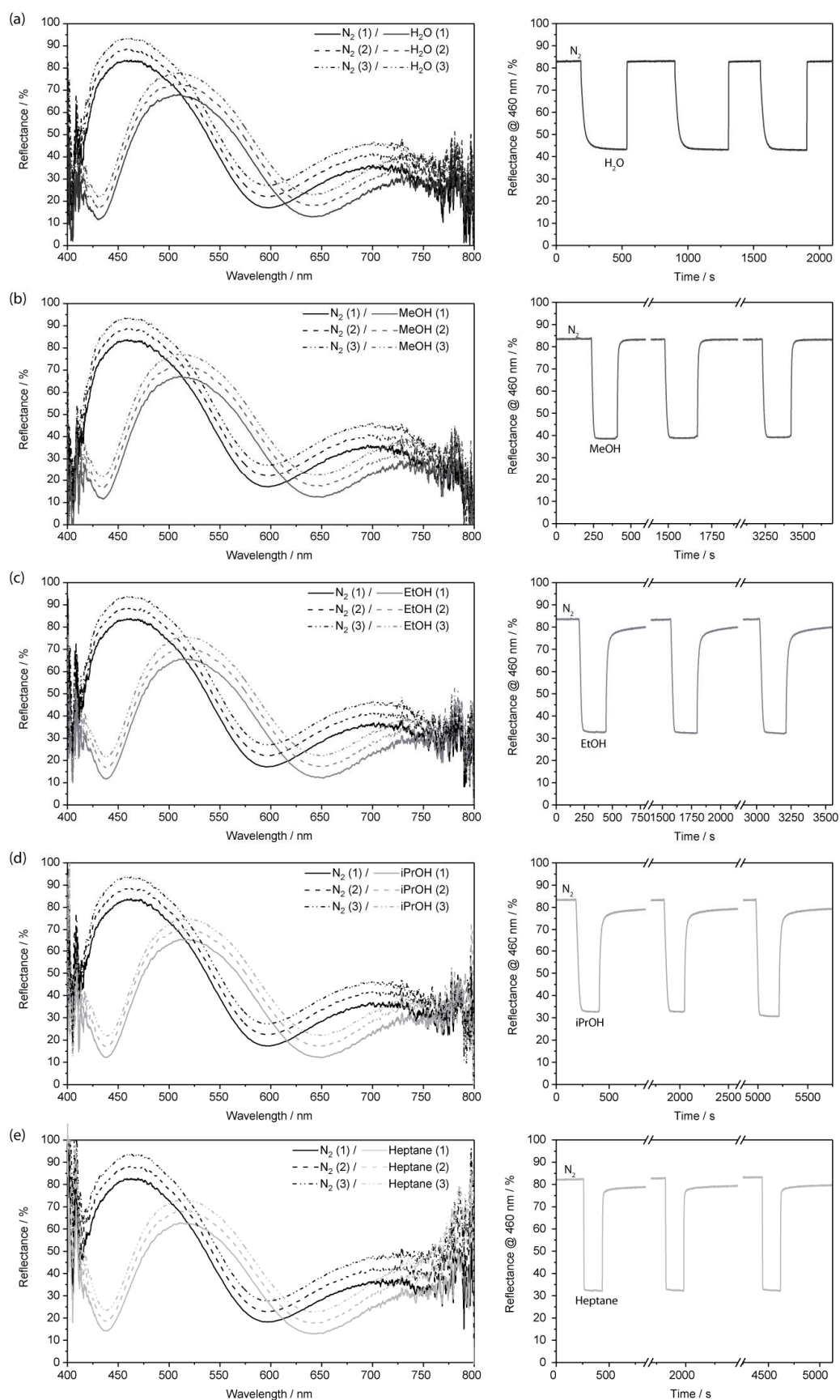
Figure S4.1.13: Reflectance spectra (left) and time-dependent reflectance at 460 nm (right) of the Bragg stack CAU-1 exposed to alternating streams of nitrogen and (a) water, (b) methanol, (c) ethanol, (d) iso-propanol and (e) hexane vapor. The lined, dashed and dotted lines represent the first, second and third acquired spectra.
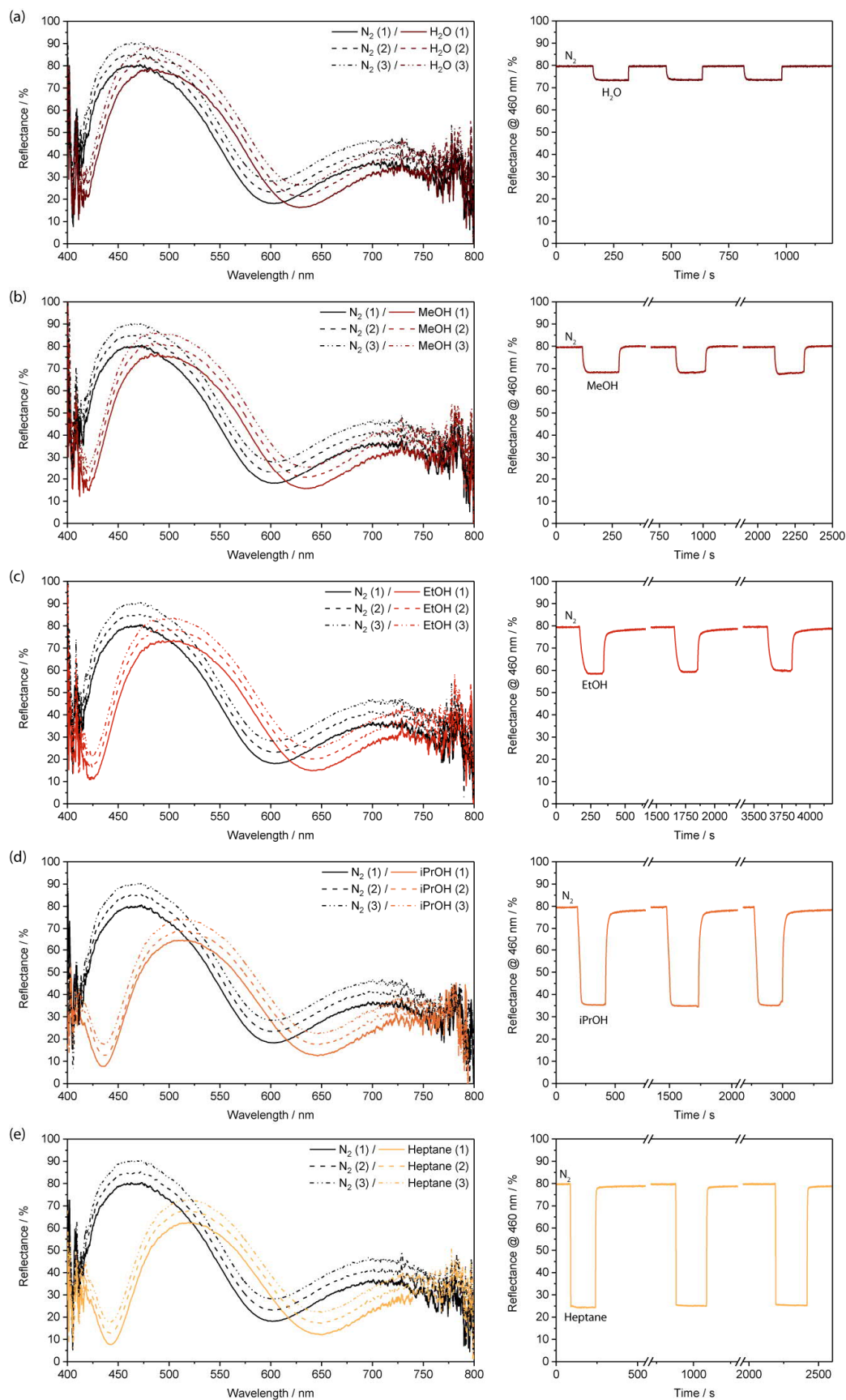
Figure S4.1.14: Reflectance spectra (left) and time-dependent reflectance at 460 nm (right) of the Bragg stack CAU-1-Hex exposed to alternating streams of nitrogen and (a) water, (b) methanol, (c) ethanol, (d) iso-propanol and (e) hexane vapor. The lined, dashed and dotted lines represent the first, second and third acquired spectra.

Table S4.1.3: Layer thicknesses and RIs obtained from spectroscopic ellipsometry.

	CAU-1-SBU	CAU-1	CAU-1-Hex
d / nm	144	148	133
n_{eff}	1.388	1.362	1.350

Table S4.1.4: Modelled thicknesses and effective refractive indices of the constituent layers of the BSs. Note that the TiO_2 layer of CAU-1-SBU is also influenced by the thermal treatment as indicated by the higher RI in comparison to the other samples. Nonetheless, the discrimination capacity is still determined by the MOF layer.

	CAU-1-SBU		CAU-1		CAU-1-Hex	
	MOF	TiO_2	MOF	TiO_2	MOF	TiO_2
Thickness / nm	130	38	125	37	130	35
n_{eff} (N_2)	1.340	1.740	1.370	1.730	1.370	1.740
n_{eff} (H_2O)	1.510	1.845	1.555	1.810	1.450	1.820
n_{eff} (MeOH)	1.480	1.840	1.570	1.820	1.470	1.820
n_{eff} (EtOH)	1.530	1.850	1.580	1.830	1.500	1.840
n_{eff} (iPrOH)	1.560	1.850	1.580	1.820	1.555	1.820
n_{eff} (Heptane)	1.595	1.830	1.580	1.790	1.590	1.800
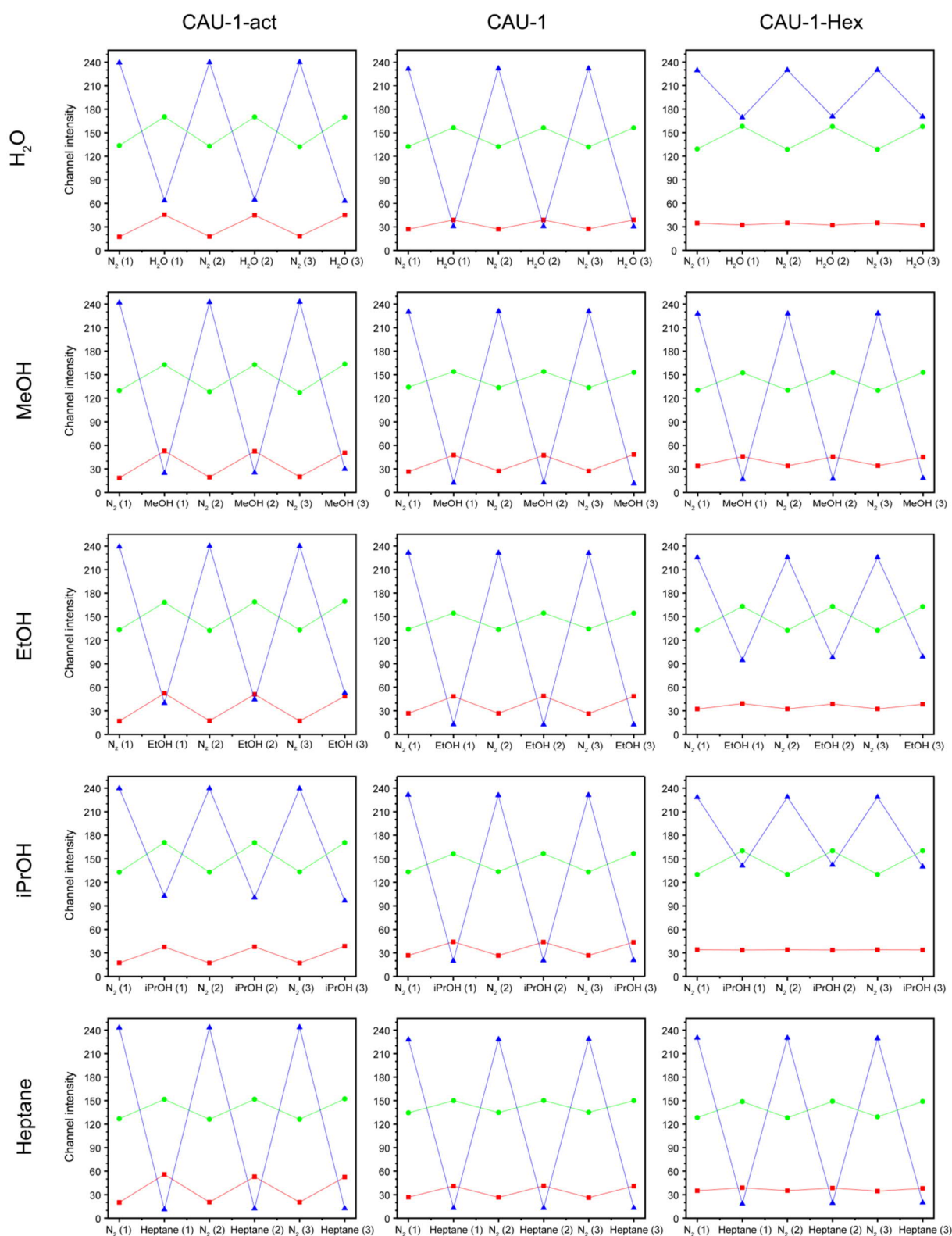
Figure S4.1.15: Intensity evolution of the R, G and B channel of photographic images for CAU-1-act, CAU-1 and CAU-1-Hex alternately exposed to nitrogen and the solvent vapors of water, methanol, ethanol, iso-propanol and heptane. The photographic images were acquired simultaneously to the reflectance spectra and processed to extract the mean values for the R, G and B channels.

Table S4.1.5: Intensities of the G channel and calculated ΔG values for CAU-1-act, CAU-1 and CAU-1-Hex extracted from the photographic images upon nitrogen and solvent vapor (water, methanol, ethanol, iso-propanol and heptane) exposure.

		Red Channel								
		CAU-1-act			CAU-1			CAU-1-Hex		
Sorptive	No.	N2	Sorptive	Δ	N2	Sorptive	Δ	N2	Sorptive	Δ
H$_2$O	1	17.29	45.43	27.56	27.12	38.81	11.59	34.62	32.19	-2.78
	2	17.65	44.97		27.2	38.79		34.9	31.94	
	3	17.96	45.17		27.41	38.89		34.91	31.97	
	σ	0.33	0.23	0.50	0.15	0.05	0.10	0.16	0.14	0.30
MeOH	1	18.49	52.73	32.63	26.49	47.49	20.74	33.84	45.68	11.36
	2	19.35	52.47		27.19	47.3		34.01	45.38	
	3	19.89	50.40		27.19	48.32		34.06	44.94	
	σ	0.70	1.28	1.91	0.40	0.54	0.55	0.11	0.37	0.48
EtOH	1	16.94	52.43	33.59	26.73	48.41	21.99	32.31	39.25	6.43
	2	17.39	51.09		26.75	48.83		32.44	38.78	
	3	17.1	48.69		26.31	48.53		32.48	38.47	
	σ	0.23	1.90	1.95	0.25	0.22	0.28	0.09	0.39	0.48
iPrOH	1	17.42	37.62	20.75	26.87	44.11	17.03	34.2	33.55	-0.52
	2	17.26	37.83		26.7	43.87		34.13	33.58	
	3	17.16	38.63		26.87	43.56		34.08	33.74	
	σ	0.13	0.54	0.65	0.10	0.27	0.3	0.59	0.10	0.16
Heptane	1	20.11	55.89	33.47	26.81	41.13	14.64	34.98	38.91	3.64
	2	20.48	52.96		26.56	41.34		35.16	38.55	
	3	20.45	52.6		26.27	41.07		34.53	38.12	
	σ	0.21	1.81	2.01	0.27	0.14	0.27	0.32	0.40	0.28

Table S4.1.6: Intensities of the R channel and calculated ΔR values for CAU-1-act, CAU-1 and CAU-1-Hex extracted from the photographic images upon nitrogen and solvent vapor (water, methanol, ethanol, iso-propanol and heptane) exposure.

		Green Channel								
		CAU-1-act			CAU-1			CAU-1-Hex		
Sorptive	No.	N2	Sorptive	Δ	N2	Sorptive	Δ	N2	Sorptive	Δ
H$_2$O	1	133.67	170.39	37.31	132.45	156.48	24.18	129.15	158.11	29.1
	2	132.89	170.25		132.3	156.4		128.67	157.83	
	3	132.15	170.01		131.91	156.33		128.65	157.83	
	σ	0.76	0.19	0.57	0.28	0.08	0.12	0.28	0.16	0.12
MeOH	1	129.77	162.83	34.65	134.31	153.99	19.79	130.34	152.49	22.52
	2	128.4	162.89		133.65	154.05		130.24	152.65	
	3	127.37	163.75		133.66	152.94		129.96	152.96	
	σ	1.21	0.51	1.66	0.38	0.63	0.57	0.19	0.24	0.43
EtOH	1	133.45	168.3	35.90	133.96	154.5	20.52	132.95	162.98	30.18
	2	132.47	168.84		133.55	154.56		132.54	162.86	
	3	133.04	169.54		134.39	154.42		132.47	162.67	
	σ	0.49	0.62	0.91	0.42	0.07	0.49	0.26	0.16	0.14
iPrOH	1	132.77	170.67	37.59	133.1	156.41	23.37	129.94	160.06	30.12
	2	132.91	170.45		133.5	156.69		130.02	160.12	
	3	133.19	170.52		133.06	156.67		130.02	160.17	
	σ	0.22	0.11	0.29	0.24	0.16	0.22	0.05	0.05	0.02
Heptane	1	126.92	151.7	25.49	134.54	150.09	15.27	128.45	148.81	20.29
	2	126.21	151.8		134.86	150.25		128.2	149.12	
	3	126.2	152.3		135.16	150.03		129.38	148.99	
	σ	0.41	0.32	0.67	0.31	0.12	0.36	0.62	0.15	0.66

Table S4.1.7: Intensities of the B channel and calculated ΔB values for CAU-1-act, CAU-1 and CAU-1-Hex extracted from the photographic images upon nitrogen and solvent vapor (water, methanol, ethanol, iso-propanol and heptane) exposure.

		Blue Channel								
		CAU-1-act			CAU-1			CAU-1-Hex		
Sorptive	No.	N2	Sorptive	Δ	N2	Sorptive	Δ	N2	Sorptive	Δ
H_2O	1	239.38	63.57	-175.95	231.4	30.69	-201.15	229.33	169.32	-59.55
	2	239.68	64.56		231.83	30.67		229.65	170.5	
	3	240.00	63.08		231.93	30.35		229.85	170.36	
	σ	0.31	0.75	0.91	0.39	0.40	0.78	0.26	0.65	0.44
MeOH	1	241.77	24.75	-215.74	230.27	12.26	-218.61	227.63	16.73	-210.49
	2	242.38	25.16		230.84	12.52		227.84	17.23	
	3	242.84	29.86		230.9	11.39		228.15	18.19	
	σ	0.54	2.84	2.39	0.34	0.59	0.79	0.26	0.74	0.48
EtOH	1	239.29	39.88	-194.08	231.37	12.73	-218.57	225.29	94.52	-128.3
	2	240.13	44.42		231.1	12.38		225.55	97.91	
	3	239.98	52.87		230.86	12.48		225.51	99.02	
	σ	0.45	6.59	6.31	0.25	0.18	0.18	0.14	2.35	2.22
iPrOH	1	239.72	102.48	-139.74	231.41	19.74	-210.77	228.4	141.16	-87.43
	2	239.64	100.55		230.81	20.43		228.63	142.28	
	3	239.48	96.58		231.12	20.85		228.6	139.89	
	σ	0.12	3.01	2.88	0.30	0.56	0.78	0.13	1.19	1.19
Heptane	1	243.13	11.19	-231.33	227.92	12.97	-215.25	230.11	18.55	-210.58
	2	243.31	12.36		228.26	13.05		230.05	19.44	
	3	243.63	12.53		228.7	13.12		229.48	19.91	
	σ	0.25	0.73	0.54	0.39	0.08	0.32	0.35	0.69	1.00

Supplemental References

S1   A. Ranft, F. Niekiel, I. Pavlichenko, N. Stock and B. V. Lotsch, Chem. Mater. 2015, 27, 1961-1970.

S2   T. Ahnfeldt, D. Gunzelmann, J. Wack, J. Senker and N. Stock, CrystEngComm 2012, 14, 4126-4136.

5 POST-SYNTHETICALLY MODIFIED MOFS FOR SORPTION APPLICATIONS

The intrinsic micro- and mesoporosity of MOFs render them ideal materials for the adsorption of gases and small molecules. The vast combination possibilities of SBUs and linker geometries yields a plethora of pore geometries of distinct sizes, shapes and properties. In principle, this structural diversity allows for the specific and selective adsorption of guest molecules. In addition, post-synthetic modification of the framework enables the fine-tuning of the pore characteristics affecting its size, shape and guest-affinity.

This chapter covers the concept of pore engineering by creating a library of post-synthetically modified CAU-1 nanoparticles. The modifications include changes in the coordination environment of the SBU as well as diverse covalent amidifications of the linker amine-moiety. The particles were structurally characterized and their altered sorption behavior investigated, with a special focus on the impact on carbon dioxide and methane adsorption. Furthermore, selectivities of CO_2 over CH_4 and N_2 at 273 and 288 K were calculated and the framework affinity of these gases assessed by determining the heats of adsorption.

5.1   POST-SYNTHETIC MODIFICATION OF CAU-1 NANOPARTICLES: INFLUENCE ON CO_2/N_2 AND CO_2/CH_4 SELECTIVITY

Alberto von Mankowski, Alejandro Jiménez-Solano, Marie Bayer and Bettina V. Lotsch

unpublished work

Abstract

Anthropogenic carbon dioxide (CO_2) emission is considered a major greenhouse gas source with long lasting impact on the climate. In addition, its presence in combustible hydrocarbon gases, such as natural gas or biogas, lowers their energetic value leading to a fundamental interest in developing materials for selective CO_2 separation and storage. Metal-organic frameworks have evolved as promising materials for this purpose, as they offer permanent porosity with suitable pore sizes for the adsorptive capture of CO_2. Furthermore, the properties of MOFs can be fine-tuned by post-synthetic modifications. In our study, the influence of diverse post-synthetic modifications on CAU-1 nanoparticles and their impact on the sorption properties was investigated. To this end, Ar, CO_2, N_2 and CH_4 adsorption isotherms were measured and the selectivities of CO_2 over N_2 and CH_4 at 273 and 288 K were calculated by the Henry theory and the ideal adsorbed solution theory (IAST). Our results identified the best storage as well as separation capacity for the modification providing free amine groups and polar hydroxy groups in the SBU, whereas increasing hydrophobicity by the introduction of long-chain alkyl groups was counterproductive.
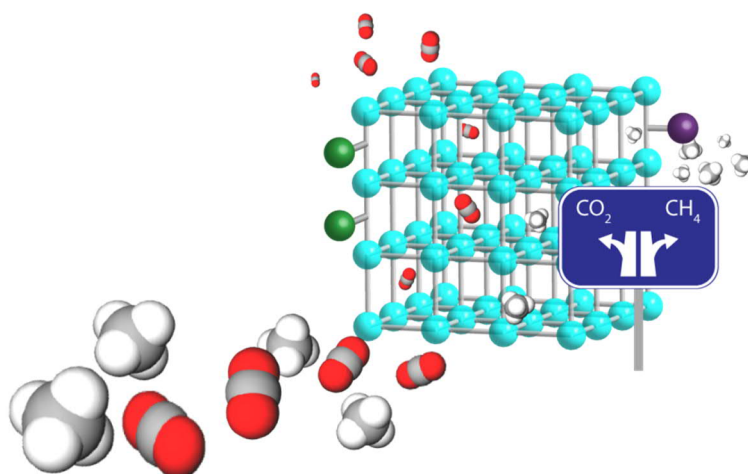

Table of content: Tailoring the sorption propreties of porous MOFs via post-synthetic modification allows to control framework affinities for CO_2 storage and separation purposes.

5.1.1 INTRODUCTION

Within the last 25 years, the chemistry of metal-organic frameworks (MOFs) has experienced a remarkably fast-paced development, attracting the attention of coordination, solid-state and physical chemists and chemical engineers, among many others.[1] MOFs are composed of inorganic clusters, the secondary building units (SBUs), that act as nodes and are linked through organic linkers to assemble into highly crystalline structures with defined nano- to mesoporosity.[2,3] The innumerable structural possibilities that arise from the employable building blocks – both inorganic and organic – allow the design of defined pore shapes, sizes and environments. In addition, further chemical functionality and diversity can be introduced by post-synthetic strategies, e.g. the covalent modification of the linker or change in the coordination environment of the inorganic cluster on the already assembled framework, enabling further fine-tuning of the MOF properties that would not be accessible via direct synthesis.[4-6] Due to the permanent intrinsic porosity in the nanometer regime, MOFs are ideally suited as storage and separation materials for gases and small molecules.[7,8] Possible applications include many industrial relevant processes, such as toxic gas removal, e.g. SO_x, NO_x, NH_3, CO,[9-11] or the storage of energy-related gases, e.g. H_2, C_xH_y.[12-15]

A special interest lies in the selective adsorption of CO_2. In view of the increased anthropogenic emission of this greenhouse gas and its contribution to climate change,[16] sequestration of CO_2 has been proposed as a (transitional) measure to reduce its release into the atmosphere.[17] In addition, CO_2 is a main "contaminant" in natural gas and biogas, where its presence significantly reduces the energetic footprint of these fuel gases.[18] Also, its tendency to form carbonic acid in presence of water can cause corrosion to related pipes and equipment, requiring its removal.[19] On the other hand, concentrated and purified CO_2 can provide a chemical feedstock for conversion into value-added chemicals, like methanol or formate.[20,21] In all cases, the selective and efficient adsorption of CO_2 is desired and required. Numerous reviews have not only highlighted the potential of MOFs for this purpose,[22-25] but also compiled the beneficial chemical and structural features in various MOFs for high CO_2 uptakes. These can be summarized into, 1) coordinatively unsaturated or exposed metal sites to provide Lewis acidity at which the CO_2 molecules can coordinate,[26-28] 2) incorporation of or grafting with primary and secondary amines, due to their nucleophilic nature,[29-31] as well as 3) other strongly polarizing groups, such as carboxy, hydroxy, ketone, sulfoxy groups, which beneficially interact with CO_2 due to its polarizability (quadrupole moment).[32-36]

Although these structural features may lead to high uptakes, the behavior can change substantially in gas mixtures. In fact, this can indeed be desired when it comes to the separation of gases. In this case, it is more complicated to define beneficial structural properties as they will also depend on the separation mechanism. In principle, two can be distinguished, either kinetic or thermodynamic separation.[37,38] For the former, the gas components are separated due to size exclusion by molecular

sieving or different diffusivity at non-equilibrium conditions, whereas in equilibrium separation the affinity of the adsorptives to the framework is decisive for the separation performance. Usually, it can be enhanced by providing strong binding sites for the gas of interest, although, at the same time, this can also lead to strong interactions with water. Hence, the introduction of hydrophobicity has also been proposed as a sensible approach to improve CO_2 adsorption.[39-41]

In this study, we have investigated the influence of various modifications altering the pore sizes and chemical functionality of an amine containing MOF, namely CAU-1, with reportedly favorable properties for CO_2 adsorption.[42] CAU-1 is an aluminium-oxo-methoxy cluster based MOF connected by 2-aminoterephthalates with distorted octahedral pores of 10 Å and smaller tetrahedral pores of 4.5 Å,[43] and, thus, capable of adsorbing the gases of interest CO_2, N_2 and CH_4 with respective kinetic diameters of 3.3, 3.7 and 3.8 Å.[44] We have systematically investigated post-synthetic modifications, which target the aluminum-oxo-methoxy cluster, as well as the amine moiety of the organic linker. The modifications include the replacement of the methoxylates of the inorganic cluster with hydroxy groups, increasing the polarity of the SBU, and the conversion of the amine group of the linker into amides with several acidic anhydrides. A summary of the modifications is presented in Figure 5.1.1.
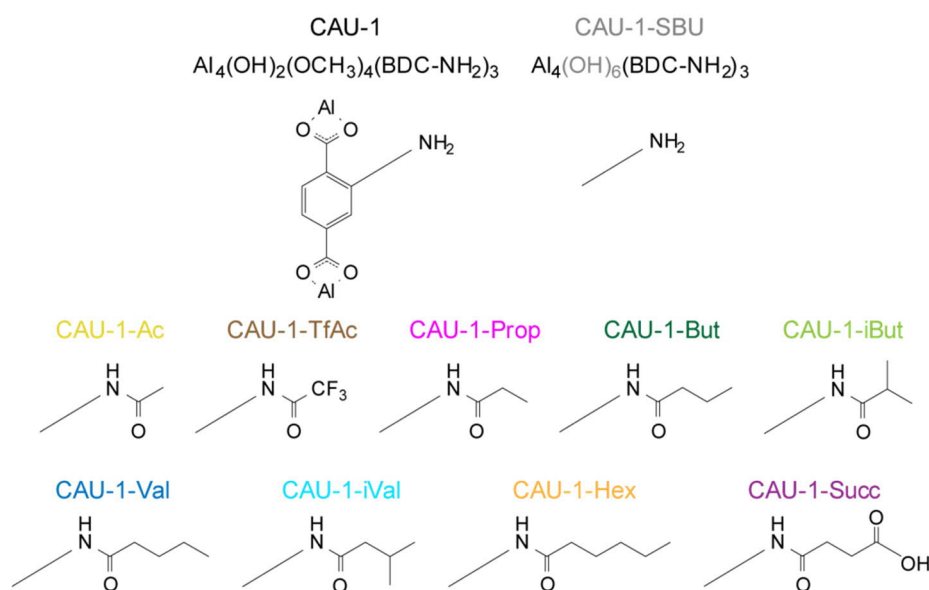
Figure 5.1.1: Pristine and post-synthetic modifications of CAU-1 nanoparticles targeting the SBU (CAU-1-SBU) and the amine group. The denominations for the different samples are highlighted in the color code used throughout this work.

The modified MOF nanoparticles were structurally characterized and their porosity assessed by argon ad- and desorption isotherms at 87 K. Subsequently, the storage capacity of CO_2, CH_4 and N_2 at 273 and 288 K was determined. Furthermore, the MOFs were evaluated for their selectivity and, hence, their separation performance of CO_2 over N_2 and CH_4 under equilibrium conditions to identify advantageous functionalizations. For this purpose, the Henry and IAST selectivities were calculated, as well as the heats of adsorption to quantify the affinity of the gases to the (modified) CAU-1 nanoparticles.

5.1.2 EXPERIMENTAL

Synthesis of CAU-1 nanoparticles

In a typical synthesis, 377 mg $AlCl_3 \cdot 6 H_2O$ (1.55 mmol) and 93.3 mg 2-aminoterephthalic acid (0.515 mmol) were dissolved in 10 mL methanol. The solutions were heated in a microwave (Biotage Initiator, Biotage) at 140 °C for 2.5 min. The product was obtained by centrifugation at 24 krpm for 10 min and washed twice with 20 mL methanol. The particles were resuspended in methanol by ultra-sonication. For spin-coating experiments, the suspension was diluted to 4 wt% with methanol.

Post-synthetic modification of CAU-1 nanoparticles

Three batches of CAU-1 nanoparticles were prepared for each modification according to the synthesis route described above and merged.

In case of CAU-1-SBU, the MOF nanoparticles were separated by centrifugation and left to dry overnight. The final product was obtained by a final heating step at 120 °C for 48 h.

For all other modifications, the suspensions were washed twice with 20 mL dimethylformamide and centrifuged under the same conditions as for pure CAU-1. The particles were then resuspended in 2.5 mL DMF and treated with an excess of the corresponding anhydride. For CAU-1-Ac, 2.5 mL acetic anhydride was added and heated at 60 °C for 20 h. For CAU-1-TfAc, 2.5 mL trifluoroacetic acid was added and sonicated in an ultrasonic (US) bath for 4 h at a maximum temperature of 40 °C. CAU-1-Prop and CAU-1-But were obtained by adding 2.5 mL propionic and n-butyric anhydride, respectively, and heating at 60 °C for 20 h. For the samples CAU-1-iBut, -Val, -iVal and -Hex, 2.5 mL of iso-butyric, valeric, iso-valeric and n-hexanoic anhydride were added and left to react at 80 °C for 24 h. Modification with 2370 mg of succinic anhydride at 100 °C for 24 h yielded CAU-1-Succ. All of these reactions were quenched by adding methanol. The products were washed three times with 20 mL methanol and finally obtained via centrifugation. The nanoparticles were left to dry overnight. Overall yields ranged from 40 to 100 mg for each modification.

The reaction conditions of the post-synthetic modifications are summarized in Table 5.1.1.

Table 5.1.1: Reaction conditions for the modification of the CAU-1 nanoparticles.

	Anhydride used	Reaction type and temperature	Reaction time	Amount of reactant
CAU-1	-	-	-	-
CAU-1-SBU	-	120 °C at air	48 h	-
CAU-1-Ac	Acetic anhydride	60 °C	20 h	2.5 mL
CAU-1-TfAc	Trifluoroacetic anhydride	US bath, max. 40 °C	4 h	2.5 mL
CAU-1-Prop	Propionic anhydride	60 °C	20 h	2.5 mL
CAU-1-But	Butyric anhydride	60 °C	20 h	2.5 mL
CAU-1-iBut	iso-Butyric anhydride	80 °C	24 h	2.5 mL
CAU-1-Val	Valeric anhydride	80 °C	24 h	2.5 mL
CAU-1-iVal	iso-Valeric anhydride	80 °C	24 h	2.5 mL
CAU-1-Hex	Hexanoic anhydride	80 °C	24 h	2.5 mL
CAU-1-Succ	Succinic anhydride	100 °C	24 h	2370 mg

Sorption experiments

All samples were activated at 120 °C for at least 12 h under high vacuum for sorption experiments. For further sorption experiments, the nanoparticles were re-activated at 120 °C until the pressure change fell below 21 mTorr/min. The experiments were performed on an Autosorb iQ-MP2 (Quantachrome Instruments, USA) with Ar of 99.999% purity at 87 K, CO_2 of 99.95% at 273 and 288 K, CH_4 of 99.995% at 273 and 288 K, N_2 of 99.99% at 273 and 288 K. Evaluation of the data was done with the ASiQwin (v5.2) software.

BET surface areas were calculated from argon adsorption isotherms. The pressure range was selected via the micropore BET assistant implemented evaluation software. Pore size distributions were determined with the equilibrium NLDFT model for Ar at 87 K on zeolites/silica assuming spherical/cylindrical pores. For the calculation of the Henry selectivities, pressure ranges below 0.1 bar for the N_2 and below 0.05 bar for the CO_2 and CH_4 adsorption isotherms were considered for fitting to the Henry law. IAST selectivities were calculated from one- and dual-site Langmuir fitted isotherms. Heats of adsorption were calculated using the software. A detailed description can be found in Chapter 2.9.4.

5.1.3 RESULTS AND DISCUSSION

Nanoparticle characterization

Prior to the evaluation of the sorption properties of the CAU-1 nanoparticles and its modifications, the particles were characterized towards their structural integrity, nanoparticle size and morphology, as well as their successful modification and the degree of modification.

In a first step, powder x-ray diffraction (PXRD) patterns were recorded to confirm that the MOF nanoparticles retained the CAU-1 topology, as the reaction conditions may have led to the decomposition of the MOFs. The diffractograms of the samples, shown in Figure 5.1.2, exhibit all the expected reflections with similar intensities with the exception of CAU-1-SBU and CAU-1-Succ, in which the first and most prominent reflection shows decreased intensity. The decrease of intensity in the first reflection is typically observed in MOFs in case of (partial) pore filling. Furthermore, all samples show similar reflex broadening attributed to the nanocrystalline nature of the MOF particles. Nonetheless, the degree of peak broadening is not evenly distributed among the reflections. This is particularly observable for the (0 2 0) and (0 0 2) reflections, which overlap in the recorded patterns. In fact, the (0 2 0) reflections appear as a broad shoulder to a narrower (0 0 2) reflex, indicating an anisotropic domain morphology. This phenomenon was further investigated by Pawley refinement of the powder patterns using a macro implemented in Topas (v5.0) developed by Ectors et al., which allows a description of anisotropic peak broadening due to domain morphology.[45] Assuming an ellipsoidal morphology, the domain sizes along the x/y-axis (0 1 0) and z-axis (0 0 1) could be extracted and are summarized in Table 5.1.2. Refinement details are given in Figure S5.1.1 and Figure S5.1.2. For the x/y-axes crystalline domain sizes from 9 to 14 nm and for the z-axis from 41 to 51 nm were calculated neglecting strain contributions to reflex broadening. The small differences can plausibly be explained by batch-to-batch variations and prove that the domain sizes and, probably, the particle sizes, are not or only barely affected by the modification procedures. Furthermore, an approximate aspect ratio of 1:4 can be extracted from the refinements for the particles.
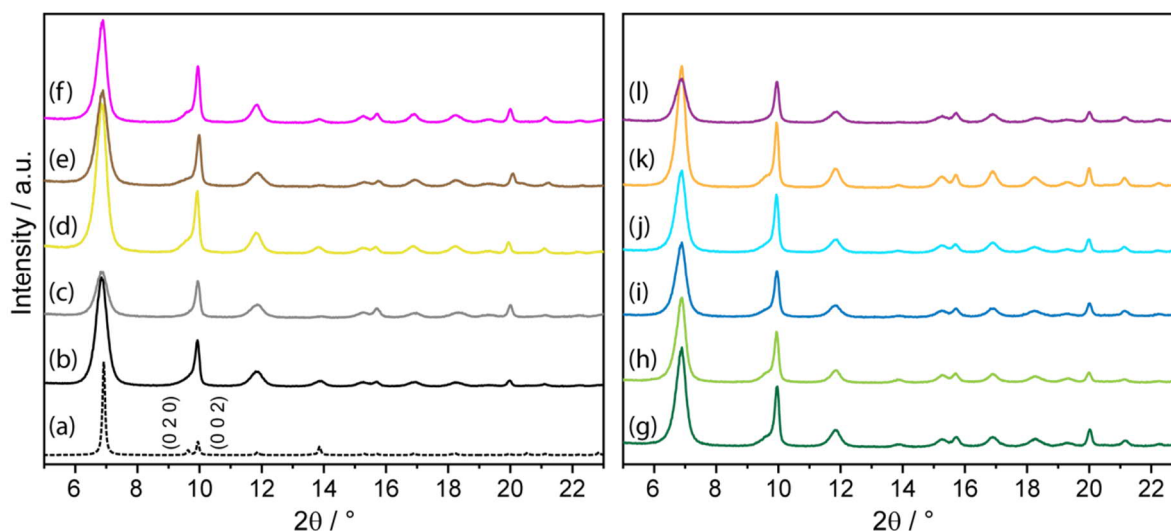
Figure 5.1.2: PXRD patterns of (a) simulated CAU-1, (b) CAU-1, (c) CAU-1-SBU, (d) CAU-1-Ac, (e) CAU-1-TfAc, (f) CAU-1-Prop, (g) CAU-1-But, (h) CAU-1-iBut, (i) CAU-1-Val, (j) CAU-1-iVal, (k) CAU-1-Hex and (l) CAU-1-Succ.

Table 5.1.2: Crystalline domain sizes estimated from the anisotropic peak broadening.

	CAU-1	CAU-1-SBU	CAU-1-Ac	CAU-1-TfAc	CAU-1-Prop	CAU-1-But	CAU-1-iBut	CAU-1-Val	CAU-1-iVal	CAU-1-Hex	CAU-1-Succ
ø Size x/y-domain / nm	9.5	9.2	11.6	9.7	13.1	11.4	13.3	10.4	10.9	13.7	9.3
ø Size z-domain / nm	45.2	42.1	46.9	45.1	47.2	45.5	44.0	41.2	45.6	51.0	41.5

To gain further insights into the particle sizes and distributions, dynamic light scattering (DLS) measurements of the strongly diluted nanoparticle suspensions in methanol were made. These measurements were taken both before and after the modification to uncover possible alterations in the distributions due to the modification procedure. The particle size distributions before the modification are shown in Figure 5.1.3 (left), those after in Figure 5.1.3 (right). In Table 5.1.3 the mean sizes and polydispersity indices (PDIs) are summarized. All in all, the particle sizes prior to the modification range from approximately 40 to 150 nm with mean sizes around 90±10 nm. Although this might seem to be a broad distribution, the PDIs, which do not exceed 0.100, suggest a relatively narrow distribution. In addition, the relatively small differences in the average sizes acknowledge the reproducibility of the CAU-1 synthesis with negligible batch-to-batch variations. A similar situation is found for the modified samples, where the average sizes are 81±6 nm – with the exception of CAU-1-Succ, which shows a clearly larger average size of 125 nm. This could be caused by Ostwald ripening at the expense of smaller particles, as this would yield larger particles, although this has not been reported for MOFs. Naturally, the reduced particle size distributions can be explained by a partial decomposition or surface degradation of the MOF. Hence, aggregation is the most plausible cause. Nonetheless, the obtained values can best be explained bearing in mind that the calculated size

distributions only reflect the solvodynamic radii and not merely the size of the particles themselves. Hence, it is indeed reasonable to assume a reduced solvation with methanol of the amidified samples, as the polarity is decreased, whereas the functionalization containing a carboxylic acid moiety can lead to an increased interaction with methanol.
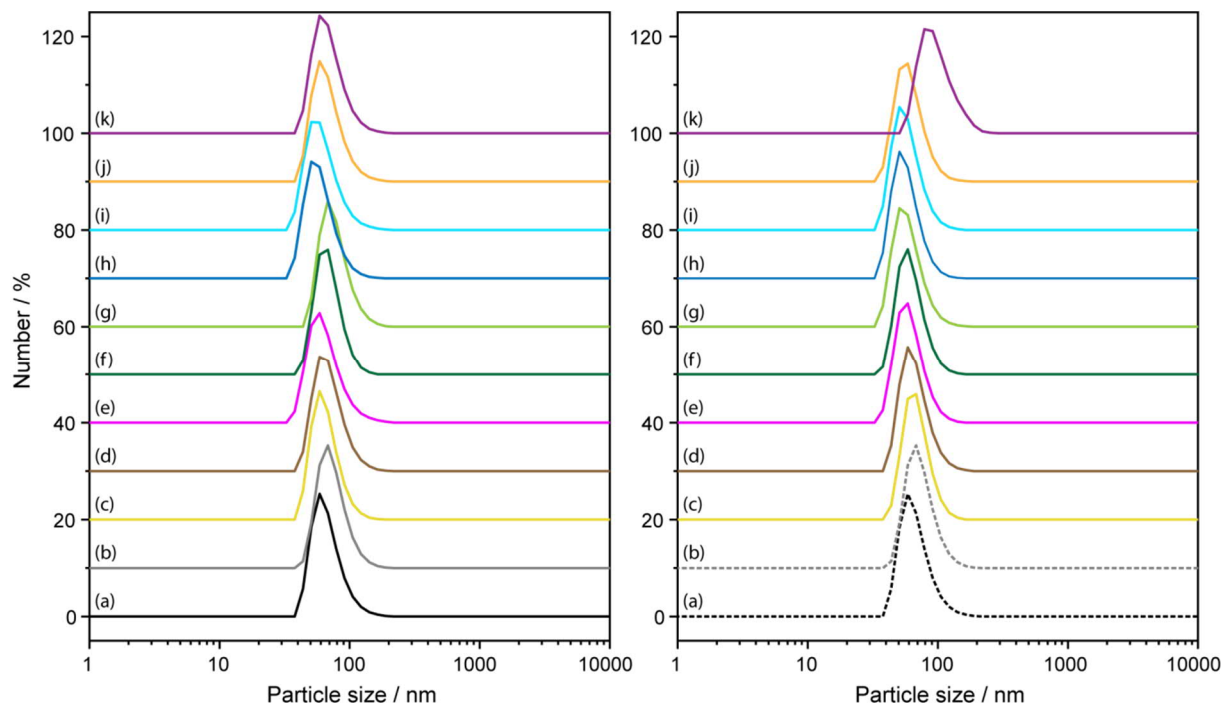
Figure 5.1.3: Particle size distributions (left) before and (right) after the modification based on DLS of (a) CAU-1, (b) CAU-1-SBU , (c) CAU-1-Ac , (d) CAU-1-TfAc , (e) CAU-1-Prop , (f) CAU-1-But , (g) CAU-1-iBut , (h) CAU-1-Val , (i) CAU-1-iVal, (j) CAU-1-Hex and (k) CAU-1-Succ. Note that for CAU-1 and CAU-1-SBU the identical values as before the modification are shown.

Table 5.1.3: Mean sizes and polydispersity indices (PDIs) of the CAU-1 nanoparticles (top) prior to and (bottom) after modification. Values prior to the modification are highlighted by a dark grey, those after the modification in light grey background color.

	CAU-1	CAU-1-SBU	CAU-1-Ac	CAU-1-TfAc	CAU-1-Prop	CAU-1-But	CAU-1-iBut	CAU-1-Val	CAU-1-iVal	CAU-1-Hex	CAU-1-Succ
ø size / nm	93	94	84	93	96	100	97	83	91	92	92
PDI	0.085	0.069	0.057	0.061	0.100	0.079	0.061	0.083	0.098	0.081	0.071
ø size/ nm	-	-	84	87	81	80	80	75	78	81	125
PDI	-	-	0.034	0.066	0.034	0.044	0.076	0.066	0.053	0.050	0.074

In order to gain further insights into the particle sizes and morphologies of the MOFs, these were studied by scanning electron microscopy (SEM). A representative image of the CAU-1 nanoparticles is shown in Figure 5.1.4, further images of the modified nanoparticles are provided in Figure S5.1.5 and Figure S5.1.6. In all images, the typical rice-corn shaped morphology of the CAU-1 nanoparticles can be appreciated with longitudinal sizes of approximately 90±15 nm and perpendicular to it 22±7 nm.

This aspect ratio of approximately 4:1 is in line with that derived from the XRD data assuming an ellipsoidal particle morphology. However, the crystalline domain sizes are only half the overall particle size suggesting intergrowth of the particles. Interestingly, the increased particle sizes of CAU-1-Succ as expected from the DLS measurements can be barely confirmed with the SEM measurements. Despite the poor resolution, only a marginal difference of 5 – 10 nm can be extracted from the SEM images, pointing towards the mentioned solvation effect in the DLS measurement.
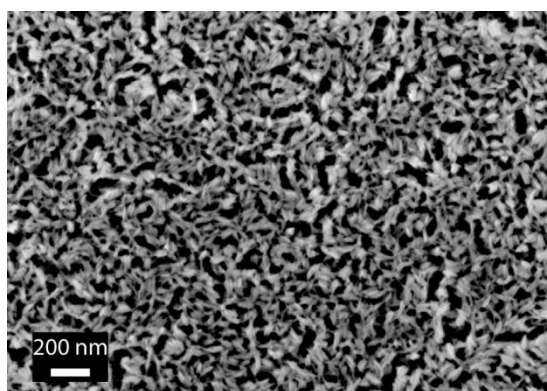
Figure 5.1.4: Representative SEM image of pristine CAU-1 acquired with an Inlense detector.

In order to prove the successful modifications, IR spectra were recorded and the relevant vibrational bands of the modified MOFs compared to those of pristine CAU-1. Extracts of the IR spectra highlighting the affected vibrational bands are shown in Figure S5.1.3 and Figure S5.1.4. The complete spectra are given in Figure S5.1.3, the band positions are summarized in Table S5.1.1. In case of CAU-1-SBU, the methoxylate related vibrational bands at 2941 and 2836 cm^{-1} (-C-H) as well as the one at approximately 1080 cm^{-1} (O-CH$_3$) disappear, proving the removal of the methoxy groups in this sample. For the rest, the amidification is expected to cause a shift of the aromatic vibrational band at 1500 cm^{-1} and the amine related ones at 3387, 1340 and 1260 cm^{-1}.[46] Naturally, the appearance of a carbonyl and alkyl peak is expected as well. For the latter, changes can indeed be seen in the region of 3000 to 2800 cm^{-1} throughout the amidified samples. Nevertheless, this region overlaps with that of the methoxylate in the SBU and is therefore a poor indication for a successful modification. On the contrary, the other expected changes are clearly observable confirming the successful modification of the rest of the samples. This can be seen by a shift of the amine stretch band at 3387 shifting to 3330 cm^{-1} (3280 cm^{-1} in case of CAU-1-TfAc) and the amine bands from 1340 to 1300 – 1295 and 1260 to 1270 cm^{-1}. In addition, the aromatic band at 1500 shifts to higher wavenumbers of approximately 1516 cm^{-1} (1526 cm^{-1} for CAU-1-TfAc). Likewise, the rise of a prominent shoulder at 1715 – 1690 cm^{-1} (1739 cm^{-1} for CAU-1-TfAc) indicates the carbonyl band of the amide in the samples. Furthermore, another unknown absorption band, partially as a shoulder, at 1595 – 1590 cm^{-1} arises consistently in all modified samples. Among these samples, CAU-1-TfAc and CAU-1-Succ differ as expected. For example, the heavier -CF$_3$ group leads to the anticipated shift towards lower wavenumbers compared

to its alkyl analogue CAU-1-Ac for the amine vibration (3286 vs. 3330 cm^{-1}). Also, a prominent band appears at 1160 cm^{-1}, probably the C-F vibration. In case of CAU-1-Succ, the carboxylic group is indicated by the very broad -OH stretch absorption at 3670 – 3070 cm^{-1} and the broader shoulder at 1715 cm^{-1}. In addition, these two sample still shows the presence of peaks of pristine CAU-1 indicating no complete conversion. Even so, the IR data strongly suggests that all MOFs could be modified to a large degree.

Figure 5.1.5: Extracts of the IR spectra of (a) CAU-1, (b) CAU-1-SBU , (c) CAU-1-Ac , (d) CAU-1-TfAc , (e) CAU-1-Prop , (f) CAU-1-But , (g) CAU-1-iBut , (h) CAU-1-Val , (i) CAU-1-iVal, (j) CAU-1-Hex and (k) CAU-1-Succ. The vibrational bands affected by the modifications are shaded in light red, the changes of the methoxy groups in CAU-1-SBU is labeled with m.

These findings were further corroborated with ^{13}C solid-state cross-polarization NMR measurements under magic angle spinning (MAS). Figure 5.1.6 shows the NMR spectra. For easier interpretation, numbers are used for signal assignment of the framework linker, greek letters for the amide groups starting with α for the carbonyl group. The most prominent changes in the chemical shifts of the modified CAU-1 nanoparticles are expected for the methanolate in CAU-1-SBU and for the amides in the carbons adjacent to the nitrogen (carbon signals 3, 2, 4) and, naturally, the emergence of those corresponding to the amide tail (greek letters). For CAU-1-SBU, the methanolate signal of the SBU at 48 ppm significantly decreases, indicating that substantial amount of methanolate could be replaced with hydroxy groups. For the amidifications, several changes can be observed. The most striking is the shift of the aromatic carbon signal 3 at 150 ppm directly adjacent to the nitrogen atom of the amine, which shifts to 141 ppm. In line with that, the neighboring aromatic carbons 2 and 4, with signals in

the range of 120 – 116 ppm (overlapping with carbon 6) shift downfield to form a broad peak centered at 123 ppm. In contrast, the other aromatic and carboxylate peak positions barely change. For the amide tail, the carbonyl signals are barely distinguishable as they either superimpose on the carboxylate carbon signals or the signal-to-noise ratio is too poor. In CAU-1-Ac, the carbonyl signal appears to be the shoulder at 169 ppm, whereas for the modifications with longer alkyl chains the carbonyl signal can be assigned between 180 to 175 ppm. However, the chemical shifts of the carbons of the alkyl chains are clearly distinct below 50 ppm. For longer chains, the chemical shifts towards the terminal carbon decrease as expected. In total the ^{13}C chemical shifts of the alkyl chains range from 45 to 6 ppm.

Similar to the IR measurement, the chemical functionalities in CAU-1-TfAc and CAU-1-Succ give a slightly differing picture. In CAU-1-TfAc, the carbonyl signal is clearly visible at 155 ppm and does therefore not superimpose with the carboxylate signal as in the other samples. However, the strong inductive effects (-I) of the fluorine atoms significantly deshields the fluorinated carbon atom β to 114 ppm, shifting it closely to a signal at 116 ppm, potentially originating from unreacted CAU-1. The corresponding ^{19}F-NMR, given in Figure S5.1.7, shows a multiplet centered at -78.6 ppm. In case of CAU-1-Succ, the carbonyl signal is barely visible as a shoulder of the carboxylate signals at approximately 173 ppm. The two methylene groups β and γ arise at 31 and 28 ppm, respectively, whereas the carboxylic carbon δ is barely visible at 180 ppm.

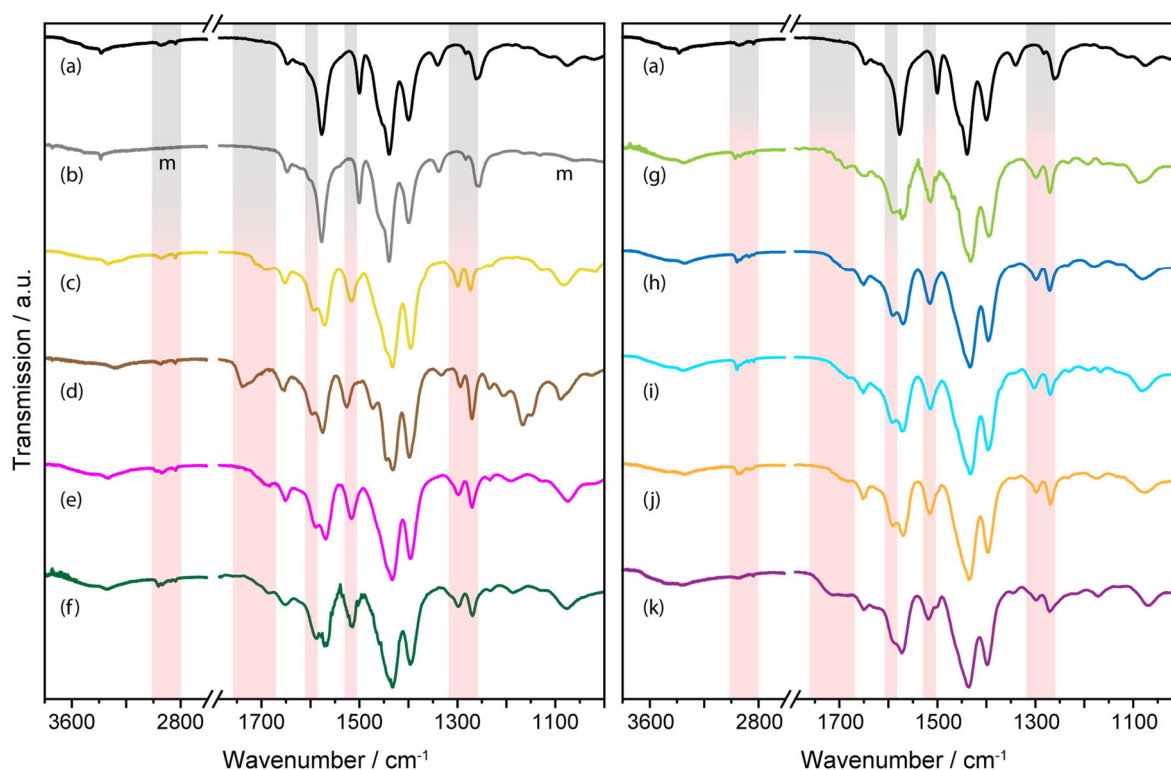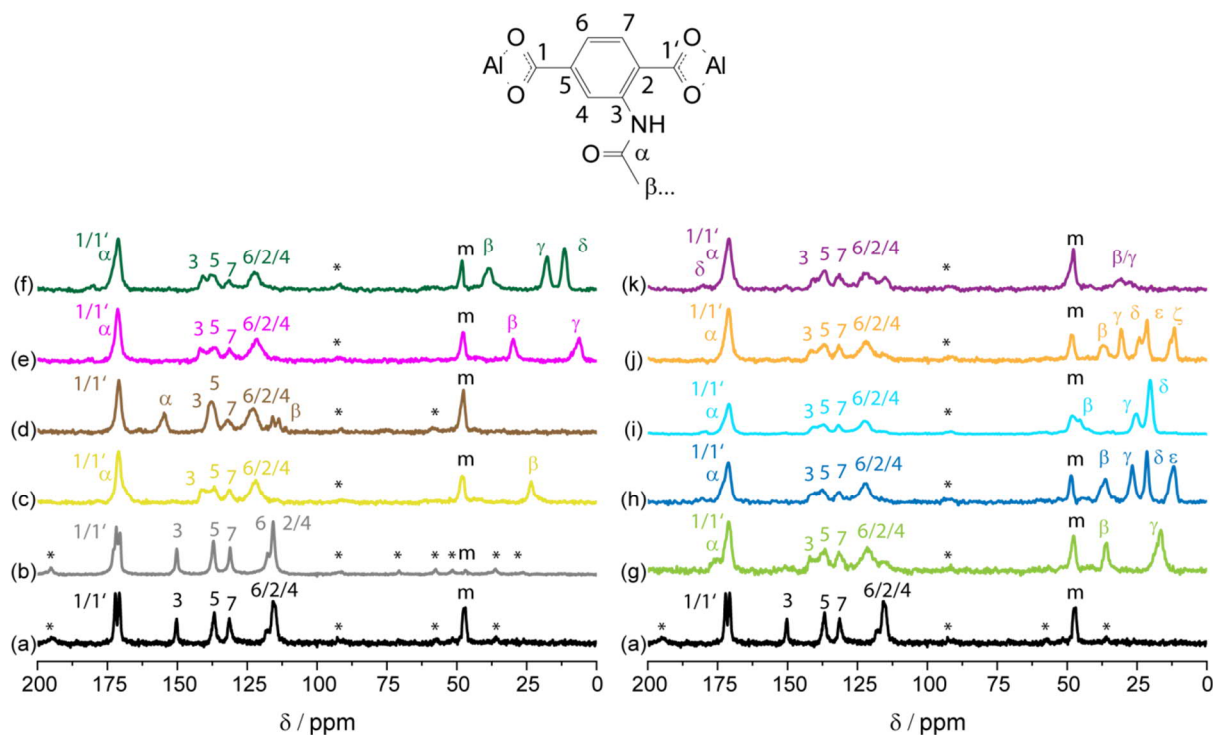Figure 5.1.6: (top) Simplified carbon signal assignment and (bottom) ^{13}C-NMR spectra of (a) CAU-1, (b) CAU-1-SBU , (c) CAU-1-Ac , (d) CAU-1-TfAc , (e) CAU-1-Prop , (f) CAU-1-But , (g) CAU-1-iBut , (h) CAU-1-Val , (i) CAU-1-iVal, (j) CAU-1-Hex and (k) CAU-1-Succ. Asterisks mark spinning side bands, m the methanolate carbon signal.

Although the solid-state NMR measurements strongly support the results derived from the IR spectroscopic measurements, the use of cross-polarization prevent a reliable quantification of the modification degree. For this purpose, the MOFs were digested under alkaline conditions to subsequently perform liquid ^{1}H-NMR measurements of the solvated modified linker. The modification degree was then determined by calculating the ratio of the aromatic protons of the modified linker to the total amount of aromatic linkers. The degree of methoxylation of the samples was calculated by comparison of the amount of methoxy protons to the theoretical amount assuming a SBU composition of $Al_4(OH)_2(OCH_3)_4$. Extracts of the ^{1}H NMR spectra showing the aromatic protons are given in Figure 5.1.7, the complete spectra are given in Figure S5.1.8 and Figure S5.1.9. The complete signal assignment can be found in Figure S5.1.10. The modification and methoxy degrees are summarized in Table 5.1.4. The results show the highest modification (equal to the methoxylation) degree for CAU-1-SBU with 97%, and lower ones for the amidifications, ranging from 83 to 92%, except for CAU-1-Succ with 72%. In case of CAU-1-TfAc, a quantification was not possible as the digestion conditions led to the cleavage of the amide bond. It should be noted that the alkaline conditions necessary for the digestion generally lead to the cleavage of the amide bond, which indeed is most drastically observed for CAU-1-TfAc. To minimize amide bond cleavage, the spectra were measured within 15 minutes after digestion. Attempts to obtain spectra via direct ^{1}H-NMR measurements of the CAU-1-TfAc nanoparticles in D_2O failed to give signals in the aromatic region, impeding a quantification for this sample. Likewise, the share of methoxy-groups in the SBU remains similar throughout the modifications and the small variations can be assumed to be caused by batch-to-batch variations. Furthermore, the spectra also show minor amounts of the corresponding free acids which can either result from alkaline hydrolysis due to the digestion procedure or as byproducts from the modification reaction, which suggests that washing of the modified MOFs did not remove these completely. Although it cannot be excluded that unremoved byproducts can lead to pore blocking in the intact MOF, their amount is assumed to be negligible.

All in all, the modification degrees above 80% demonstrate that the amine moieties can successfully be functionalized to a large extent. Possibly, the most inner pores are inaccessible for the reactants with advancing modification. It is reasonable to assume that the modification first occurs on the outer pores and surface, diminishing the accessibility of further reactants to the inner pores.
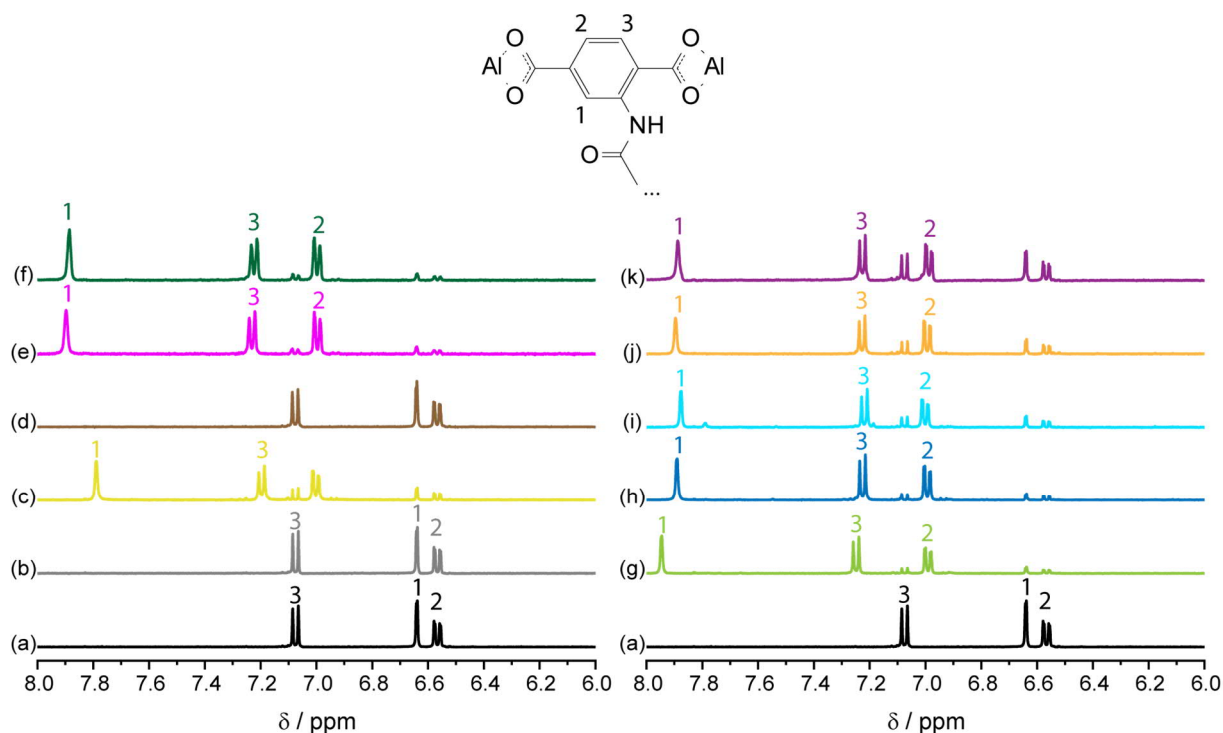
Figure 5.1.7: (top) Simplified proton signal assignment and (bottom) aromatic region of the ^{1}H-NMR spectra of (a) CAU-1, (b) CAU-1-SBU, (c) CAU-1-Ac, (d) CAU-1-TfAc, (e) CAU-1-Prop, (f) CAU-1-But, (g) CAU-1-iBut, (h) CAU-1-Val, (i) CAU-1-iVal, (j) CAU-1-Hex and (k) CAU-1-Succ. Note that for CAU-1-TfAc, the digestion conditions lead to the cleavage of the trifluoracetamidic bond, giving the 2-aminoterphthalate signals as in CAU-1 and CAU-1-SBU.

Table 5.1.4: Modification degrees and share of methoxy-groups in the SBU of the pristine and modified CAU-1 nanoparticles.

	CAU-1	CAU-1-SBU	CAU-1-Ac	CAU-1-TfAc	CAU-1-Prop	CAU-1-But	CAU-1-iBut	CAU-1-Val	CAU-1-iVal	CAU-1-Hex	CAU-1-Succ
Modification degree	-	97%	86%	-	92%	92%	89%	92%	83%	83%	72%
Methoxy degree	79%	3%	80%	83%	84%	83%	80%	78%	82%	84%	84%

Storage and separation capacity

In order to characterize the sorption properties of the MOF nanoparticles, the porosity was assessed by measurement of argon ad- and desorption isotherms at 87 K, which are shown in Figure 5.1.8. All isotherms share a very steep increase at very low partial pressures, typical for microporous materials. The differences in the amount adsorbed, with CAU-1-SBU and CAU-1 showing the largest uptakes ($\approx$ 420 - 400 cm^{3}g^{-1} at 0.1 p/p$_0$) and the modifications partly far below 300 cm^{3}g^{-1}, is in line with the expected reduction of the pore volume accompanied by the covalent modifications. This is most prominent for the large hexanoyl chain in CAU-1-Hex ($\approx$ 140 cm^{3}g^{-1}) compared to the acetylic group in CAU-1-Ac ($\approx$ 270 cm^{3}g^{-1}). From 0.1 to approx. 0.8 p/p$_0$ all isotherms exhibit a similar, relatively flat linear increase. Above 0.8 p/p$_0$, additional pronounced uptakes can be observed in all samples, which in some cases even exceed the amount adsorbed in the microporous region. This significant uptake is due to the textural porosity arising from the nanoparticulate nature of the samples, as already

indicated in the SEM images (see Figure 5.1.4). While the isotherms are clearly defined below 0.1 p/p$_0$, the meso- to macroporous regions exhibit noticeable differences between the samples, e.g. the pressure onset of the increased uptake, the hysteresis loops and the additional amount of adsorbed volume. This is attributed to the small batch-to-batch variations and resulting "packing" of the nanoparticles, i.e. the textural porosity. However, in case of CAU-1-Succ, the difference cannot be explained solely by this, considering a total adsorbed volume of approximately 1100 cm^{3}g^{-1} compared to ≈ 220 cm^{3}g^{-1} at 0.1 p/p$_0$. In this particular case, this would be in line with larger particles as indicated by the DLS measurements, which in turn would result in larger textural pores.
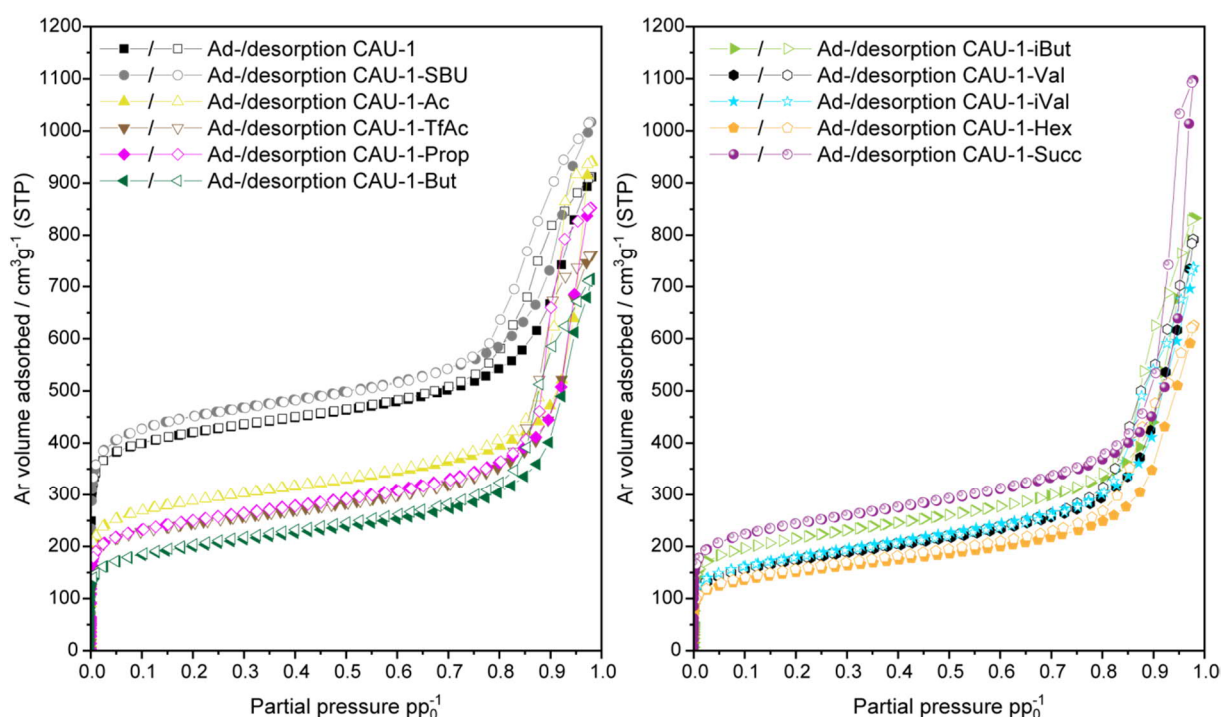
Figure 5.1.8: Argon isotherms at 87 K of the (modified) CAU-1-nanoparticles. Filled symbols depict the adsorption branch, empty symbols the desorption branch.

Based on the argon isotherms, the BET surface areas of the samples were calculated and are summarized in Table 5.1.5. The BET plots can be found in Figure S5.1.11 and the calculation in Table S5.1.2. The results show the expected increase in surface area for CAU-1-SBU and decrease for the alkanoyl chains, with CAU-1-Hex having the lowest value (473 m^{2}g^{-1}). CAU-1-Succ shows an intermediate value of 776 m^{2}g^{-1}, which would probably be lower in case of a larger modification degree. Nonetheless, the values show a clear trend of decreasing BET surface areas with increasing sizes of the modification agents.

Table 5.1.5: BET surface areas of the (modified) CAU-1 nanoparticles.

	CAU-1	CAU-1-SBU	CAU-1-Ac	CAU-1-TfAc	CAU-1-Prop	CAU-1-But	CAU-1-iBut	CAU-1-Val	CAU-1-iVal	CAU-1-Hex	CAU-1-Succ
BET SA / m^{2}g^{-1}	1405	1707	936	798	809	638	683	546	567	473	776

In a next step, the influence of the modifications on the pore sizes was investigated by calculation of the pore size distributions (PSDs) based on the argon isotherms using several NLDFT and QSDFT calculation models. The results shown in this thesis are based on the NLDFT equilibrium model of zeolitic type materials assuming spherical and cylindrical pores, which showed the best fitting results for the experimental isotherms. The microporous regime of the PSD is depicted in Figure 5.1.9, the complete distributions in Figure S5.1.13 and the fittings in Figure S5.1.14 as well as Figure S5.1.15. According to the literature, two types of pores with 0.45 (tetrahedral) and 1.00 nm (octahedral) diameters are derived from the crystallographic structure.[43] CAU-1 and CAU-1-SBU show two very close but distinct pores of 0.96 and 1.09 nm, which are not in line with the data based on the XRD extracted values and are probably an artifact of the method. For the other modifications, single, flat and very broad micropores are modeled. In CAU-1-Ac the PSD is centered at 0.96 nm and gradually decreases with increasing side chain sizes towards 0.83 nm in CAU-1-Hex. In addition to the micropores, undefined and very broad pores are calculated in the mesoporous regime reflecting the textural porosity of the nanoparticles (Figure S5.1.13). For CAU-1-Succ, the PSD is shifted towards larger pore sizes of 20 – 50 nm compared to the other samples (10 – 25 nm), which again indicates that the particles in this particular sample are indeed larger. Although the calculated PSDs reflect the expected trend with very good fitting errors (<0.7%), the exact pore sizes in the micropore regime cannot be extracted. In fact, the lower limit of the modeled pores is 0.68 nm and therefore cannot account for the tetrahedral pore, evidencing the need of DFT kernels that can reliably describe pores below that limit.
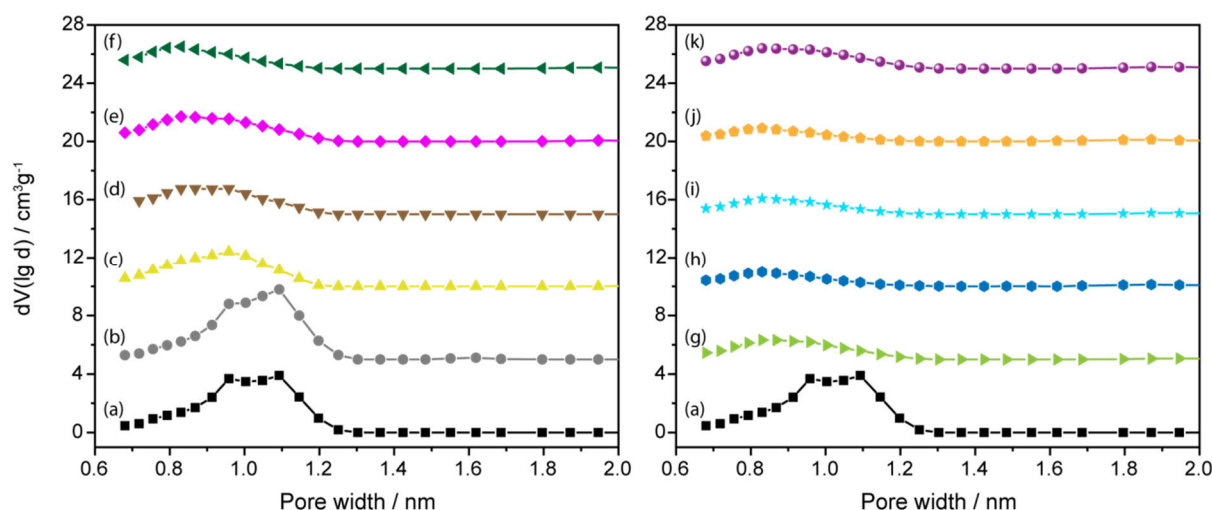
Figure 5.1.9: PSD of the micropores of (a) CAU-1, (b) CAU-1-SBU, (c) CAU-1-Ac, (d) CAU-1-TfAc, (e) CAU-1-Prop, (f) CAU-1-But, (g) CAU-1-iBut, (h) CAU-1-Val, (i) CAU-1-iVal, (j) CAU-1-Hex and (k) CAU-1-Succ.

However, if the cumulative pore volumes covering the micropores are considered, a more exact picture can be appreciated. The cumulative pore volume up to 2 nm based on the DFT model is shown in Figure 5.1.10 and is summarized in Table 5.1.6 for the different modifications. The pore volumes change

according to the size of the introduced modification and saturate above 1.2 nm, indicating complete micropore filling at that point. As can be seen, the onset of filling of CAU-1-SBU commences at the highest pore width, closely followed by CAU-1. For the rest, the onset is shifted towards lower pore diameters, as expected. Furthermore, the correlation of the modeled pore volume with the BET surface areas exhibits a fairly linear behavior advocating for the consistency of the data (Figure 5.1.11).
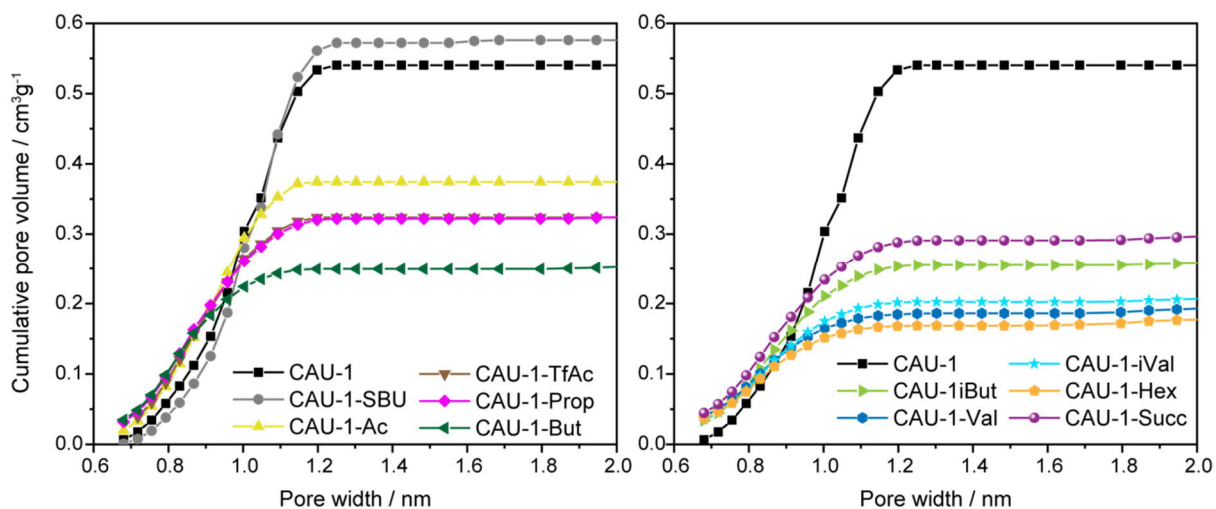
Figure 5.1.10: Cumulative pore volume of the micropores of the (modified) CAU-1 nanoparticles.

Table 5.1.6: Cumulative micropore volume of the (modified) CAU-1 nanoparticles.

	CAU-1	CAU-1-SBU	CAU-1-Ac	CAU-1-TfAc	CAU-1-Prop	CAU-1-But	CAU-1-iBut	CAU-1-Val	CAU-1-iVal	CAU-1-Hex	CAU-1-Succ
Micropore volume / cm^3g^{-1}	0.54	0.58	0.37	0.32	0.32	0.25	0.26	0.19	0.21	0.18	0.30
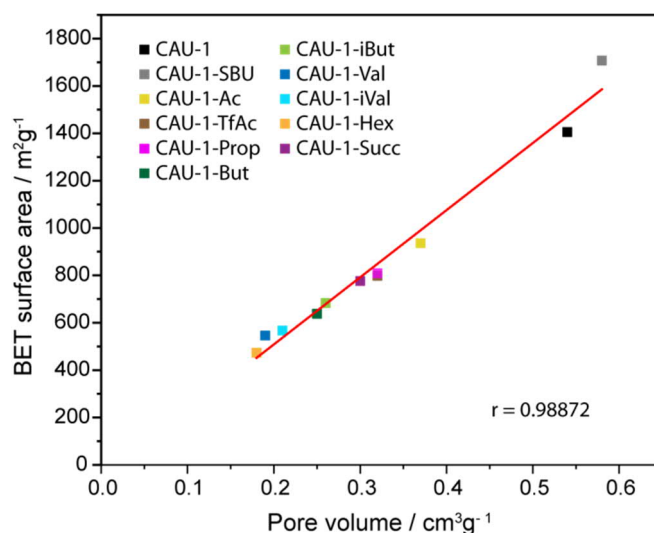
Figure 5.1.11: Micropore volume vs. BET surface area plot of the (modified) CAU-1 nanoparticles. The correlation coefficient r of the linear fit is given at the lower right of the graph.

In a next step, the uptake capacities for CO_2 of the (modified) CAU-1 nanoparticles were evaluated. The isotherms at 273 and 288 K are shown in Figure 5.1.12 and the uptake capacities at 1 bar

summarized in Table 5.1.7. The uptakes of the different samples for both temperatures resemble the trend observed for the micropore volumes derived from the argon isotherms. Overall uptakes are larger at the lower temperature with CAU-1-SBU showing the largest uptake of 5.74 mmol·g^{-1} (3.91 at 288 K) and CAU-1-Hex the lowest of 1.61 mmol·g^{-1} (1.14 at 288 K). Again, the intermediate values of the alkanoyl modifications evidence that larger modifications lead to lower amounts being adsorbed. In case of CAU-1-Succ, the relatively high uptake can be due to the incomplete modification.
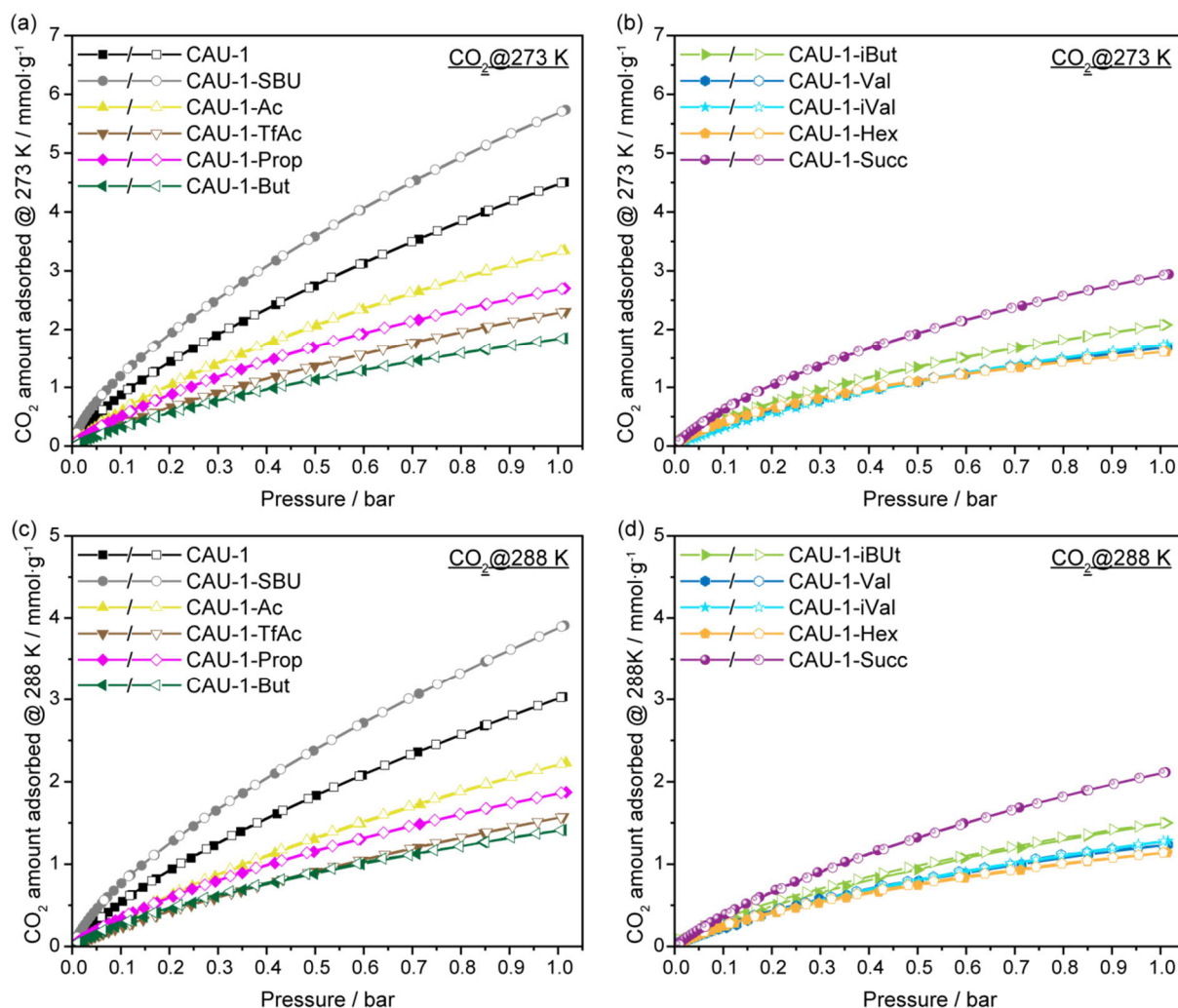
Figure 5.1.12: CO_2 ad- and desorption isotherms of the (modified) CAU-1-nanoparticles at (a+b) 273 and (c+d) 288 K. Filled symbols depict the adsorption, empty symbols the desorption branch.

In order to quantify the relative changes in the uptakes and the influence of the determined surface areas, the overall uptakes were plotted as a function of the BET surface areas (Figure 5.1.13). Again, a linear correlation can be extracted, which was fitted to the data with CAU-1 as the reference material. As can be seen, for both temperatures the values correlate surprisingly well, suggesting that the uptake of CO_2 primarily is a (linear) function of the surface area. At a closer look, the deviation from the linear fit reveals an increased adsorption for CAU-1-SBU, -Succ and -Ac, whereas modifications larger than the propanoyl amide have slightly decreased uptakes. Hence, the presence of polar groups, either

through demethoxylation of the SBU or by introduction of polar carboxylic groups seems to be beneficial. In the special case of CAU-1-Ac and -Prop, it adds evidence that amides can be helpful as well,[47-52] although their beneficial role cannot be generalized.[53] In contrast, when the hydrophobic character becomes dominant, it is rather counterproductive, confirming the findings of the literature.[25] This is most dramatically seen in CAU-1-TfAc, which shows that the fluorinated acetyl group compensates the positive influence of the amide. To quantify these variances from the linear fit, the relative changes from the data points to the linear fit were extracted and are given in Table 5.1.7. It should be noted that these values should not be overrated, as they strongly depend on the linear fit, which was only referenced to one data point, namely CAU-1.

Figure 5.1.13: BET surface area vs. CO_2 uptake plot of the (modified) CAU-1 nanoparticles at (a) 273 and (b) 288 K. The equation of the linear fit and its correlation coefficient are given in the lower right of each graph.

Table 5.1.7: CO_2 amount adsorbed by the (modified) CAU-1 nanoparticles at 1 bar, 273 and 288 K and relative changes to the linear fit of the BET vs. uptake plot.

	CAU-1	CAU-1-SBU	CAU-1-Ac	CAU-1-TfAc	CAU-1-Prop	CAU-1-But	CAU-1-iBut	CAU-1-Val	CAU-1-iVal	CAU-1-Hex	CAU-1-Succ
CO_2 uptake @ 273 K / mmol·g^{-1}	4.51	5.74	3.35	2.29	2.70	1.85	2.08	1.69	1.74	1.61	2.94
Rel. change to linear correl. fit	±0%	+5.9%	+9.7%	-12.3%	+3.2%	-11.8%	-7.1%	-7.1%	-6.1%	-1.8%	+15.6%
CO_2 uptake @ 288 K / mmol·g^{-1}	3.03	3.91	2.23	1.57	1.87	1.41	1.50	1.23	1.28	1.14	2.11
Rel. change to linear correl. fit	±0%	+5.9%	+6.1%	-14.2%	+0.9%	-6.2%	-10.7%	-6.5%	-5.6%	-2.1%	+16.3%

Furthermore, the adsorption capacities for methane were measured, which are shown in Figure 5.1.14 and summarized in Table 5.1.8. Albeit considerably lower uptakes, the overall picture seems very similar to that of the CO_2 isotherms. However, CAU-1-SBU behaves considerably different: the demethoxylation does not lead to any noteworthy change in the adsorption compared to CAU-1. Apparently, the polar nature of the hydroxy groups impedes an increased uptake into the additional pore space. At 273 K, the uptakes range from 0.50 (CAU-1-Hex) to 1.21 mmol·g^{-1} (CAU-1) and decrease even further at 288 K to 0.36 and 0.79 mmol·g^{-1}, respectively. If plotted against the BET surface area as for the CO_2 uptakes, it becomes evident that the surface area does not play the dominant role in determining the methane storage performance of the (modified) MOFs. In fact, the results are not intuitive as CAU-1-Succ, possessing a strong polar carboxylate group shows relatively high uptakes, contrasting with the also polar CAU-1-SBU with relatively low uptakes. As the overall adsorbed amounts are very low, the error in the measurements are probably giving a distorted view. All in all, the adsorption capacities of the modified CAU-1 particles for CH_4 are poor and, hence, unsuited for storage purposes, although to evaluate this thoroughly the uptake capacities at 35 bar should also be measured.[54,55]

Figure 5.1.14: CH$_4$ ad- and desorption isotherms of the (modified) CAU-1-nanoparticles at (a+b) 273 and (c+d) 288 K. Filled symbols depict the adsorption, empty symbols the desorption branch.
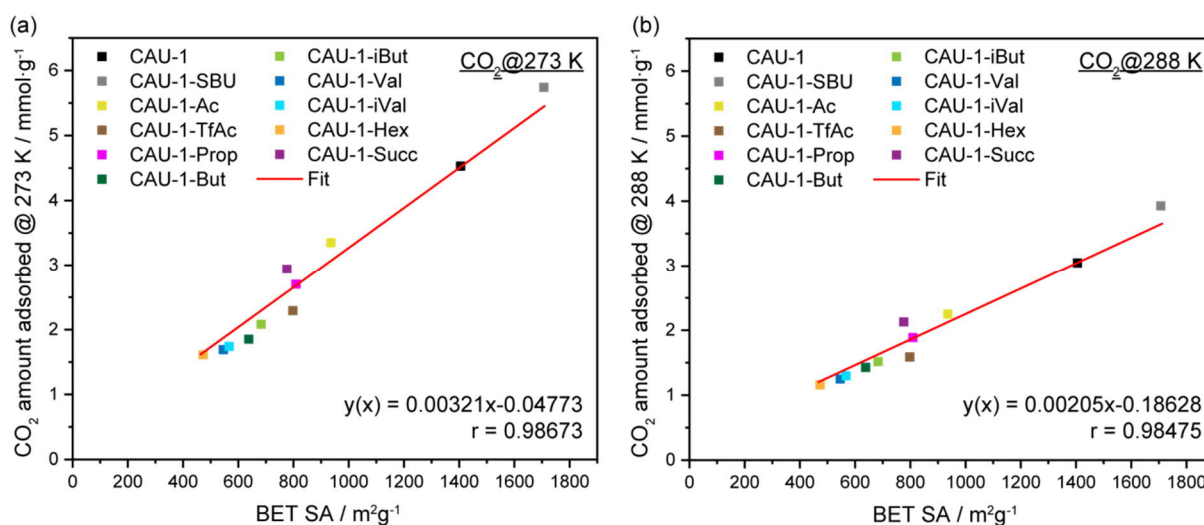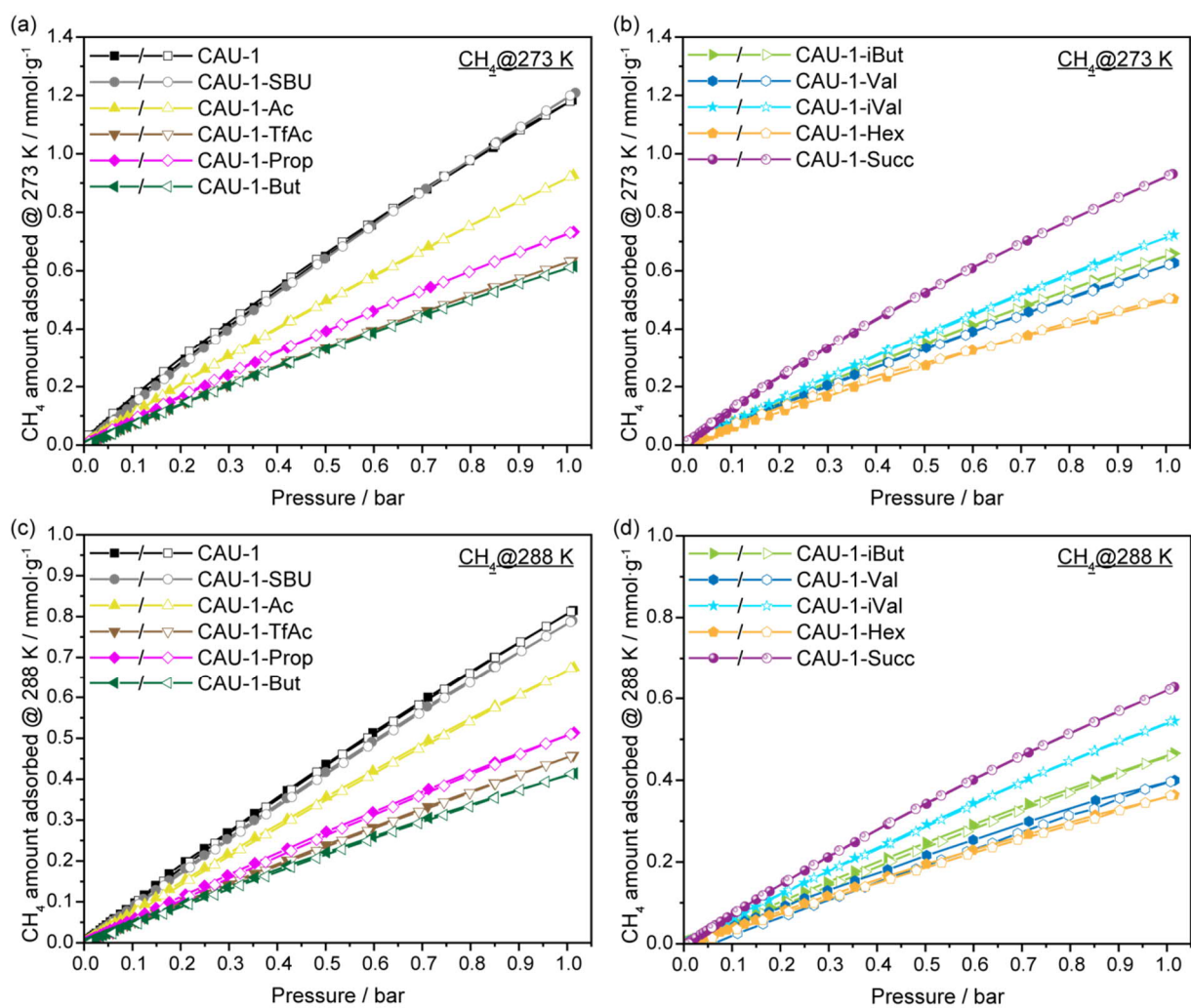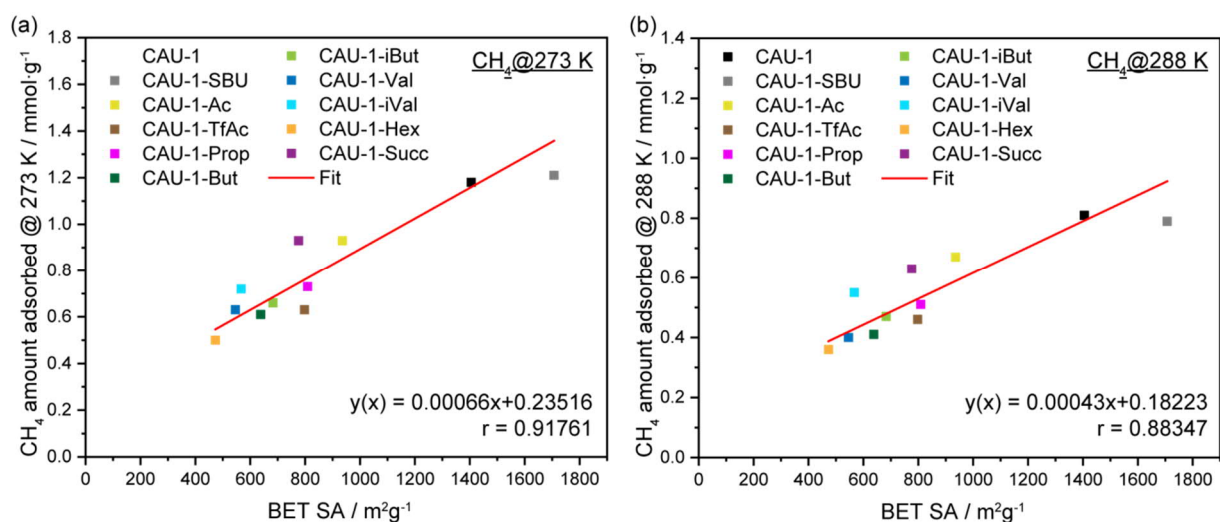

Figure 5.1.15: BET surface area vs. CH$_4$ uptake plot of the (modified) CAU-1 nanoparticles at (a) 273 and (b) 288 K. The equation of the linear fit and its correlation coefficient are given in the lower right of each graph.

Table 5.1.8: CH_4 amount adsorbed by the (modified) CAU-1 nanoparticles at 1 bar, 273 and 288 K.

	CAU-1	CAU-1-SBU	CAU-1-Ac	CAU-1-TfAc	CAU-1-Prop	CAU-1-But	CAU-1-iBut	CAU-1-Val	CAU-1-iVal	CAU-1-Hex	CAU-1-Succ
CH_4 uptake @ 273 K / mmol·g^{-1}	1.18	1.21	0.93	0.63	0.73	0.61	0.66	0.63	0.72	0.50	0.93
CH_4 uptake @ 288 K / mmol·g^{-1}	0.81	0.79	0.67	0.46	0.51	0.41	0.47	0.40	0.55	0.36	0.63

Nonetheless, the modifications can be indeed of use for the sequestration of CO_2, e.g. for the separation from nitrogen or for the purification of methane, e.g. for fuel applications. In the following, the selectivities of CO_2 over N_2 and CH_4 are discussed. To assess the performance, the Henry and IAST selectivities were calculated, evaluated and compared. For the former, the calculation is based on the Henry law that is assumed to describe the adsorption isotherms at very low pressures very well. The selectivity for equimolar mixtures is then calculated as the ratio of the initial slopes of the Henry fits of the two different gases. The results are summarized in Table 5.1.9. The corresponding N_2 isotherms are given in Figure S5.1.16, the Henry fits in Figure S5.1.17 to Figure S5.1.27. The results show relatively good selectivities towards CO_2 over N_2 for the pristine CAU-1 of 38 at 273 K, and a moderate selectivity of 12 over CH_4. The selectivities decrease as expected for the higher temperature. The overall best performing MOF is CAU-1-SBU, as expected from the superior CO_2 uptakes, with a value of 64 at 273 K (24 over CH_4) comparable to other selectivities reported for MOFs.[56] For CAU-1-Ac, the selectivity is decreased and further drops for CAU-1-TfAc. In case of CAU-1-Succ, a selectivity of 24 was calculated close to the performance of CAU-1-Ac. Based on the decreasing uptakes for larger hydrophobic groups, a decreasing selectivity is expected. However, for the rest of the modifications no clear trend can be identified with values comprising the range of 3 to 35. Rather than reflecting realistic selectivities, these values likely originate from low-quality primary data. This is for example evidenced by some of the hysteresis curves, in which the desorption curve is shifted below the adsorption branch and the marginal uptakes, especially for the N_2 and CH_4 measurements, leading to a large measurement error. This is exemplified in the CH_4 adsorption isotherms of CAU-1-Val, -iVal and -Hex, which not even exhibit a consistent continuous adsorption, frustrating any sensible (linear) fit at very low pressures (Figure S5.1.24 to Figure S5.1.26). Consequently, irrational values are calculated and yield higher selectivities at higher temperatures, e.g. for CAU-1-Prop, -But, -Val, -iVal. Hence, the calculated values are therefore misleading and not significant. This becomes even clearer for the CO_2/CH_4 selectivities. While CAU-1, -SBU, -Ac, -TfAc, and to some extent -Prop, show sensible values, the rest of the modifications give no well-founded results. Altogether, the selectivity over CH_4 is decreased at higher temperatures, and with CAU-1-SBU again showing the best performance (24 at 273 K, 17 at 288 K).

Table 5.1.9: Henry selectivities of CO_2/N_2 and CO_2/CH_4 at 273 and 288 K of the (modified) CAU-1 nanoparticles.

	CAU-1	CAU-1-SBU	CAU-1-Ac	CAU-1-TfAc	CAU-1-Prop	CAU-1-But	CAU-1-iBut	CAU-1-Val	CAU-1-iVal	CAU-1-Hex	CAU-1-Succ
CO_2/N_2 @ 273 K	38	64	26	20	25	3	35	14	7	37	24
CO_2/N_2 @ 288 K	22	46	12	5	31	22	22	18	10	25	25
CO_2/CH_4 @ 273 K	12	24	11	9	12	6	17	-	-	-	8
CO_2/CH_4 @ 288 K	9	17	5	7	12	9	11	-	-	-	-

A more realistic and accurate description can be achieved applying the ideal adsorbed solution theory (IAST) that accounts for the whole pressure range and, in addition, for the gas mixture composition to yield reasonable estimations for the selectivities. It is based on the thermodynamic vapor-liquid equilibrium for binary gas mixtures at which the spreading pressures are equal.[57,58] Despite its limitations for heterogeneous surfaces, it is commonly used for the prediction of selectivities. In this work, the IAST selectivities for CO_2 over N_2 were calculated for a mixture of 15% CO_2 to 85% N_2 as this is the typical post-combustion composition.[59] The selectivities are shown in Figure 5.1.16. CAU-1-SBU clearly outperforms the other modifications and the pristine CAU-1 at both temperatures (273 K: 65.3, 288 K: 20.2). For the samples CAU-1-Ac and -TfAc, the expected behavior of decreasing selectivity of 24.4 and 18.1 is observed, with a further decrease at the higher temperature (15.9 and 16.1). CAU-1-Succ ranks in the intermediate regime with a selectivity of 23.7 (20.7 at 288 K). As for the Henry selectivities, the rest of the calculated values are inconsistent and do not follow a readily identifiable trend. In case of CAU-1-Hex, the calculated IAST selectivity first increases and then drops again towards higher loadings. This could be due to the poor interaction of CO_2 with the pore wall, but as the adsorbate-adsorbate interaction becomes more relevant, it increases again. Whether this is an artifact of the calculation or reflects a realistic behavior is unclear, as this behavior is not seen at higher temperatures. Paradoxically, CAU-1-Prop, -Val, -iVal show higher selectivities at the higher temperatures, while CAU-1-iBut and -Hex exhibit relatively high selectivities in absolute numbers (32.0 and 24.2 at 273 K). Again, these deviant values originate from the large error of the isotherms themselves. Hence, the most accurate description is only possible for the samples CAU-1, -SBU, -Ac, -TfAc and Succ of which CAU-1-SBU, again and as expected, possesses the best selectivity.
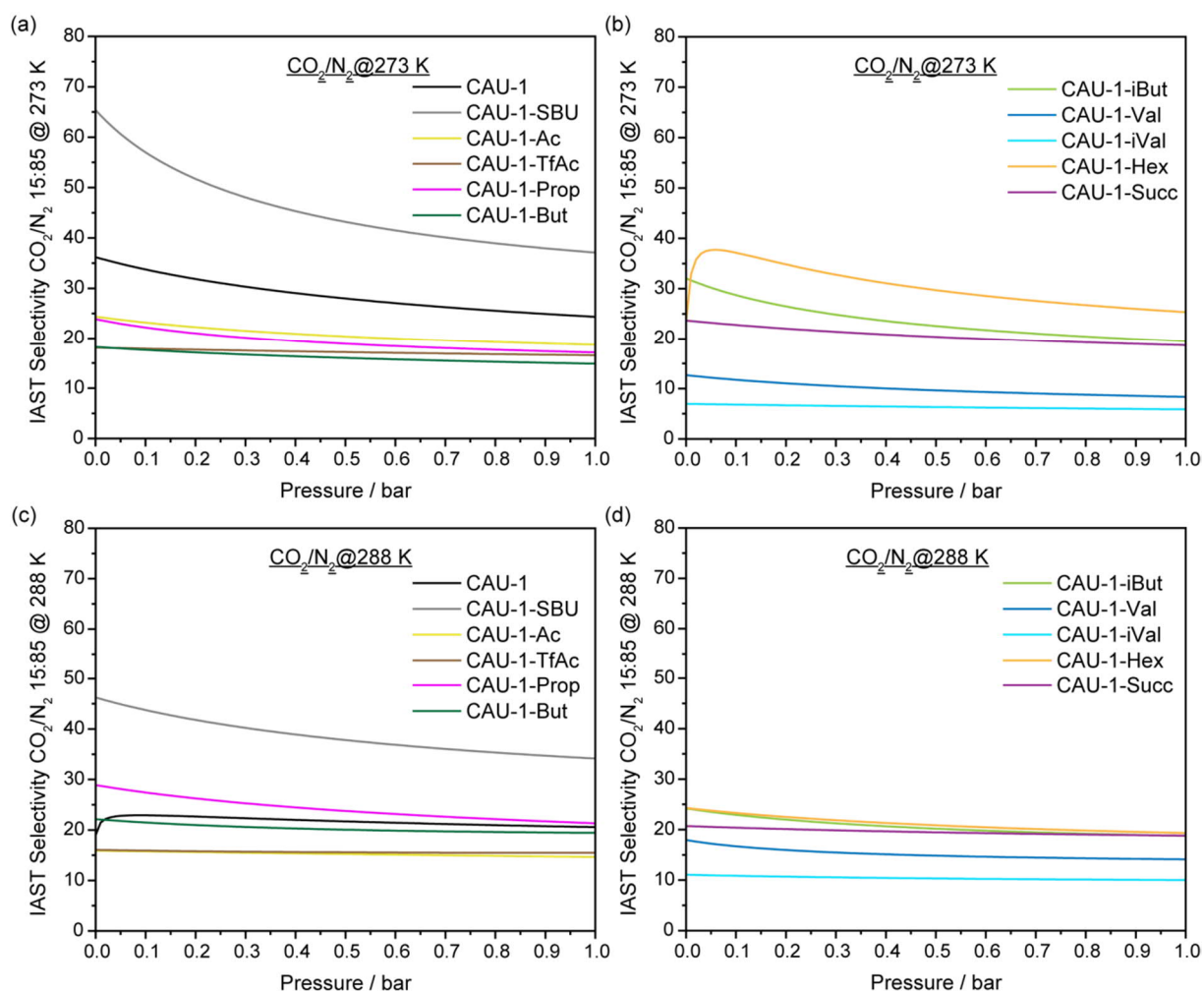
Figure 5.1.16: IAST selectivities for a gas mixture of 15% CO_2 and 85% N_2 at (a+b) 273 and (c+d) 288 K.

Furthermore, the IAST selectivities for an equimolar mixture of CO_2 and CH_4 are displayed in Figure 5.1.17, giving a similar picture to that found for CO_2. Again, CAU-1-SBU outperforms the rest of the CAU-1 nanoparticles with the best selectivity of 20.2 at 273 K, while the pristine CAU-1 gives an intermediate value of 9.4. With the amidification, the values drop further to 7.6 (CAU-1-Ac) and 6.0 (CAU-1-TfAc). Meanwhile, CAU-1-Succ, with 6.5, does not show a remarkably improve of the selectivity. Both Henry and IAST selectivities are summarized in Table 5.1.10.

All in all, the demethoxylated CAU-1-SBU gives the best selectivities, although it cannot compete with several benchmark MOFs exceeding selectivities of >200 for CO_2/N_2,[56,60] or of >100 for CO_2/CH_4.[61] Furthermore, our results failed to confirm the values reported by Si et al. for the pristine CAU-1 (CO_2/N_2: 101, CO_2/CH_4: 28 at 273 K),[42] probably due to different sample treatment and activation procedures. Overall, the poor quality of the measurements, especially for samples with minor uptakes and very small pores, impede a reasonable and rational evaluation of the calculated selectivities.
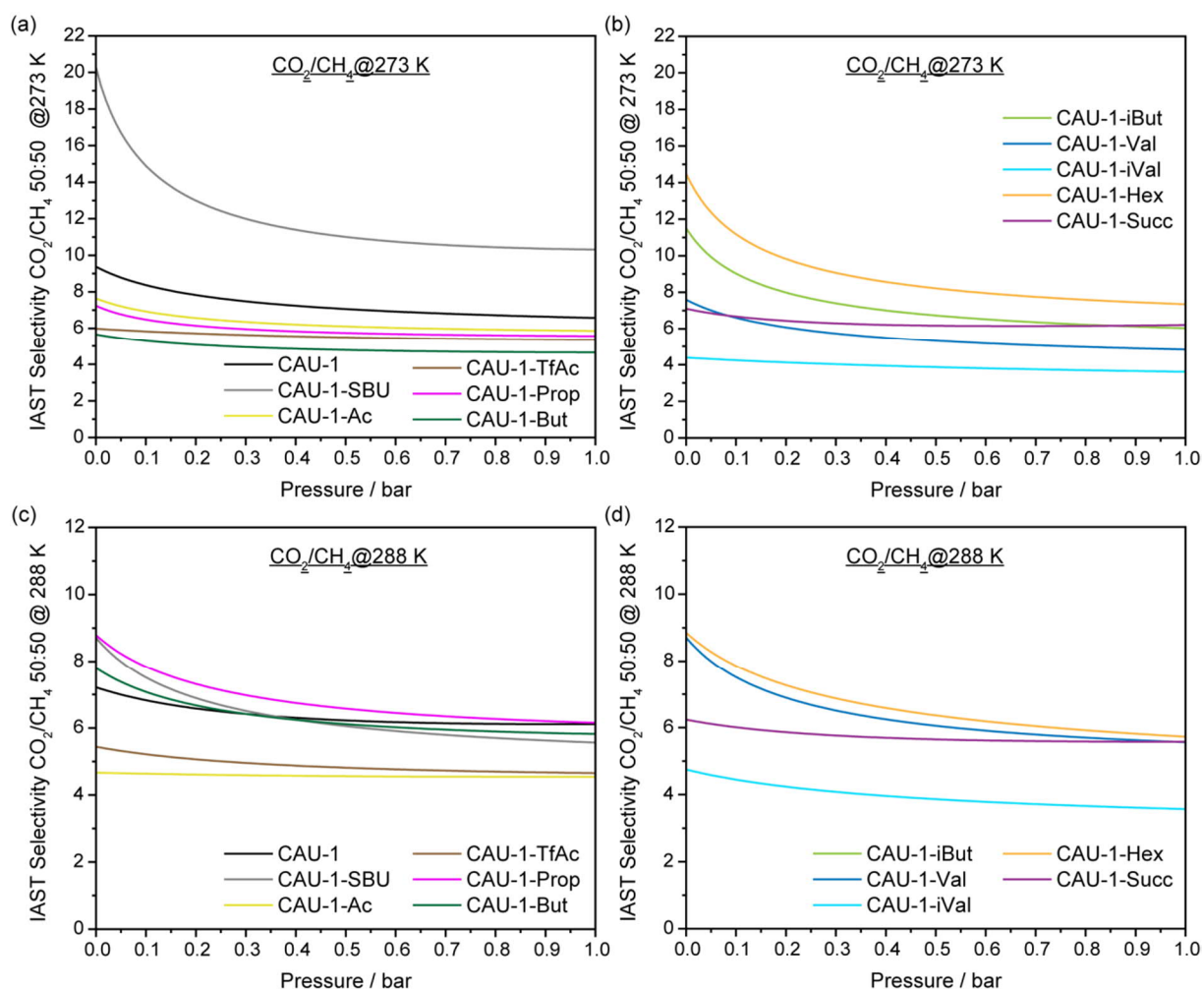
Figure 5.1.17: IAST selectivities for an equimolar gas mixture of CO_2 and CH_4 at (a+b) 273 and (c+d) 288 K.

Table 5.1.10: Henry and IAST selectivities of CO_2/N_2 and CO_2/CH_4 at 273 and 288 K of the (modified) CAU-1 nanoparticles.

| | CO_2/N_2 | | | | CO_2/CH_4 | | | |
| | Henry | | IAST[a] | | Henry | | IAST | |
	273 K	288 K	273 K	288 K	273 K	288 K	273 K	288 K
CAU-1	38	22	36.2	19.2	12	9	9.4	7.2
CAU-1-SBU	64	46	65.3	46.2	24	17	20.2	8.7
CAU-1-Ac	26	12	24.4	15.9	11	5	7.6	4.7
CAU-1-TfAc	20	5	18.1	16.1	9	7	6.0	5.4
CAU-1-Prop	25	31	23.1	28.9	12	12	7.2	8.8
CAU-1-But	3	22	18.2	22.1	6	9	5.6	7.8
CAU-1-iBut	35	22	32.0	24.2	17	11	11.5	8.7
CAU-1-Val	14	18	12.7	17.9	-	-	7.6	8.7
CAU-1-iVal	7	10	7.0	11.1	-	-	4.4	4.7
CAU-1-Hex	37	25	24.2	24.3	-	-	14.4	8.8
CAU-1-Succ	24	25	23.7	20.7	8	-	7.1	6.2

[a] for a gas mixture of 15% CO_2 and 85% N_2

To gain further information on the affinity of the adsorptive to the frameworks, the isosteric heats of adsorption (HoA) for CO_2 and CH_4 were calculated and are illustrated in Figure 5.1.18. In case of CO_2, the quadrupole moment of the adsorptive is expected to interact better with polar functionalities within the (modified) MOFs, resulting in higher HoA. With increasing loading, the heat of adsorption is

dominated by adsorbate-adsorbate interactions and is therefore expected to converge to a constant value. This expected behavior is indeed observed for CAU-1-SBU (-37.8), -Ac (-60.1) and -Succ ($\approx$ -45.0) compared to the 32.3 kJ·mol^{-1} of the pristine CAU-1. As predicted, the HoA level to values between 23 and 27 kJ·mol^{-1}. For CAU-1-SBU, the increased HoA can be attributed to beneficial interactions of the adsorptive with the hydroxy groups of the SBU, in CAU-1-Succ with the carboxylic groups, with values typical for physisorption. However, the unexpectedly high value of CAU-1-Ac suggests a very strong, chemisorptive interaction with the framework, exceeding by far those values reported in other amides (20 – 30 kJ·mol^{-1}).[47,48] We therefore attribute this behavior to the error-prone measurement at very low pressures. CAU-1-Prop also shows an unexpected behavior with decreasing HoA at low pressures experiencing a sudden rise. The non-uniform, irrational behavior is well seen for the rest of the modifications, giving an inconsistent picture. Bearing in mind the poor quality of the isotherms for the very low uptakes, the validity of the calculated HoA is questionable. This is also the case for CH_4. While CAU-1, -SBU, -Ac, -TfAc and, surprisingly -Prop, show converging values between -15 and -20 kJ·mol^{-1} at higher uptakes, the rest of the modifications exhibit a large deviance (12. Interestingly, the highest HoA for methane is observed for CAU-1-Succ ($\approx$ -45 kJ·mol^{-1}). Whether this is actually a realistic value, is questionable. All in all, the calculated HoA for CAU-1, -SBU, -Ac, -TfAc and -Prop seem to converge on values in line with the order of magnitude with those reported for other MOFs (-10 to -30 kJ·mol^{-1}).[13,62,63]
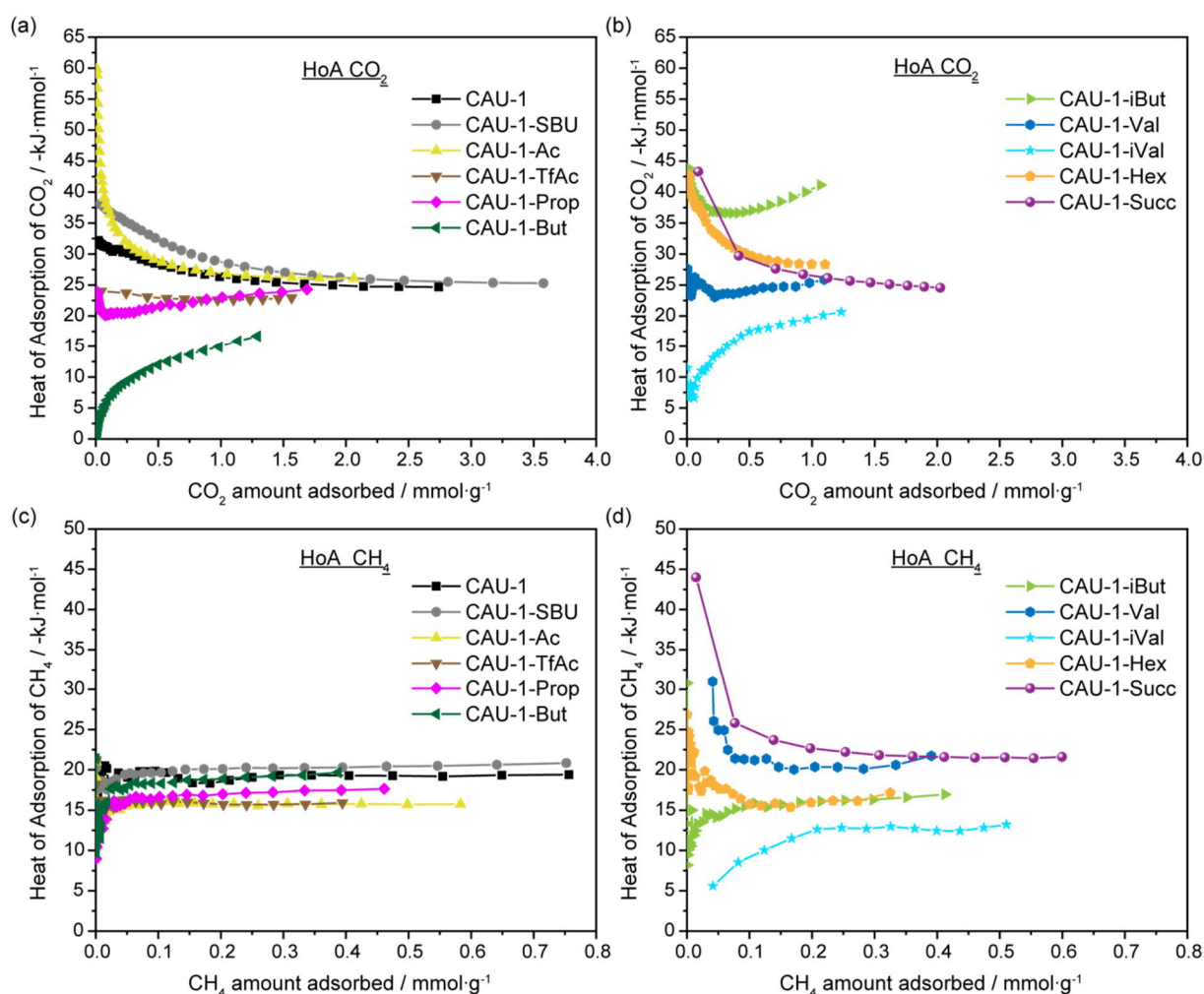
Figure 5.1.18: Heats of adsorption of the (modified) CAU-1 nanoparticles of (a+b) CO_2 and (c+d) CH_4.

5.1.4 CONCLUSIONS

In this work, several post-synthetic modifications of CAU-1 nanoparticles were successfully conducted and evaluated for their adsorptive behavior towards Ar, CO_2, N_2 and CH_4. The modification procedures proved to retain the crystallinity and nanoparticulate sizes of approximately 80 – 120 nm with modification degrees above 83%, only unaccomplished by CAU-1-Succ with 72%. Furthermore, characterization by argon physisorption experiments yielded decreasing BET surfaces areas and micropore volumes with increasing sizes of the introduced groups by the PSMs. In order to assess the efficiency of the modifications for CO_2 storage capacity and separation performance from N_2 and CH_4, adsorption isotherms were measured and the Henry and IAST selectivities calculated. The CO_2 uptakes proved to be primarily determined by the surface area available. In addition, the results highlight the importance of polar groups for superior affinity to CO_2 over N_2 and CH_4, as evidenced by the sample CAU-1-SBU exposing a beneficial amine group on the organic linker and several hydroxy groups at the

SBU – although the selectivities are not competitive with benchmark MOFs. The results calculated from the equilibrium isotherms are summarized in Table 5.1.11.

Table 5.1.11: Summary of BET surface areas, micropore volumes, adsorption isotherms, heats of adsorption at the lowest uptakes as well as derived Henry and IAST selectivities of the (modified) CAU-1 nanoparticles.

	BET SA / m^2g^{-1}	μ-pore volume / cm^3g^{-1}	CO_2 uptake at 1 bar / $mmol·g^{-1}$		Heat of adsorption CO_2/ $kJ·mol^{-1}$	CH_4 uptake at 1 bar / $mmol·g^{-1}$		Heat of adsorption CH_4/ $kJ·mol^{-1}$
			273 K	288 K		273 K	288 K	
CAU-1	1405	0.54	4.51	3.03	-32.3	1.18	0.81	-20.7
CAU-1-SBU	1707	0.58	5.74	3.91	-37.8	1.21	0.79	-21.3
CAU-1-Ac	936	0.37	3.35	2.23	-60.1	0.93	0.67	-21.0
CAU-1-TfAc	798	0.32	2.29	1.57	-24.8	0.63	0.46	-21.2
CAU-1-Prop	809	0.32	2.70	1.87	-24.9	0.73	0.51	-15.2
CAU-1-But	638	0.25	1.85	1.41	-1.0	0.61	0.41	-21.4
CAU-1-iBut	683	0.26	2.08	1.50	-43.9	0.66	0.47	-30.8
CAU-1-Val	546	0.19	1.69	1.23	-27.5	0.63	0.40	-30.9
CAU-1-iVal	567	0.21	1.74	1.28	-11.5	0.72	0.55	-5.6
CAU-1-Hex	473	0.18	1.61	1.14	-42.8	0.50	0.36	-26.8
CAU-1-Succ	776	0.30	2.94	2.11	-44.3	0.93	0.63	-44.0
	CO_2/N_2				CO_2/CH_4			
	Henry		IAST[a]		Henry		IAST[a]	
	273 K	288 K	273 K	288 K	273 K	288 K	273 K	288 K
CAU-1	38	22	38	22	38	22	38	22
CAU-1-SBU	64	46	64	46	64	46	64	46
CAU-1-Ac	26	12	26	12	26	12	26	12
CAU-1-TfAc	20	5	20	5	20	5	20	5
CAU-1-Prop	25	31	25	31	25	31	25	31
CAU-1-But	3	22	3	22	3	22	3	22
CAU-1-iBut	35	22	35	22	35	22	35	22
CAU-1-Val	14	18	14	18	14	18	14	18
CAU-1-iVal	7	10	7	10	7	10	7	10
CAU-1-Hex	37	25	37	25	37	25	37	25
CAU-1-Succ	24	25	24	25	24	25	24	25

[a] for a gas mixture of 15% CO_2 and 85% N_2

More importantly, this study highlights synthetic issues when it comes to ultramicroporous materials. Bearing in mind a pore size of 10 Å for the pristine MOF CAU-1, the introduced post-synthetic modifications diminish the pore sizes significantly and, hence, reduce the overall uptake capacities of the modified MOFs. Small reaction yields require several batches to be merged to accumulate enough material, introducing batch-to-batch errors. If a total of a maximum of 50 mg of sample is available measurement accuracy is considerably decreased. This, in turn, leads to large errors in the measured isotherms at those minimal uptakes. Consequently, an evaluation of the selectivities – as well as the calculation of the HoA – is prone to a large error preventing a sensible and rational classification of their performance compared to other MOF materials and the elucidation of trends. This is particularly exasperating as the sorption behavior at very low pressures reflects the adsorbate-adsorbent interaction most accurately. For a rational evaluation, a considerably larger amount of material has to be measured to avoid these errors. Naturally, further measurements at different temperatures would also help to improve the quality of the data.

Furthermore, we consider that evaluation methods for the selectivities based on non-equilibrium conditions, such as breakthrough experiments, might describe effects dominant in very small pores better, as the nanoparticle nature of the samples would become evident, e.g. due to the altered interparticulate diffusion pathways. Nonetheless, we stress that the results for the demethoxylated sample CAU-1-SBU evidence that the surface area and polarity of the functional groups are predominant in contributing to enhanced and preferential CO_2 adsorption, affirmed by the selectivity and HoA calculations.

5.1.5 Acknowledgments

We thank V. Duppel (MPI for Solid State Research) and C. Minke (LMU Munich) for help with the material characterization. Further, we thank S. Harm for Pawley fitting and crystallite domain size extraction from the PXRD patterns.

5.1.6 References

1   J. R. Long and O. M. Yaghi, Chem. Soc. Rev. 2009, 38, 1213-1214.

2   J. L. C. Rowsell and O. M. Yaghi, Microporous Mesoporous Mater. 2004, 73, 3-14.

3   M. J. Rosseinsky, Microporous Mesoporous Mater. 2004, 73, 15-30.

4   S. M. Cohen, Chem. Rev. (Washington, DC, U. S.) 2012, 112, 970-1000.

5   S. M. Cohen, J. Am. Chem. Soc. 2017, 139, 2855-2863.

6   K. K. Tanabe and S. M. Cohen, Chem. Soc. Rev. 2011, 40, 498-519.

7   B. Li, H.-M. Wen, W. Zhou and B. Chen, J. Phys. Chem. Lett. 2014, 5, 3468-3479.

8   R. E. Morris and P. S. Wheatley, Angew. Chem. Int. Ed. 2008, 47, 4966-4981.

9   E. Barea, C. Montoro and J. A. R. Navarro, Chem. Soc. Rev. 2014, 43, 5419-5430.

10   X. Han, H. G. W. Godfrey, L. Briggs, A. J. Davies, Y. Cheng, L. L. Daemen, A. M. Sheveleva, F. Tuna, E. J. L. McInnes, J. Sun, C. Drathen, M. W. George, A. J. Ramirez-Cuesta, K. M. Thomas, S. Yang and M. Schröder, Nat. Mater. 2018, 17, 691-696.

11   J. Liu, B. P. McGrail, D. M. Strachan, J. Liu, J. Tian and P. K. Thallapally, in Encyclopedia of Inorganic and Bioinorganic Chemistry, Ed. R. A. Scott, John Wiley & Sons, Ltd., 2014.

12   X. Lin, J. Jia, N. R. Champness, P. Hubberstey and M. SchröDer, in Solid-State Hydrogen Storage, Ed. G. Walker, Woodhead Publishing, 2008, 288-312.

13   J. A. Mason, M. Veenstra and J. R. Long, Chem. Sci. 2014, 5, 32-51.

14   M. P. Suh, H. J. Park, T. K. Prasad and D.-W. Lim, Chem. Rev. (Washington, DC, U. S.) 2012, 112, 782-835.

15   B. Wang, L.-H. Xie, X. Wang, X.-M. Liu, J. Li and J.-R. Li, Green Energy & Environment 2018, 3, 191-228.

16   IPCC, 2013, Climate Change 2013: The Physical Science Basis. Contribution of Working Group I to the Fifth Assessment Report of the Intergovernmental Panel on Climate Change, Eds. T. F. Stocker, D. Qin, G.-K. Plattner, M. Tignor, S. K. Allen, J. Boschung, A. Nauels, Y. A. Xia, V. Bex and P. M. Midgley, Cambridge, United Kingdom and New York, NY, USA.

17   IPCC, 2005, Special Report on Carbon Dioxide Capture and Storage, B. Metz, O. Davidson, H. de Coninck, M. Loos and L. Meyer, Cambridge, United Kingdom/New York, NY, USA.

18   T. E. Rufford, S. Smart, G. C. Y. Watson, B. F. Graham, J. Boxall, J. C. Diniz da Costa and E. F. May, J. Pet. Sci. Eng. 2012, 94-95, 123-154.

19   T. E. Perez, JOM 2013, 65, 1033-1042.

20   J. W. Maina, C. Pozo-Gonzalo, L. Kong, J. Schütz, M. Hill and L. F. Dumée, Mater. Horiz. 2017, 4, 345-361.

21   Y. Chen, D. Wang, X. Deng and Z. Li, Catal. Sci. Technol. 2017, 7, 4893-4904.

22   J. Yu, L.-H. Xie, J.-R. Li, Y. Ma, J. M. Seminario and P. B. Balbuena, Chem. Rev. (Washington, DC, U. S.) 2017, 117, 9674-9754.

23   K. Sumida, D. L. Rogow, J. A. Mason, T. M. McDonald, E. D. Bloch, Z. R. Herm, T.-H. Bae and J. R. Long, Chem. Rev. (Washington, DC, U. S.) 2012, 112, 724-781.

24   K. C. Stylianou and W. L. Queen, CHIMIA 2015, 69, 274-283.

25   C. A. Trickett, A. Helal, B. A. Al-Maythalony, Z. H. Yamani, K. E. Cordova and O. M. Yaghi, Nat. Rev. Mater. 2017, 2, 17045.

26   Y.-S. Bae, O. K. Farha, A. M. Spokoyny, C. A. Mirkin, J. T. Hupp and R. Q. Snurr, Chem. Commun. 2008, 4135-4137.

27   R. M. Marti, J. D. Howe, C. R. Morelock, M. S. Conradi, K. S. Walton, D. S. Sholl and S. E. Hayes, J. Phys. Chem. C 2017, 121, 25778-25787.

28   J. Qian, Q. Li, L. Liang, T.-T. Li, Y. Hu and S. Huang, Dalton Trans. 2017, 46, 14102-14106.

29   Y. Lin, C. Kong and L. Chen, RSC Adv. 2012, 2, 6417-6419.

30   R. Vaidhyanathan, S. S. Iremonger, G. K. H. Shimizu, P. G. Boyd, S. Alavi and T. K. Woo, Science 2010, 330, 650-653.

31   D. Wu, T. M. McDonald, Z. Quan, S. V. Ushakov, P. Zhang, J. R. Long and A. Navrotsky, J. Mater. Chem. B 2015, 3, 4248-4254.

32   P. Kanoo, A. C. Ghosh, S. T. Cyriac and T. K. Maji, Chem. Eur. J. 2011, 18, 237-244.

33   Z. Lu, Y. Xing, L. Du, H. He, J. Zhang and C. Hang, RSC Adv. 2017, 7, 47219-47224.

34   G. Feng, Y. Peng, W. Liu, F. Chang, Y. Dai and W. Huang, Inorg. Chem. 2017, 56, 2363-2366.

35   Z.-R. Jiang, H. Wang, Y. Hu, J. Lu and H.-L. Jiang, ChemSusChem 2015, 8, 878-885.

36   Z. Xiang, S. Leng and D. Cao, J. Phys. Chem. C 2012, 116, 10573-10579.

37   Y. Wang and D. Zhao, Cryst. Growth Des. 2017, 17, 2291-2308.

38   J.-R. Li, R. J. Kuppler and H.-C. Zhou, Chem. Soc. Rev. 2009, 38, 1477-1504.

39   N. T. T. Nguyen, H. Furukawa, F. Gándara, H. T. Nguyen, K. E. Cordova and O. M. Yaghi, Angew. Chem. Int. Ed. 2014, 53, 10645-10648.

40   D. Andirova, Y. Lei, X. Zhao and S. Choi, ChemSusChem 2015, 8, 3405-3409.

41   A. Sayari and Y. Belmabkhout, J. Am. Chem. Soc. 2010, 132, 6312-6314.

42   X. Si, C. Jiao, F. Li, J. Zhang, S. Wang, S. Liu, Z. Li, L. Sun, F. Xu, Z. Gabelica and C. Schick, Energy Environ. Sci. 2011, 4, 4522-4527.

43   T. Ahnfeldt, N. Guillou, D. Gunzelmann, I. Margiolaki, T. Loiseau, G. Férey, J. Senker and N. Stock, Angew. Chem. 2009, 121, 5265-5268.

44   D.-J. Lee, Q. Li, H. Kim and K. Lee, Microporous Mesoporous Mater. 2012, 163, 169-177.

45   D. Ectors, F. Goetz-Neunhoeffer and J. Neubauer, J. Appl. Crystallogr. 2015, 48, 189-194.

46   M. Karabacak, M. Cinar, Z. Unal and M. Kurt, J. Mol. Struct. 2010, 982, 22-27.

47   C.-H. Lee, H.-Y. Huang, Y.-H. Liu, T.-T. Luo, G.-H. Lee, S.-M. Peng, J.-C. Jiang, I. Chao and K.-L. Lu, Inorg. Chem. 2013, 52, 3962-3968.

48   B. Zheng, J. Bai, J. Duan, L. Wojtas and M. J. Zaworotko, J. Am. Chem. Soc. 2011, 133, 748-751.

49   L. Du, S. Yang, L. Xu, H. Min and B. Zheng, CrystEngComm 2014, 16, 5520-5523.

50   S. Xiong, Y. He, R. Krishna, B. Chen and Z. Wang, Cryst. Growth Des. 2013, 13, 2670-2674.

51   Z. Lu, J. Bai, C. Hang, F. Meng, W. Liu, Y. Pan and X. You, Chem. Eur. J. 2016, 22, 6277-6285.

52   Y.-Q. Chen, Y.-K. Qu, G.-R. Li, Z.-Z. Zhuang, Z. Chang, T.-L. Hu, J. Xu and X.-H. Bu, Inorg. Chem. 2014, 53, 8842-8844.

53   O. Benson, I. da Silva, S. P. Argent, R. Cabot, M. Savage, H. G. W. Godfrey, Y. Yan, S. F. Parker, P. Manuel, M. J. Lennox, T. Mitra, T. L. Easun, W. Lewis, A. J. Blake, E. Besley, S. Yang and M. Schröder, J. Am. Chem. Soc. 2016, 138, 14828-14831.

54   Y. He, W. Zhou, G. Qian and B. Chen, Chem. Soc. Rev. 2014, 43, 5657-5678.

55   B. Li, H.-M. Wen, W. Zhou, Jeff Q. Xu and B. Chen, Chem 2016, 1, 557-580.

56   Y. Lin, C. Kong, Q. Zhang and L. Chen, Adv. Energy Mater. 2016, 7, 1601296.

57   A. L. Myers and J. M. Prausnitz, AIChE J. 1965, 11, 121-127.

58   K. S. Walton and D. S. Sholl, AIChE J. 2015, 61, 2757-2762.

59   D. M. D'Alessandro, B. Smit and J. R. Long, Angew. Chem. Int. Ed. 2010, 49, 6058-6082.

60   Z. Zhang, Z.-Z. Yao, S. Xiang and B. Chen, Energy Environ. Sci. 2014, 7, 2868-2899.

61   P. Nugent, Y. Belmabkhout, S. D. Burd, A. J. Cairns, R. Luebke, K. Forrest, T. Pham, S. Ma, B. Space, L. Wojtas, M. Eddaoudi and M. J. Zaworotko, Nature 2013, 495, 80.

62   H. Wu, W. Zhou and T. Yildirim, J. Am. Chem. Soc. 2009, 131, 4995-5000.

63   D. Wu, X. Guo, H. Sun and A. Navrotsky, J. Phys. Chem. Lett. 2015, 6, 2439-2443.

5.1.7 SUPPORTING INFORMATION

Supplementary Figures and Tables
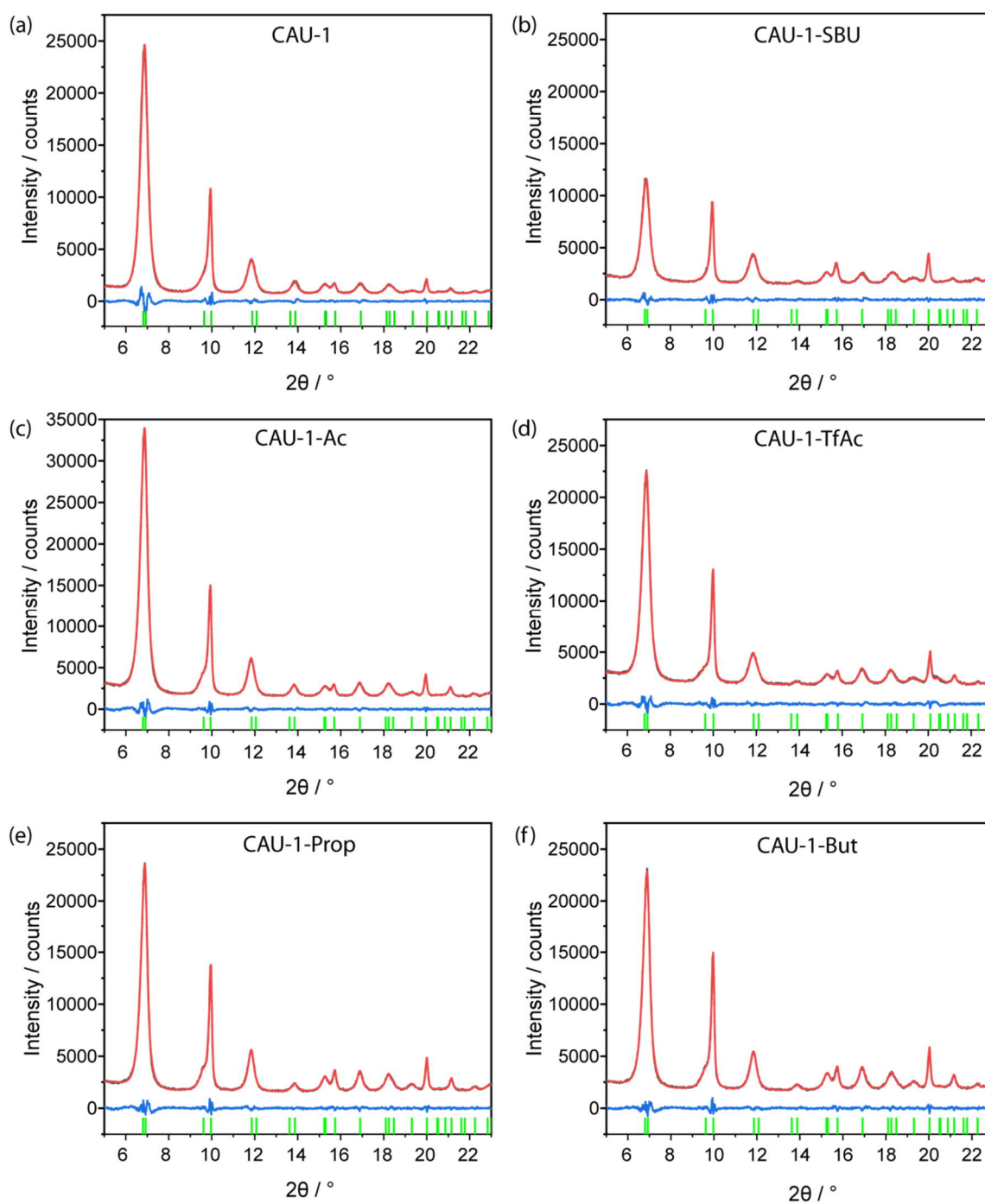
Figure S5.1.1: Pawley fits of of (a) CAU-1, (b) CAU-1-SBU, (c) CAU-1-Ac, (d) CAU-1-TfAc, (e) CAU-1-Prop, (f) CAU-1-But. The black, red, blue and red lines represent the experimental data, the calculated pattern, the difference plots and the reflex positions.

Figure S5.1.2: Pawley fits of of (a) CAU-1-iBut, (b) CAU-1-Val, (c) CAU-1-iVal, (d) CAU-1-Hex and (e) CAU-1-Succ. The black, red, blue and red lines represent the experimental data, the calculated pattern, the difference plots and the reflex positions.
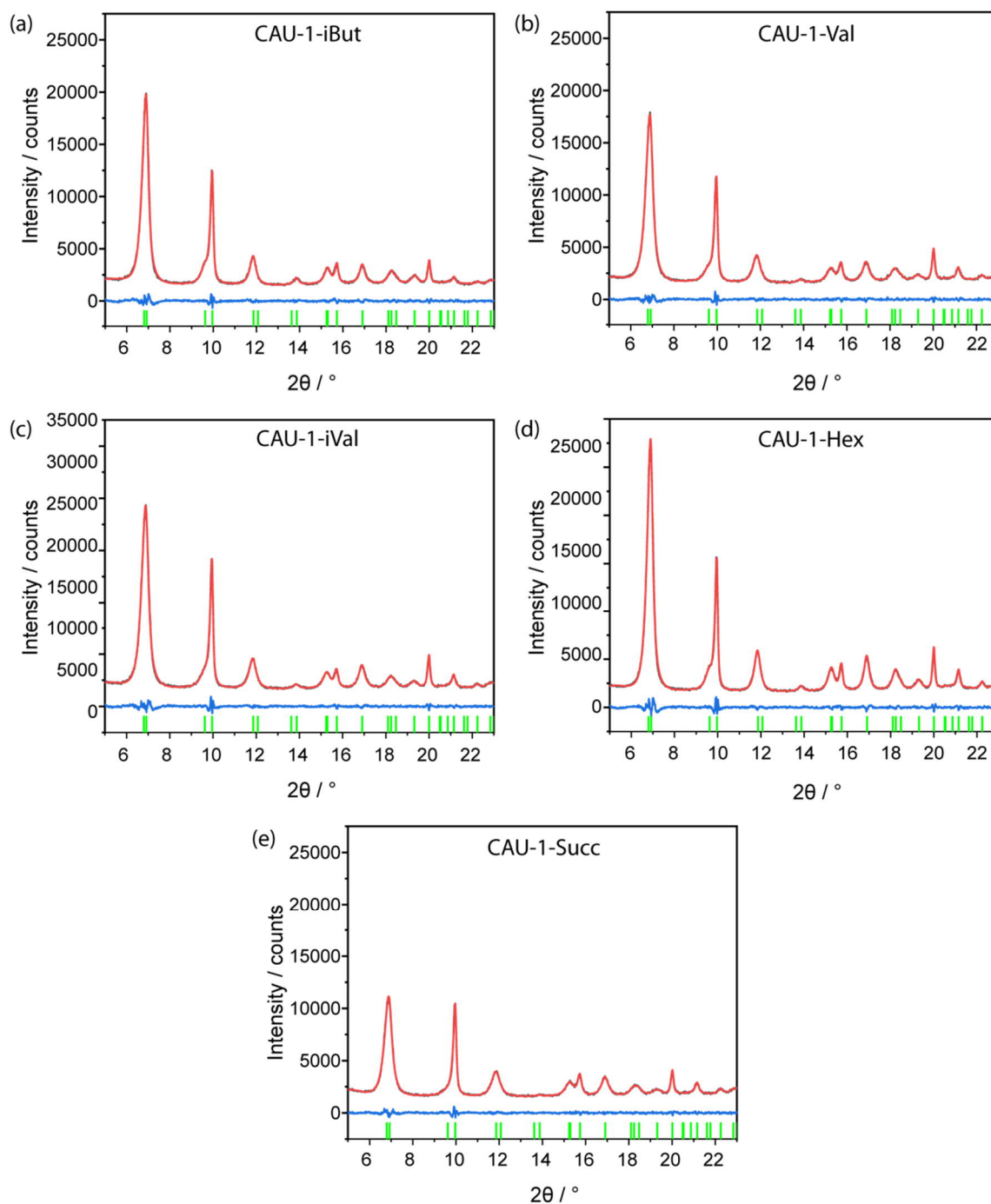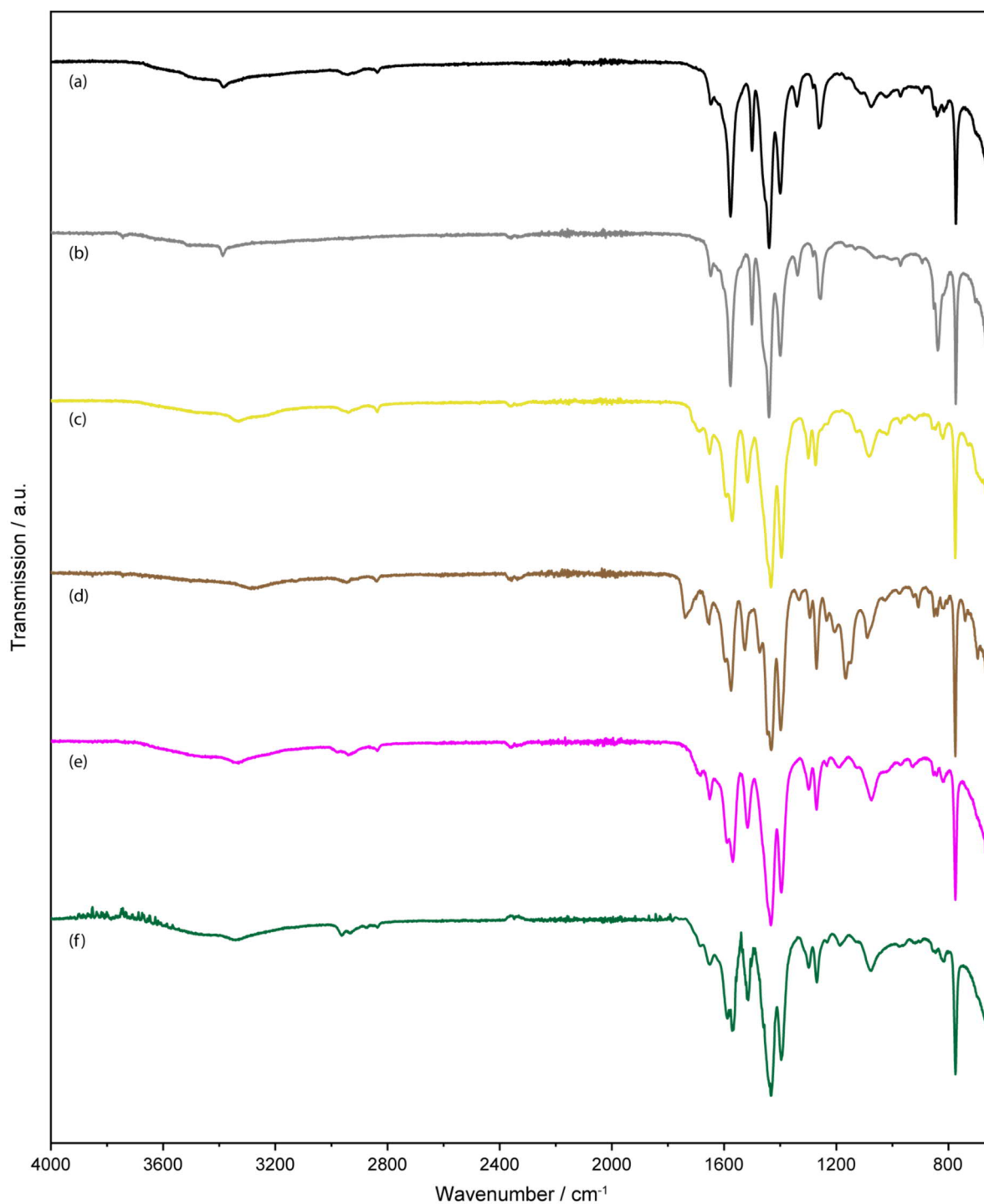
Figure S5.1.3: IR spectra of (a) CAU-1, (b) CAU-1-SBU, (c) CAU-1-Ac, (d) CAU-1-TfAc, (e) CAU-1-Prop and (f) CAU-1-But.
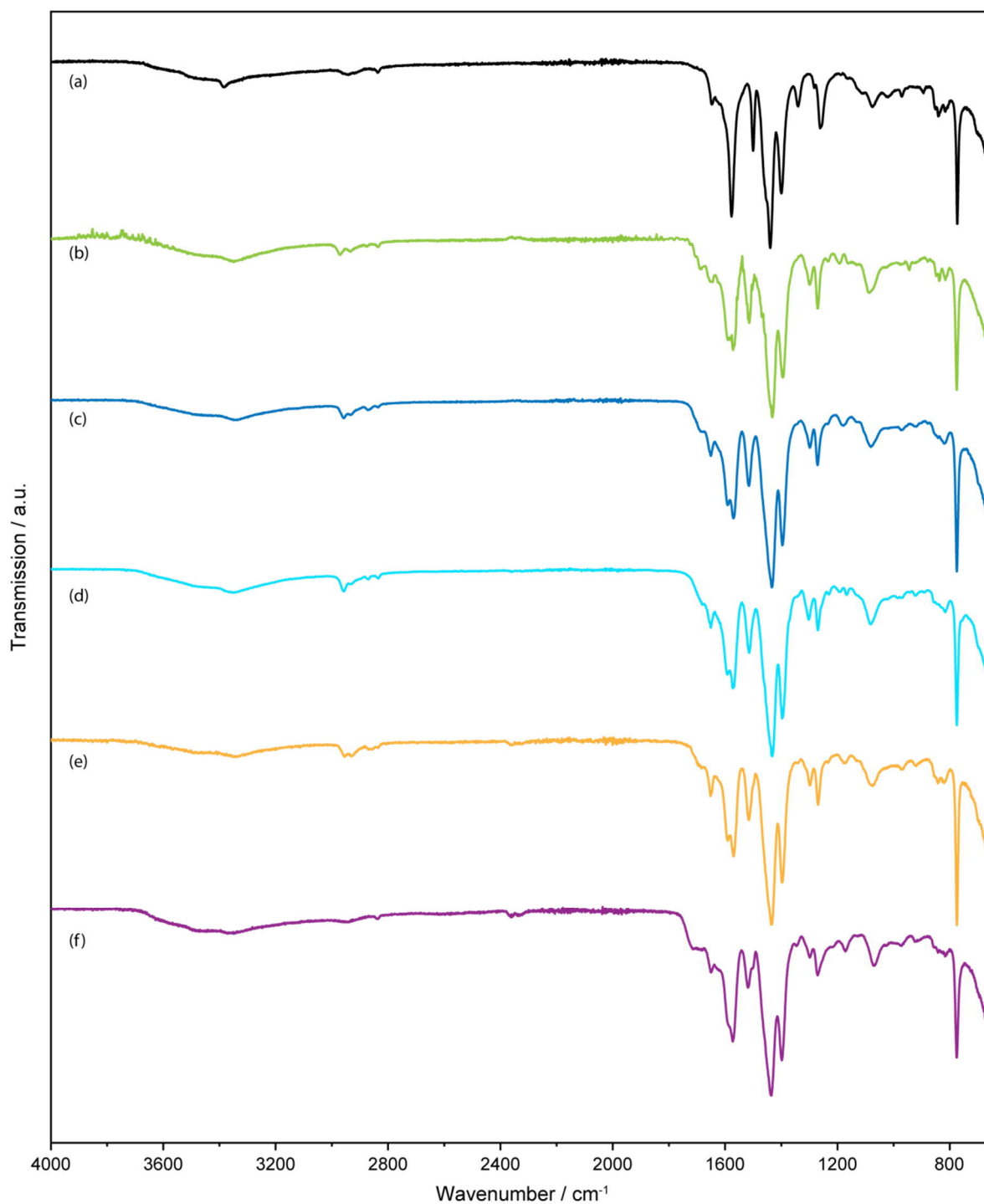
Figure S5.1.4: IR spectra of (a) CAU-1, (b) CAU-1-iBut, (c) CAU-1-Val, (d) CAU-1-iVal, (e) CAU-1-Hex and (f) CAU-1-Succ.

Table S5.1.1: Alkyl, amide, amine, carbonyl and methanolate related vibrational bands of the (modified) CAU-1 nanoparticles in cm^{-1}. Note that the alkyl bands of the modification and methanolate of the SBU overlap and only the most prominent is absorption band is given.

	amine / amide	carbonyl (of amide)	unknown	aromate	amine/ amide		alkyl/ methanolate
CAU-1	3384	-	-	1500	1341	1261	~2941 / 1077
CAU-1-SBU	3385	-	-	1501	1339	1259	- / -
CAU-1-Ac	3330	1698	1595	1517	1300	1272	2942 / 1083
CAU-1-TfAc	3286	1739	1595	1526	1295	1270	2951 / 1086
CAU-1-Prop	3332	1695	1590	1517	1298	1270	2935 / 1077
CAU-1-But	3348	1690	1589	1515	1299	1270	2966 / 1075
CAU-1-iBut	3349	1689	1588	1514	1298	1269	2967 / 1079
CAU-1-Val	3352	1690	1590	1513	1298	1270	2960 / 1079
CAU-1-iVal	3350 (very broad)	1692	1593	1514	1302	1270	2955 / 1081
CAU-1-Hex	3352	1704	1591	1515	1299	1270	2962 / 1081
CAU-1-Succ	3360 (very broad)	1715	1590	1518	1299	1271	2961 / 1069
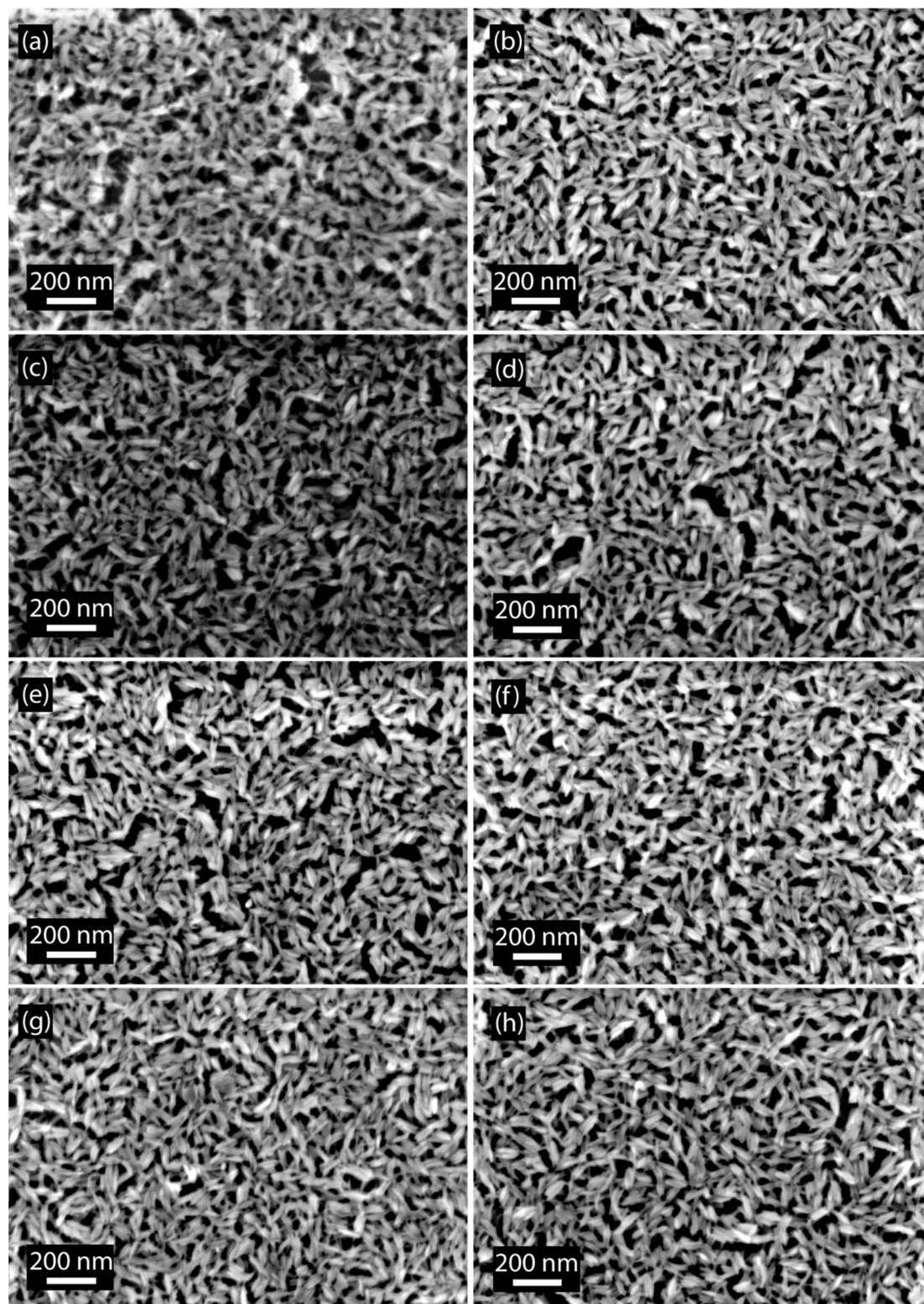
Figure S5.1.5: SEM images of (a) CAU-1-SBU, (b) CAU-1-Ac, (c) CAU-1-TfAc, (d) CAU-1-Prop, (e) CAU-1-But, (f) CAU-1-iBut, (g) CAU-1-Val, (h) CAU-1-iVal. Images were acquired with an InLense detector.
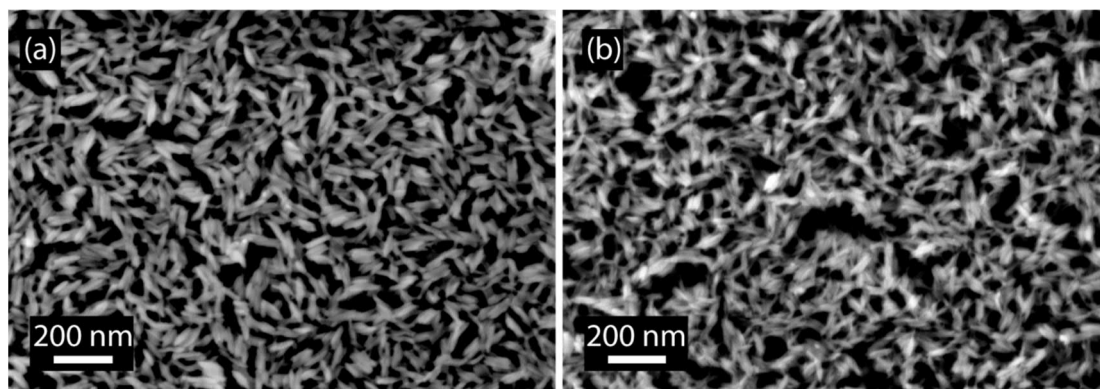
Figure S5.1.6: SEM images of (a) CAU-1-Hex and (b) CAU-1-Succ. Images were acquired with an InLense detector.
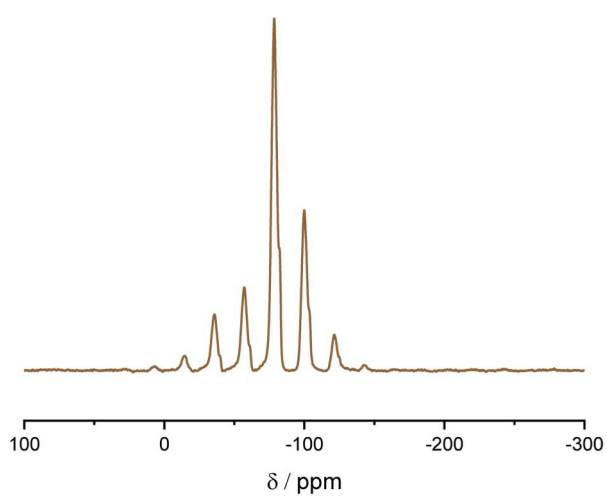
Figure S5.1.7: ^{19}F-NMR of CAU-1-TfAc.
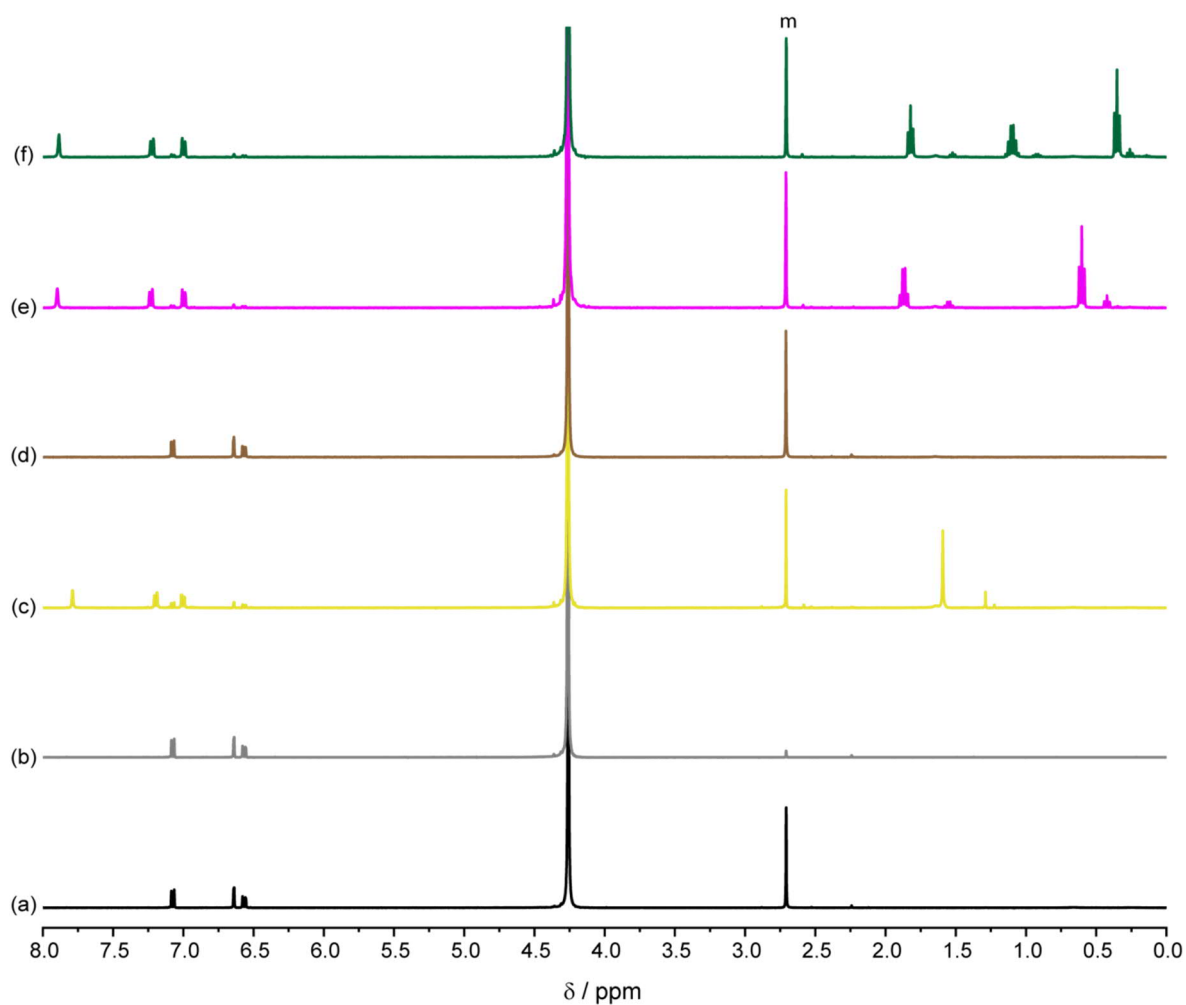
Figure S5.1.8: 1H-NMR spectra of digested (a) CAU-1, (b) CAU-1-SBU, (c) CAU-1-Ac, (d) CAU-1-TfAc, (e) CAU-1-Prop and (f) CAU-1-But. Note that for CAU-1-TfAc digestion led to the cleavage of the trifluoracetamidic bond and, hence, the 2-aminoterephthalate was obtained, as for CAU-1 and CAU-1-SBU. The most intense peak at 4.26 ppm corresponds to the the NaOD/D_2O digestion mixture.

Figure S5.1.9: 1H-NMR spectra of digested (a) CAU-1, (b) CAU-1-iBut, (c) CAU-1-Val, (d) CAU-1-iVal, (e) CAU-1-Hex and (f) CAU-1-Succ. The most intense peak at 4.26 ppm corresponds to the the NaOD/D$_2$O digestion mixture.

CAU-1/CAU-1-SBU

δ 7.07 (d, J = 8.1 Hz, 1H), 6.64 (d, J = 1.7 Hz, 1H), 6.57 (dd, J = 8.1, 1.6 Hz, 1H)

CAU-1-Ac

δ 7.79 (s, 1H), 7.20 (d, J = 8.0 Hz, 1H), 7.00 (dd, J = 8.1, 1.5 Hz, 1H)

CAU-1-Prop

δ 7.90 (s, 1H), 7.23 (d, J = 8.0 Hz, 1H), 7.00 (dd, J = 8.0, 0.8 Hz, 1H), 1.87 (q, J = 7.6 Hz, 2H), 0.60 (t, J = 7.6 Hz, 3H)

CAU-1-But

δ 7.88 (s, 1H), 7.22 (d, J = 8.0, 1H), 6.99 (d, J = 8.0 Hz, 1H), 1.82 (t, J = 7.3 Hz, 2H), 1.10 (h, J = 7.4 Hz, 2H), 0.35 (t, J = 7.4 Hz, 3H)

CAU-1-iBut

δ 7.95 (s, 1H), 7.25 (d, J = 8.0 Hz, 1H), 6.99 (dd, J = 8.1, 1.6 Hz, 1H), 2.05 (p, J = 7.0 Hz, 1H), 0.62 (d, J = 7.0 Hz, 6H)

CAU-1-Val

δ 7.89 (s, 1H), 7.23 (d, J = 8.1 Hz, 1H), 6.99 (dd, J = 8.1, 1.7 Hz, 1H), 1.84 (t, J = 7.4 Hz, 2H), 1.06 (p, J = 7.4 Hz, 2H), 0.76 (h, J = 7.4 Hz, 2H), 0.30 (t, J = 7.4 Hz, 3H)

CAU-1-iVal

δ 7.88 (s, 1H), 7.22 (d, J = 8.1 Hz, 1H), 7.00 (dd, J = 8.1, 1.7 Hz, 1H), 1.71 (d, J = 7.4 Hz, 2H), 1.50 (hept, J = 13.7, 6.8 Hz, 1H), 0.37 (d, J = 6.6 Hz, 6H)

CAU-1-Hex

δ 7.90 (s, 1H), 7.23 (d, J = 8.1 Hz, 1H), 6.99 (dd, J = 8.1, 1.7 Hz, 1H), 1.84 (t, J = 7.4 Hz, 2H), 1.09 (p, J = 7.1 Hz, 2H), 0.77 – 0.68 (m, 4H), 0.30 (t, J = 7.4 Hz, 3H)

CAU-1-Succ

δ 7.89 (s, 1H), 7.23 (d, J = 8.1 Hz, 1H), 6.99 (dd, J = 8.1, 1.7 Hz, 1H), 2.08 (t, J = 7.4 Hz, 2H), 1.94 (t, J = 7.4 Hz, 2H)

Figure S5.1.10: Chemical shifts of the ^{1}H signals of the digested linker of pristine and modified CAU-1 nanoparticles. Note that for CAU-1-TfAc digestion led to the cleavage of the trifluoracetamidic bond and, hence, the 2-aminoterephthalate was obtained, as for CAU-1 and CAU-1-SBU.
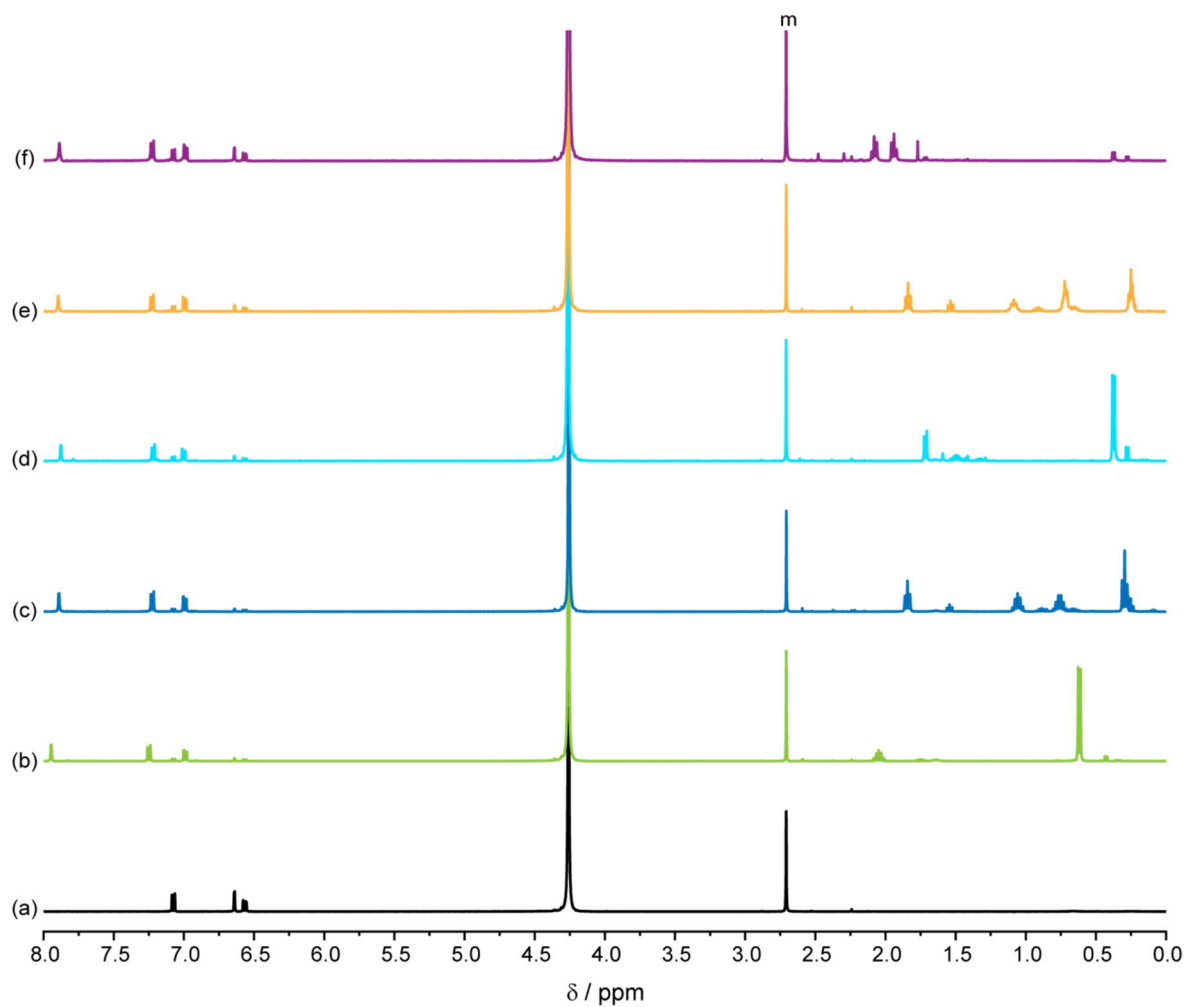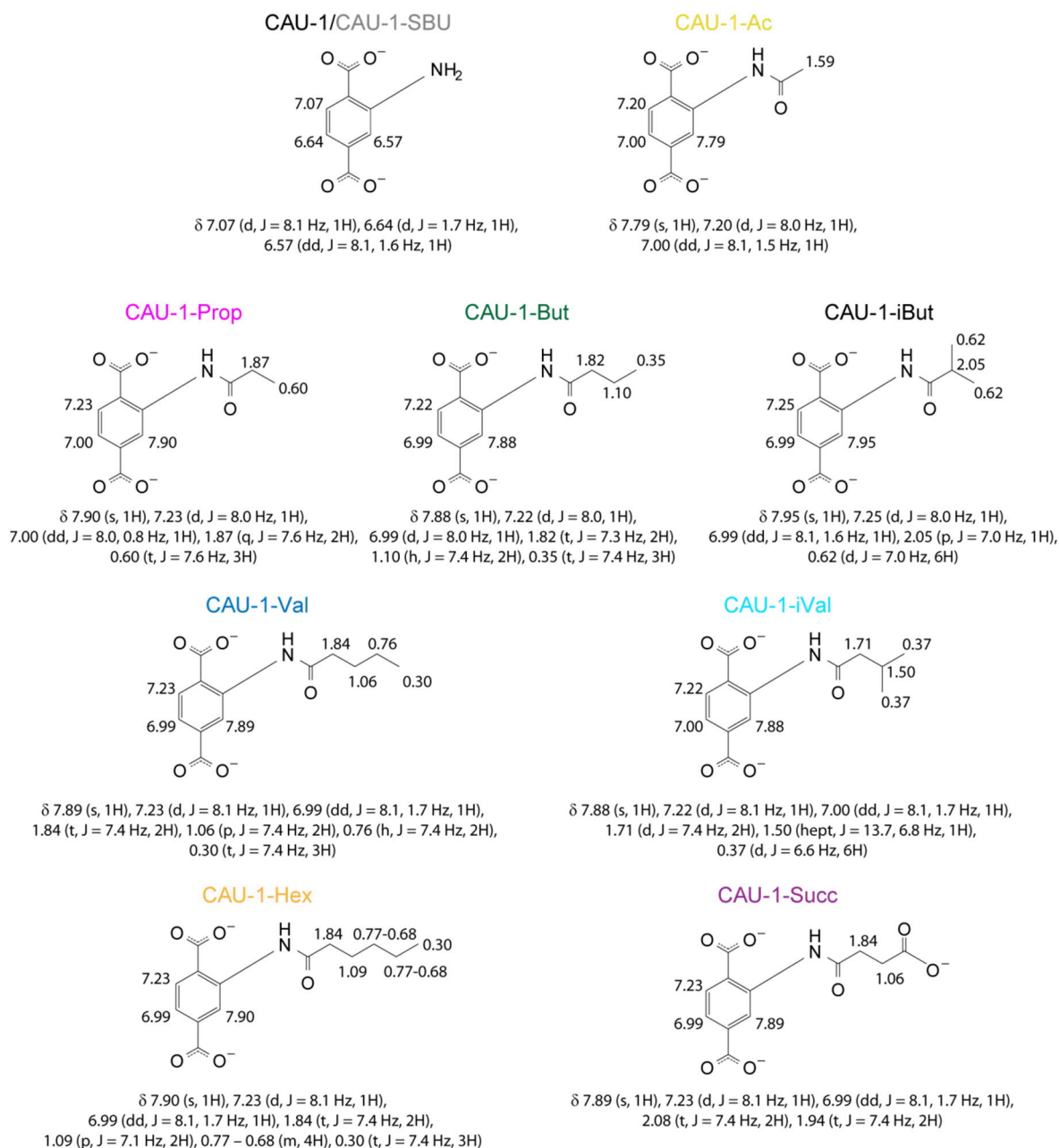
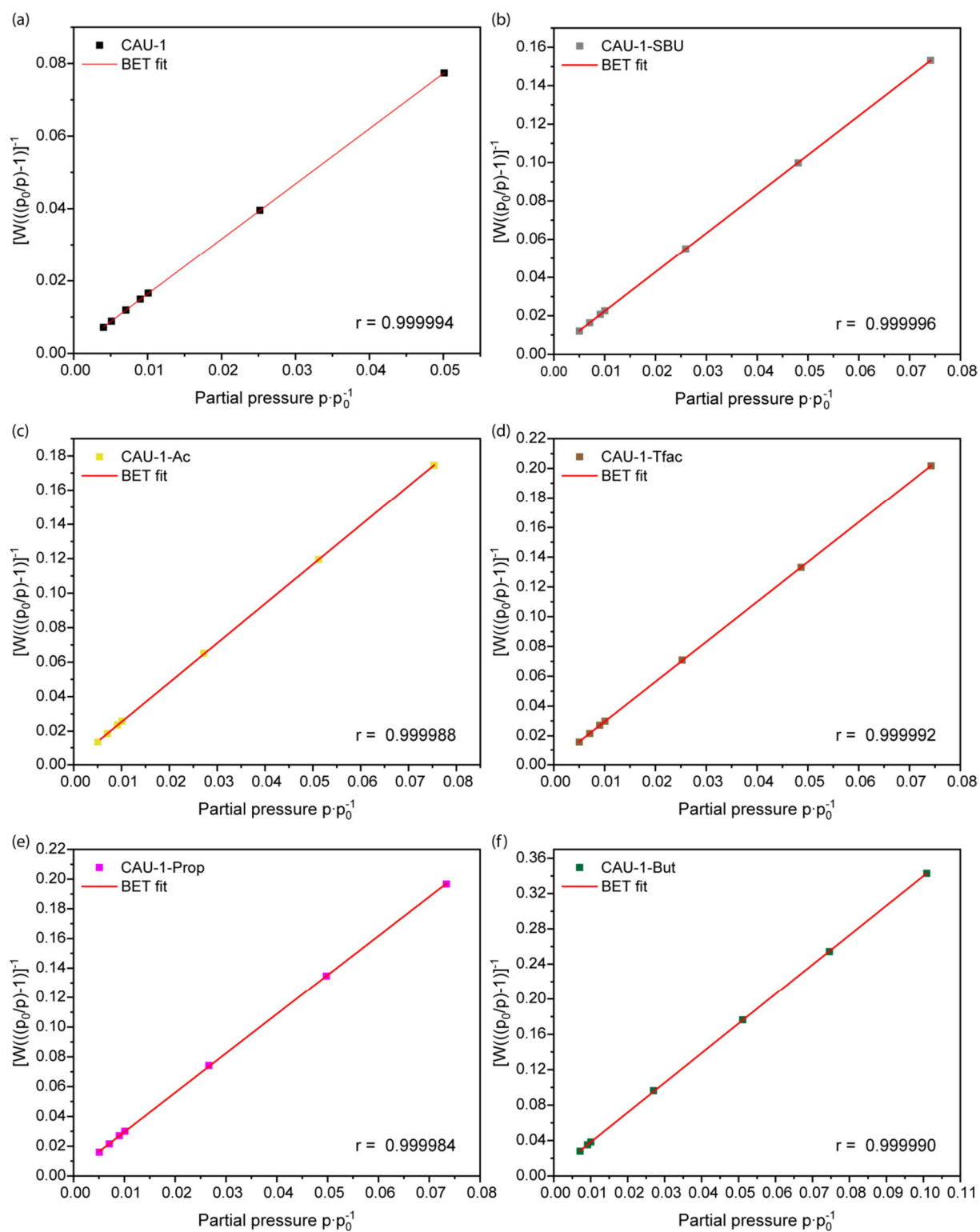Figure S5.1.11: BET plots of (a) CAU-1, (b) CAU-1-SBU, (c) CAU-1-Ac, (d) CAU-1-TfAc, (e) CAU-1-Prop and (f) CAU-1-But. The correlation coefficient r is given at the lower right of each graph.
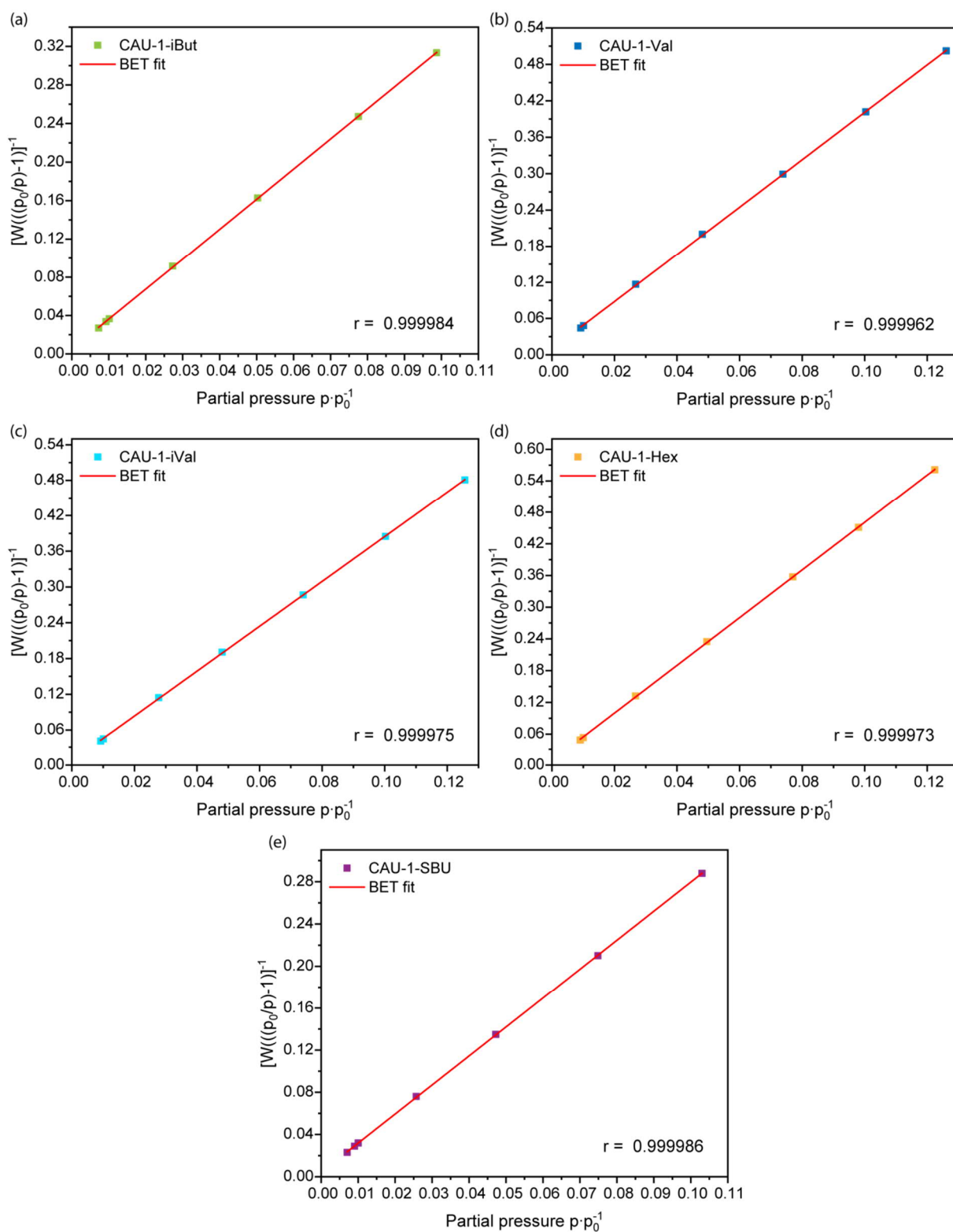
Figure S5.1.12: Argon ad- and desorption isotherms at 87 K of (a) CAU-1-iBut, (b) CAU-1-Val, (c) CAU-1-iVal, (d) CAU-1-Hex and (e) CAU-1-Succ. The correlation coefficient r is given at the lower right of each graph.

Table S5.1.2: BET surface area calculation details.

	CAU-1	CAU-1-SBU	CAU-1-Ac	CAU-1-TfAc	CAU-1-Prop	CAU-1-But
BET SA / m^{2}g^{-1}	1405.153	1707.008	936.194	797.554	808.708	637.654
Slope / g^{-1}	1.522	2.038	2.284	2.681	2.644	3.352
Intercept / g^{-1}	1.151·10^{-3}	4	2.538·10^{-3}	2.728·10^{-3}	3.087·10^{-3}	4.700·10^{-3}
C constant	1323.435	1006.563	900.786	983.726	857.419	714.293
Correlation coefficient	0.999994	0.999996	0.999988	0.999992	0.999984	0.999990
	CAU-1-iBut	CAU-1-Val	CAU-1-iVal	CAU-1-Hex	CAU-1-Succ	
BET SA / m^{2}g^{-1}	683.355	545.917	567.537	473.360	776.286	
Slope / g^{-1}	3.127	3.911	3.764	4.513	2.753	
Intercept / g^{-1}	5.021·10^{-3}	9.931·10^{-3}	8.245·10^{-3}	9.496·10^{-3}	4.340e-03	
C constant	623.937	394.853	457.476	476.218	635.345	
Correlation coefficient	0.999984	0.999962	0.999975	0.999973	0.999986	
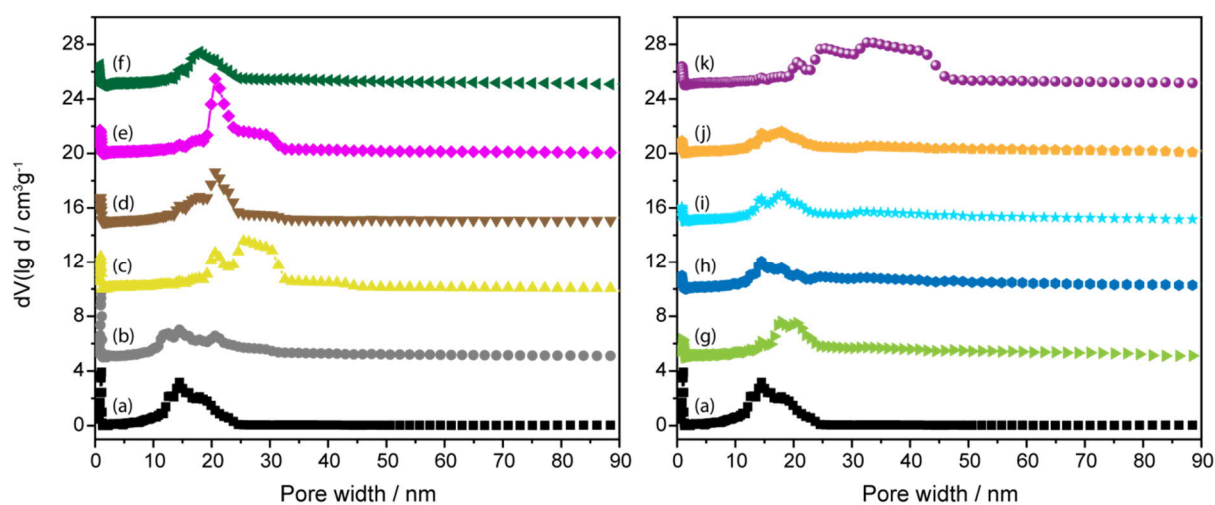
Figure S5.1.13: PSD of (a) CAU-1, (b) CAU-1-SBU, (c) CAU-1-Ac, (d) CAU-1-TfAc, (e) CAU-1-Prop, (f) CAU-1-But, (g) CAU-1-iBut, (h) CAU-1-Val, (i) CAU-1-iVal, (j) CAU-1-Hex and (k) CAU-1-Succ.
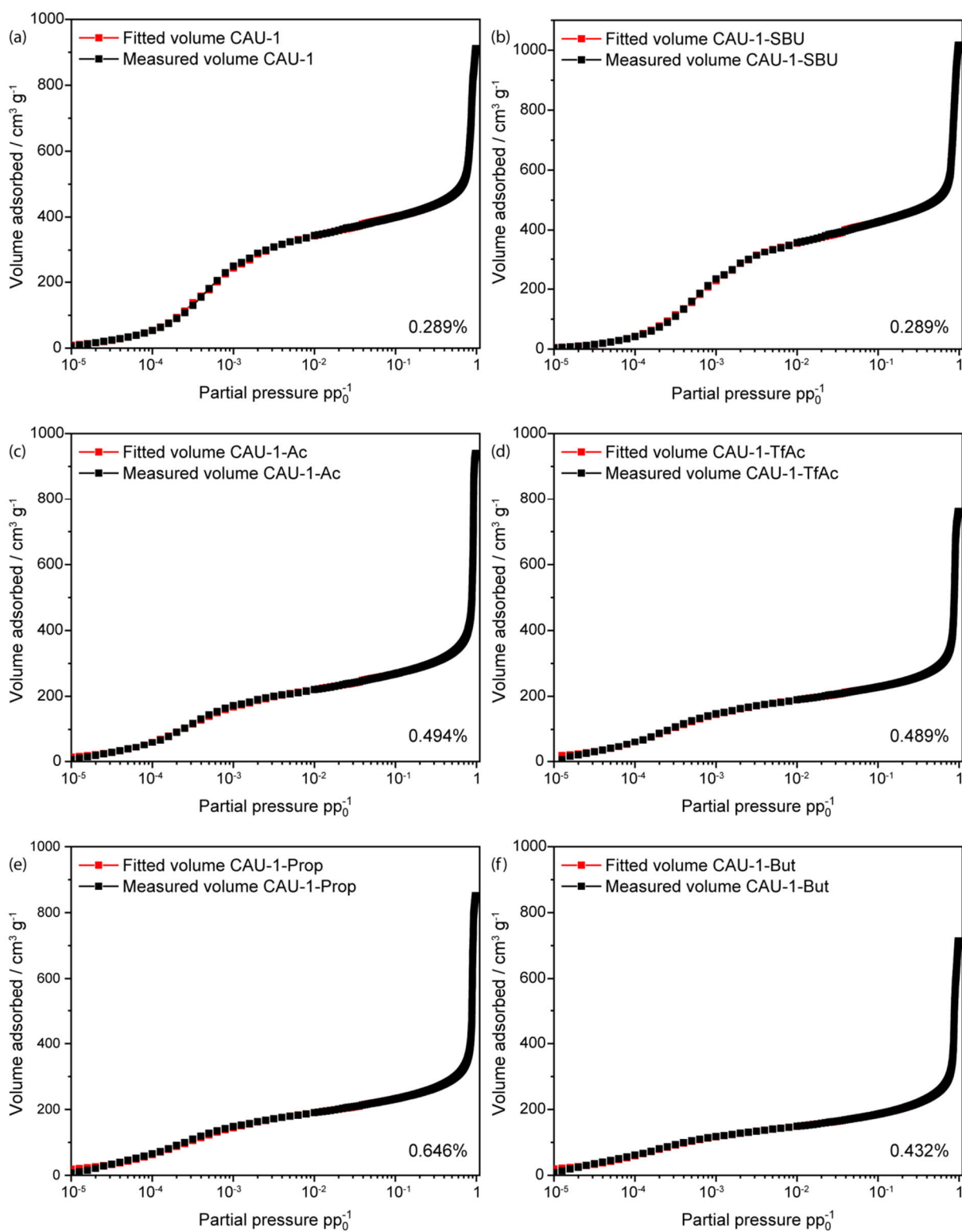
Figure S5.1.14: Argon NLDFT fits of (a) CAU-1, (b) CAU-1-SBU, (c) CAU-1-Ac, (d) CAU-1-TfAc, (e) CAU-1-Prop and (f) CAU-1-But. The fitting error is given at the lower right of each graph.
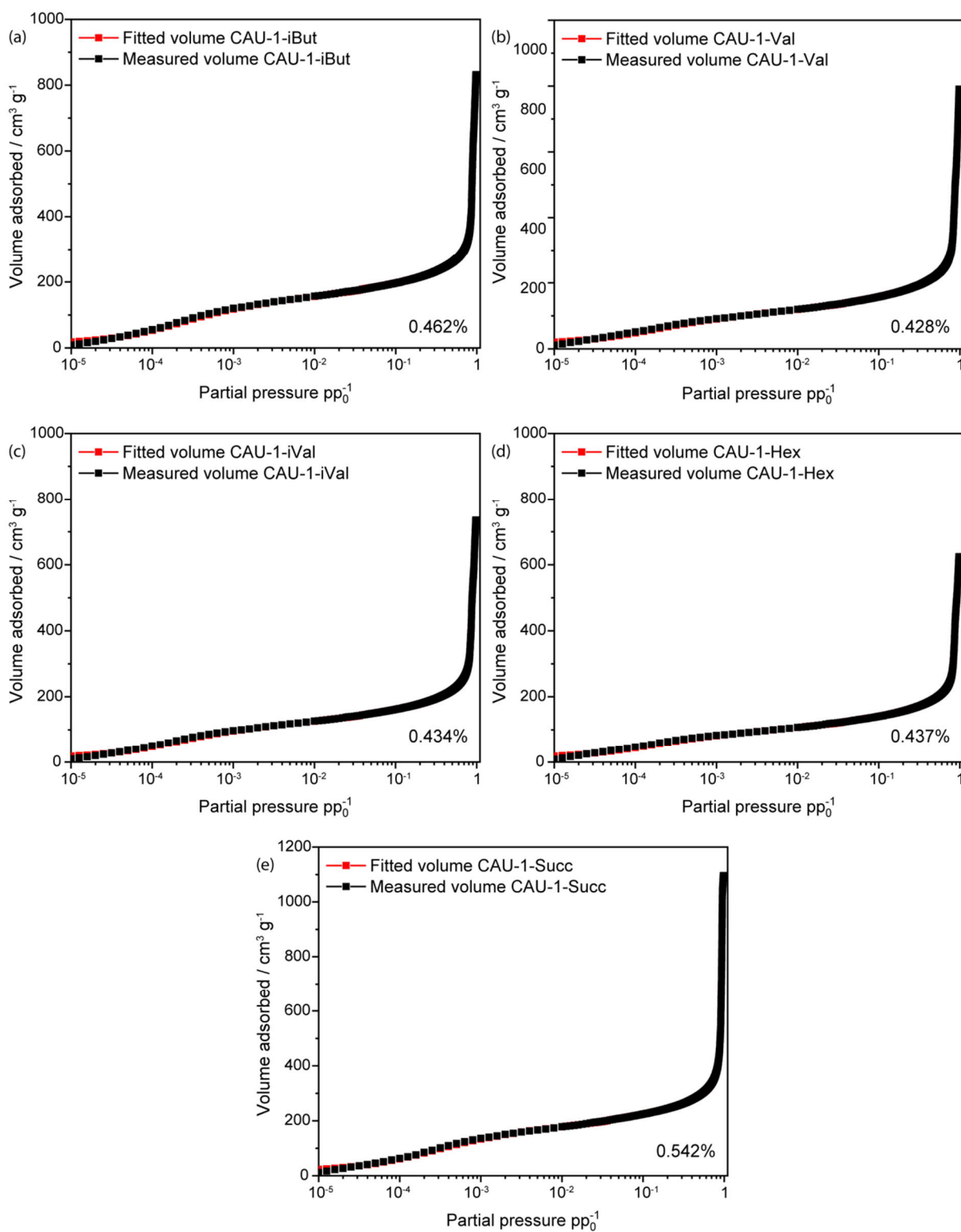
Figure S5.1.15: Argon NLDFT fits of (a) CAU-1-iBut, (b) CAU-1-Val, (c) CAU-1-iVal, (d) CAU-1-Hex and (e) CAU-1-Succ. The fitting error is given at the lower right of each graph.
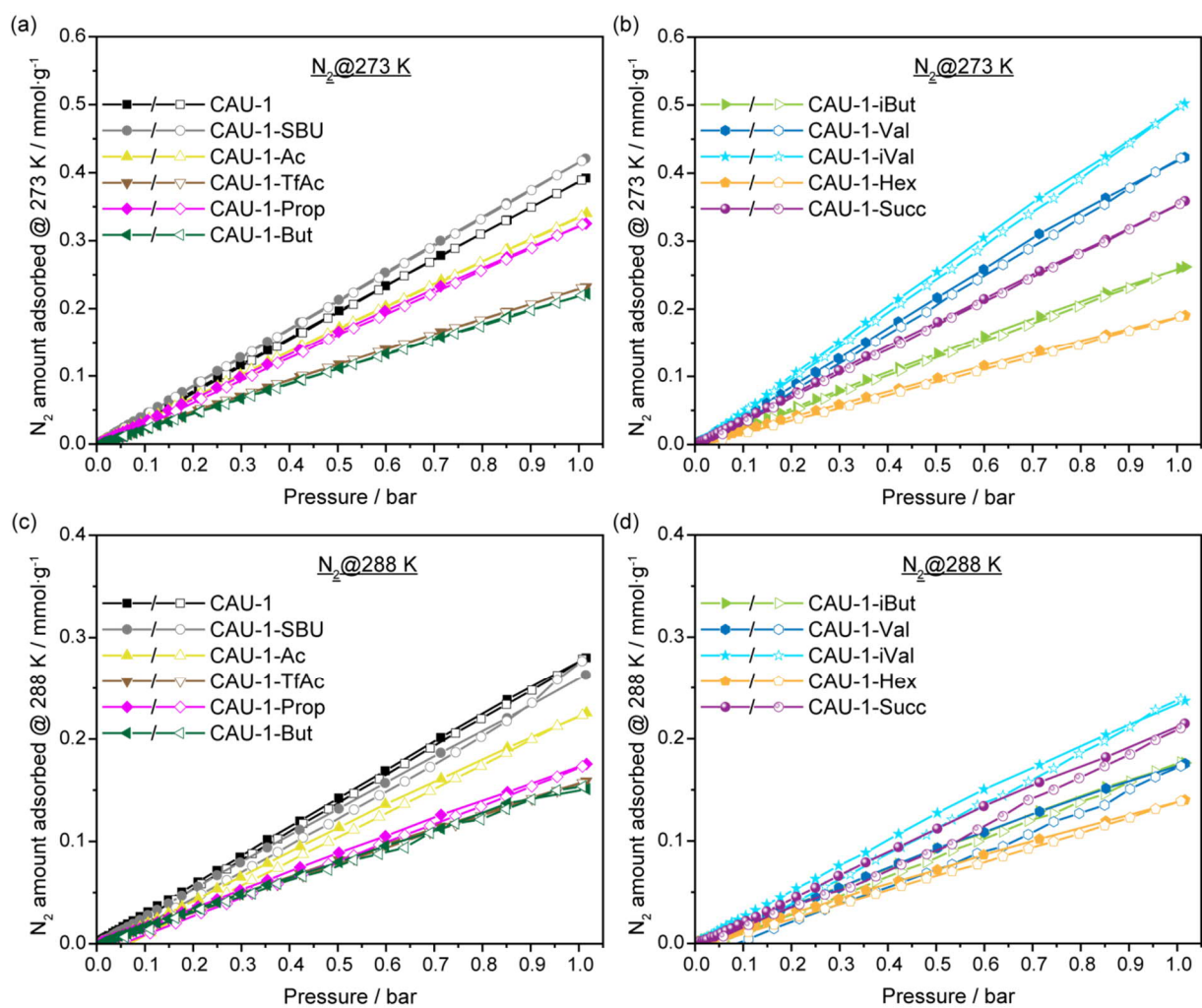
Figure S5.1.16: N$_2$ ad- and desorption isotherms of the (modified) CAU-1-nanoparticles at (a+b) 273 and (c+d) 288 K. Filled symbols depict the adsorption branch, empty symbols the desorption branch.

Figure S5.1.17: Henry fits of the adsorption isotherms at low pressures of CAU-1 of (a) CO_2 at 273 K, (b) CO_2 at 288 K, (c) N_2 at 273 K, (d) N_2 at 288 K, (e) CH_4 at 273 K and (f) CH_4 at 288 K. The Henry equation and correlation coefficient are given at the lower right of each graph.

Figure S5.1.18: Henry fits of the adsorption isotherms at low pressures of CAU-1-SBU of (a) CO_2 at 273 K, (b) CO_2 at 288 K, (c) N_2 at 273 K, (d) N_2 at 288 K, (e) CH_4 at 273 K and (f) CH_4 at 288 K. The Henry equation and correlation coefficient are given at the lower right of each graph.

Figure S5.1.19: Henry fits of the adsorption isotherms at low pressures of CAU-1-Ac of (a) CO_2 at 273 K, (b) CO_2 at 288 K, (c) N_2 at 273 K, (d) N_2 at 288 K, (e) CH_4 at 273 K and (f) CH_4 at 288 K. The Henry equation and correlation coefficient are given at the lower right of each graph.

Figure S5.1.20: Henry fits of the adsorption isotherms at low pressures of CAU-1-TfAc of (a) CO_2 at 273 K, (b) CO_2 at 288 K, (c) N_2 at 273 K, (d) N_2 at 288 K, (e) CH_4 at 273 K and (f) CH_4 at 288 K. The Henry equation and correlation coefficient are given at the lower right of each graph.
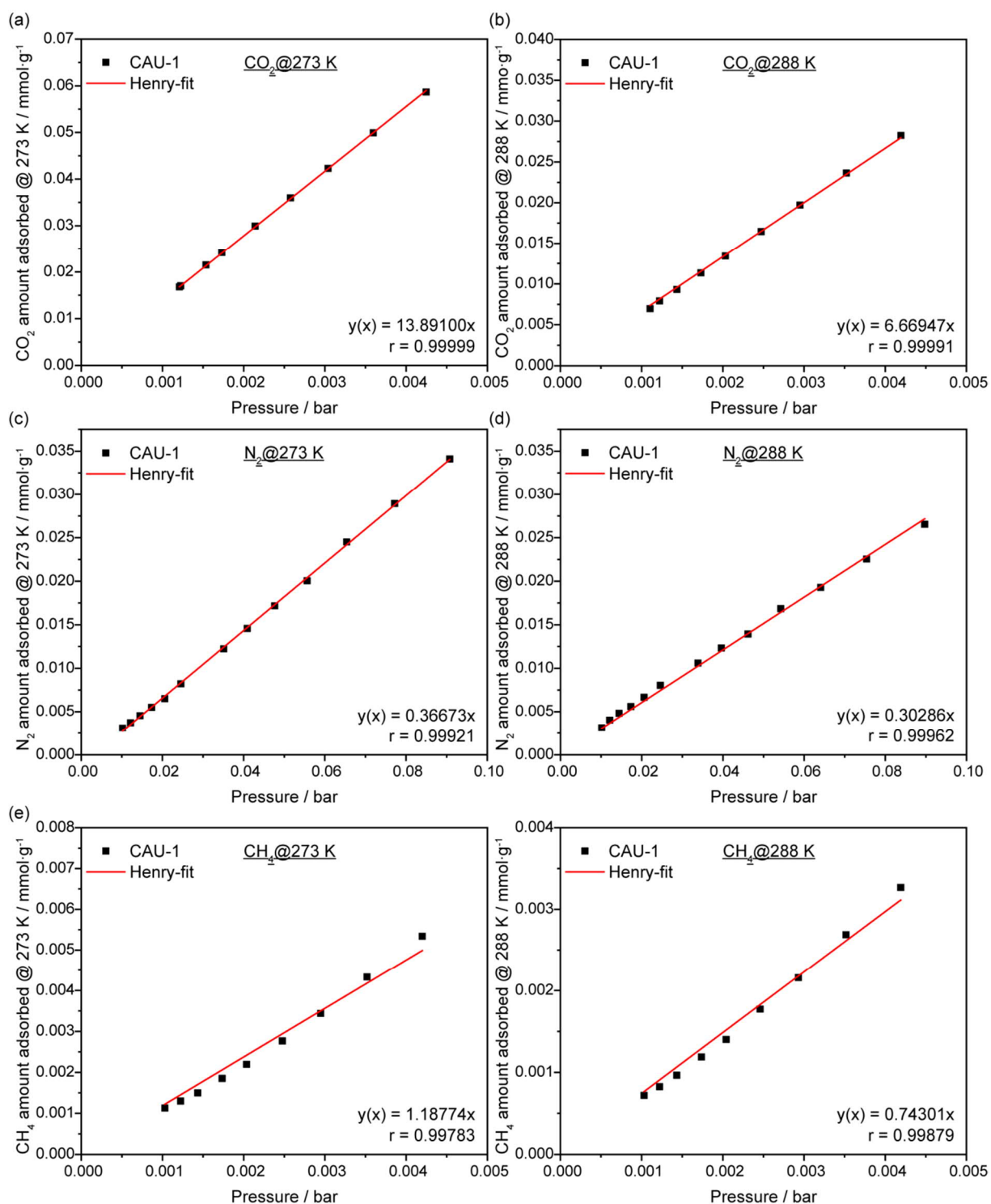
Figure S5.1.21: Henry fits of the adsorption isotherms at low pressures of CAU-1-Prop of (a) CO_2 at 273 K, (b) CO_2 at 288 K, (c) N_2 at 273 K, (d) N_2 at 288 K, (e) CH_4 at 273 K and (f) CH_4 at 288 K. The Henry equation and correlation coefficient are given at the lower right of each graph.
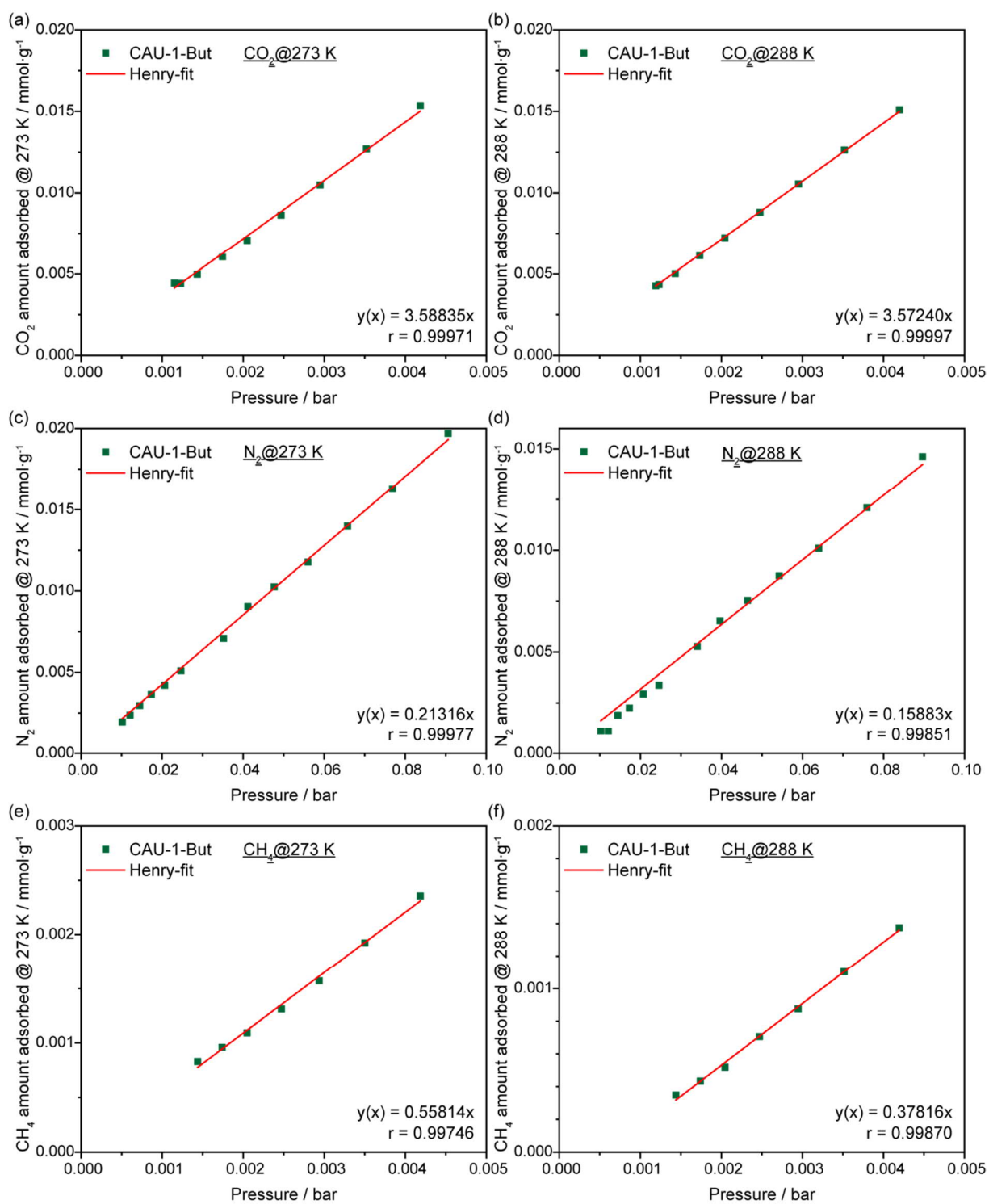
Figure S5.1.22: Henry fits of the adsorption isotherms at low pressures of CAU-1-But of (a) CO_2 at 273 K, (b) CO_2 at 288 K, (c) N_2 at 273 K, (d) N_2 at 288 K, (e) CH_4 at 273 K and (f) CH_4 at 288 K. The Henry equation and correlation coefficient are given at the lower right of each graph.
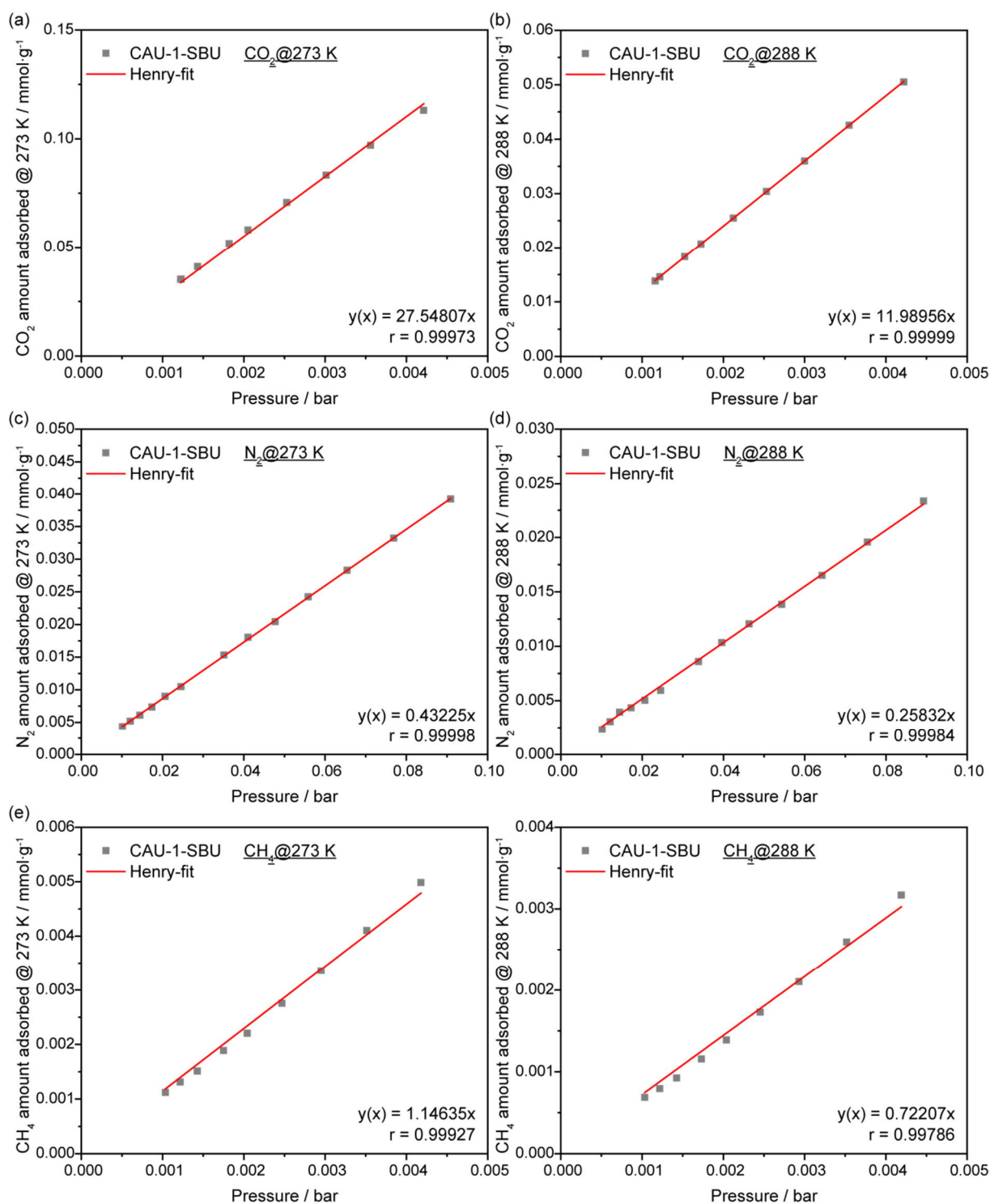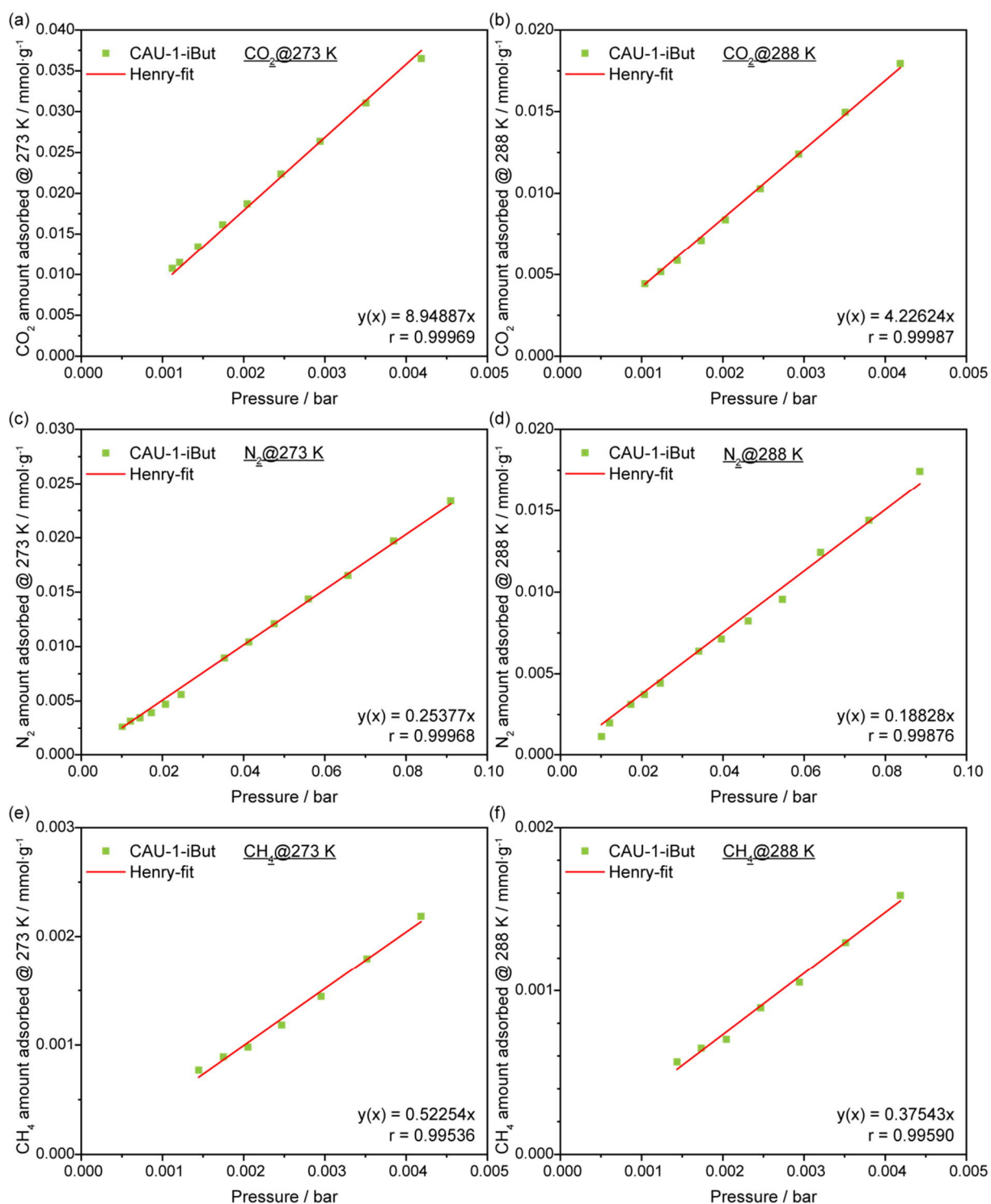
Figure S5.1.23: Henry fits of the adsorption isotherms at low pressures of CAU-1-iBut of (a) CO_2 at 273 K, (b) CO_2 at 288 K, (c) N_2 at 273 K, (d) N_2 at 288 K, (e) CH_4 at 273 K and (f) CH_4 at 288 K. The Henry equation and correlation coefficient are given at the lower right of each graph.
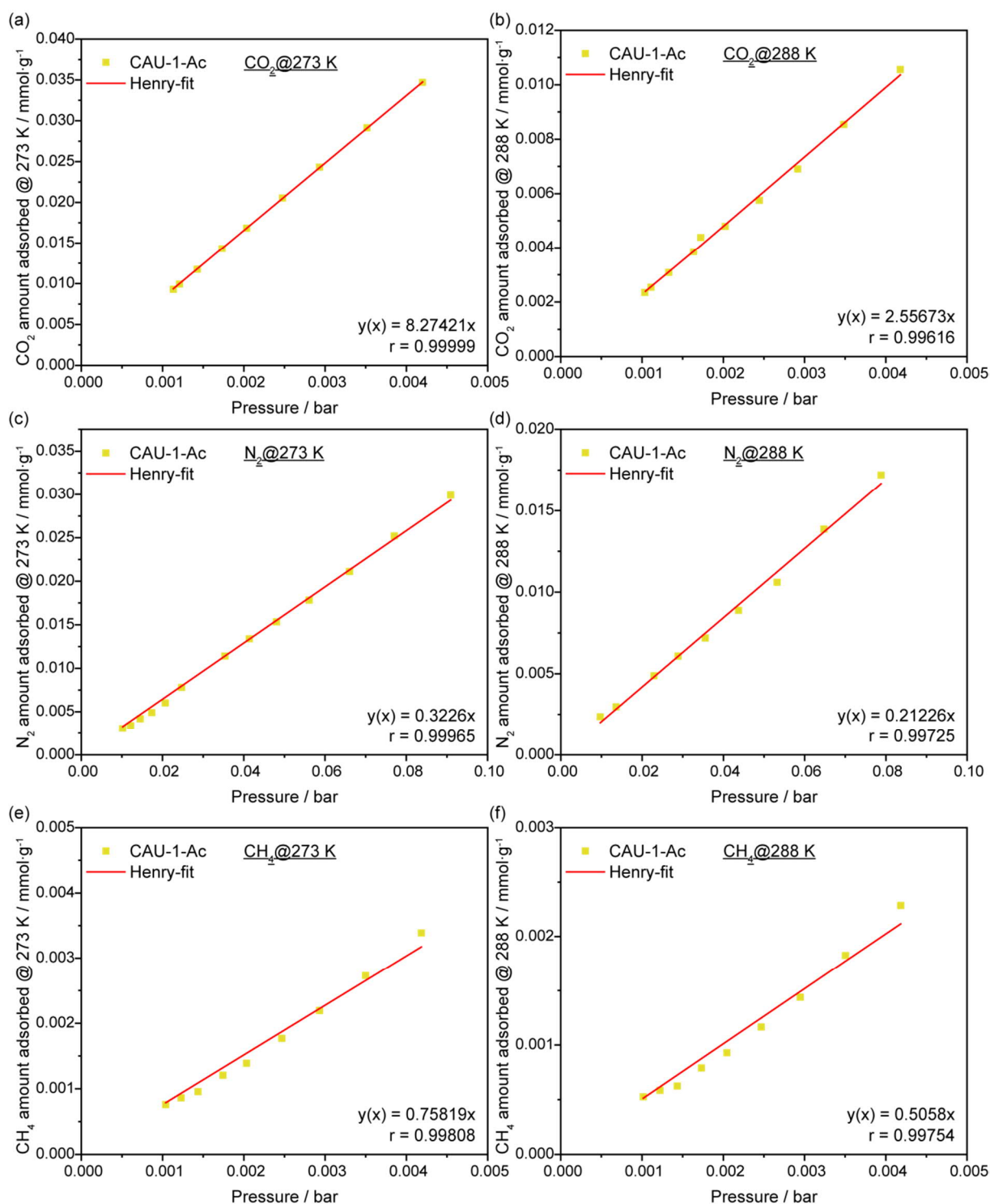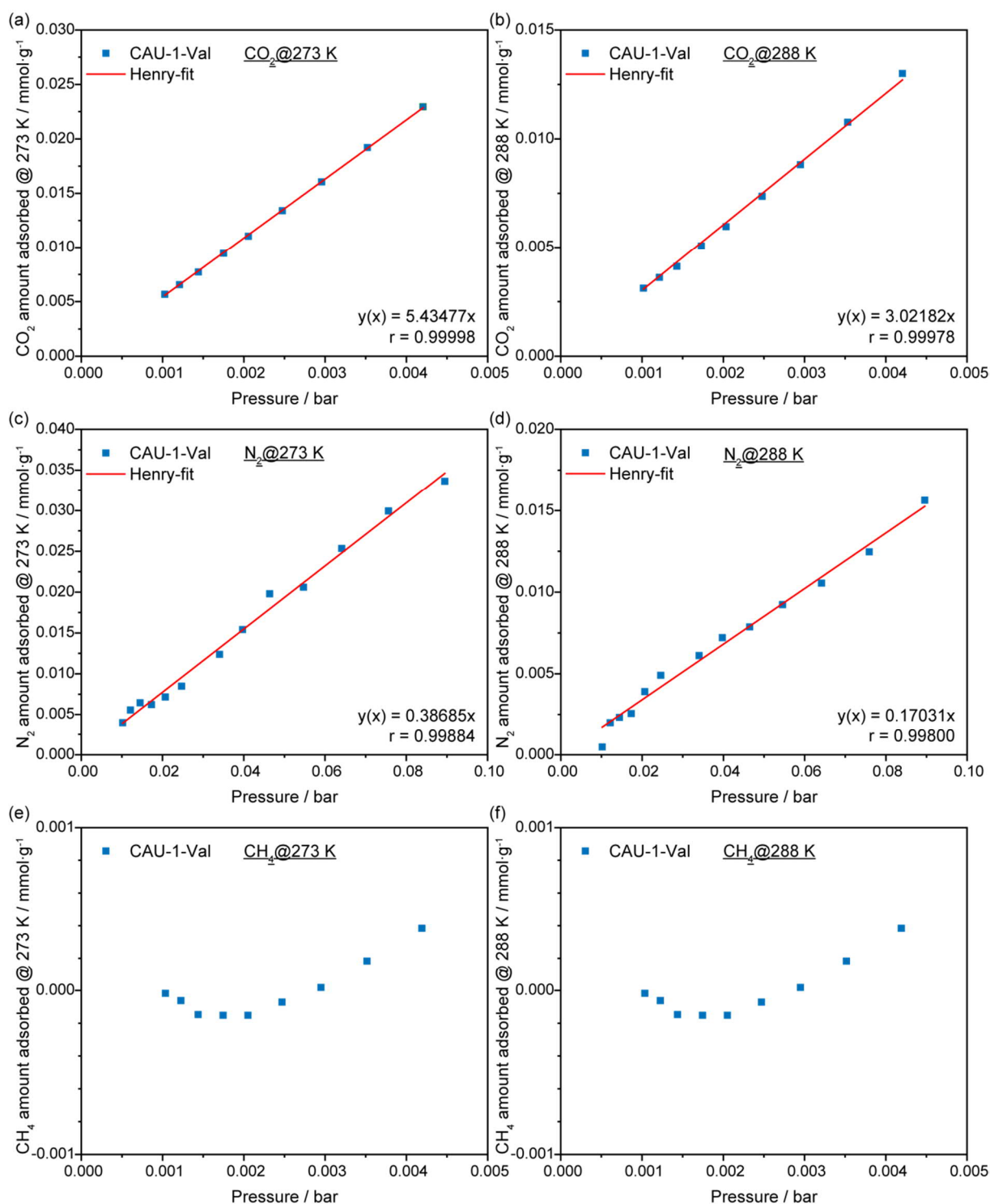
Figure S5.1.24: Henry fits of the adsorption isotherms at low pressures of CAU-1-Val of (a) CO_2 at 273 K, (b) CO_2 at 288 K, (c) N_2 at 273 K, (d) N_2 at 288 K, (e) CH_4 at 273 K and (f) CH_4 at 288 K. The Henry equation and correlation coefficient are given at the lower right of each graph.
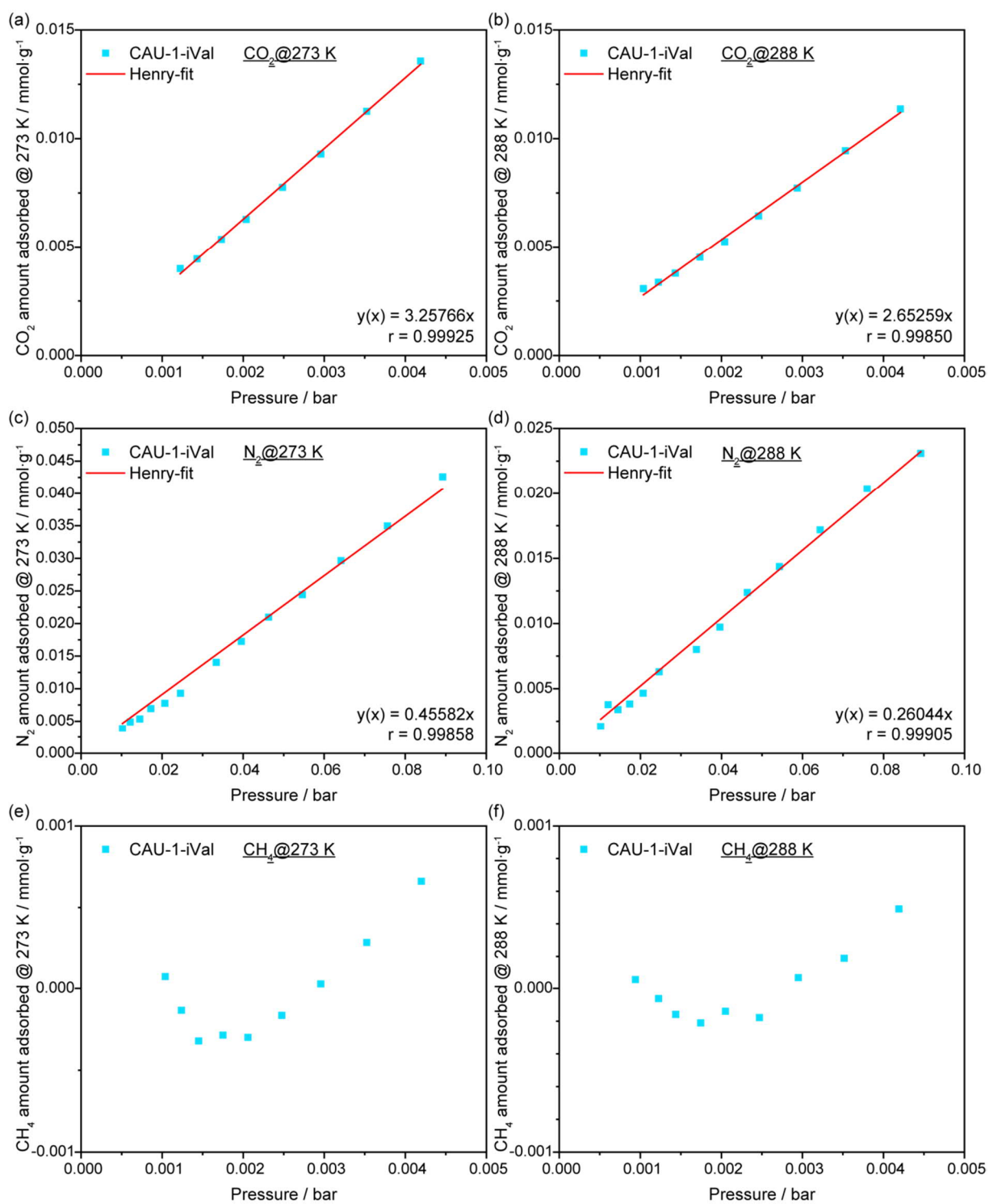
Figure S5.1.25: Henry fits of the adsorption isotherms at low pressures of CAU-1-iVal of (a) CO_2 at 273 K, (b) CO_2 at 288 K, (c) N_2 at 273 K, (d) N_2 at 288 K, (e) CH_4 at 273 K and (f) CH_4 at 288 K. The Henry equation and correlation coefficient are given at the lower right of each graph.
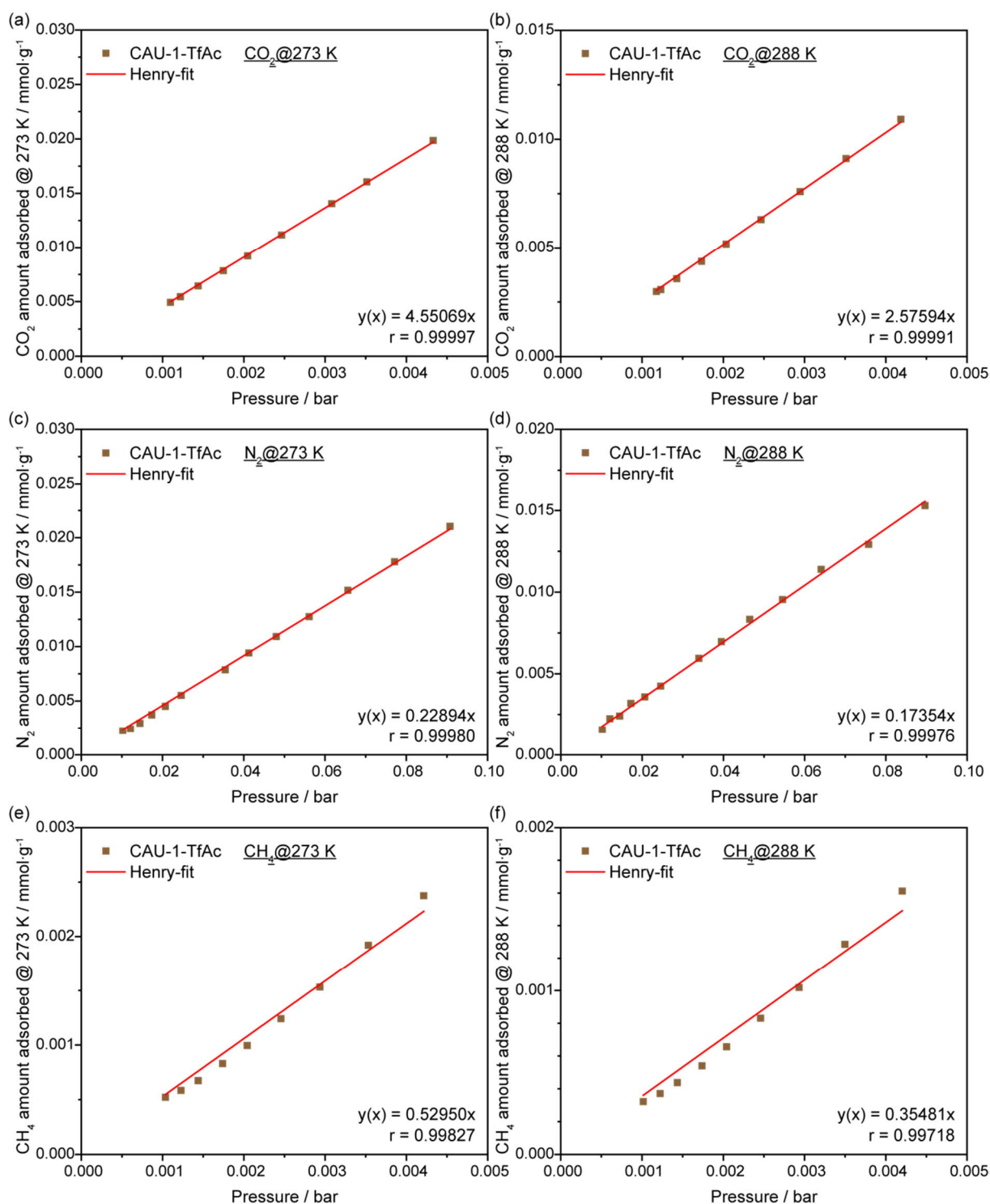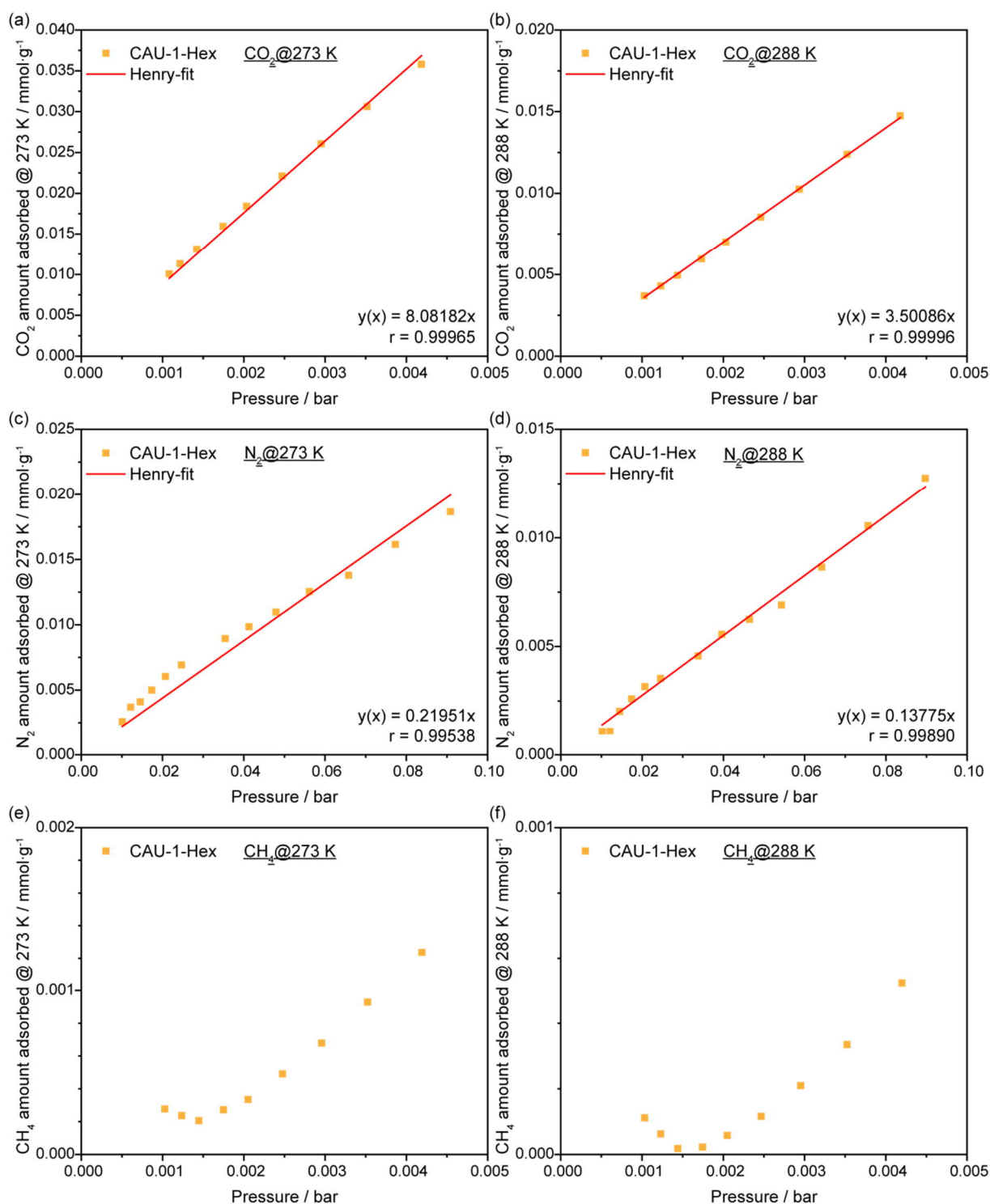
Figure S5.1.26: Henry fits of the adsorption isotherms at low pressures of CAU-1-Hex of (a) CO_2 at 273 K, (b) CO_2 at 288 K, (c) N_2 at 273 K, (d) N_2 at 288 K, (e) CH_4 at 273 K and (f) CH_4 at 288 K. The Henry equation and correlation coefficient are given at the lower right of each graph.
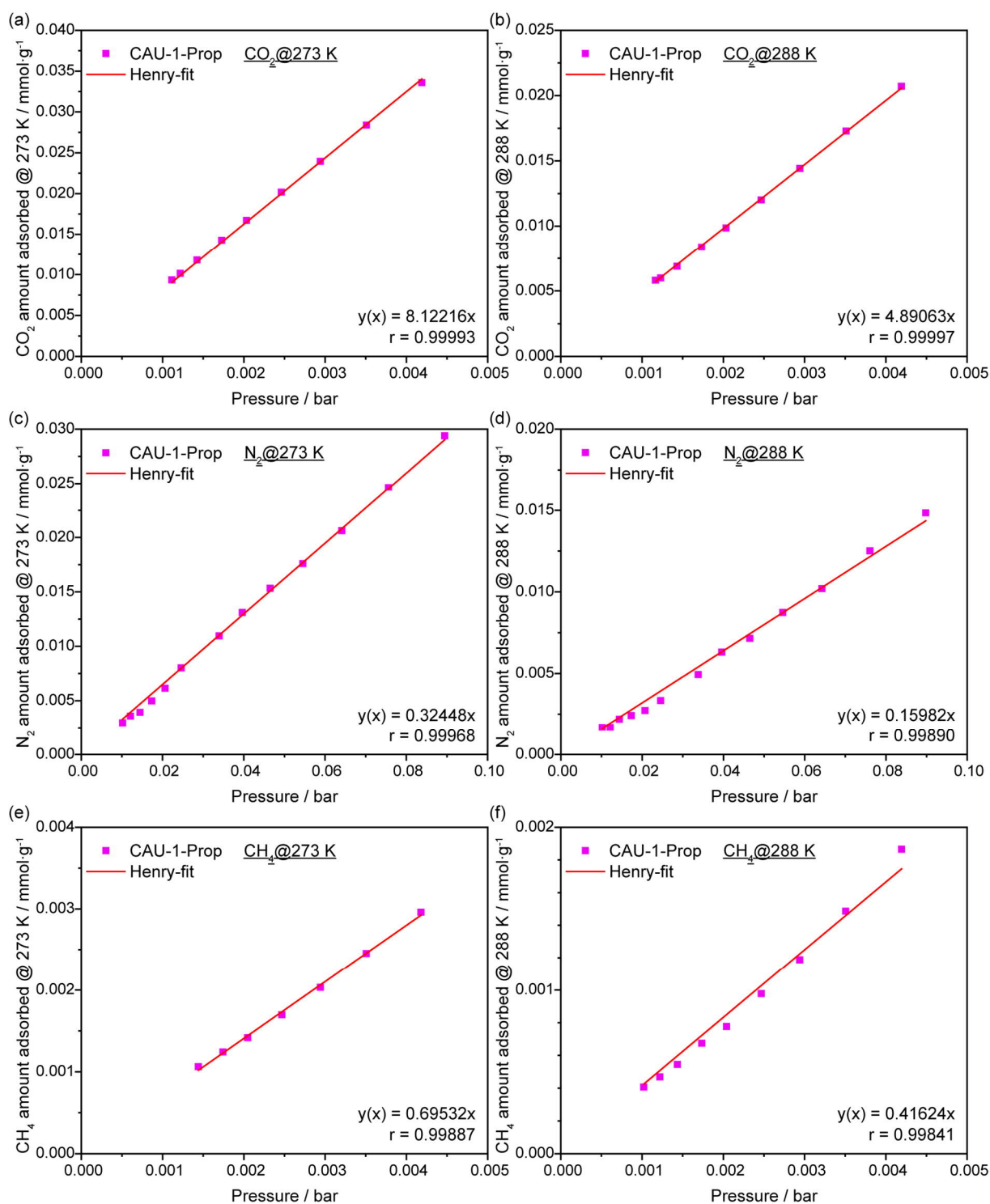
Figure S5.1.27: Henry fits of the adsorption isotherms at low pressures of CAU-1-Succ of (a) CO_2 at 273 K, (b) CO_2 at 288 K, (c) N_2 at 273 K, (d) N_2 at 288 K, (e) CH_4 at 273 K and (f) CH_4 at 288 K. The Henry equation and correlation coefficient are given at the lower right of each graph.
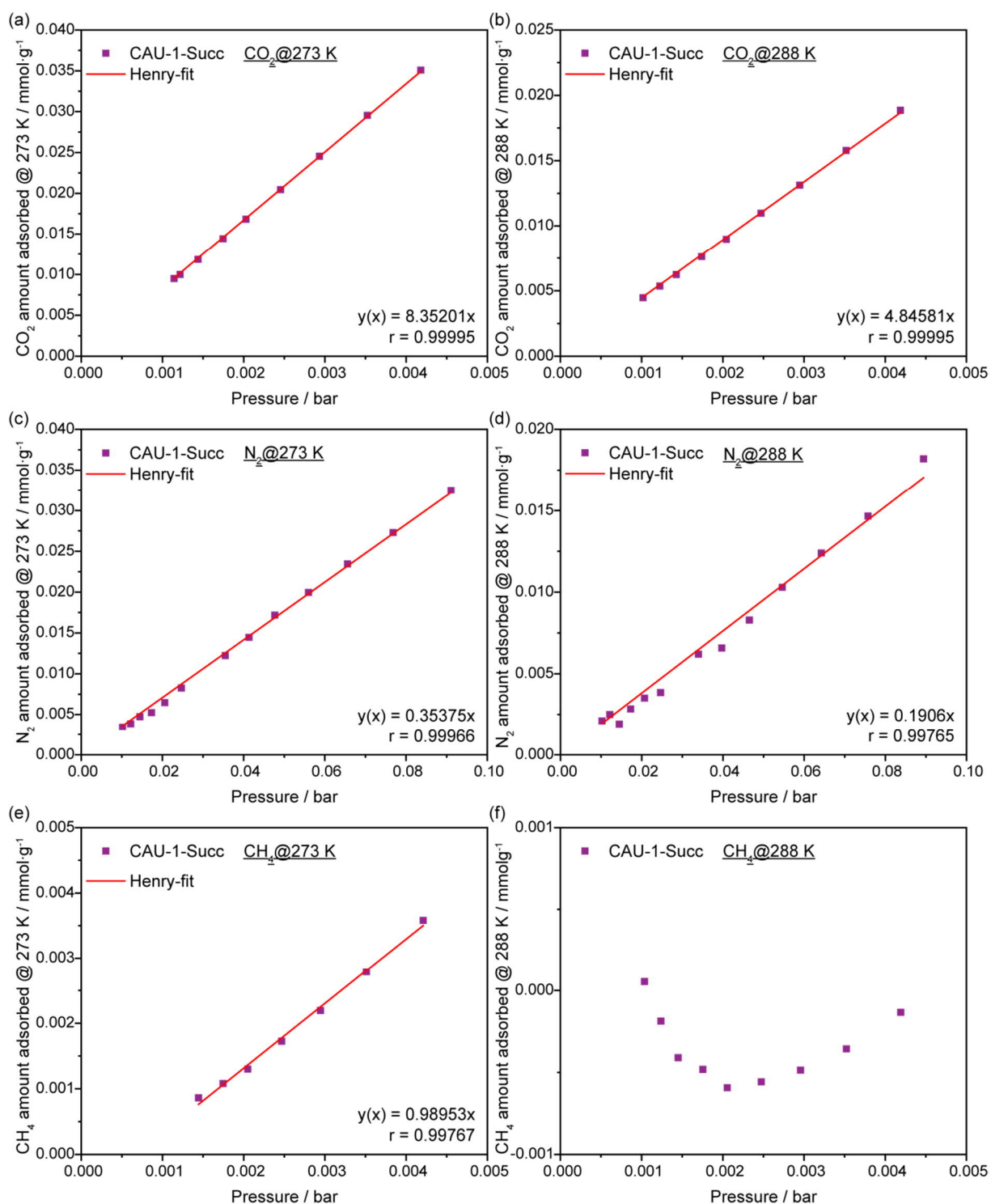
Table S5.1.3: Single and dual-site Langmuir fit parameters used for IAST selectivity calculations and the respective coefficient of determination of the fits.

Sample	T / K	Adsorptive	q_1 / mmol·g^{-1}	b_1 / Pa^{-1}	q_2 / mmol·g^{-1}	b_2 / Pa^{-1}	R^2
CAU-1	273	CO_2	0.64866027	14.02568988	16.77702656	0.29911438	0.99986752
		N_2	66.09847817	0.00590078	-	-	0.99996846
		CH_4	5.70505104	0.25777802	-	-	0.99989332
	288	CO_2	0.58041964	6.67120259	13.55351124	0.22668162	0.99998255
		N_2	5.12987060	0.05703176	-	-	0.99999002
		CH_4	4.92080332	0.19555324	-	-	0.99991377
CAU-1-SBU	273	CO_2	16.76963026	0.42773344	0.67521533	31.36672555	0.99938674
		N_2	9.94404507	0.04359791	-	-	0.99999911
		CH_4	7.91644364	0.17706919	-	-	0.99996410
	288	CO_2	0.61455113	13.24357765	15.09887008	0.27999593	0.99993866
		N_2	8.14478090	0.03283450	-	-	0.99999464
		CH_4	6.42929474	0.13870325	-	-	0.99998501
CAU-1-Ac	273	CO_2	9.85591473	0.44750306	0.29076940	13.58231944	0.99996843
		N_2	15.59115362	0.02199626	-	-	0.99998311
		CH_4	5.82494399	0.18654551	-	-	0.99997751
	288	CO_2	1.38888963	1.49671069	19.33735268	0.07636301	0.99935439
		N_2	266109.74044637	0.00000084	-	-	0.99977373
		CH_4	5.38692479	0.14146096	-	-	0.99998148
CAU-1-TfAc	273	CO_2	43.02607746	0.03989739	0.86213636	2.97603047	0.99872087
		N_2	7.20180315	0.03288442	-	-	0.99999670
		CH_4	5.13218584	0.13966234	-	-	0.99999311
	288	CO_2	7.54876052	0.23261118	0.15928474	6.03710277	0.99999820
		N_2	2.17309606	0.07787302	-	-	0.99999792
		CH_4	4.98366327	0.10023069	-	-	0.99998973
CAU-1-Prop	273	CO_2	0.21989799	19.02009043	6.96075028	0.54993200	0.99992627
		N_2	7.73881770	0.04337193	-	-	0.99998996
		CH_4	5.13960436	0.16461440	-	-	0.99997566
	288	CO_2	0.23465906	11.87669745	5.73617984	0.39942749	0.99990087
		N_2	16.02335256	0.01097060	-	-	0.99998283
		CH_4	4.22965115	0.13660003	-	-	0.99999380
CAU-1-But	273	CO_2	0.18603579	9.10438060	5.53796371	0.43054777	0.99997868
		N_2	11.69184762	0.01914178	-	-	0.99999228
		CH_4	3.86428361	0.18668720	-	-	0.99998343
	288	CO_2	0.17245845	11.12542143	3.96818594	0.45728909	0.99999012
		N_2	1.60264528	0.10526978	-	-	0.99994989
		CH_4	2.84825673	0.16798190	-	-	0.99999252
CAU-1-iBut	273	CO_2	0.23851055	23.82444911	4.87958588	0.60302669	0.99979999
		N_2	7.28719412	0.03692504	-	-	0.99997256
		CH_4	5.00671089	0.14956557	-	-	0.99994747
	288	CO_2	4.27520415	0.44415024	0.18689373	14.44140708	0.99977388
		N_2	2.24023848	0.08483668	-	-	0.99998715
		CH_4	3.62468546	0.14562612	-	-	0.99998046
CAU-1-Val	273	CO_2	3.95332071	0.58030722	0.23627440	13.42365650	0.99990684
		N_2	21.89025121	0.01970574	-	-	0.99979307
		CH_4	4.31846058	0.16668462	-	-	0.99953522
	288	CO_2	2.59590339	0.82748790	0.04384441	28.40722930	0.99801151
		N_2	2.26862832	0.08338691	-	-	0.99997590
		CH_4	3.36398731	0.13488075	-	-	0.99977255
CAU-1-iVal	273	CO_2	5.57683927	0.27774419	0.69212064	2.89090483	0.99989816
		N_2	22.55378317	0.02259864	-	-	0.99980352
		CH_4	6.36030357	0.12716087	-	-	0.99967806
	288	CO_2	3.94183305	0.36491715	0.24901082	6.06541448	0.99995052
		N_2	1.97584220	0.13493547	-	-	0.99997558
		CH_4	4.20936330	0.14748919	-	-	0.99987483

Table S5.1.3 (continued): Single and dual-site Langmuir fit parameters used for IAST selectivity calculations and the respective coefficient of determination of the fits.

CAU-1-Hex	273	CO_2	3.04303784	0.81483543	0.24292138	25.34294946	0.99981376
		N_2	2.44772753	0.08302548	-	-	0.99997420
		CH_4	3.07186578	0.19399272	-	-	0.99988599
	288	CO_2	0.19475466	10.92454843	2.67939617	0.55233301	0.99998309
		N_2	2.12860493	0.06976381	-	-	0.99999145
		CH_4	3.24389375	0.12558608	-	-	0.99988556
CAU-1-Succ	273	CO_2	6.64467689	0.57769124	0.53503766	9.01977421	0.99997050
		N_2	10.25344167	0.03570315	-	-	0.99998918
		CH_4	3.71962004	0.32803940	-	-	0.99992515
	288	CO_2	0.34055837	5.94512085	5.80142211	0.45318727	0.99999142
		N_2	4.27735933	0.05254825	-	-	0.99991384
		CH_4	3.73488503	0.19973669	-	-	0.99972617

6 SUMMARY AND OUTLOOK

Within only a few decades, MOF chemistry has become one of the most dynamic and fast-growing research fields. The molecular building block approach and so-called reticular chemistry has allowed to direct synthesis towards specific net topologies, in which the structure-related properties can be engineered to particular needs. This is reflected in the permanent intrinsic porosity, showing an impressive manifoldness in pore sizes and shapes, which are generally accompanied by high accessible surface areas. In addition, the concept of PSM adds a vast number of possibilities to further tune and alter the MOF properties, most notably in the pore environments. Hence, it is no surprise that the potential of MOFs for several applications that require defined pores has been identified very soon within this research field and shifts gradually more towards their use as functional materials and further implementation into integrated devices. For the latter, this adds the necessity to control and manipulate the structuring of MOFs at several length scales, e.g. the fabrication of nanoparticles and thin films of defined sizes, thicknesses, morphologies, etc.

In this thesis, the impact and possibilities that arise from PSM of MOFs for diverse applications have been demonstrated. In Chapter 3, we could prove the so far undescribed deposition of a porous MOF from the gas/vapor phase by femtosecond pulsed laser deposition, expanding the structuring and film formation methods available for MOFs. We could achieve this by a reversible, non-covalent PSM, which reinforces the MOF structurally to prevent its degradation. In Chapter 4, we extend the concept of PSM to an integrated device as a whole, namely a one-dimensional photonic crystal sensor. Here, the functional MOF layer is decisive for the optical discrimination of the vaporized analytes tested. By a PSM of the entire, as-assembled photonic crystal, we could show enhanced selectivities towards the analytes while guaranteeing comparability with the other samples. In Chapter 5, we have systematically studied the influence of several PSMs on the sorption properties of these (modified) MOFs and identified the sample with the most polar groups as the best performing MOF in regard to selectivity of CO_2 over N_2 and CH_4.

Physical Vapor Deposition of MOFs

The work presented demonstrates the successful fabrication of a MOF film by physical vapor deposition, namely femto-second pulsed laser deposition. The experiments showed that direct irradiation of a pure MOF target, namely ZIF-8 nanoparticles pressed into a pellet, failed to produce crystalline films on a sapphire substrate. If, however, the ZIF-8 particles were protected via a non-covalent modification with the polymer PEG-400, a crystalline film of the ZIF-8 composite material was formed. The data further shows that the polymer not only protects the nanoparticles by encapsulation but also reinforces the framework structurally by penetration and filling of the MOF pores. It is reasonable to assume that this modification prevents the pore collapse upon ablation and simultaneously aids the reassembly on the substrate. Furthermore, the porosity could be recovered by a simple washing step with ethanol. All in all, the work proves that the deposition of a ZIF-8 film from the gas phase is indeed possible. Therefore, this study acts as a proof-of-concept for the PLD of a MOF and provides a general strategy for the stabilization of fragile compounds that else would not be amenable to this deposition method.

Nonetheless, this study can only be seen as the first step towards establishing this as a general stabilization approach. Naturally, a broad number of MOFs should be deposited by this method to experimentally generalize the concept, as well as optimize the deposition parameters for a full control of film thickness, crystallinity and morphology. More importantly, many incognita related to the underlying mechanism, remain to be elucidated and would require further in-depth investigation. This encompasses several aspects, from the elucidation of the light-matter interaction of the laser with the target, the influence of the wavelength and pulse length, to the ejected fragments formed during irradiation, the possible processes within the ablation plume and, finally, the dynamics, recrystallization and reassembly of the fragments or particles on the substrate. By successfully fabricating a MOF film by PLD and establishing a structural model of the hybrid material, the basis for further investigations has been laid.

Post-modification of MOFs in Bragg Stack Sensors

Up to date, the optical response of MOF based PC sensors towards organic vapors was owed to the particular structure of the individual PC and type of MOF used in it. Hence, the observed optical shifts were sample specific and barely comparable. In this work, this major drawback was addressed by providing a generic platform with similar optical properties, which can be modified as desired to enhance the sensor selectivity whilst retaining the comparability of the optical answer. To this end, CAU-1 nanoparticles were stacked alternatively into thick MOF layers and thin TiO_2 layers yielding BSs of three bilayers, in which the MOF layers dominate and account for the optical response. Post-modification of the entire BS targeting either the SBU by demethoxylation or the linker by amidification with hexanoic anhydride yielded structurally intact BSs with similar optical properties like the pristine

BSs, but, with an altered optical response to analytes and, hence, improved selectivity. Additionally, by performing the modification step on the already assembled BS, tedious, time-consuming and, potentially expensive adjustments at other steps are avoided. The BS sensors exhibit reproducible sensing signals, which can be detected by various routes, e.g. by the readout of the reflectance spectra shift, by a time-dependent reflectivity measurement at a specific wavelength or by a color-based image analysis via PCA, facilitating analyte discrimination.

Obviously, the data evidence the significant impact of the modification, nonetheless, it is still unknown which factors are mainly responsible for the optical response. It is therefore still necessary to dissect the individual contributions to the spectral shift of the analytes` RIs and sizes, as well as their chemical affinity and interaction with the MOF. Additionally, an important aspect that needs to be considered is the microporosity of the MOF nanoparticles vs. the textural porosity of the layer. It would be of interest to assess how the (re-)activation procedure impacts on the accessibility of the micropores and how uptake into the framework pores contributes to the optical shift compared to that of the textural pores. Hand in hand with this aspect, the diffusion processes relevant upon adsorption and desorption need to be studied in detail in order to extract information that could finally help to improve sensing and reactivation kinetics. A focus could lie on the relatively dense TiO_2 layer that, potentially, acts as a diffusion barrier. Furthermore, the impact of the measurement itself must be taken into consideration, e.g. whether the vapor is allowed to equilibrate within the sensor or is exposed dynamically as it is the case in this study. All in all, having a more in-depth understanding of the aspects mentioned could help to engineer and tune MOF based BS sensors significantly improving their performance.

Post-synthetically modified MOFs for sorption applications

In this work, several post-synthetic modifications on CAU-1 nanoparticles were successfully performed and their altered sorption behavior towards Ar, CO_2, N_2 and CH_4 investigated. The modifications include the demethoxylation of the SBU and the amidification of the amine moiety at the bridging organic linker. The modifications were structurally confirmed by IR and NMR, the structural integrity with XRD and the nanoparticle nature by DLS and SEM. Subsequently, physisorption experiments were conducted for the pore characterization and to evaluate the storage and separation capacity of CO_2, N_2 and CH_4 of the (modified) MOFs. The results can be summarized into two main conclusions. On one hand, CO_2 adsorption capacities are mainly dominated by the surface areas of the different samples. Furthermore, an improved performance could be achieved by providing polar groups and amines, as evidenced by CAU-1-SBU, exposing hydroxy groups at the SBU and a polar amine group on the linker. This sample not only showed the best uptakes for CO_2, but also proved to perform best for the separation of CO_2 from gas mixtures with N_2 and CH_4, according to Henry and IAST selectivity measurements. On the other hand, the resulting data for the largest modifications, and, consequently, smallest pores, uncover the problem of very small uptakes as these isotherms exhibited large errors

and, in some cases, erratic behavior, e.g. inverted hysteresis curves or negative uptakes. We therefore point out that for small sample amounts exhibiting poor uptakes, equilibrium physisorption measurements are not the method of choice. We therefore suggest that for the evaluation of the separation performance, breakthrough experiments are probably more sensible and reliable.

Despite having identified CAU-1-SBU as the best modification by the means described in Chapter 5, we admit that the absolute values are not competitive with benchmark MOFs reported in the literature. Nonetheless, our data adds experimental proof of the beneficial structural features, such as the presence of polar groups. Future work will have to specifically show that the improved performance is indeed structurally related to the SBU by exactly identifying the relevant binding sites. For this MOF, it also includes to modify the amidified CAU-1 samples at the SBU. More importantly, realistic conditions, such as the presence of humidity, must be taken into account experimentally to reliably assure that these materials can be applied outside laboratory conditions. In regard to the CH_4 measurements, this also includes to extend the pressure range far beyond 1 bar, e.g. for storage application. Likewise, the activation procedure should be modified, e.g. by supercritical CO_2 extraction, to ensure the mild and complete removal of pore blocking reaction products and solvents.

7 APPENDIX

In the following, the chapter contributions, a list of abbreviations and the curriculum vitae of the author is given.

7.1 CHAPTER CONTRIBUTIONS

In the following, an overview of the work and contribution of the authors listed at the beginning of each chapter and other people involved to a minor degree is given. Analysis by technical staff and service groups, which is acknowledged in the chapter, is not mentioned specifically.

In Chapter 3, the first synthesis of the ZIF-8 compound and its modification was done by Annekathrin Fischer. Pressing of the material into a target, subsequent femto-second laser deposition of it, as well as the XRD and Raman characterization of the obtained films was done by Dieter Fischer. Further material was synthesized and characterized by Alberto von Mankowski. ^{1}H-NMR and ^{1}H–^{13}C-HETCOR experiments and their interpretation, given in the Supporting Information, were performed by Suresh K. Vasa and Rasmus Linser. Screening the literature, writing the manuscript and creating the graphs was done to equal parts by Dieter Fischer and Alberto von Mankowski. The Table of Content graphic was designed by Alberto von Mankowski. The manuscript was revised by Jochen Mannhart and Bettina V. Lotsch. The parts concerning the ^{1}H-NMR and ^{1}H–^{13}C-HETCOR experiments were written and revised by Suresh K. Vasa and Rasmus Linser. The work was supervised by Bettina V. Lotsch.

For Chapter 4, preliminary experiments including material synthesis, Bragg stack production and their optical characterization were performed by Charlotte Koschnick under the supervision of Alberto von Mankowski. This work mainly served to improve and minimize errors in the experimental setup of the optical characterization during vapor exposure. The samples discussed in the chapter were synthesized, fabricated, characterized and investigated by Alberto von Mankowski. Theoretical calculations of the reflectance spectra and the RIs were done by Katalin Szendrei-Temesi. Screening of the literature, writing the manuscript and creating the graphs was done by Alberto von Mankowski. The Table of Content graphic was designed by Katalin Szendrei-Temesi and Alberto von Mankowski. The work was supervised and the manuscript was revised by Bettina V. Lotsch.

For Chapter 5, Marie Bayer identified optimum reaction conditions for the post-synthetic modifications. The samples discussed in the chapter were synthesized, modified and investigated by Alberto von Mankowski. Fitting of the XRD patterns and crystalline domain size extraction was performed by Sascha Harm. Fitting of the CO_2, N_2 and CH_4 isotherms and the calculation of IAST selectivities was done by Alberto Jiménez-Solano. The work was supervised by Bettina V. Lotsch.

7.2 LIST OF ABBREVIATIONS

BS	Bragg stack	NMR	Nuclear Magnetic Resonance
CAU	Christian-Albrecht University (University of Kiel)	NLDFT	Non-local DFT
		PC	Photonic crystal
conc.	concentrated	PCA	Principal component analysis
correl.	correlation	PDI	Polydispersity index
DFG	Deutsche Forschungsgemeinschaft	PEG	Polyethylene glycol
		PLD	Pulsed laser deposition
DFT	Density functional theory	PSD	Pore size distribution
HoA	Heats of adsorption	PXRD	Powder XRD
IAST	Ideal adsorbed solution theory	QSDFT	Quenched-solid DFT
IR	Infrared	RI	Refractive Index
LMU	Ludwig-Maximilian University (University of Munich)	SA	Surface area
		SEM	Scanning electron microscopy
MAS	Magic angle spinning	TEM	Transmission electron microscopy
MBB	Molecular building block	vs.	versus
MOF	Metal-organic framework	XRD	X-ray diffraction
MPI-FKF	Max-Planck-Institute for Solid State Research	ZIF	Zeolitic imidazolate framework

7.3 CURRICULUM VITAE

Personal Information

Name	Olaf Alberto von Mankowski
Date of birth	30.08.1989
Place of birth	Munich, Germany
Nationality	German

Education

Postgraduate

10/2013 – 10/2018	Ph.D., LMU, Munich, Germany
	MPI-FKF, Stuttgart, Germany
	Ph.D. thesis: Prof. Dr. Bettina V. Lotsch

Master of Science

10/2011 – 08/2013	M.Sc. of Chemistry, LMU, Munich, Germany
	Master thesis: Prof. Dr. Bettina V. Lotsch

Bachelor

10/2007 – 04/2011	B. Sc. of Chemistry and Biochemistry, LMU, Munich, Germany
	Bachelor thesis: Prof. Dr. Ulrich Koszinowski

School

09/1995 – 07/2007	European School Munich
09/1995 – 07/2004	St. Anna Schule, Munich, Spanish

Publications

2018	„Improving analyte selectivity by post-assembly modification of metal-organic framework based photonic crystal sensors", A. von Mankowski, Katalin Szendrei-Temesi, Charlotte Koschnick, Bettina V. Lotsch Nanoscale Horizons 2018, 3, 383-390
2017	„ZIF-8 Films Prepared by Femtosecond Pulsed-Laser Deposition", D. Fischer, A. von Mankowski, A. Ranft, S. K. Vasa, R. Linser, J. Mannhart, B. V. Lotsch, Chemistry of Materials 2017, 29 (12), 5148-5155

2015   „1D photonic defect structures based on colloidal porous frameworks: Reverse pore engineering and vapor sorption" A. Ranft, I. Pavlichenko, K. Szendrei, P. M. Zehetmaier, Y. Hu, A. von Mankowski, B. V. Lotsch

Microporous and Mesoporous Materials 2015, 216, 216-224